Dissertations

Fall 12-1-2018

Polyhedral Oligomeric Silsesquioxane-phosphate Glass Matrix Nanocomposites with Additional Chapter on Phosphate Glass-Poly(ethylene terephthalate) Matrix Composites

Kyoungtae Kim
University of Southern Mississippi

Follow this and additional works at: https://aquila.usm.edu/dissertations

Part of the Ceramic Materials Commons, Inorganic Chemistry Commons, Polymer and Organic Materials Commons, and the Polymer Chemistry Commons

POLYHEDRAL OLIGOMERIC SILSESQUIOXANE-PHOSPHATE GLASS MATRIX

NANOCOMPOSITES WITH ADDITIONAL CHAPTER ON PHOSPHATE GLASS-

POLY(ETHYLENE TEREPHTHALATE) MATRIX COMPOSITES

by

Kyoungtae Kim

A Dissertation
Submitted to the Graduate School,
the College of Arts and Sciences
and the School of Polymer Science and Engineering
at The University of Southern Mississippi
in Partial Fulfillment of the Requirements
for the Degree of Doctor of Philosophy

Approved by:

Dr. Joshua U. Otaigbe, Committee Chair
Dr. Sarah E. Morgan
Dr. William L. Jarrett
Dr. Derek L. Patton
Dr. Joseph D. Lichtenhan

_____ _____ _____
Dr. Joshua U. Otaigbe   Dr. Jeffrey S. Wiggins   Dr. Karen S. Coats
Committee Chair   Director of School   Dean of the Graduate School

December 2018

Published by the Graduate School

THE UNIVERSITY OF
SOUTHERN
MISSISSIPPI.

ABSTRACT

Preparation and characterization of tin fluorophosphate glass (Pglass) matrix nanocomposites incorporating polyhedral oligomeric silsesquioxane (POSS) were investigated on the structural, thermal, morphological, mechanical, and rheological properties. Various processes including synthesis, extrusion and sintering processes were applied to prepare the nanocomposite samples, and a series of characterizations were performed to enhance a comprehensive understanding of POSS/Pglass system. Another application of POSS with hydrophobic functional groups on the well-structured nanoscale silicate cage with three silanol groups was investigated to present the feasibility to use POSS molecule as a coating material on the surface of the hydrophilic inorganic glass. In addition, Poly(ethylene terephthalate) polymer matrix composites incorporating Pglass was studied to present the benefits of the Pglass with ultra-low glass transition temperature.

Obtained nanocomposites via one pot synthesis method using Pglass and trisilanol phenyl POSS (TSP-POSS) showed significant increase of glass transition temperature (T_g) due to the bulky POSS molecules. The synthesized nanocomposites were effectively mixed in the carbon crucible by gases produced during the process, resulting in homogeneous dispersion of POSS in the Pglass matrix, showing transparent optical property and improved rheological, mechanical, and thermal properties. While during the extrusion process mechanical force was used to homogeneously mix the TSP-POSS in the Pglass matrix, determining highly porosity due to the function of a foaming agent of POSS. The studies revealed tunable morphology with respect to the amount of POSS and the extrusion conditions. ^{29}Si Solid state NMR showed that after extrusion process silanol

groups of TSP-POSS are all consumed by condensation reaction, consistent with the result of NMR analysis using the Pglass matrix nanocomposites prepared by sintering process. POSS molecules effectively were dispersed in the Pglass and chemically reacted with Pglass molecules lead to ingenerate the increase of T_g and increased chemical stability of nanocomposites compared to that of pure Pglass.

The novel approach using POSS molecule which is grafting hydrophobic function groups on the core, are utilized to lead increased hydrophobicity of the glass surface. To mimick a lotus leaf with a combination of roughness and low surface energy, the micro-sized Pglass particle and hydrophobic POSS were used. Contact angle of the obtained surface-modified hydrophobic Pglass showed significant improvement compared to bulk pure Pglass. The umbrella effect of the long alkyl chains on bulky POSS core effectively covered the hydrophilic Pglass surface and significantly improved water repellency of the surface of bulk Pglass. In addition, Pglass/PET hybrids were successfully prepared using a mixing process. Various characterizations were performed to understand structure-property correlation in the hybrids with respect to amount of Pglass in the PET and experimental conditions. The investigation of morphological, structural, rheological, and crystallization properties revealed unique properties of Pglass/PET hybrids, attributed to the plasticizer and nucleation effects of polydispersed Pglass particles as well as the increased interfacial interaction between two components in the hybrids.

ACKNOWLEDGMENTS

DEDICATION

First and foremost, I would like to thank my wife, Hyunjung, for her sacrifice, understanding, support and invaluable love during my study.

I would like to thank my parents for their devotional love and support in the pursuit of my education. I am sure that my father be happy in the heaven.

I would like to thank my sons, Kyuryeon and Euiryeon. Their love made me stronger and gave me motivation to go forward continuously. And I would like to thank my brothers, sisters, and their family.

TABLE OF CONTENTS

LIST OF TABLES

LIST OF ILLUSTRATIONS

xvii

CHAPTER I - INTRODUCTION

1.1 Thesis Organization

  This thesis consists of seven chapters. Chapter 1 is a summary of literature on

organic polymer matrix composites and inorganic tin fluorophosphate glass (Pglass)

matrix composite materials with the various preparation methods, characterizations, and

properties. In addition, the principles of surface modification using polyhedral oligomeric

silsesquioxane (POSS) for hydrophobic property is reviewed. Mainly, the scientific study

and information related with POSS/Pglass composites in addition to Pglass/PET hybrid

will be discussed including the introduction of POSS and Pglass. Chapter 2 is a published

journal article in Journal of Non-Crystalline Solids, which showes the effect of addition

of POSS molecules in the inorganic Pglass matrix composites using one pot synthesis

method. Chapter 3 is a published journal article in Materials Letters, which examines the

unique effects of the amount of POSS and process conditions in the Pglass matrix and for

the porous structure of composites prepared by extrusion in the melting condition.

Chapter 4 discusses the thermal, physical and structural studies of POSS/Pglass

composites prepared by the sintering method. Chapter 5 examines another aspect using

Pglass and POSS materials to achieve nature-inspired hydrophobic modification using

POSS on the hydrophilic glass surface via dip coating method. Modified hydrophobic

surface structure-property relationship was investigated including the effect of surface

roughness on the hydrophobicity. Chapter 6 is a published journal article in Polymer,

which mainly discusses unexpected effects of Pglass in organic polymer matrix on the

crystallization and rheological properties characterized by solid-state NMR and

rheometer, respectively. Finally, Chapter 7 presents a summary of conclusions of the

thesis and the future works to be conducted on intensive study related with current topics and the extension of new topics.

1.2 Literature Review

Polymer materials remarkably replaced many materials such as natural organic materials and metals. New applications of polymer materials dramatically increased over the last several decades because of the advantages of polymer materials in processing, cost, and light weight [1-3]. However, there was a limitation of polymer for the high-performance applications due to the lower mechanical properties such as modulus, toughness, and strength compared to metals and ceramics. In addition, there are needs of new materials for new advanced technologies recently developed, requiring various specific properties such as thermal, morphological, rheological, optical and mechanical properties. Polymer composite technology is a suitable approach to prepare new materials with improved properties [4-7] for the new applications with the needs from industry and scientific research with synergetic properties [8]. Simply, more than two polymers can be mixed to obtain new materials with predictable combined properties of each pure component [9, 10]. However, there is a limitation to satisfy the various needs of complicated and advanced applications with this simple method.

Hybrid types of composites are widely studied and developed to prepare new materials due to their remarkable enhanced benefits, satisfying the needs from various advanced applications in the industrial and scientific areas. Organic/inorganic hybrid materials are common types of composite materials which can achieve various tailorable properties with various fillers [11] and preparation techniques [12]. In general, polymer composite materials are defined as combined materials with matrix materials of organic

2

polymers and fillers including carbon nanotubes, carbon fibers, graphene, exfoliated layered silicates and inorganic particles (e.g. glass, SiO_2, Al_2O_3, $CaCO_3$) which can improve the composites' properties not to be obtained by either component (i.e. matrix and filler) [13-16]. There are several main key factors about fillers which can influence the properties of the organic polymer matrix composite. First, the size of fillers in the organic polymer matrix is closely related with the interface area between matrix materials and fillers. Conventionally, the size of filler was microscale; however, nanoscale fillers are widely utilized due to the advantages of their small size, so called "nano-effect" studied by many researchers [17, 18]. Second, the dispersion of fillers in the organic polymer matrix is critical. Therefore, many researchers applied various techniques to improve the dispersion ability of fillers in the matrix [19, 20].

There are many methods in preparation of composites including in-situ polymerization, mixing in melt states, and other techniques (e.g. extrusion and solution method) [21-23]. Some researchers used only one technique while many researchers utilized combinations of each technique rather than only one method to achieve better dispersed composites with improved properties [24]. First, in-situ polymerization is the most common technique in preparation of composites [25]. For better dispersion of fillers in monomers before polymerization, an additional technique can be applied such as stirring and sonication [26]. In addition, the homogeneous dispersion of fillers in the matrix was enhanced by the surface modification of fillers to improve the compatibility between matrix molecules and fillers [27]. Second, mechanical mixing in the melt state is an effective method to disperse the fillers in the polymer matrix. The mechanical mixing process can be performed using a mixer and an extruder with mechanical shear forces, in

3

addition to hot-pressing with a compressor [28]. There are many other effective methods to prepare polymer composites including covalent functionalization, solution method, grafting and combinations of each method listed. The combination of more than two methods listed is efficient to produce the complicated material structures and improved properties for advanced and elaborate applications [29-32].

Obtained composite materials are analyzed and studied using various characterizations to comprehend the properties of prepared composite materials in-depth. Mechanical, thermal, viscoelastic, morphological, and crystalline properties are critical in defining material structures and fundamental properties. Mechanical properties consist of modulus, toughness, and strength properties, which are crucial mechanical properties for replacement of metal by polymer composite materials prepared by the addition of fillers with high modulus [18, 33]. Thermal properties include thermal stability, melting and glass transition temperature generally improved by addition of fillers in the polymer matrix, attributed to good compatibility between matrix and filler [28, 34]. Viscoelastic properties such as storage modulus and viscosity in a composite system generally increase with increasing filler content due to intercalation, cross-linking, and interaction on the interface between matrix and filler materials [20, 35]. Morphological properties are a key factor to determine various material properties due to close relation with each other [36]. The effect of the addition of fillers in the crystallization of the polymer composites can be characterized by DSC and NMR [37, 38]. The crystallinity is closely related with surface property, degree of dispersion, and size and amount of fillers in the polymer composites [39].

In the current study, polyethylene terephthalate (PET) polymer was utilized as an organic matrix polymer material. PET polymer is widely used in fibers, films, bottles and various injection molding industries for packaging, electrical and automotive applications due to its remarkable properties such as optical clarity, chemical resistance, and thermal stability [40]. However, PET polymer has been limited in wide industrial applications due to a relatively low crystallization rate [33, 41]. To improve the properties of PET polymer such as mechanical, thermal, crystallization and morphological properties, various fillers including SiO_2, clay, CNTs, and glass were applied in the PET polymer matrix [42-45]. In addition, PET has a melting temperature (T_m) around 250 ^{o}C, which is enough temperature to make Pglass melt and mix with melted PET polymer during the mixing process.

Inorganic phosphate glass as a filler in the organic polymer composites has been continuously studied in Otaigbe research group. Pglass has unique properties of low glass transition and excellent chemical and physical properties such as non-toxic, low process temperature similar to an organic polymer, chemical durability, flame resistance, optical clarity, and chemical durability [46-51]. In the current study, Pglass is used as a filler in PET organic matrix material. Pglass is reviewed to understand and predict the behavior in the polymer matrix system in the literature. Tick [52, 53] proposed new phosphate glass which has an ultra-low glass transition temperature. The recent research on the tin fluorophosphate glass (Pglass) with the specific composition of 50% SnF_2 + 20% SnO + 30% P_2O_5 has been carried out by many researchers [46, 47, 54]. Pglass is believed to have a polymer-like chain structure attributed to the phosphate glass network (sp3 hybrid orbital formation) [50, 55]. These phosphate anion tetrahedra structures were named (Q^i)

as shown in Fig. 1.1 according to the number of bridging oxygens. However, the chain structure of the Pglass is relatively smaller than polymer chains attributed to the fluorine in the Pglass molecules. Pglass networks can be disrupted by fluorine, and bridging oxygens in the phosphate glass is replaced by non-bridging fluorine, resulting in smaller molecules and ultra-low glass transition temperature [56, 57].

Ultra-low glass transition temperature and process temperature of Pglass facilitate blending of Pglass with organic polymer materials using conventional processing instruments including mixer and extruder [48]. Pglass with low T_g can be prepared using a specific procedure reported in the literature [52]. Usually, the Pglass/polymer hybrid materials were prepared by mixing the prepared Pglass and various organic polymers in the mixer (i.e. Polydrive® Melt Mixer) at the temperature around the melting temperature of an organic polymer (180 ^{o}C ~ 250 ^{o}C). Recently, hybrid materials prepared in melt-states of Pglass and various organic polymer materials were studied by many researchers [46-48, 54, 58-60]. Rheological, mechanical, thermal and crystalline properties of Pglass/polymer hybrids were investigated with respect to the matrix materials and processing methods. Urman et al. [36] reported that Pglass concentration significantly effects both shear and elongational viscosity. Adalja et al. [54] observed that the shear-thinning characteristics of the Pglass-LDPE hybrids were enhanced due to the addition of Pglass, indicating that there are nonlinear chemical and physical interactions between Pglass and LDPE molecules. Urman et al. [46, 61] showed the results of the decrease of T_g up to 10°C with increasing Pglass content in the polyamide 6 matrix in DMA analysis. This indicates the plasticizing effect of Pglass in the polyamide 6 matrix and the structural change of Pglass/polyamide 12 hybrids, which occurs in hybrids containing $\geq$

6

2 vol% Pglass at above 220ºC. This result is attributed to the microstructure change caused by the enhanced interactions between two compatible pure materials. In addition, polymer crystallinity was decreased with increasing Pglass concentration in the hybrid composite materials [60, 62] because the molecular motion of the polymer chains surrounding inorganic filler phase was hindered by inorganic Pglass molecules, resulting in a decrease in molecular relaxation of the organic polymer [63].

Inorganic glass or glass-ceramic matrix (i.e. glass-ceramic, soda-lime glass, borosilicate glass, and phosphate glass) composites can be prepared with filler materials such as carbon nanotubes, graphene, and carbon fibers with high modulus to achieve significant improvement in their thermal stability, electric insulation, corrosion resistance, and mechanical properties such as strength, toughness, and hardness [64-66]. Even if inorganic glass-ceramic materials showed good mechanical properties, there are intrinsic disadvantages of brittleness. Moreover, glass-ceramic materials generally show poor tensile strength and low resistance to mechanical and thermal stress [67]. To overcome this limitation, many researchers contributed to the research using composite technologies with incorporation of fillers having higher mechanical properties. Many researchers tried to prepare the glass or glass-ceramic matrix composites using nanofillers including CNTs, nanosized SiC, Al_2O_3, graphene and carbon fiber [66, 68-71]. The incorporation of carbon fiber and CNTs significantly improve the mechanical properties attributed to the putout and debonding mechanism in the inorganic glass-ceramic matrix composites [72-77]. Boccardi et al. [78] introduced glass matrix composite with a porous glass foam structure to be used in the catalyst, membrane, and biotechnology applications. It is worthy to note that the compositions and sample preparation are

essential in determination of functionality of glass-ceramic matrix composites, which is closely related to the structural and morphological properties of composites. In the current study, instead of using Pglass as a filler, Pglass was used as a continuous matrix material for inorganic Pglass matrix nanocomposites to obtain improved thermal, rheological, and mechanical properties rather than pure Pglass. The current Pglass matrix nanocomposites are prepared via one pot synthesis, extrusion, and sintering methods with POSS at remarkably lower temperatures compared to other glass-ceramics and borosilicate matrix composites already mentioned.

POSS is a unique material widely utilized as a nanoscale filler in the composites [79-83]. POSS is a hybrid material with inorganic and organic parts in one structure [84], which generally has silicon-based cages (closed or open) and organic functional groups grafted on the cages as shown in Fig. 1.2 [85]. This core cage with silicon and oxygen of the POSS molecule shows excellent thermal, mechanical and oxidative stability [83, 86-88]. The nanostructured POSS materials can be utilized as a bridging material in the surface modification between inorganic and organic materials due to their well-defined inorganic/organic segments. POSS incorporated polymeric matrix composites were prepared using various preparation methods such as blending, copolymerization, and grafting [34, 89-93] for the polymeric matrix composites with the improved properties including thermal, rheological and mechanical properties. Zhao et al. [34] reported that the obtained trisilanolphenyl-POSS and polycarbonate matrix composites have good compatibility, resulting in transparent sample with 5 wt.% POSS content. In addition, the tensile and dynamic mechanical modulus were increased with the increase of the amount of POSS content. To my knowledge, this is the first comprehensive study on inorganic

Pglass composites incorporating POSS, which might be a basis for future investigations on the inorganic matrix materials incorporating POSS as a nanoscale filler.

Glass-ceramic matrix composites can be prepared through many different preparation methods such as extrusion [94, 95], sol-gel [96-98], hot-pressing [99], and sintering process [72, 100]. The extrusion method has an enhanced benefit on continuous production with low cost. However, there is a limitation of high processing temperature for glasses. Hot-pressing is widely utilized to produce the ceramic composites due to benefits on the reduction of the porosity and improvement of the mechanical properties of composite materials. The sol-gel method is more suitable than other methods for the preparation of thin films for surface coating. One of the effective methods is the sintering process to prepare inorganic composites by the addition of filler materials in the glass-ceramic powders for regenerating the bulk glass-ceramic materials. Fig. 1.3 showed the SEM micrograms of the fracture surface of borosilicate glass matrix composite samples prepared by the sintering process with CNTs [72]. In the sample prepared by one-step process as shown in Fig. 1.3(a), the CNTs are clearly visible with not completely sintered glass grains, while the two-step sintered composite with intermediate stage at 400°C in Fig. 1.3(b) showed better dispersion of CNTs due to the improved sintering process.

In the current study, there are three methods used in preparation of inorganic Pglass matrix composites incorporating POSS. First, the one pot synthesis method was used to chemically synthesize POSS and Pglass composites via a chemical reaction between POSS and Pglass, which have reactive hydroxyl functionalities, respectively, indicating that chemical synthesis process is potentially useable in preparation of composites with POSS and Pglass molecules. Second, the extrusion method was

9

conducted to prepare inorganic Pglass matrix composites incorporating POSS. In general, the extrusion method for preparation of composites is a common method for polymeric matrix materials such as PP, PE and PET materials for the applications of the packaging industry [101, 102]. On the other hand, the extrusion process was applied to prepare porous glass foam materials for the applications such as biotechnology, catalyst, and membrane [78]. Minay and co-workers [70] reported that glass matrix composites reinforced with Al_2O_3 platelets were prepared using recycled TV set screen glass by extrusion process. Relatively high process temperature is a disadvantage in the usage of conventional processing instruments for normal inorganic glass materials. However, Pglass has an outstanding advantage on processing temperature, which is in the range of processing temperature of general organic polymers. Effective dispersion of the nanoscale POSS using the extrusion process will provide an increase in interfacial surface area between inorganic glass and POSS in nanocomposites, which will improve nano-effect in the composites [35].

This current study is the first approach to prepare inorganic porous Pglass matrix composites using POSS as a filler with a function of a foaming agent similar to calcium carbonate which is generally utilized to generate the gas phase in the composites [103]. Pglass with ultra-low processing temperature is an appropriate inorganic material for the extrusion process using conventional instruments to produce the composites with unique porous property with the addition of POSS. Third, the sintering method was applied for the preparation of inorganic glass matrix composites using Pglass powder as a matrix and POSS as a filler. Glass matrix materials generally exhibit ordinary Newtonian liquids at high temperature as elucidated by Ross et al. [104]. Therefore, the viscous flow sintering

10

process can be considered as a method to prepare the inorganic glass matrix composites

through the regeneration of the bulk materials from the powder with fillers [100]. The

compatibility of Pglass and POSS due to the hydrophilic functional groups of each

component will help the mixing process with POSS and Pglass.

Based on the unique property of POSS, which has both silanol groups and

hydrophobic functional groups, POSS can be considered as a potential material for

hydrophobic surface coating on the hydrophilic surface which attracts water causing

corrosion on the metal surface, resulting in a malfunction of the electronic device.

Hydrophobicity is a very critical property in advance research and industrial applications

including anti-corrosion, anti-fouling, and self-cleaning applications related with surface

energy and structure [105-109]. Hydrophobic surface can be achieved by the combination

[110] of low surface energy materials including alkyl chains [111, 112] and fluorinated

functional groups [105, 113] in addition to surface roughness [114-117]. Based on

Young's equation [118], the contact angle (θ) of a water droplet on the flat solid surface

can be calculated using equation (1)

$$\cos \theta = \frac{\gamma_{SV} - \gamma_{SL}}{\gamma_{LV}} \tag{1}$$

where, γ_{SV}, γ_{SL}, and γ_{LV} indicate the interfacial free energies per unit area of the solid-

gas, solid-liquid, and liquid-gas interfaces, respectively. However, surface roughness, the

other crucial factor for hydrophobicity, is not considered in this equation. Wenzel [119]

and Cassie et al. [120] proposed models showing the relationship between roughness and

water repellency. Wenzel [119] proposed the equation (2) modified from the Young's

equation (1), which includes the effect of surface roughness on the substrate.

$$\cos \theta = R_f \cos\theta_0 \qquad\qquad (2)$$

where, θ_0 is the contact angle for a smooth flat surface, R_f (>1) is a roughness factor

defined as the ratio of the solid-liquid area (A_{SL}) to its projection on a flat plane (A_{FP}), R_f

= A_{SL}/A_{FP} and θ is the contact angle for a rough surface. Based on this equation (2),

when θ_0 is greater than 90° the water repellency is increased as the R_f is increased. On

the other hand, when θ_0 is smaller than 90° the water repellency is decreased as the R_f is

increased. However, Wenzel could not explain the effect of roughness with air trapped in

the surface for the water repellency. Cassie et al. [120] proposed a new model

considering the air captured on the surface as follows:

$$\cos \theta' = f_1 \cos \theta_1 + f_2 \cos \theta_2 \qquad\qquad (3)$$

where θ' is the contact angle of a rough hydrophobic surface with trapped air, which is

the combination of a surface area fraction f_1 with a contact angle θ_1 for the water-solid

surface and the other surface area fraction f_2 with a contact angle θ_2 for the water-air

surface.

The difference between the Wenzel and Cassie model was illustrated in Fig. 1.4,

showing the difference in two models due to the presence of the trapped air on the rough

surface. Many studies were conducted to investigate the fundamental principle of

hydrophobicity of the surface and tried to mimick the lotus leaf for achievement of superhydrophobicity [121-123]. For example, Yuan et al. [121] successfully produced a stable super-hydrophobic PVC film showing $157 \pm 1.8^\circ$, mimicking the surface structure of a natural lotus leaf by the nanocasting method using PDMS layer as a negative template. Liu et al. [122] fabricated the superhydrophobic surface structure by plating nano-C/Ni and nano-Cu/Ni two-layer coating on carbon steel substrate. Obtained surface showed 155.5° attributed to the micro/nano scale roughness with coating of perfluorooctyl trimethoxysilane, mimicking a lotus leaf. Barthlott et al. [123] studied an anti-adhesive property against particulate contamination of a hydrophobic surface. This self-cleaning mechanism is attributed to the "Lotus effect" of superhydrophobic property of the surface.

After investigating the hydrophobic microstructure of a lotus leaf in nature as shown in Fig. 1.5, many researchers [124-126] studied various types of structural effects on the hydrophobicity. For example, Onda et al. [127] reported that they made a super-water-repellent surface (contact angle: 174°) with a fractal surface using alkylketene dimer, indicating that the fractal surface structure was remarkably effective on the achievement of hydrophobicity. Bittoun et al. [128] reported that sinusoidal topography with multiscale roughness is beneficial to achieve the lower wetted area and the higher contact angle. Drelich [129] studied the wetting and spreading phenomena on heterogeneous solid surface having microscopic, nanoscopic, and molecular heterogeneities. Based on the theoretical study on a lotus leaf and the structural relationship between the surface micro/nano-structure and water-repellency, enormous efforts were devoted to fabricating the artificial hydrophobic rough surfaces by various

methods [117, 130, 131]. Lau et al. [132] used carbon nanotube to fabricate a rough matrix using plasma enhanced chemical vapor deposition (PECVD). Erbil et al. [133] successfully re-formed superhydrophobic i-PP having high roughness, which can be utilized for coating on a wide variety of substrates including glass slides, aluminum foil, stainless steel, Teflon, high density polyethylene, and polypropylene. In addition, lithography [134] and multilayer [135] methods were used to fabricate the rough surface as well.

However, there is a limitation of preparation of higher contact angle with only roughness. The rough surface with hydrophilic property needs to be modified or coated with low-surface-energy materials having fluorinated functional groups or long alkyl chains to achieve a higher contact angle [136, 137]. It is worthy to note that increase of roughness is more effective for the improvement of hydrophobicity when there are already low surface energy materials on the solid surface. To impose hydrophobicity on the hydrophilic glass surface, organic-inorganic hybrid materials with organic hydrophobic functional groups for hydrophobicity and inorganic functional groups to react with the glass surface are useful. In this case, POSS can be utilized as a bridging material between the inorganic surface of glass and hydrophobic functional groups grafted on the core of POSS molecules because the unique inorganic cage structure includes silanol groups at the core. Various organic functional groups can be grafted on the inorganic silicate cage which is either closed or open [85, 138]. The open type of POSS cage has generally three silanol groups while the closed type has none. The open type of POSS with hydrophobic functional groups, such as long alkyl chains or fluorinated functional groups [105, 139] is an appropriate material to coat the hydrophilic

glass surface for achievement of hydrophobicity because the open type of POSS has reactive silanol groups for the chemical and physical bonds with glass materials. In the current study, roughness of bulk Pglass was prepared by grafting micro-size Pglass particles on the surface of bulk Pglass by grafting process (fusion) between bulk Pglass and Pglass particles using instant high temperature.

As discussed in the literature [46, 48], Pglass has an ultra-low T_g and lower processing temperature compared to silicate-based glasses. This unique property can be used in wide applications of Pglass such as optoelectronics, bioengineering, protective coatings and sealant for adhesion between metals or glass materials in very low processing temperature, which is a unique advantage of Pglass distinguished from other glass materials with higher processing temperatures. Hydrophobically surface-modified Pglass might be used with enhanced benefits on applications of coating to protect hydrophilic metals and micro/nanoscale electronic devices [140] from corrosion [141, 142] caused by water.

1.3 References

1.   Po, R., et al., Polymer-and carbon-based electrodes for polymer solar cells: Toward low-cost, continuous fabrication over large area. Solar Energy Materials and Solar Cells, 2012. 100: p. 97-114.

2.   Drury, C., et al., Low-cost all-polymer integrated circuits. Applied Physics Letters, 1998. 73(1): p. 108-110.

3.   Mittal, G., et al., A review on carbon nanotubes and graphene as fillers in reinforced polymer nanocomposites. *Journal of Industrial and Engineering Chemistry*, 2015. 21: p. 11-25.

4.   Sinha Ray, S. and M. Okamoto, Polymer/layered silicate nanocomposites: a review from preparation to processing. *Progress in Polymer Science*, 2003. 28(11): p. 1539-1641.

5.   Huang, Z.-M., et al., A review on polymer nanofibers by electrospinning and their applications in nanocomposites. *Composites Science and Technology*, 2003. 63(15): p. 2223-2253.

6.   Han, Z. and A. Fina, Thermal conductivity of carbon nanotubes and their polymer nanocomposites: A review. *Progress in Polymer Science*, 2011. 36(7): p. 914-944.

7.   Ma, P.-C., et al., Dispersion and functionalization of carbon nanotubes for polymer-based nanocomposites: A review. *Composites Part A: Applied Science and Manufacturing*, 2010. 41(10): p. 1345-1367.

8.   Paul, D. and L.M. Robeson, Polymer nanotechnology: nanocomposites. *Polymer*, 2008. 49(15): p. 3187-3204.

9.   Elmendorp, J.J., A study on polymer blending microrheology. *Polymer Engineering & Science,* 1986. 26(6): p. 418-426.

10.   Verhoogt, H., B.A. Ramsay, and B.D. Favis, Polymer blends containing poly(3-hydroxyalkanoate)s. *Polymer,* 1994. 35(24): p. 5155-5169.

11.   Friedrich, K., Z. Zhang, and A.K. Schlarb, Effects of various fillers on the sliding wear of polymer composites. *Composites Science and Technology*, 2005. 65(15): p. 2329-2343.

12.   Jordan, J., et al., Experimental trends in polymer nanocomposites—a review. *Materials science and engineering: A*, 2005. 393(1-2): p. 1-11.

13.   Spitalsky, Z., et al., Carbon nanotube–polymer composites: chemistry, processing, mechanical and electrical properties. *Progress in polymer science*, 2010. 35(3): p. 357-401.

14.   Tibbetts, G.G., et al., A review of the fabrication and properties of vapor-grown carbon nanofiber/polymer composites. *Composites Science and Technology*, 2007. 67(7-8): p. 1709-1718.

15.   Giannelis, E.P., Polymer layered silicate nanocomposites. *Advanced materials,* 1996. 8(1): p. 29-35.

16.   Liu, Y., J. Lee, and L. Hong, In situ preparation of poly (ethylene oxide)–SiO2 composite polymer electrolytes. *Journal of Power Sources*, 2004. 129(2): p. 303-311.

17.   Gacitua, W., A. Ballerini, and J. Zhang, Polymer nanocomposites: synthetic and natural fillers a review. *Maderas. Ciencia y tecnología*, 2005. 7(3): p. 159-178.

18.   Crosby, A.J. and J.Y. Lee, Polymer nanocomposites: the "nano" effect on mechanical properties. *Polymer reviews*, 2007. 47(2): p. 217-229.

19.   Ramanathan, T., et al., Functionalized graphene sheets for polymer nanocomposites. *Nature nanotechnology*, 2008. 3(6): p. 327-331.

20.   Du, F., et al., Nanotube networks in polymer nanocomposites: rheology and electrical conductivity. *Macromolecules,* 2004. 37(24): p. 9048-9055.

21.   Isayev, A. and M. Modic, Self-Reinforced melt processible polymer composites: Extrusion, compression, and injection molding. *Polymer composites*, 1987. 8(3): p. 158-175.

22.   Kuilla, T., et al., Recent advances in graphene based polymer composites. *Progress in polymer science*, 2010. 35(11): p. 1350-1375.

23.   Andrews, R., et al., Fabrication of carbon multiwall nanotube/polymer composites by shear mixing. *Macromolecular Materials and Engineering*, 2002. 287(6): p. 395-403.

24.   Haggenmueller, R., et al., Aligned single-wall carbon nanotubes in composites by melt processing methods. *Chemical Physics Letters*, 2000. 330(3): p. 219-225.

25.   Ou, Y., F. Yang, and Z.Z. Yu, A new conception on the toughness of nylon 6/silica nanocomposite prepared via in situ polymerization. *Journal of Polymer Science Part B: Polymer Physics,* 1998. 36(5): p. 789-795.

26.   Park, S.J., et al., Synthesis and dispersion characteristics of multi-walled carbon nanotube composites with poly (methyl methacrylate) prepared by in-situ bulk polymerization. *Macromolecular Rapid Communications*, 2003. 24(18): p. 1070-1073.

27.   Kim, J.A., et al., Effects of surface modification on rheological and mechanical properties of CNT/epoxy composites. *Carbon,* 2006. 44(10): p. 1898-1905.

28.   Suryanegara, L., A.N. Nakagaito, and H. Yano, The effect of crystallization of PLA on the thermal and mechanical properties of microfibrillated cellulose-reinforced PLA composites. *Composites Science and Technology*, 2009. 69(7-8): p. 1187-1192.

29.   Qin, S., et al., Functionalization of single-walled carbon nanotubes with polystyrene via grafting to and grafting from methods. *Macromolecules,* 2004. 37(3): p. 752-757.

30.	Hwang, G.L., Y.T. Shieh, and K.C. Hwang, Efficient load transfer to polymer-grafted multiwalled carbon nanotubes in polymer composites. *Advanced Functional Materials*, 2004. 14(5): p. 487-491.

31.	Tong, X., et al., Surface modification of single-walled carbon nanotubes with polyethylene via in situ Ziegler–Natta polymerization. *Journal of Applied Polymer Science,* 2004. 92(6): p. 3697-3700.

32.	Banerjee, S., T. Hemraj-Benny, and S.S. Wong, Covalent surface chemistry of single-walled carbon nanotubes. *Advanced Materials*, 2005. 17(1): p. 17-29.

33.	Wang, Y., et al., Study on mechanical properties, thermal stability and crystallization behavior of PET/MMT nanocomposites. *Composites Part B: Engineering,* 2006. 37(6): p. 399-407.

34.	Zhao, Y. and D.A. Schiraldi, Thermal and mechanical properties of polyhedral oligomeric silsesquioxane (POSS)/polycarbonate composites. *Polymer,* 2005. 46(25): p. 11640-11647.

35.	Madbouly, S.A. and J.U. Otaigbe, Recent advances in synthesis, characterization and rheological properties of polyurethanes and POSS/polyurethane nanocomposites dispersions and films. *Progress in Polymer Science*, 2009. 34(12): p. 1283-1332.

36.	Urman, K., T. Schweizer, and J.U. Otaigbe, Uniaxial elongational flow effects and morphology development in LDPE/phosphate glass hybrids. *Rheologica acta*, 2007. 46(7): p. 989-1001.

37.   Apperley, D.C., et al., Characterisation of indomethacin and nifedipine using variable-temperature solid-state NMR. *Magnetic Resonance in Chemistry*, 2005. 43(11): p. 881-892.

38.   Wang, Y., et al., Nonisothermal melt crystallization kinetics of poly (ethylene terephthalate)/clay nanocomposites. *Journal of applied polymer science*, 2004. 91(1): p. 308-314.

39.   Osman, M.A. and A. Atallah, High-density polyethylene micro-and nanocomposites: Effect of particle shape, size and surface treatment on polymer crystallinity and gas permeability. *Macromolecular rapid communications*, 2004. 25(17): p. 1540-1544.

40.   Chang, J.-H., et al., Poly (ethylene terephthalate) nanocomposites by in situ interlayer polymerization: the thermo-mechanical properties and morphology of the hybrid fibers. *Polymer,* 2004. 45(3): p. 919-926.

41.   Run, M., et al., Melting behaviors and isothermal crystallization kinetics of poly (ethylene terephthalate)/mesoporous molecular sieve composite. *Polymer,* 2005. 46(14): p. 5308-5316.

42.   Frenzel, H., et al., Influence of different glass fiber sizings on selected mechanical properties of PET/glass composites. *Journal of Adhesion Science and Technology,* 2000. 14(5): p. 651-660.

43.   Wan, T., et al., Crystalline morphology and isothermal crystallization kinetics of poly (ethylene terephthalate)/clay nanocomposites. *Journal of Applied Polymer Science,* 2004. 94(4): p. 1381-1388.

44.   Ke, Y.-C., T.-B. Wu, and Y.-F. Xia, The nucleation, crystallization and dispersion behavior of PET–monodisperse SiO2 composites. *Polymer,* 2007. 48(11): p. 3324-3336.

45.   Yoo, H.J., et al., Effects of carbon nanotube functionalization and annealing on crystallization and mechanical properties of melt-spun carbon nanotubes/poly (ethylene terephthalate) fibers. *Composites Science and Technology*, 2012. 72(15): p. 1834-1840.

46.   Urman, K. and J. Otaigbe, Novel phosphate glass/polyamide 6 hybrids: miscibility, crystallization kinetics, and mechanical properties. *Journal of Polymer Science Part B: Polymer Physics*, 2006. 44(2): p. 441-450.

47.   Rawal, A., et al., Detection of nanometer-scale mixing in phosphate-glass/polyamide-6 hybrids by 1H− 31P NMR. *Chemistry of materials*, 2006. 18(26): p. 6333-6338.

48.   Urman, K. and J.U. Otaigbe, New phosphate glass/polymer hybrids—Current status and future prospects. *Progress in Polymer Science*, 2007. 32(12): p. 1462-1498.

49.   Sammler, R., et al., Melt rheology of zinc alkali phosphate glasses. *Journal of Rheology,* 1996. 40(2): p. 285-302.

50.   Brow, R.K., the structure of simple phosphate glasses. *Journal of Non-Crystalline Solids,* 2000. 263: p. 1-28.

51.   Loong, C.-K., et al., Structure and dynamics of phosphate glasses: from ultra-to orthophosphate composition. *Physica B: Condensed Matter,* 1997. 241: p. 890-896.

52.   Tick, P.A., Tin-phosphorus oxyfluoride glass containing aromatic organic compound. 1983, Google Patents.

53.   Tick, P.A., Water durable glasses with ultra-low melting temperatures. *Physics and Chemistry of glasses*, 1984. 25(6): p. 149-154.

54.   Adalja, S.B., J.U. Otaigbe, and J. Thalacker, Glass-polymer melt hybrids. I: Viscoelastic properties of novel affordable organic-inorganic polymer hybrids. *Polymer Engineering & Science*, 2001. 41(6): p. 1055-1067.

55.   Otaigbe, J.U. and G.H. Beall, Inorganic phosphate glasses as polymers. *Trends in Polymer science*, 1997. 11(5): p. 369-379.

56.   Clifford, A. and R. Hill, Apatite-mullite glass-ceramics. *Journal of Non-Crystalline Solids,* 1996. 196: p. 346-351.

57.   Rafferty, A., et al., Influence of fluorine content in apatite–mullite glass-ceramics. *Journal of the American Ceramic Society*, 2000. 83(11): p. 2833-2838.

58.   Guschl, P.C. and J.U. Otaigbe, Experimental observation and prediction of interfacial tension and viscoelastic emulsion model behavior in novel phosphate glass–polymer hybrids. *Journal of colloid and interface science*, 2003. 266(1): p. 82-92.

59.   Adalja, S.B. and J.U. Otaigbe, Creep and recovery behavior of novel organic-inorganic polymer hybrids. *Polymer composites*, 2002. 23(2): p. 171-181.

60.   Guschl, P.C. and J.U. Otaigbe, Crystallization kinetics of low-density polyethylene and polypropylene melt-blended with a low-Tg tin-based phosphate glass. *Journal of applied polymer science*, 2003. 90(12): p. 3445-3456.

61.   Urman, K., T. Schweizer, and J.U. Otaigbe, Rheology of tin fluorophosphate glass/polyamide 12 hybrids in the low concentration regime. *Journal of rheology*, 2007. 51(6): p. 1171-1187.

62.   Guschl, P.C., J.U. Otaigbe, and C.K. Loong, Investigation of phase behavior during melt processing of novel inorganic-organic polymer hybrid material. *Polymer Engineering & Science*, 2004. 44(9): p. 1692-1701.

63.   Bikiaris, D., et al., Use of silanes and copolymers as adhesion promoters in glass fiber/polyethylene composites. *Journal of applied polymer science*, 2001. 80(14): p. 2877-2888.

64.   Brennan, J.J. and K.M. Prewo, Silicon carbide fibre reinforced glass-ceramic matrix composites exhibiting high strength and toughness. *Journal of Materials Science,* 1982. 17(8): p. 2371-2383.

65.   Marshall, D.B. and A.G. Evans, Failure mechanisms in ceramic-fiber/ceramic-matrix composites. *Journal of the American Ceramic Society*, 1985. 68(5): p. 225-231.

66.   Cho, J., A.R. Boccaccini, and M.S. Shaffer, Ceramic matrix composites containing carbon nanotubes. *Journal of Materials Science,* 2009. 44(8): p. 1934-1951.

67.   Sambell, R., D. Bowen, and D. Phillips, Carbon fibre composites with ceramic and glass matrices. *Journal of Materials Science*, 1972. 7(6): p. 663-675.

68.   Bai, S. and X. Shen, Graphene–inorganic nanocomposites. *Rsc Advances,* 2012. 2(1): p. 64-98.

69.   Boccaccini, A., et al., Assessment of damage induced by thermal shock in SiC-fiber-reinforced borosilicate glass composites. *Composites science and technology*, 1999. 59(1): p. 105-112.

70.   Minay, E., V. Desbois, and A. Boccaccini, Innovative manufacturing technique for glass matrix composites: extrusion of recycled TV set screen glass reinforced with Al2O3 platelets. *Journal of materials processing technology*, 2003. 142(2): p. 471-478.

71.   Kumar, S., et al., Fibers from polypropylene/nano carbon fiber composites. *Polymer,* 2002. 43(5): p. 1701-1703.

72.   Boccaccini, A., et al., Borosilicate glass matrix composites containing multi-wall carbon nanotubes. *Journal of the European Ceramic Society*, 2005. 25(9): p. 1515-1523.

73.   Crivelli-Visconti, I. and G. Cooper, Mechanical properties of a new carbon fibre material. *Nature,* 1969. 221(5182): p. 754.

74.   Ning, J., et al., Fabrication and mechanical properties of SiO2 matrix composites reinforced by carbon nanotube. *Materials Science and Engineering: A*, 2003. 357(1-2): p. 392-396.

75.   Boccaccini, A., H. Kern, and I. Dlouhy, Determining the fracture resistance of fibre-reinforced glass matrix composites by means of the chevron-notch flexural technique. *Materials Science and Engineering: A,* 2001. 308(1-2): p. 111-117.

76.   Bianchi, V., et al., Carbon-fibre-reinforced (YMAS) glass-ceramic matrix composites. I. Preparation, structure and fracture strength. *Journal of the European Ceramic Society*, 1997. 17(12): p. 1485-1500.

77.	Evans, A.G., The mechanical performance of fiber-reinforced ceramic matrix composites. *Materials Science and Engineering: A*, 1989. 107: p. 227-239.

78.	Boccardi, E., F.E. Ciraldo, and A.R. Boccaccini, Bioactive glass-ceramic scaffolds: Processing and properties. *MRS Bulletin*, 2017. 42(3): p. 226-232.

79.	Nanda, A.K., et al., Nanostructured polyurethane/POSS hybrid aqueous dispersions prepared by homogeneous solution polymerization. *Macromolecules*, 2006. 39(20): p. 7037-7043.

80.	Phillips, S.H., T.S. Haddad, and S.J. Tomczak, Developments in nanoscience: polyhedral oligomeric silsesquioxane (POSS)-polymers. *Current Opinion in Solid State and Materials Science,* 2004. 8(1): p. 21-29.

81.	Kuo, S.-W. and F.-C. Chang, POSS related polymer nanocomposites. *Progress in Polymer Science*, 2011. 36(12): p. 1649-1696.

82.	Wang, W., Y.-l. Guo, and J.U. Otaigbe, The synthesis, characterization and biocompatibility of poly (ester urethane)/polyhedral oligomeric silsesquioxane nanocomposites. *Polymer*, 2009. 50(24): p. 5749-5757.

83.	Gnanasekaran, D., K. Madhavan, and B. Reddy, Developments of polyhedral oligomeric silsesquioxanes (POSS), possnanocomposites and their applications: A review. *Journal of Scientific and Industrial Research*, 2009. 68(6): p. 437-464.

84.	Chujo, Y., Organic—inorganic hybrid materials. *Current Opinion in Solid State and Materials Science,* 1996. 1(6): p. 806-811.

85.   Misra, R., et al., POSS-nylon 6 nanocomposites: Influence of POSS structure on surface and bulk properties. *Journal of Polymer Science Part B: Polymer Physics*, 2009. 47(11): p. 1088-1102.

86.   Lichtenhan, J.D., Y.A. Otonari, and M.J. Carr, Linear hybrid polymer building blocks: methacrylate-functionalized polyhedral oligomeric silsesquioxane monomers and polymers. *Macromolecules*, 1995. 28(24): p. 8435-8437.

87.   Gonzalez, R.I., S.H. Phillips, and G.B. Hoflund, In situ oxygen-atom erosion study of polyhedral oligomeric silsesquioxane-siloxane copolymer. *Journal of Spacecraft and Rockets*, 2000. 37(4): p. 463-467.

88.   Zheng, L., R.J. Farris, and E.B. Coughlin, Novel polyolefin nanocomposites: synthesis and characterizations of metallocene-catalyzed polyolefin polyhedral oligomeric silsesquioxane copolymers. *Macromolecules*, 2001. 34(23): p. 8034-8039.

89.   Hany, R., et al., Chemical synthesis and characterization of POSS-functionalized poly [3-hydroxyalkanoates]. *Polymer,* 2005. 46(14): p. 5025-5031.

90.   Yoon, K.H., et al., Properties of poly (ethylene terephthalate) containing epoxy-functionalized polyhedral oligomeric silsesquioxane. *Polymer International*, 2005. 54(1): p. 47-53.

91.   Xu, H., et al., Preparation, thermal properties, and T g increase mechanism of poly (acetoxystyrene-co-octavinyl-polyhedral oligomeric silsesquioxane) hybrid nanocomposites. *Macromolecules,* 2005. 38(25): p. 10455-10460.

92.   Li, G.Z., et al., Synthesis and properties of poly (isobutyl methacrylate-co-butanediol dimethacrylate-co-methacryl polyhedral oligomeric silsesquioxane)

nanocomposites. *Journal of Polymer Science Part A: Polymer Chemistry*, 2005. 43(2): p. 355-372.

93.   Huang, C.-F., et al., Influence of PMMA-chain-end tethered polyhedral oligomeric silsesquioxanes on the miscibility and specific interaction with phenolic blends. *Macromolecules,* 2006. 39(1): p. 300-308.

94.   Roeder, E., Extrusion of glass. *Journal of Non-Crystalline Solids*, 1971. 5(5): p. 377-388.

95.   Bertan, F., et al., Extruded ZrSiO4 particulate-reinforced LZSA glass–ceramics matrix composite. *Journal of materials processing technology*, 2009. 209(3): p. 1134-1142.

96.   Mackenzie, J.D., Applications of the sol-gel process. *Journal of Non-Crystalline Solids,* 1988. 100(1-3): p. 162-168.

97.   Tsionsky, M., et al., Sol-gel-derived ceramic-carbon composite electrodes: introduction and scope of applications. *Analytical Chemistry*, 1994. 66(10): p. 1747-1753.

98.   Wang, B., J. Zhang, and S. Dong, Silica sol–gel composite film as an encapsulation matrix for the construction of an amperometric tyrosinase-based biosensor. *Biosensors and Bioelectronics*, 2000. 15(7-8): p. 397-402.

99.   Deng, J., T. Can, and J. Sun, Microstructure and mechanical properties of hot-pressed Al2O3/TiC ceramic composites with the additions of solid lubricants. *Ceramics International*, 2005. 31(2): p. 249-256.

100.   Champion, E., Sintering of calcium phosphate bioceramics. *Acta biomaterialia*, 2013. 9(4): p. 5855-5875.

101.   Azeredo, H.M.C.d., Nanocomposites for food packaging applications. *Food Research International*, 2009. 42(9): p. 1240-1253.

102.   Silvestre, C., D. Duraccio, and S. Cimmino, Food packaging based on polymer nanomaterials. *Progress in Polymer Science*, 2011. 36(12): p. 1766-1782.

103.   Chen, B., et al., Study of foam glass with high content of fly ash using calcium carbonate as foaming agent. *Materials Letters*, 2012. 79: p. 263-265.

104.   Ross, J., W. Miller, and G. Weatherly, Dynamic computer simulation of viscous flow sintering kinetics. *Journal of Applied Physics*, 1981. 52(6): p. 3884-3888.

105.   Tuteja, A., et al., Designing superoleophobic surfaces. *Science*, 2007. 318(5856): p. 1618-1622.

106.   Ivanova, N. and A. Zaretskaya, Simple treatment of cotton textile to impart high water repellent properties. *Applied Surface Science*, 2010. 257(5): p. 1800-1803.

107.   Tian, P. and Z. Guo, Bioinspired silica-based superhydrophobic materials. *Applied Surface Science*, 2017. 426: p. 1-18.

108.   Yu, M., et al., Positive effect of polymeric silane-based water repellent agents on the durability of superhydrophobic fabrics. *Applied Surface Science*, 2018. 450: p. 492-501.

109.   Neinhuis, C. and W. Barthlott, Characterization and distribution of water-repellent, self-cleaning plant surfaces. *Annals of botany*, 1997. 79(6): p. 667-677.

110.   Murase, H., et al., Interactions between heterogeneous surfaces of polymers and water. *Journal of Applied Polymer Science*, 1994. 54(13): p. 2051-2062.

111.   Gautam, K.S. and A. Dhinojwala, Molecular structure of hydrophobic alkyl side chains at comb polymer-air interface. *Macromolecules*, 2001. 34(5): p. 1137-1139.

112.   Huo, L., et al., Fabrication and tribological properties of self-assembled monolayer of n-alkyltrimethoxysilane on silicon: Effect of SAM alkyl chain length. *Applied Surface Science*, 2017. 396: p. 865-869.

113.   Huang, M. and J. Yang, Long-term performance of 1H, 1H′, 2H, 2H′-perfluorooctyl triethoxysilane (POTS) microcapsule-based self-healing anticorrosive coatings. *Journal of Intelligent Material Systems and Structures*, 2014. 25(1): p. 98-106.

114.   Nakajima, A., et al., Preparation of hard super-hydrophobic films with visible light transmission. *Thin Solid Films*, 2000. 376(1-2): p. 140-143.

115.   Blossey, R., Self-cleaning surfaces—virtual realities. *Nature materials*, 2003. 2(5): p. 301.

116.   Wei, Z., et al., Preparation of lotus-like superhydrophobic fluoropolymer films. *Applied Surface Science*, 2010. 256(12): p. 3972-3976.

117.   Yan, Y.Y., N. Gao, and W. Barthlott, Mimicking natural superhydrophobic surfaces and grasping the wetting process: A review on recent progress in preparing superhydrophobic surfaces. *Advances in colloid and interface science*, 2011. 169(2): p. 80-105.

118.   Yoshimitsu, Z., et al., Effects of surface structure on the hydrophobicity and sliding behavior of water droplets. *Langmuir*, 2002. 18(15): p. 5818-5822.

119.   Wenzel, R.N., Resistance of solid surfaces to wetting by water. *Industrial & Engineering Chemistry*, 1936. 28(8): p. 988-994.

120.   Cassie, A. and S. Baxter, Wettability of porous surfaces. *Transactions of the Faraday society,* 1944. 40: p. 546-551.

121.   Yuan, Z., H. Chen, and J. Zhang, Facile method to prepare lotus-leaf-like super-hydrophobic poly (vinyl chloride) film. *Applied Surface Science*, 2008. 254(6): p. 1593-1598.

122.   Liu, H., X. Wang, and H. Ji, Fabrication of lotus-leaf-like superhydrophobic surfaces via Ni-based nano-composite electro-brush plating. *Applied Surface Science,* 2014. 288: p. 341-348.

123.   Barthlott, W. and C. Neinhuis, Purity of the sacred lotus, or escape from contamination in biological surfaces. *Planta,* 1997. 202(1): p. 1-8.

124.   Hazlett, R.D., Fractal applications: wettability and contact angle. *Journal of Colloid and Interface Science,* 1990. 137(2): p. 527-533.

125.   Karumuri, A.K., L. He, and S.M. Mukhopadhyay, Tuning the surface wettability of carbon nanotube carpets in multiscale hierarchical solids. *Applied Surface Science,* 2015. 327: p. 122-130.

126.   Zhang, X., et al., Superhydrophobic surfaces: from structural control to functional application. *Journal of Materials Chemistry*, 2008. 18(6): p. 621-633.

127.   Onda, T., et al., Super-water-repellent fractal surfaces. *Langmuir*, 1996. 12(9): p. 2125-2127.

128.   Bittoun, E. and A. Marmur, The role of multiscale roughness in the lotus effect: is it essential for super-hydrophobicity? *Langmuir*, 2012. 28(39): p. 13933-13942.

129.   Drelich, J., Static contact angles for liquids at heterogeneous rigid solid surfaces. *Polish Journal of Chemistry*, 1997. 71(5): p. 525-549.

130. Abdulhussein, A.T., et al., Current trend in fabrication of complex morphologically tunable superhydrophobic nano scale surfaces. *Applied Surface Science*, 2016. 384: p. 311-332.

131. Shibuichi, S., et al., Super water-repellent surfaces resulting from fractal structure. *The Journal of Physical Chemistry*, 1996. 100(50): p. 19512-19517.

132. Lau, K.K., et al., Superhydrophobic carbon nanotube forests. *Nano letters*, 2003. 3(12): p. 1701-1705.

133. Erbil, H.Y., et al., Transformation of a simple plastic into a superhydrophobic surface. *Science*, 2003. 299(5611): p. 1377-1380.

134. Shiu, J.-Y., et al., Fabrication of tunable superhydrophobic surfaces by nanosphere lithography. *Chemistry of materials*, 2004. 16(4): p. 561-564.

135. Zhang, X., et al., Polyelectrolyte multilayer as matrix for electrochemical deposition of gold clusters: toward super-hydrophobic surface. *Journal of the American Chemical Society*, 2004. 126(10): p. 3064-3065.

136. Guo, Z., et al., Stable biomimetic super-hydrophobic engineering materials. *Journal of the American Chemical Society*, 2005. 127(45): p. 15670-15671.

137. Shi, F., et al., To adjust wetting properties of organic surface by in situ photoreaction of aromatic azide. *Langmuir*, 2007. 23(3): p. 1253-1257.

138. Misra, R., et al., Molecular miscibility and chain dynamics in POSS/polystyrene blends: control of POSS preferential dispersion states. *Polymer*, 2009. 50(13): p. 2906-2918.

139.   Zucchi, I.A., M.J. Galante, and R.J.J. Williams, Surface energies of linear and cross-linked polymers based on isobornyl methacrylate and methacryl-heptaisobutyl POSS. *European Polymer Journal,* 2009. 45(2): p. 325-331.

140.   Osenbach, J.W., Corrosion-induced degradation of microelectronic devices. *Semiconductor science and technology*, 1996. 11(2): p. 155.

141.   Comizzoli, R., et al., Corrosion of electronic materials and devices. *Science*, 1986. 234(4774): p. 340-345.

142.   Shen, G., et al., Study on a hydrophobic nano-TiO2 coating and its properties for corrosion protection of metals. *Electrochimica Acta*, 2005. 50(25-26): p. 5083-5089.
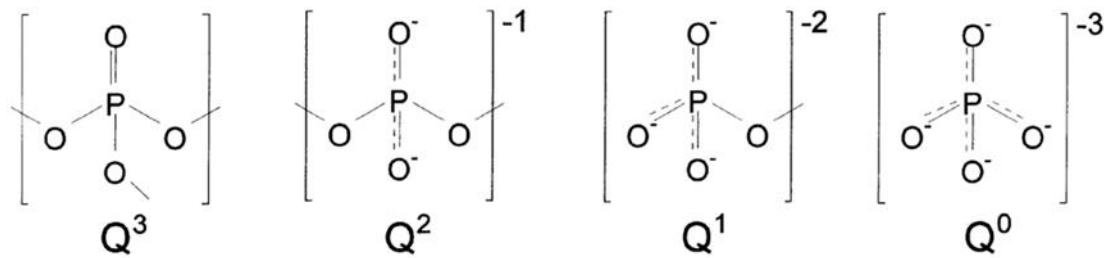
Figure 1.1 Phosphate tetrahedral sites that can exist in phosphate glasses.

reproduced with permission from (Ref 50). Copyright (2000), Elsevier
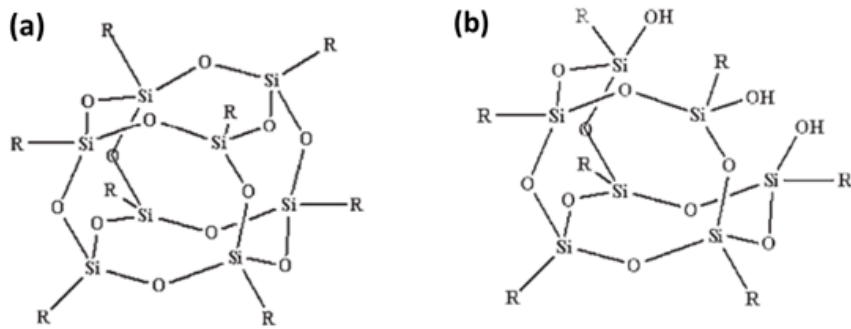
Figure 1.2 Schematic structures of (a) closed-POSS (b) open-POSS (R: various functional groups)

reproduced with permission from (ref 85). Copyright (2009), John Wiley and Sons
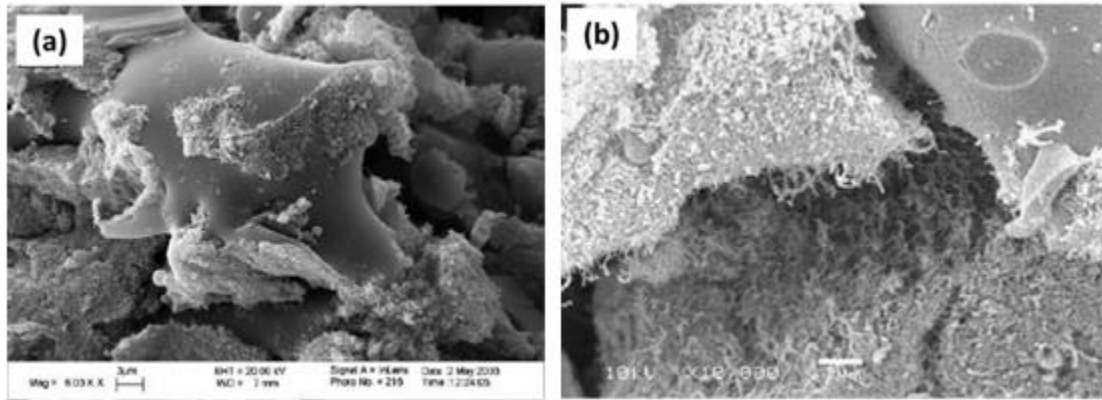
Figure 1.3 SEM micrographs of the fracture surface of pressureless sintered samples: (a) one-step sintered sample showing CNT agglomerates around not fully sintered glass grains (b) two-step sintered sample.
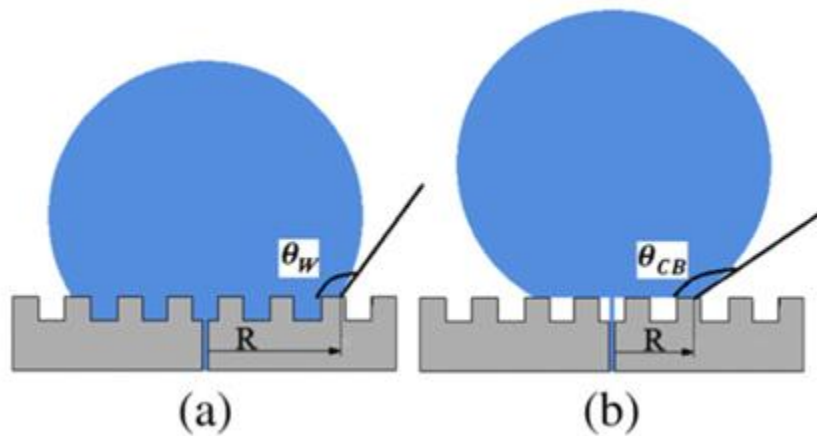
Figure 1.4 Filling the liquid up to a rough surface through the solid substrate: (a) Wenzel model and (b) Cassie model with air trapped on the surface. (R is the radius of the circular contact area between solid and liquid.)
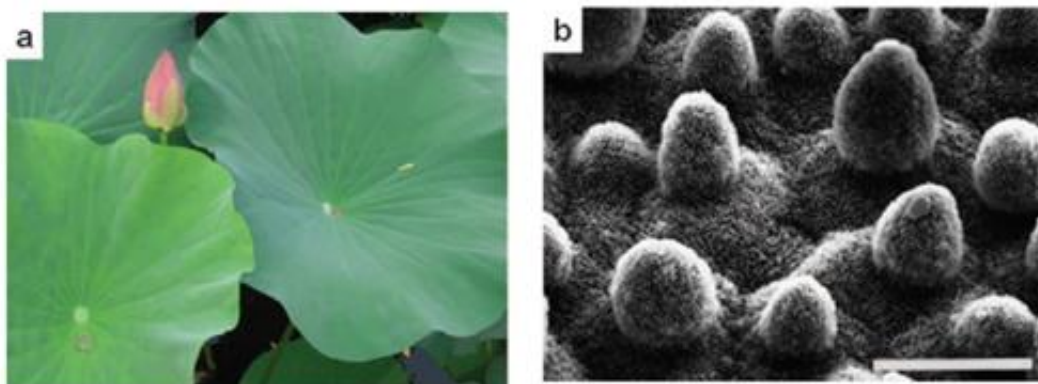
Figure 1.5 Superhydrophobic surface in nature. (a) lotus leaves show self-cleaning properties (b) SEM image of the surface structures on the lotus leaf. (The scale bar of the image (b) represents 20 μm)

Fig. 1.5(a) is reproduced with permission from (Ref 126). Copyright (2007), Royal Society of Chemistry. Fig. 1.5(b) is reproduced with permission from (Ref 123). Copyright (1997), Springer Nature

CHAPTER II – SYNTHESIS AND CHARACTERIZATION ON NOVEL
PHOSPHATE GLASS MATRIX NANOCOMPOSITES CONTAINING
POLYHEDRAL OLIGOMERIC SILSESQUIOXANE WITH IMPROVED
PROPERTIES

Published Manuscript

Abstract

The preparation and characterization of novel tin fluorophosphate glass (Pglass)
matrix nanocomposite materials containing nanoscale trisilanolphenyl polyhedral
oligomeric silsesquioxane (POSS) prepared via classical glass synthesis was investigated
to accelerate efforts to develop novel hybrid Pglass/POSS nanocomposites with enhanced
benefits in suitable diverse applications. The glass transition temperatures (T_g) of the
obtained nanocomposites ranged from 121.6° to 147.6°C to an extent that depends on the
nano-POSS concentrations ($\leq$ 10 wt.% POSS) in the nanocomposites. The obtained
scanning electron microscopy with energy-dispersive x-ray spectroscopy and atomic
force microscopy results confirmed the homogeneous molecular level dispersion of the
POSS cages in the continuous Pglass matrix of the nanocomposite. Chemical reaction (or
bonding) between the constituents of the nanocomposites was confirmed by Fourier
transform infrared spectroscopy, X-ray photoelectron spectroscopy, and nuclear magnetic
resonance spectroscopy. The rheological (storage and loss modulus) and nanomechanical

(elastic modulus) properties of the nanocomposites significantly improved with increasing nano-POSS concentrations up to 10 wt.% POSS. The molecular dispersion of the POSS and its strong physicochemical interaction with the continuous Pglass matrix can be tailored to satisfy requirements of a number of optomechanical applications where the pure glass is not useable.

2.1 Introduction

Due to their design flexibility, improved performance properties, and relative ease of processing, nanocomposites composed of a continuous polymer matrix incorporating inorganic fillers such as exfoliated layered silicates, alumina, carbon fibers, carbon nanotubes and borosilicate glasses have spurred significant academic and industrial research interests in exploring feasibility of their uses in a wide range of diverse application areas like automotive, aerospace, and packing applications [1-9]. In general, composites materials can be prepared by physical mixing [9] or chemical (sol-gel) reactions [10] between the composite matrix and filler materials as previously reported in the literature.

Nanocomposites can be defined as matrix materials (e.g. glass-ceramics and polymers) that are chemically or physically combined with relatively small concentrations of nanofillers (e.g., carbon nanotubes, graphene, exfoliated layered silicates) to produce materials with improved mechanical and melt rheological properties. Nanocomposites include hybrid composite materials in which at least one of the phases has nanometer length scale dimensions that facilitate significant improvement of the limited properties of the continuous matrix materials in the nanocomposites. The reported enhanced nanoscale size effects in nanocomposites avoid the disadvantages and

37

limitations of traditional microcomposites [11, 12]. It is worthy to note that as the size of the nanofiller decreases, the interaction between the nanoscale dispersed fillers and the continuous matrix materials in the nanocomposite increase significantly, and in turn, leads to mechanical and melt rheological properties by several orders of magnitude. The molecular size similarity between the nanofiller and matrix materials and the relative increased surface area allows efficient control of morphology and physical properties such as chain motion and glass transition temperature (T_g) of the nanocomposite materials.

In traditional polymer matrix composites, glass and carbon fibers with micrometer length scales are widely used as fillers to improve thermal, mechanical and chemical resistant properties of the continuous polymer matrices in the composites. Recently, phosphate glasses (Pglass) have been investigated as filler materials in polymer matrices [9, 13-18] because they have unique properties of low-T_g and excellent desirable properties like chemical durability, intrinsic flame resistance, higher thermal expansion, optical clarity, non-toxic, low process temperature and biocompatibility [19-23]. In the current study, inorganic phosphate glass is used as the continuous matrix to yield optomechanical phosphate glass matrix nanocomposites that are somewhat similar to glass-ceramic matrix nanocomposites reinforced with nanofillers such as carbon nanotubes and nanosized SiC with improved mechanical properties reported in the literature [24-29]. Note that the current Pglass matrix nanocomposites are made via a one pot synthesis method at remarkably lower temperatures than that used for making glass-ceramics and borosilicate matrix microcomposites already mentioned.

In contrast to the current study, other researchers have reported incorporation of ceramic fillers in the form of addition of carbon or silicon carbide particles or fibers into borosilicate glass matrices to produce glass matrix composites with improvements in performance in applications such as structural components for high temperature and impact resistant panels, which in itself is noncompliant as a result of elasticity and thermal expansion coefficient mismatch of the composite constituents. The current study explores the feasibility of an alternative radical approach of incorporating silicon in the form of special nanoscale POSS molecules as an integral part of Pglass short-range and intermediate-range (i.e., chain) structures which would preserve the favorable rheological properties of the POSS/Pglass nanocomposite dispersion in the liquid state during processing and compliance of the POSS/Pglass matrix nanocomposite film or thick sheet while significantly lowering its surface tension properties. The resulting POSS/Pglass matrix nanocomposite materials should possess mechanical and melt rheological properties such as a combination of transparency (optical clarity), improved thermo-mechanical properties, and lower surface tension than that of current pure Pglasses and borosilicate glass matrix composites reported in the literature [25, 26, 28-39] for potential uses in security glazing, armor structures, monitoring windows and impact resistant transparent panels. While the POSS/Pglass matrix nanocomposite materials and processing technology reported in the current study are different from conventional ceramic matrix composites (CMCs) and melt blending of polymer matrix nanocomposites and composites (PMCs) to maximize properties, it is hoped that the reported obtained results of the current study may shed light on the molecular dynamics of CMCs and

PMCs in general during processing at the nanometer length scales, a subject of current intense study by academic and industry researchers [40, 41].

The polyhedral oligomeric silsesquioxane (POSS) used as nanofiller materials in the current study represent a unique nanochemical materials platform that have been widely studied and found to be highly effective nanofiller in different composite materials reported in the literature [42-46]. It is worthy to note that POSS is composed of well-defined silicon-based nanoscale cage structures that possess incompletely condensed or completely condensed frameworks having the form of $SiO_{1.5}$. In addition, this intermediate silicon-oxygen framework consisting of rigid crystalline silica-like cage structures shows excellent thermal, flammable resistance and oxidative stability [42, 47-49]. POSS can be incorporated into polymeric matrices by several methods such as grafting, copolymerization and blending [50-56]. Further, POSS is an excellent nanofiller which includes inorganic and organic parts in one structure which can show organic-inorganic hybrid properties. POSS can be used as nanofiller to improve limited properties of Pglass, such as thermal and mechanical properties.

The phosphate glass used as a matrix material in the current study has remarkably low glass transition and processing temperatures as compared to silicate-based glasses. As previously reported, inorganic phosphate glasses are usually considered as polymeric materials because of their chain structures similar to polymer structure [21]. The basic structure of phosphate glass networks is based on the phosphate anion tetrahedron [23], which is denoted by Q^i, where the 'i' is the number of bridging oxygens on the unit structure of the phosphate anion tetrahedral structure. There are various phosphate glasses compositions reported in the literature including different alkali metals, e.g. Li, Na and K,

that are the crucial part of phosphate glass network formation [20]. One of these compositions is alkali zinc phosphate glass (AZP) which shows chemically durable properties and has the following composition: $x M_2O + y ZnO + z P_2O_5$ (where $x<0.25$, $y<0.5$, $0.29<z<0.5$), M is an alkali such as Li, Na and K, and numbers are in mole fractions) [21]. AZP glasses have high T_g values as compared with that of tin fluorophosphates (TFP) glasses [19], which shows very low T_g values ranging between 90°C and 140°C and favorable rheological properties similar to that reported in the current study. The low-T_g, favorable rheological properties and other desirable characteristics of the TFP glasses make them promising materials for a wide range of uses in diverse application areas, including optoelectronic components, biomedical/bioengineering, and protective coatings. To our knowledge, there is no prior reported research study on POSS/Pglass matrix nanocomposites as in the current study, making it easy to say that the current work is important and timely and may provide a basis upon which future studies on the interesting concept of phosphate glass matrix nanocomposites can be launched.

This study is part of a long-range research project aimed at developing novel opto-mechanical glass matrix nanocomposites with controllable chemistry and properties (e.g., strength and light transmittance) for diverse applications, and at discovering novel tunable structure-property relations for the nanocomposites. It is worthy to note that the glass and POSS synthesis parameter space is potentially broad because it is a function of the reactive hydroxyl functionalities of the glass composition and the various chemical functionalities of the prescribed POSS chemistry. The POSS chemistry platform is a diverse nanochemical platform that is chemically tailored to be compatible with

41

appropriate chemicals and materials as already mentioned. By working with the industrial

manufacturer of these innovative POSS nanochemicals, it is reasonable to expect that a

range of chemical reaction mechanisms will result from this long-range research project

that is likely to yield special products with controllable properties to meet the vast

requirements of diverse applications. While the current work is focused on low-T_g Pglass

and POSS systems as a proof of concept of the novel glass matrix nanocomposites

materials platform, it is hoped that the work described here will provide a fundamental

basis for a better understanding of application of the novel materials chemistry strategy to

other glass chemistries and of new facile methods of modifying the properties of pure

glasses at molecular length scales with enhanced benefits including several orders of

magnitude improvement in their reinforcing ability of pure glass and pure polymer

matrices than traditional glass fibers and particles with micrometer length scales.

2.2 Experimental methods

2.2.1 Materials and preparation of nanocomposites

Trisilanol phenyl POSS (TSP-POSS, $C_{42}H_{38}O_{12}Si_7$, solid powder) was supplied by

Hybrid Plastics Co., Ltd. Analytical grade reagents used {i.e., tin(II) oxide (SnO), tin(II)

fluoride (SnF_2) and ammonium dihydrogen phosphate ((NH_4)H_2PO_4)} were purchased

from Sigma-Aldrich and used as received. The neat tin fluorophosphates glass

(hereinafter referred to as Pglass) and Pglass matrix nanocomposites incorporating POSS

was synthesized with molar composition $50SnF_2 + 20SnO + 30P_2O_5$ and various

concentrations of POSS ranging from 0 wt.% to 10 wt.% via a one pot chemical synthesis

method. The chemical structures of the Pglass [9] and TSP-POSS are shown in Fig. 2.1.

The synthesis method was conducted using analytical grade powders of SnF_2, SnO,

$(NH_4)H_2PO_4$, and TSP-POSS in the required stoichiometric ratios that were homogeneously mixed in a mortar. The obtained mixtures were subsequently melted in a carbon crucible at a temperature of 430°C for 30 min in a furnace. The resulting melts were poured into a pre-shaped steel mold at ambient temperature to yield glass disk specimens with 10mm diameter and 2 mm thick dimensions as depicted in Fig. 2.2. The obtained samples were subsequently annealed around their glass transition temperature ranging from 130 – 160°C for 90min depending on the POSS content in the compositions. A portion of the obtained sample was ground into powder and then sifted through a sieve with 150 µm mesh for thermal and chemical characterizations. In a second preparation method, 5 wt.% POSS and *premade* Pglass particles were manually ground and mixed, heated in a carbon crucible maintained at 300°C for 10 min in the furnace, and subsequently cooled down to ambient temperature. The morphology and dispersion of the POSS in the Pglass matrix nanocomposites will be compared as a function of the preparation method used (i.e., synthesis method and physical blending).

2.2.2 Measurements

2.2.2.1 Differential Scanning Calorimetry (DSC)

A DSC (PerkinElmer Pyris Diamond® DSC) equipped with an intracooler and a computer for data acquisition and analysis was used in a dry nitrogen atmosphere to determine the glass transition temperature (T_g) of the samples. Approximately 150 micrometer glass particle size weighing about 15 mg were used for the DSC measurements in the temperature range from 30°C to 180°C and a 10 °C/min heating rate in an alumina crucible under a nitrogen atmosphere. The samples were subjected to a heat-cool-heat cycle, with cooling accomplished by intracooler cooling system prior to

43

reheating. The glass transition temperature data obtained in the second heating run are reported in this article.

2.2.2.2 Thermogravimetric analysis (TGA)

TGA was carried out on the samples using TA instrument Q500® operating from 30°C to 600°C at a heating rate of 10 °C/min with 10mL/min N_2 sample purge flow to investigate the thermal stability of the samples. The thermal degradation temperature was taken as the onset temperature of thermal degradation using the universal analysis software from TA instruments.

2.2.2.3 Attenuated total reflectance Fourier transform infrared spectroscopy (ATR-FTIR)

ATR-FTIR measurements were conducted on a Fourier transform spectrometer (Thermo Scientific Nicolet 6700®) equipped with Smart iTR^{TM} Attenuated Total Reflectance (ATR) Sampling Accessory having a single bounce diamond crystal, at an ambient condition in the frequency region from 650 - 4000 cm^{-1} for each sample. In all cases, 32 scans at a resolution of 4 cm^{-1} were used to record the spectra. The desired amount of the samples was ground to a fine powder (less than 150 □m particle size) and analyzed on the diamond ATR surface.

2.2.2.4 Atomic force microscopy (AFM)

Surface topography of the samples was characterized by AFM (a Dimension Icon AFM, Bruker) in tapping mode for both height and phase image using RTESPA300® probe with a spring constant (k) of 40N/m attached to a silicon tip (antimony (n) doped Si) to analyze the fracture surface of bulk Pglass and nanocomposites samples. AFM measurements were performed to quantify the difference between the neat Pglass and the

POSS/Pglass nanocomposites. To investigate the surface topography of POSS/Pglass nanocomposites, the samples were fractured using a diamond glass cutter and the smooth fractured surfaces were used for the AFM experiments. The PeakForce Quantitative Nanomechanical Property Mapping (QNM) mode [57, 58] was performed to measure the moduli on the fracture surfaces of the samples, using the modulus data of polystyrene film as the reference. The elastic modulus was fitted with the Derjajuin-Muller-Toporov (DMT) model [58, 59] using Nanoscope Analysis software (Bruker).

2.2.2.5 X-ray photoelectron spectroscopy (XPS)

XPS spectra were obtained using a Kratos AXIS 165® spectrometer equipped with monochromatic Al-Kα X-rays at 12 kV and 12 mA as the excitation radiation in UHV, 5×10^{-9} torr. The cross-sectional surfaces of the bulk Pglass and naocomposites samples were analyzed because fractured cross section surface is compositionally most representative of the bulk of the samples. To reduce surface charging on the glass samples, a charge neutralizer was used. The O 1s spectra collected from the Pglass and nanocomposites samples were fit using a Gaussian curve-fitting method in ORIGIN® software.

2.2.2.6 Scanning electron microscopy (SEM) - Energy Dispersive X-ray spectroscopy (EDX)

To investigate the morphology of the POSS-containing Pglass matrix nanocomposites, the samples were fractured and coated with silver using a Quorum Emitech K550X sputter coater to make the samples conductive. A Zeiss Sigma VP® field emission scanning electron microscope (SEM) operating at 20kV with an attached energy-dispersive X-ray spectroscopy (EDX) having a Thermo Scientific UltraDry EDX

detector was used to obtain the morphology and elemental compositions with NSS3®

micro-analysis software on the surfaces of the fractured neat Pglass and nanocomposites

incorporating POSS.

2.2.2.7 Transmission electron microscopy (TEM)

TEM measurements were performed (Zeiss 900®) with an acceleration voltage of

50 kV to identify the POSS molecules in the nanocomposites. Specimens for TEM were

prepared by addition of Pglass nanocomposite particles (Max. 53 μm diameter) in an

epoxy resin matrix which was cured for 36 hr at 70°C. The samples were cut and trimmed

using a microtome blade and the specimen sections were placed in 200 mesh copper grids

for observation.

2.2.2.8 Melt rheology

Rheological behavior of the samples was studied using an Anton Paar Physica

MCR501® with a 25mm diameter parallel-plate geometry at temperatures ranging from

270°C to 290°C. A linear strain of 1% was used for all the small-amplitude oscillatory

shear tests based on the result of a strain sweep test to determine the linear viscoelastic

region. Dynamic frequency sweep tests over a frequency range of 0.1 – 200 rad/s were

carried out on the samples. All the rheological experiments were conducted in a nitrogen

atmosphere to preclude oxidative degradation of the samples. The obtained data

replicated to within about 10% from sample to sample

2.2.2.9 Solid-state NMR

Solid-state ^{31}P magic angle spinning (MAS) NMR spectra of the samples were

obtained on a Bruker Avance III 600 (14.1 T) NMR instrument using a 4 mm broadband

MAS probe spinning at 12.5 kHz following standard acquisition conditions and ^{1}H

decoupling. The 1D direct polarization (DP) NMR spectra were obtained using a single pulse Bloch decay with a 240 s recycle delay with 16 scan averages, while the 1D ^{1}H-^{31}P cross polarization (CP) MAS NMR where obtained using a 1 ms contact time and a 2 s recycle delay, and 8K scan averages. The ^{31}P NMR chemical shift was referenced to the external secondary standard $(NH_4)H_2PO_4$ $\delta = 0.8$ ppm with respect to phosphoric acid $\delta = 0$ ppm. The ^{19}F MAS NMR spectra were obtained on a Bruker Avance III 400 (9.6 T) NMR instrument using a 2.5 mm broadband MAS probe spinning at 25 kHz. A rotor synchronized Hahn Echo with a 120 s recycle delay were used to obtain the 1D ^{19}F NMR DP spectrum. The ^{19}F chemical shift was referenced to the secondary standard ammonia trifluoro acetate $\delta = -72$ ppm with respect to $CFCl_3$ $\delta = 0$ ppm. Deconvolutions were performed in DMFIT [60] .

2.2.2.10 Experimental error analysis

The reported experimental data are obtained from at least three samples and the obtained data are reported as averages with standard deviations and shown as error bars in the relevant tables and figures, respectively.

2.3 Results and discussion

2.3.1 Thermal properties

The thermal stability of the samples is depicted in Fig. 2.3 showing the TGA curves of the neat Pglass and the nanocomposites samples. Within the experimental temperature range tested (i.e., 30°C to 600°C), there is no significant difference in the on-set temperature of thermal degradation between the neat Pglass and nanocomposites. Clearly, the initial thermal degradation respectively occurred at 367°C and 365°±5°C for the neat Pglass and nanocomposites as Fig. 2.3(b) shows. All the samples showed only

4 ± 1 wt.% of decomposition at elevated temperature 600°C. The observed relative insignificant effect of POSS on the thermal stability of the samples is ascribed to formation of new P-O-Si or Sn-O-Si bonds via condensation reaction between -OH in the POSS and -OH in the Pglass during the synthesis of the samples [61, 62] that are relatively thermally stable like the Si-O-Si bond in the POSS and P-O-P or P-O-Sn in the Pglass.

The glass transition temperatures (T_g) of the samples were obtained via DSC as already described in the experimental section. The T_g of the neat Pglass was found to be 121.6°C and the T_g of the nanocomposites steadily increased with increasing POSS content (up to a $T_g = 147.6$°C for 10 wt.% POSS nanocomposite) as shown in Fig. 2.4. This observation indicates a significant influence of POSS on the glass transition relaxation process in the Pglass matrix of the nanocomposites that is attributed to the bulky structure of POSS molecules like other researchers have reported in the literature [45]. In general, POSS has rigid silsesquioxane cages at the center of molecules and organic groups around the cages. The interaction of the organic groups around the cages and matrix materials is known to strongly influence POSS nanocomposites properties including glass transition temperature. In addition, the open cage type structure of POSS used in this study has silanol groups that can be reactive via condensation reaction [62] with other -OH groups of Pglass, providing chemical bonds between POSS cage and Pglass matrix materials. This suggests that the bulky and rigid POSS molecules are grafted onto the main chains of the Pglass thereby causing the observed increase of glass transition temperature of the Pglass matrix nanocomposites via restriction of Pglass chains mobility.

48

2.3.2 Chemical structure analysis

The chemical structure of the samples was probed by FTIR, XPS, MAS NMR following standard methods reported in the literature as already described in the experimental section. The FTIR spectra of the samples in Fig. 2.5 clearly shows a peak around $1070 cm^{-1}$ that is assigned to the Sn-O-P linkage and P-O$^-$ stretching vibration, which is composed of the phosphate linked to a non-bridging oxygen in the Pglass structure [63-66]. This peak is relatively broader as the amount of POSS is increased in the nanocomposites due to the formation of new chemical P-O-Si bond assigned to 1160 cm^{-1} [61]. The bond just mentioned results from condensation reaction of -OH in the POSS and -OH in the Pglass during the chemical synthesis of the samples. The additional peak of Si-O-Si symmetric stretching occurring at $1100 cm^{-1}$ is ascribed to the core cages of POSS [61]. The peak near $1015 cm^{-1}$ is associated with the $(-PO_3)^{2-}$ end groups which becomes broader as the amount of POSS in the nanocomposite is increased [67]. This last observation is probably caused by the overlapping of the $1015 cm^{-1}$ peak with the Si-O stretching vibration peak assigned to $1028 cm^{-1}$ from the POSS structure [68]. The peaks near $920 cm^{-1}$ and $740 cm^{-1}$ are respectively due to the P-O-P asymmetric and symmetric stretching vibrations [63, 66]. As expected, location and intensity of these two P-O-P peaks are not changed by the presence of POSS in the nanocomposites, indicating that the main structure of the Pglass is not changed significantly during the synthesis of the hybrid POSS/Pglass nanocomposites samples. In addition, the peak near $840 cm^{-1}$ is assigned to the stretching mode of P-F bond, which is the terminal bond in the Pglass structure [66, 69]. These P-F bonds are diminished as the amount of POSS in the nanocomposite is increased. This last observation is conjectured to be caused by the

bonding competition between F and Si-O to phosphorous that leads to a decrease in the P-F bonds due to its replacement by the new P-O-Si bonds in the nanocomposite samples. It is worthy to note that the above FTIR results provide confirmatory evidence of formation of chemical bonds between Pglass and POSS under the synthesis conditions of the samples used in this study.

Oxygen 1s X-ray photoelectron spectroscopy (XPS) was used to measure the ratio of the non-bridging oxygen to bridging oxygen in the Pglass and nanocomposites. The O 1s spectra of the neat Pglass and nanocomposites incorporating 5 wt.% POSS are deconvoluted to reveal the peaks that contain two main components representing non-bridging oxygen (NBO) and bridging oxygen (BO) in the Pglass (see Fig. 2.6). Brow et al. [70] reported results of a high ratio of NBO to BO (19:1) in the O 1s spectra of $50SnF_2$-$20SnO$-$30P_2O_5$ glass. In addition, Wagner et al. [71] reported the result of 7.8% oxygen atoms over the BO bonds in the same Pglass composition. According to our data in Fig. 2.6(a), 5.1% of BO and 94.9% of NBO are observed in the neat Pglass used, which is consistent with the result reported by Brow et al. [70]. In addition, the observed spectrum for the neat Pglass has a peak centered near the lower binding energy 531.3 eV for the BO and the other peak is centered near 529.8 eV for the NBO in the neat Pglass, respectively [72]. In the Pglass, the BO are associated with P-O-P linkage and the NBO are associated with terminal oxygen [73] such as P-O$^-$ including P-O-Sn and Sn-O-Sn. As reported in the literature [74, 75], P=O and non-bridging P-O$^-$ are not resolvable and the intensity of the XPS spectra of these oxygens is referred to as the NBO because of the peaks assigned to double-bonded (P=O) oxygens are nearly coincident with the NBO. Brow [76] reported that P=O bonds are not expected to be detected separately in the O 1s

spectra because P=O could be found only in the ultraphosphate compositions (e.g. (P_2O_5) > 50mol%) in the XPS analysis. As shown in Fig. 2.6(b) the ratio of BO to NBO in the 5 wt.% POSS nanocomposites indicate a significant 40% increase from 5.1% of the neat Pglass. This result is probably caused by the BO in Si-O-Si of POSS and the new Si-O-P linkage between Pglass and POSS in the nanocomposites. Onyiriuka [74] reported that the BO of Si-O-Si and the NBO (e.g. Si-O-M$^+$) can be distinguished by the O1s XPS spectrum similar to the oxygen in the Pglass, and other researchers have reported BO peaks centered near 531 eV for Si-O-Si that overlaps the binding energy of P-O-P linkage [77]. Overall, the obtained 40% of BO can be explained by several bridging linkages like the P-O-P, Si-O-Si and Si-O-P linkages that possibly belong to the BO in the 5 wt.% POSS nanocomposite sample. Clearly, the above results confirm the desirable chemical reaction between the POSS and the Pglass as a facile method of incorporating molecular silica into the chemical structure of the Pglass matrix nanocomposite with enhanced benefits described later.

Lastly, the chemical structure was characterized using both ^{19}F and ^{31}P solid-state nuclear magnetic resonance (SSNMR). Fig. 2.7(a) shows the ^{19}F MAS NMR for Pglass with increasing concentration of POSS. The spectra are dominated (~88 %) by a resonance at $\delta = -58$ ppm (and associated spinning sidebands) which has been assigned to a P-F environment [78]. There is also a F environment observed at $\delta = -48$ ppm (11%) assigned to SnF$_2$ species [79] and a minor species at $\delta \sim -120$ ppm (~1%) assigned to a F in a mixed tin oxide environment (spectral deconvolutions are shown in Fig. 2.7(b)) These results show that there are no large changes in the F environments and that the P-F linkage is retained in the glass structure during the formation of the nanocomposites.

51

The ^{31}P MAS NMR (Fig. 2.7(c)) and ^{1}H-^{31}P CPMAS NMR spectra (Fig. 2.7(d)) show the central isotropic resonance shift region for samples with the addition of the POSS into the Pglass matrix nanocomposite. These spectra are assigned to the overlapping Q^1 and Q^0 species at δ = -18.8 and -11.3 ppm., where the numbers 1 and 0 indicate the number of bridging oxygen connected to phosphorous in the Pglass structure [9, 23]. A few comments are warranted on these resonance assignments. It has been previously argued that substitution of a F for a bridging O within the phosphate polyhedron has minimal effect on the ^{31}P chemical shift for metaphosphate Q^2 species (two bridging oxygens and two non-bridging oxygens per phosphate or one bridging oxygen, one fluorine and two non-bridging oxygens per phosphate), while formation of a terminal P-F leads to the depolymerization of the Q^2 phosphate [80, 81]. For pure tin phosphate glasses xSnO (1-x)P_2O_5 the Q^2 phosphate species was observed between δ = -35 and -32 ppm [82, 83], arguing that Q^2 phosphate species (fluorinated or non-fluorinated) are not present in the TFP glass. For pure tin phosphate glass the Q^1 and Q^0 phosphate species were reported between δ = -20 and -15 ppm and δ = -11 and -9 ppm, respectively [82]. The assignment of the broad resonance observed at δ = -18.8 ppm to a (-OP(O$^-$)$_2$F) Q^1 phosphate species is consistent with the assignment previously reported for TFP glasses and composites [84]. The minor resonance at δ = -11.3 ppm in the pure TFP glass is assigned to orthophosphate Q^0 phosphate species.

These NMR results show that there are no huge structural or chemical changes in the Pglass structure except for a minor increase in the δ = -11.3 ppm resonance with the increasing POSS addition. This is clearly evident in Fig. 2.7(e) where a spectral deconvolution is shown. The relative concentration of the Q^1 to Q^0 phosphate species of

all the chemically synthesized samples being displayed in Table 1 for easy comparison. Note that as the amount of POSS in the nanocomposite increased the ratio of Q^0 to Q^1 increased, indicating that shorter inorganic Pglass chains are formed with the addition of POSS, or that this increase in the $\delta = -11.3$ ppm resonance may reflect direct bonding between POSS and the TFP glass. The reaction between -OH of Pglass and -OH of POSS would result in the formation of P-O-Si linkages that are predicted to occur with a ^{31}P chemical shift near $\delta = -10$ to -12 ppm [85]. In this study there is not a distinct peak for this proposed linkage species. The ^{1}H-^{31}P CPMAS NMR spectra (Fig. 2.7(d)) are similar to the DP ^{31}P MAS NMR spectra, but are much weaker, representing only ~2% of the total ^{31}P signal. Also, note that with increasing POSS concentration there is an emphasis of the $\delta = -11.30$ ppm in the CPMAS ^{31}P NMR. These CPMAS results demonstrates that for the original TFP glass there is low water and OH concentrations, confirming previously reported excellent durability for this glass composition. These results are remarkably consistent with the FTIR data already described.

2.3.3 Melt rheology

As shown in Fig. 2.8 the neat Pglass and nanocomposites revealed a Newtonian behavior (or constant viscosity with shear rate) under steady shear flow conditions at 270°C except the low shear rate region of the neat Pglass [17]. As the amount of POSS increased in the nanocomposites, the viscosity of the nanocomposites gradually increased. The obtained results showed that addition of POSS in the nanocomposites gave higher viscosity due to the influence of the bulky POSS molecules in the liquid Pglass matrix [45]. It is noteworthy that this result is consistent with the FTIR and XPS analysis already discussed in the previous sections. The significantly low viscosity

observed for the neat Pglass at the low shear rate may be due to the test instrument limitation in the very low viscosity regime. The significant increase in the viscosity of the Pglass matrix with small additions of POSS is remarkable and may provide a facile method of changing the deformation and flow properties of glass matrix nanocomposites during shaping and forming while still preserving the optical properties of the glass as already mentioned.

Complex viscosities of the neat Pglass and nanocomposites under small amplitude oscillatory shear flows are shown in Fig. 2.9(a). As expected, this figure shows an increase in the complex viscosity with increasing amount of POSS in the nanocomposites in the whole frequency range tested. In addition, Newtonian fluid behavior was observed for all the samples under the reported test conditions. As shown in Fig. 2.9(b, c), it can be seen that addition of POSS causes an increase in both the dynamic storage and loss moduli, respectively. The data scattering observed in the low frequency region for the neat Pglass and nanocomposite (2 wt.% POSS) may be due to instrument limitation in the very low storage modulus regime that is characteristic of the samples. Fig. 2.9(d) shows the so-called Han plots for the samples [86, 87], which shows the relation between storage modulus and loss modulus at similar frequency. The slope of the storage modulus versus loss modulus significantly decreased as the amount of POSS increased in the nanocomposites as clearly evident in Fig. 2.9(d). It is worthy to note that the change of slope in this figure indicates significant difference in the structure of the nanocomposites composed of the matrix and filler materials at a fixed temperature [86]. It is well know that the rheology of non-entangled melts like the current Pglass melts is well described by a modified Rouse theory [88]. Using this theory the rheological characteristics of alkali

zinc phosphate (AZP) glass was interpreted as undiluted organic polymers of low molecular weight as previously reported [89, 90]. The dynamic storage modulus and dynamic loss modulus of the current samples are expected to be predicted by this theory. Briefly, the Rouse model describes the complex dynamic viscosity according to the following equation;

$$\eta^*(\omega) = \frac{\rho RT}{M} \sum_{p=1}^{N} \frac{\tau_p}{1 + i\omega\tau_p} \qquad (1)$$

Here, the materials have a density ρ, molecular weight M, and a set of relaxation times $\{ \tau_1, \tau_2, \tau_3, \ldots, \tau_N\}$ at absolute temperature T and angular frequency ω. Here, R is the ideal gas law constant and $i = \sqrt{-1}$. This result simplifies with one relaxation time τ:

$$\eta^*(\omega) = \frac{\rho RT}{M} \frac{\tau}{1 + i\omega\tau} \qquad (2)$$

The ω dependence at any T can be summarized with two fit parameters η_0 and τ. Here, a zero shear viscosity η_0 was defined by Sammler et al. [90] as.

$$\eta_0 = \frac{\rho RT\tau}{M} \qquad (3)$$

By following the definition,

$$\eta^*(\omega) = |\eta^*(\omega)|exp\{-\phi_\eta(\omega)\} \qquad (4)$$

where,

$$\phi_\eta(\omega) = \tan^{-1}\{\omega\tau\} \tag{5}$$

The magnitude of the complex viscosity is given as

$$|\eta^*(\omega)| = \eta_0\{1 + (\omega\tau)^2\}^{-1/2} \tag{6}$$

As reported by Adalja et al. [91], the 1-parameter Rouse model (equation 6) for the dynamic shear data of the Pglass agrees very well at low values of the angular frequency, but significant deviation appeared in the higher frequency region. Therefore, the 2-parameter Rouse model was applied in the current study consistent with the assumption of two kinds of units in the Pglass. The 2-parameter Rouse model more accurately models the frequency dependence of the complex viscosity according to the equations below [91]. In the 2-parameter Rouse model, the complex viscosity as a function of frequency can be described as

$$\eta^*(\omega) = \frac{\rho RT}{M}\left\{\frac{\tau_1}{1 + i\omega\tau_1} + \frac{\tau_2}{1 + i\omega\tau_2}\right\} \tag{7}$$

and two constants with the units of viscosity

$$\eta_1 = \frac{\rho RT\tau_1}{M} \quad and \quad \eta_2 = \frac{\rho RT\tau_2}{M} \tag{8}$$

Equations (7) and (8) can be combined to give the magnitude of the complex viscosity as the following equation (9):

$$|\eta^*(\omega)| = \left\{ \left[\frac{\eta_1}{1+(\omega\tau_1)^2} + \frac{\eta_2}{1+(\omega\tau_2)^2} \right]^2 + \omega^2 \left[\frac{\eta_1\tau_1}{1+(\omega\tau_1)^2} + \frac{\eta_2\tau_2}{1+(\omega\tau_2)^2} \right]^2 \right\}^{1/2} \quad (9)$$

As shown in Fig. 2.10 the theoretical predictions of equation (9) show agreement with the obtained experimental data. The τ_i and η_i values are shown in Table 2 for the neat Pglass and nanocomposites. The fitting was carried out using Origin® software.

As shown in Fig. 2.11 the viscosity of the neat Pglass and all nanocomposites samples having different POSS concentrations decreased as the temperature increased, facilitating the processability of the materials at elevated temperatures. To determine the flow activation energy of the neat Pglass and nanocomposites in the range of temperature explored, an Arrhenius type equation was applied over the specific experimental temperature range due to the restriction of using WLF equation at temperatures close to the glass transition temperature [91]. The Time-Temperature Superposition shift factor α_T can be described as follows

$$\alpha_T = \frac{\eta_0(T)}{\eta_0(T_0)} \quad (10)$$

Here, T_0 is reference temperature, 280°C, and shift factor α_T can be fitted with temperature according to the following equation:

$$\alpha_T = exp\left[\frac{\Delta H}{R}\left(\frac{1}{T} - \frac{1}{T_0}\right)\right] \tag{11}$$

where, ΔH is the flow activation energy and R is the universal gas constant. Equation (11) can be rewritten as follows.

$$\log \alpha_T = \frac{\Delta H}{2.303R}\left(\frac{1}{T} - \frac{1}{T_0}\right) \tag{12}$$

The activation energies (ΔH) were calculated from slopes ($\Delta H/2.303R$) of lines in Fig. 2.11(b) as indicated by equation (12), using the experimental data for each sample displayed in Fig. 2.11(a); and the calculated activation energies is shown in Fig. 2.11(c). It is clearly evident from Fig. 2.11(c) that the flow activation energy of the samples is independent of the POSS concentration within the range explored. This observation is thought to be beneficial in the shaping and forming of products made from the nanocomposites

2.3.4 Morphological analysis

Figure 12 shows SEM micrographs of the fracture surfaces of the neat Pglass and nanocomposites containing 10 wt.% of POSS prepared via chemical synthesis as already described. Clearly, the samples showed featureless morphologies with no discernable microscale aggregation or phase separation in the POSS/Pglass matrix nanocomposites, confirming the homogeneous molecular-level dispersion of POSS in the Pglass matrix. Note that the white speck on the surface of the sample on the SEM images in Fig. 2.12 is shown for contrast and to show the remarkably smooth and homogeneous surface of the

sample. As shown earlier in Fig. 2.2, the nanocomposites were observed to be clearly

transparent indicating that the POSS is chemically reacted with the Pglass to yield a

hybrid POSS/Pglass nanocomposite. This last point is supported by Fig. 2.13 that shows

mapping images of elements (white spots) by SEM-EDX on the fracture surface of Pglass

matrix nanocomposites incorporating 10 wt.% POSS. Clearly, Fig. 2.13(c) and (d) shows

that the carbon (C) and silicon (Si) of the POSS are homogeneously dispersed in the

Pglass matrix composed of P (and O, Sn, H and F, not shown).

AFM was used to investigate nanoscale morphology of the fracture surface of

Pglass and nanocomposites and the obtained results are in Fig. 2.14. This figure shows

homogeneously dispersed biphasic nanostructure as the concentration of the POSS in the

nanocomposite is increased from 5 wt.% to 10 wt.%(see Fig. 2.14(d-f)). This nanoscale

structure facilitates the observed transparency and enhanced rheological properties of the

nanocomposites.

In order to compare the structure of the chemically synthesized hybrid

POSS/Pglass nanocomposite with that of the physically blended *premade* Pglass and

POSS blend as described in the experimental section 2.1, the morphology of the latter

was investigated, and the obtained result is shown in Fig. 2.15. As expected, this figure

clearly shows segregated POSS structures attached to the surface of the Pglass matrix as

depicted in Fig. 2.15(a). This observation is corroborated by Fig. 2.15(b) which shows

TEM image of aggregated nanostructured POSS molecules attached to the surface of the

Pglass matrix in the nanocomposite. Note that the structure of the physically blended

nanocomposite is remarkably different from that of the chemically synthesized

nanocomposite (Fig. 2.12) as already described. Based on all the obtained results of this

59

study a conjectured chemical bonding structure of the synthesized POSS/Pglass

nanocomposite is depicted in Fig. 2.16. The current study will provide a basis for further

elaboration of the proposed chemical structure model just mentioned and a better

understanding of the structure-property relations of the novel nanocomposites materials

platform in a future proposed study.

2.3.5 Nanomechanical properties

As a first step towards assessing the effect of the POSS on the mechanical

properties of the POSS/Pglass nanocomposite, the nanomechanical properties of fractured

surfaces of the neat Pglass and nanocomposites were investigated using AFM QNM^{TM}

(PeakForce^{TM} Quantitative Nanomechanical Mapping) mode as already described in the

experimental section [57-59, 92]. The obtained results are summarized in Fig. 2.17 for

easy comparison. To obtain the elastic modulus of the samples, the experimental data

curve was fitted with the Derjaguin-Muller-Toporov (DMT) model [59, 93]. Here, the

elastic modulus is given by

$$\text{F} = \frac{4}{3}E\sqrt{Rd^3} + F_{adh} \tag{13}$$

where F is the force, R is the tip radius, d is the deformation, and F_{adh} is the maximum

adhesion force. As clearly shown in Fig. 2.17(d) the addition of POSS to the Pglass

matrix increased the surface modulus of the nanocomposites. Fig. 2.18 shows the average

and standard deviation of the obtained moduli for five profiles on each sample. The

average modulus increased from 1.55 GPa to 6.28 GPa as the amount of POSS was

increased from 0 wt.% (neat Pglass) to 10 wt.% TSP-POSS. Overall, the results of this study point to novel "transparent" glass matrix nanocomposites with enhanced benefits for a number of wide ranging uses in applications, including biomedical engineering, thin films and coatings.

2.4 Conclusion

It can be concluded from the results of this study that novel POSS/Pglass nanocomposites can be prepared by chemically reacting the raw materials of Pglass and neat POSS using a glass synthesis and quench method to yield novel transparent glass matrix nanocomposites with improved controllable properties. Incorporation of the POSS in the Pglass matrix nanocomposite increased the glass transition temperature of the nanocomposite, suggesting that the relatively bulky POSS molecules reduce mobility of Pglass chains in the nanocomposites. The observed improved melt viscoelasticity of the nanocomposites is thought to be crucially important and desirable in the shaping/forming of parts from the nanocomposites and their use. Spectroscopic analysis of the samples via ATR-FTIR, XPS confirmed the chemical reaction of the POSS with Pglass matrix to yield novel transparent POSS/Pglass nanocomposite with excellent homogeneous distribution of the nanodispersed POSS phase with enhanced benefits for diverse applications already mentioned. The nanoscale dispersion of the POSS in the POSS/Pglass nanocomposite was confirmed by the obtained AFM and SEM-EDX data. Solid-state NMR data showed that the ratio Q^0 to Q^1 increases slightly as the addition of POSS was increased in the Pglass matrix, suggesting that the average length of the Pglass chains in the nanocomposites is smaller than that of the neat Pglass.

Nanomechanical properties of the fractured surface was investigated using AFM PeakForce Quantitative Nanomechanical Mapping (QNM) mode and the obtained results showed increased elastic modulus of nanocomposite surface with increasing concentration of the uniformly nanodispersed rigid POSS molecules in the nanocomposites. This study provides the first ever fundamental information on novel phosphate glass matrix nanocomposites incorporating POSS dispersed at the molecular level to yield interesting hybrid POSS/Pglass materials with enhanced benefits like optically transparency and improved stiffness (or modulus) that may be useful in a wide range of industrial applications such as biomedical device, optoelectronic components, impact resistant transparent panels and bioengineering.

Acknowledgements

2.5 Reference

1.   Hussain, F., et al., Review article: polymer-matrix nanocomposites, processing, manufacturing, and application: an overview. Journal of composite materials, 2006. 40(17): p. 1511-1575.

2.   Alexandre, M. and P. Dubois, Polymer-layered silicate nanocomposites: preparation, properties and uses of a new class of materials. Materials Science and Engineering: R: Reports, 2000. 28(1): p. 1-63.

3.   Schmidt, D., D. Shah, and E.P. Giannelis, New advances in polymer/layered silicate nanocomposites. Current Opinion in Solid State and Materials Science, 2002. 6(3): p. 205-212.

4.   Ray, S.S. and M. Okamoto, Polymer/layered silicate nanocomposites: a review from preparation to processing. Progress in polymer science, 2003. 28(11): p. 1539-1641.

5.   Hanemann, T., Influence of particle properties on the viscosity of polymer–alumina composites. Ceramics International, 2008. 34(8): p. 2099-2105.

1.   Hussain, F., et al., Review article: polymer-matrix nanocomposites, processing, manufacturing, and application: an overview. Journal of composite materials, 2006. 40(17): p. 1511-1575.

2.   Alexandre, M. and P. Dubois, Polymer-layered silicate nanocomposites: preparation, properties and uses of a new class of materials. Materials Science and Engineering: R: Reports, 2000. 28(1): p. 1-63.

3.   Schmidt, D., D. Shah, and E.P. Giannelis, New advances in polymer/layered silicate nanocomposites. Current Opinion in Solid State and Materials Science, 2002. 6(3): p. 205-212.

4.   Ray, S.S. and M. Okamoto, Polymer/layered silicate nanocomposites: a review from preparation to processing. Progress in polymer science, 2003. 28(11): p. 1539-1641.

5.   Hanemann, T., Influence of particle properties on the viscosity of polymer–alumina composites. Ceramics International, 2008. 34(8): p. 2099-2105.

6.   Kumar, S., et al., Fibers from polypropylene/nano carbon fiber composites. Polymer, 2002. 43(5): p. 1701-1703.

7.   Andrews, R. and M.C. Weisenberger, Carbon nanotube polymer composites. Current Opinion in Solid State and Materials Science, 2004. 8(1): p. 31-37.

8.   Ma, P.-C., et al., Dispersion and functionalization of carbon nanotubes for polymer-based nanocomposites: a review. Composites Part A: Applied Science and Manufacturing, 2010. 41(10): p. 1345-1367.

9.   Urman, K. and J.U. Otaigbe, New phosphate glass/polymer hybrids—Current status and future prospects. Progress in Polymer Science, 2007. 32(12): p. 1462-1498.

10.   Lai, Y., et al., Structural and electrochemical properties of polyurethanes/polyhedral oligomeric silsesquioxanes (PU/POSS) hybrid coatings on aluminum alloys. Materials Chemistry and Physics, 2009. 117(1): p. 91-98.

11.   Miracle, D.B., et al., ASM handbook. Vol. 21. 2001: ASM international Materials Park, OH, USA.

12.   Hull, D. and T. Clyne, An introduction to composite materials. 1996: Cambridge university press.

13.   URMAN, K. and J. OTAIGBE. Morphology, crystallization kinetics and dynamic mechanical analysis of phosphate glass-polyamide 12 hybrid materials. in ANTEC... conference proceedings. 2004. Society of Plastics Engineers.

14.   Urman, K. and J. Otaigbe, Novel phosphate glass/polyamide 6 hybrids: miscibility, crystallization kinetics, and mechanical properties. Journal of Polymer Science Part B: Polymer Physics, 2006. 44(2): p. 441-450.

15.   Rawal, A., et al., Detection of nanometer-scale mixing in phosphate-glass/polyamide-6 hybrids by 1H-31P NMR. Chemistry of materials, 2006. 18(26): p. 6333-6338.

16.   Rawal, A., et al., Promotion of the γ-phase of polyamide 6 in its nanocomposite with phosphate glass. Journal of Polymer Science Part B: Polymer Physics, 2008. 46(9): p. 857-860.

17.   Urman, K., T. Schweizer, and J.U. Otaigbe, Rheology of tin fluorophosphate glass/polyamide 12 hybrids in the low concentration regime. Journal of Rheology (1978-present), 2007. 51(6): p. 1171-1187.

18.   Belyamani, I., J.U. Otaigbe, and W.R. Fielding, Development of new sustainable inorganic flame retardant additive system for polyamide 6, 6 with improved performance. Polymer Engineering & Science, 2015. 55(8): p. 1741-1748.

19.   Sanford, L.M. and P.A. Tick, Tin-phosphorus oxyfluoride glasses. 1982, Google Patents.

20.   Beall, G.H., J.E. Dickinson Jr, and C.J. Quinn, Rare earth-containing zinc phosphate glasses. 1991, Google Patents.

21.   Otaigbe, J.U. and G.H. Beall, Inorganic phosphate glasses as polymers. Trends in Polymer science, 1997. 5(11): p. 369-379.

22.   Loong, C.-K., et al., Structure and dynamics of phosphate glasses: from ultra-to orthophosphate composition. Physica B: Condensed Matter, 1997. 241: p. 890-896.

23.   Brow, R.K., Review: the structure of simple phosphate glasses. Journal of Non-Crystalline Solids, 2000. 263: p. 1-28.

24.   Cho, J., A.R. Boccaccini, and M.S. Shaffer, Ceramic matrix composites containing carbon nanotubes. Journal of Materials Science, 2009. 44(8): p. 1934-1951.

25.   Kotoul, M., et al., Toughening effects quantification in glass matrix composite reinforced by alumina platelets. Acta Materialia, 2008. 56(12): p. 2908-2918.

26.   Boccaccini, A., et al., Assessment of damage induced by thermal shock in SiC-fiber-reinforced borosilicate glass composites. Composites science and technology, 1999. 59(1): p. 105-112.

27.   Prewo, K.M. and J.J. Brennan, High-strength silicon carbide fibre-reinforced glass-matrix composites. Journal of Materials Science, 1980. 15(2): p. 463-468.

28.   Cannillo, V., et al., Mechanical performance and fracture behaviour of glass–matrix composites reinforced with molybdenum particles. Composites science and technology, 2005. 65(7): p. 1276-1283.

29.   Boccaccini, A., et al., Borosilicate glass matrix composites containing multi-wall carbon nanotubes. Journal of the European Ceramic Society, 2005. 25(9): p. 1515-1523.

30.   Desimone, D., et al., Optically-transparent oxide fibre-reinforced glass matrix composites. Journal of Non-Crystalline Solids, 2010. 356(44): p. 2591-2597.

31.   Lee, H., et al., Glass–ceramics and composites containing aluminum borate whiskers. Ceramics International, 2010. 36(5): p. 1589-1596.

32.   Boccaccini, A., et al., Borosilicate and lead silicate glass matrix composites containing pyrochlore phases for nuclear waste encapsulation. Journal of nuclear materials, 2004. 327(2): p. 148-158.

33.   Boccaccini, A.R., et al., Glass matrix composites from coal flyash and waste glass. Waste management, 1997. 17(1): p. 39-45.

34.   Boccaccini, A.R., S. Atiq, and G. Helsch, Optomechanical glass matrix composites. Composites science and technology, 2003. 63(6): p. 779-783.

35.   Thomas, B.J., M.S. Shaffer, and A.R. Boccaccini, Sol–gel route to carbon nanotube borosilicate glass composites. Composites Part A: Applied Science and Manufacturing, 2009. 40(6): p. 837-845.

36.   Raab, D., et al., Mechanical properties of oxide-fiber reinforced glass matrix composites with BN or SnO 2 interfaces. Materials Science and Engineering: A, 2006. 417(1): p. 341-347.

37.   Boccaccini, A., et al., Processing and characterisation of model optomechanical composites in the system sapphire fibre/borosilicate glass matrix. Journal of materials processing technology, 2005. 169(2): p. 270-280.

38.   Minay, E., V. Desbois, and A. Boccaccini, Innovative manufacturing technique for glass matrix composites: extrusion of recycled TV set screen glass reinforced with Al 2 O 3 platelets. Journal of materials processing technology, 2003. 142(2): p. 471-478.

39.   Boccaccini, A., et al., Effect of thermomechanical loads on microstructural damage and on the resulting thermomechanical behaviour of silicon carbide fibre-reinforced glass matrix composites. Materials characterization, 2005. 54(1): p. 75-83.

40.   Giannelis, E., R. Krishnamoorti, and E. Manias, Polymer-silicate nanocomposites: model systems for confined polymers and polymer brushes, in Polymers in confined environments. 1999, Springer. p. 107-147.

41.   Paul, D. and C. Bucknall, Polymer blends: formulation and performance. Canada: John Wiley & Sons, 2000: p. 1224.

42.   Gnanasekaran, D., K. Madhavan, and B. Reddy, Developments of polyhedral oligomeric silsesquioxanes (POSS), POSS nanocomposites and their applications: a review. J Sci Ind Res, 2009. 68(6): p. 437-64.

43.   Wang, W., Y.-l. Guo, and J.U. Otaigbe, The synthesis, characterization and biocompatibility of poly (ester urethane)/polyhedral oligomeric silsesquioxane nanocomposites. Polymer, 2009. 50(24): p. 5749-5757.

44.   Kuo, S.-W. and F.-C. Chang, POSS related polymer nanocomposites. Progress in Polymer Science, 2011. 36(12): p. 1649-1696.

45.   Phillips, S.H., T.S. Haddad, and S.J. Tomczak, Developments in nanoscience: polyhedral oligomeric silsesquioxane (POSS)-polymers. Current Opinion in Solid State and Materials Science, 2004. 8(1): p. 21-29.

46.   Nanda, A.K., et al., Nanostructured polyurethane/POSS hybrid aqueous dispersions prepared by homogeneous solution polymerization. Macromolecules, 2006. 39(20): p. 7037-7043.

47.   Lichtenhan, J.D., Y.A. Otonari, and M.J. Carr, Linear hybrid polymer building blocks: methacrylate-functionalized polyhedral oligomeric silsesquioxane monomers and polymers. Macromolecules, 1995. 28(24): p. 8435-8437.

48.   Zheng, L., R.J. Farris, and E.B. Coughlin, Novel polyolefin nanocomposites: synthesis and characterizations of metallocene-catalyzed polyolefin polyhedral oligomeric silsesquioxane copolymers. Macromolecules, 2001. 34(23): p. 8034-8039.

49.   Gonzalez, R.I., S.H. Phillips, and G.B. Hoflund, In situ oxygen-atom erosion study of polyhedral oligomeric silsesquioxane-siloxane copolymer. Journal of Spacecraft and Rockets, 2000. 37(4): p. 463-467.

50.   Baldi, F., et al., Mechanical characterization of polyhedral oligomeric silsesquioxane/polypropylene blends. Journal of applied polymer science, 2007. 105(2): p. 935-943.

51.   Zhao, Y. and D.A. Schiraldi, Thermal and mechanical properties of polyhedral oligomeric silsesquioxane (POSS)/polycarbonate composites. Polymer, 2005. 46(25): p. 11640-11647.

52.   Yoon, K.H., et al., Properties of poly (ethylene terephthalate) containing epoxy-functionalized polyhedral oligomeric silsesquioxane. Polymer international, 2005. 54(1): p. 47-53.

53.   Xu, H., et al., Preparation, Thermal Properties, and T g Increase Mechanism of Poly (acetoxystyrene-co-octavinyl-polyhedral oligomeric silsesquioxane) Hybrid Nanocomposites. Macromolecules, 2005. 38(25): p. 10455-10460.

54.   Li, G.Z., et al., Synthesis and properties of poly (isobutyl methacrylate-co-butanediol dimethacrylate-co-methacryl polyhedral oligomeric silsesquioxane) nanocomposites. Journal of Polymer Science Part A: Polymer Chemistry, 2005. 43(2): p. 355-372.

55.   Huang, C.-F., et al., Influence of PMMA-chain-end tethered polyhedral oligomeric silsesquioxanes on the miscibility and specific interaction with phenolic blends. Macromolecules, 2006. 39(1): p. 300-308.

56.   Hany, R., et al., Chemical synthesis and characterization of POSS-functionalized poly [3-hydroxyalkanoates]. Polymer, 2005. 46(14): p. 5025-5031.

57.   Dokukin, M.E. and I. Sokolov, Quantitative mapping of the elastic modulus of soft materials with HarmoniX and PeakForce QNM AFM modes. Langmuir, 2012. 28(46): p. 16060-16071.

58.   Lorenzoni, M., et al., Nanomechanical properties of solvent cast polystyrene and poly (methyl methacrylate) polymer blends and self-assembled block copolymers. Journal of Micro/Nanolithography, MEMS, and MOEMS, 2015. 14(3): p. 033509-033509.

59.   Cappella, B. and G. Dietler, Force-distance curves by atomic force microscopy. Surface science reports, 1999. 34(1): p. 1-104.

60.   Massiot, D., et al., Modelling one-and two-dimensional solid-state NMR spectra. Magnetic Resonance in Chemistry, 2002. 40(1): p. 70-76.

61.   Kannan, A.G., N.R. Choudhury, and N.K. Dutta, Synthesis and characterization of methacrylate phospho-silicate hybrid for thin film applications. Polymer, 2007. 48(24): p. 7078-7086.

62.   Borisov, S., Organosilicon derivatives of Phosphorus and Sulfur. 2012: Springer Science & Business Media.

63.   Fang, Y., et al., Tin fluorophosphate nonwovens by melt state centrifugal Forcespinning. Journal of Materials Science, 2014. 49(24): p. 8252-8260.

64.   Bartholomew, R.F., Structure and properties of silver phosphate glasses—Infrared and visible spectra. Journal of Non-Crystalline Solids, 1972. 7(3): p. 221-235.

65.   Bunker, B., G. Arnold, and J.A. Wilder, Phosphate glass dissolution in aqueous solutions. Journal of Non-Crystalline Solids, 1984. 64(3): p. 291-316.

66.   Ding, J., et al., The properties and structure of Sn-Ca-P-O-F glasses. Materials chemistry and physics, 2003. 82(1): p. 61-67.

67.   Sun, K. and W.M. Risen, Rare earth phosphate glasses. Solid state communications, 1986. 60(9): p. 697-700.

68.   Liang, K., et al., Cyanate ester/polyhedral oligomeric silsesquioxane (POSS) nanocomposites: synthesis and characterization. Chemistry of materials, 2006. 18(2): p. 301-312.

69.   Anma, M., et al., Structure of glasses in the system Sn-Pb-P-F-O. Journal of Non-Crystalline Solids, 1991. 135(1): p. 79-85.

70.   Brow, R.K., et al., An x-ray photoelectron spectroscopy study of anion bonidng in tin (II) fluorophosphate glass. Physics and chemistry of glasses, 1992. 33(2): p. 33-39.

71.   Wagner, T., et al., 10th International Conference on Solid State Chemistry, Pardubice, Czech Republic, Structure of SnF2-SnO-P2O5 Glasses. Physics Procedia, 2013. 44: p. 159-165.

72.   York-Winegar, J., et al., Structure of SnF2-SnO-P2O5 Glasses. Physics Procedia, 2013. 44: p. 159-165.

73.   Brow, R.K., R.J. Kirkpatrick, and G.L. Turner, Nature of alumina in phosphate glass: II, structure of sodium alurninophosphate glass. Journal of the American Ceramic Society, 1993. 76(4): p. 919-928.

74.   Onyiriuka, E., Zinc phosphate glass surfaces studied by XPS. Journal of non-crystalline solids, 1993. 163(3): p. 268-273.

75.   Brow, R.K., M.R. Reidmeyer, and D.E. Day, Oxygen bonding in nitrided sodium- and lithium-metaphosphate glasses. Journal of Non-Crystalline Solids, 1988. 99(1): p. 178-189.

76.   Brow, R.K., An XPS study of oxygen bonding in zinc phosphate and zinc borophosphate glasses. Journal of non-crystalline solids, 1996. 194(3): p. 267-273.

77.   Mekki, A., D. Holland, and C. McConville, X-ray photoelectron spectroscopy study of copper sodium silicate glass surfaces. Journal of non-crystalline solids, 1997. 215(2): p. 271-282.

78.   Zhang, L., C.C. de Araujo, and H. Eckert, A new sol-gel route to aluminum fluoride phosphate glasses: Mechanistic investigations by NMR spectroscopy. Chemistry of materials, 2005. 17(12): p. 3101-3107.

79.   Bräuniger, T., S. Ghedia, and M. Jansen, Covalent Bonds in α-SnF2 Monitored by J-Couplings in Solid-State NMR Spectra. Zeitschrift für anorganische und allgemeine Chemie, 2010. 636(13-14): p. 2399-2404.

80.   Haubenreisser, U., U. Sternberg, and A.-R. Grimmer, High-field 31P NMR investigations of the chemical shielding and indirect dipolar coupling of polycrystalline fluorophosphates. Molecular Physics, 1987. 60(1): p. 151-163.

81.   Brow, R.K., Z. Osborne, and R.J. Kirkpatrick, A multinuclear MAS NMR study of the short-range structure of fluorophosphate glass. Journal of materials research, 1992. 7(07): p. 1892-1899.

82.   Holland, D., et al., Lone-pair effects and structural trends in x SnO·(1− x) P2O5 glasses deduced from 31P and 119Sn nuclear magnetic resonance. Journal of Physics: Condensed Matter, 2002. 14(49): p. 13609.

83.   Bekaert, É., et al., Structure and properties of x SnO–(100–x) P 2 O 5 glasses. Comptes Rendus Chimie, 2004. 7(3): p. 377-382.

84.   Tischendorf, B.C., et al., Investigation of structure and morphology dynamics in tin fluorophosphate glass-polyethylene hybrids using solid-state 1H, 13C, and 31P MAS NMR. Chemistry of materials, 2002. 14(1): p. 341-347.

85.   Cody, G.D., et al., Silicate-phosphate interactions in silicate glasses and melts: I. A multinuclear (27 Al, 29 Si, 31 P) MAS NMR and ab initio chemical shielding (31 P) study of phosphorous speciation in silicate glasses. Geochimica et Cosmochimica Acta, 2001. 65(14): p. 2395-2411.

86.   Tian, J., W. Yu, and C. Zhou, The preparation and rheology characterization of long chain branching polypropylene. Polymer, 2006. 47(23): p. 7962-7969.

87.   Wu, D., L. Wu, and M. Zhang, Rheology of multi-walled carbon nanotube/poly (butylene terephthalate) composites. Journal of Polymer Science Part B: Polymer Physics, 2007. 45(16): p. 2239-2251.

88.   Rouse Jr, P.E., A theory of the linear viscoelastic properties of dilute solutions of coiling polymers. The Journal of Chemical Physics, 1953. 21(7): p. 1272-1280.

89.   Ferry, J.D., Viscoelastic properties of polymers. 1980: John Wiley & Sons.

90.   Sammler, R., et al., Melt rheology of zinc alkali phosphate glasses. Journal of Rheology (1978-present), 1996. 40(2): p. 285-302.

91.   Adalja, S.B. and J.U. Otaigbe, Melt rheology of tin phosphate glasses. Appl Rheol, 2001. 11(1): p. 10-18.

92.   Yang, C.-W., Y.-H. Lu, and S. Hwang, Imaging surface nanobubbles at graphite–water interfaces with different atomic force microscopy modes. Journal of Physics: Condensed Matter, 2013. 25(18): p. 184010.

93.   Derjaguin, B.V., V.M. Muller, and Y.P. Toporov, Effect of contact deformations on the adhesion of particles. Journal of Colloid and interface science, 1975. 53(2): p. 314-326.
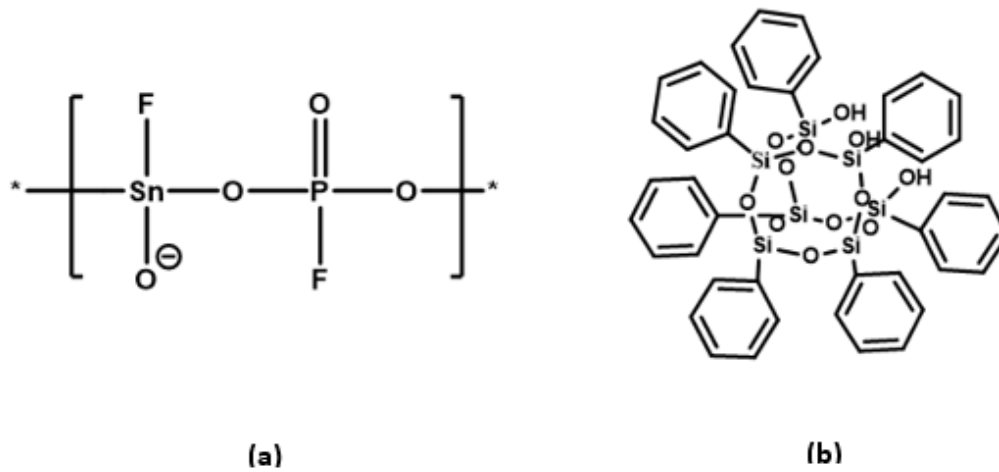
Figure 2.1 Structure of (a) Pglass and (b) TSP POSS

Figure 2.2 Comparison of synthesized Pglass matrix nanocomposites incorporating TSP-POSS prepared by the synthesis method described in the text; (a) neat Pglass, (b) 5 wt.% TSP-POSS, (c) 10 wt.% TSP-POSS.
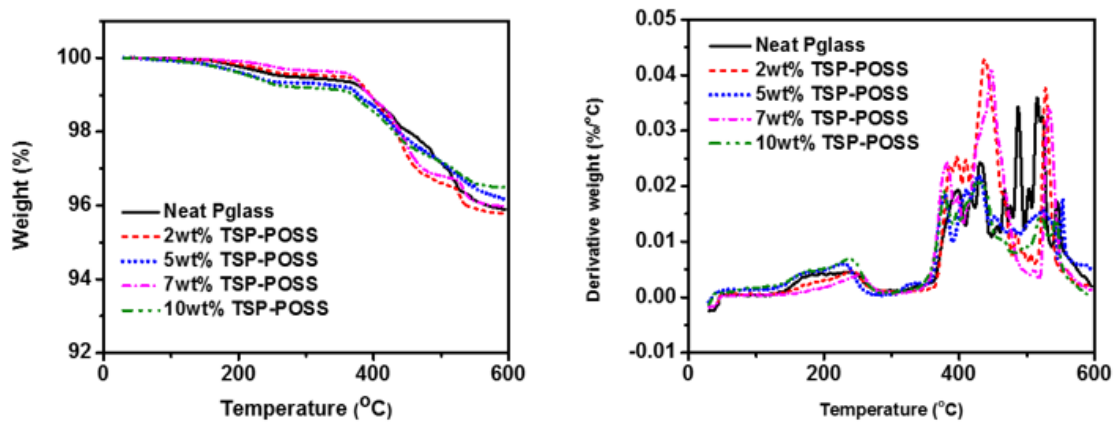
Figure 2.3 TGA curves for the neat Pglass and its nanocomposites containing POSS concentrations indicated, recorded at 10 °C/min in N_2 gas atmosphere.
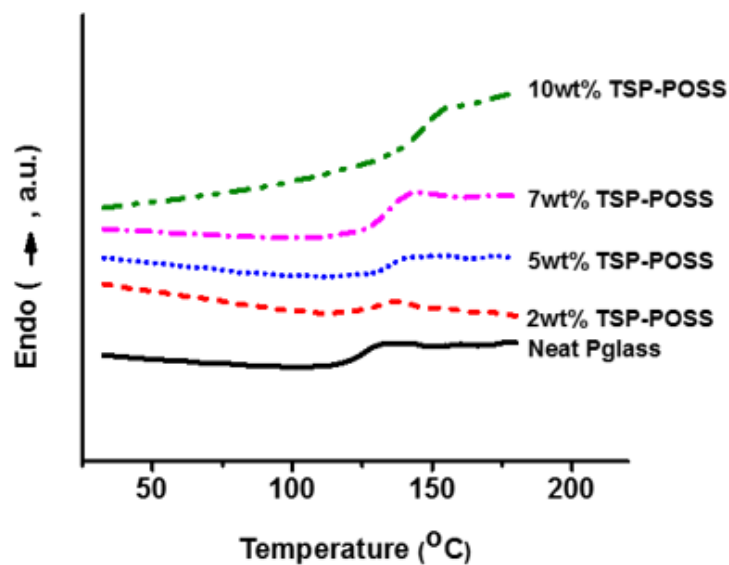
Figure 2.4 DSC scan (10 °C/min) for neat Pglass and nanocomposites containing the POSS concentrations indicated.
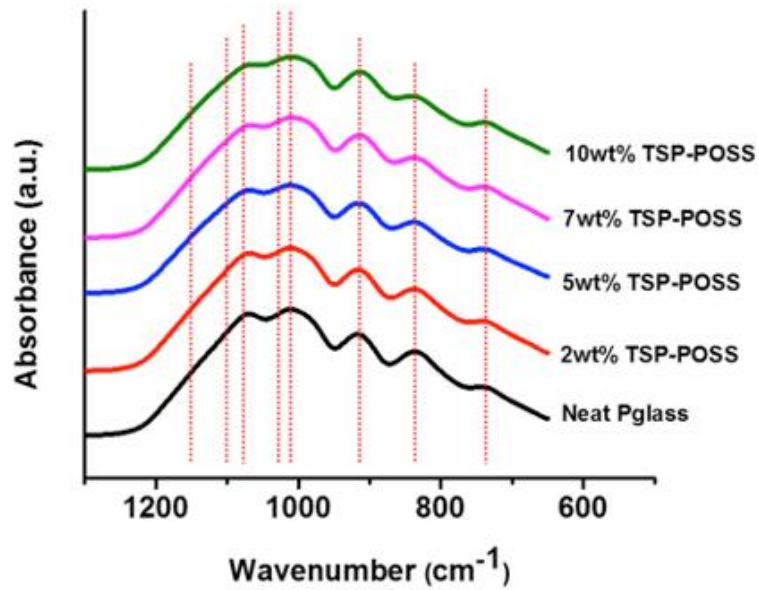
Figure 2.5 ATR-FTIR spectra of neat Pglass and nanocomposites incorporating various amount of TSP-POSS. The broken lines are guides to the peak values.
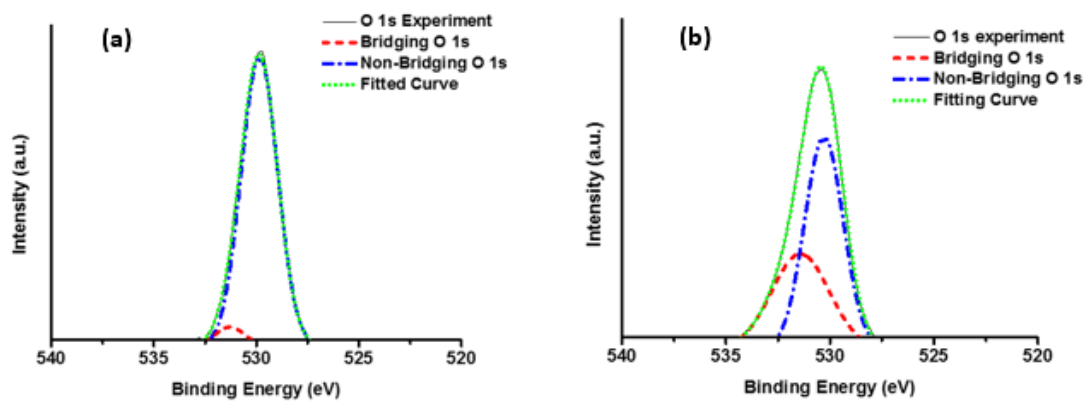
Figure 2.6 XPS spectra of (a) neat Pglass and (b) nanocomposite incorporating 5 wt.% TSP-POSS.
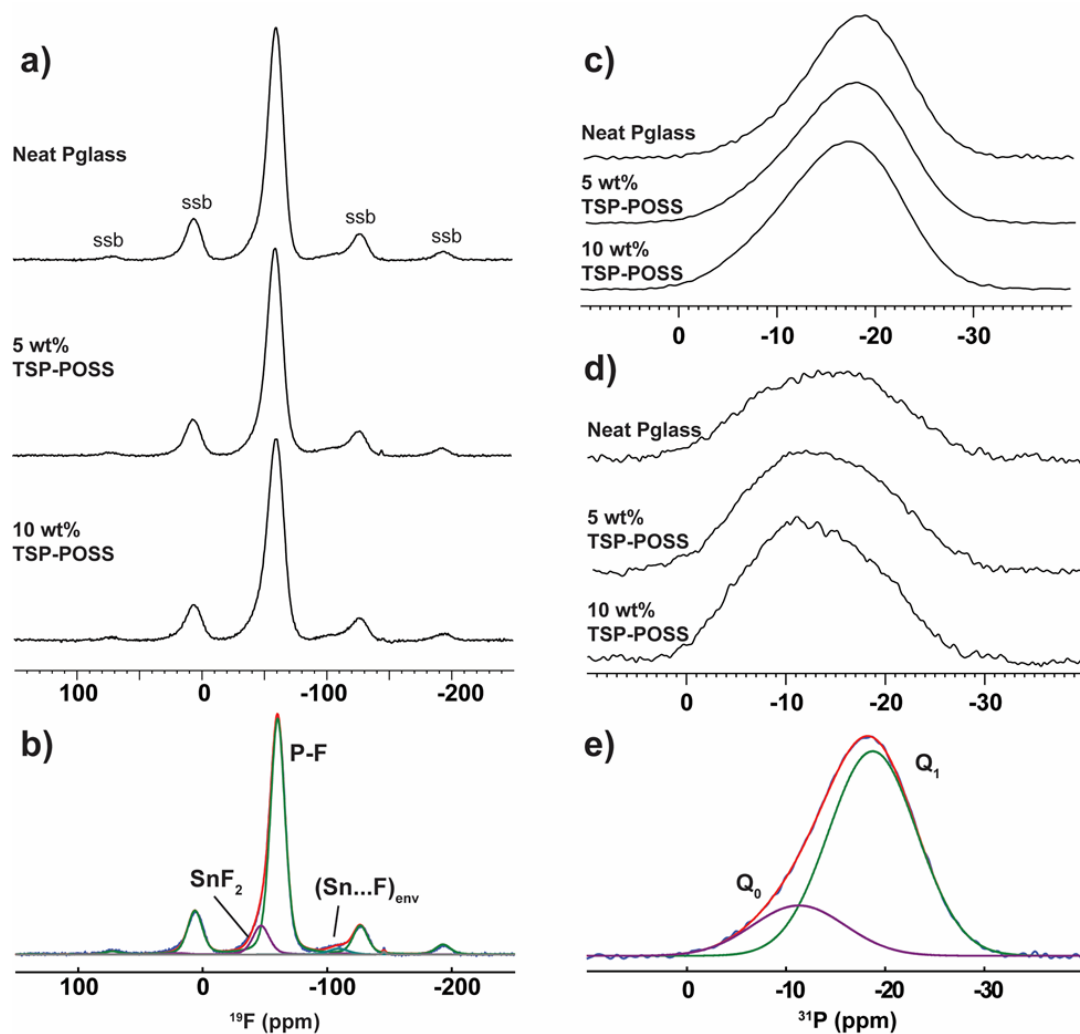
Figure 2.7 (a) ^{19}F DP MAS NMR spectra, (b) deconvolution showing the different F environment, (c) ^{31}P DP MAS NMR spectra and (d) ^{1}H-^{31}P CPMAS NMR spectra of nanocomposites prepared by synthesis method, along with the (e) deconvolution of the TFP glass spectra into assigned Q^0 and Q^1 phosphate environments (ssb = spinning side bands).
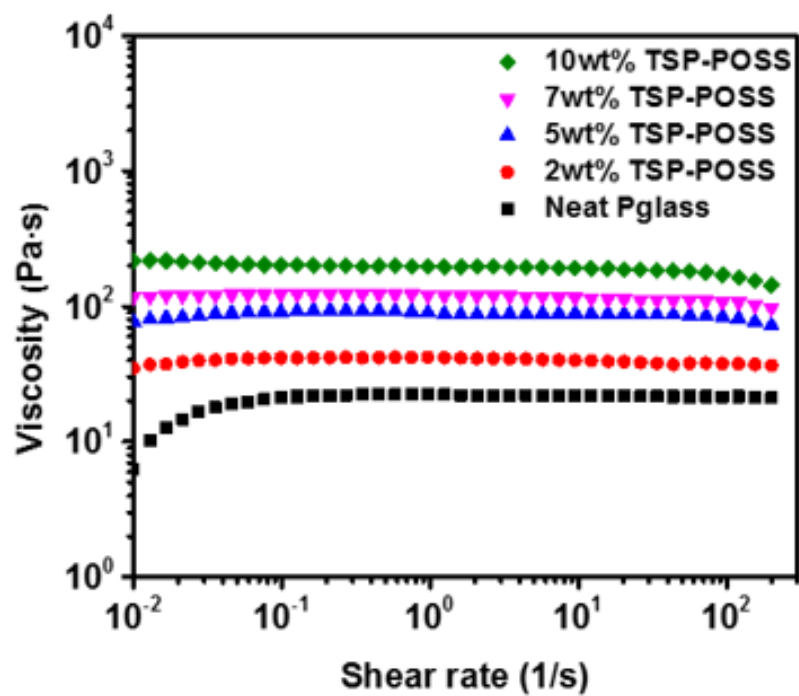
Figure 2.8 Variation of viscosity versus shear rate for the neat Pglass and nanocomposites.
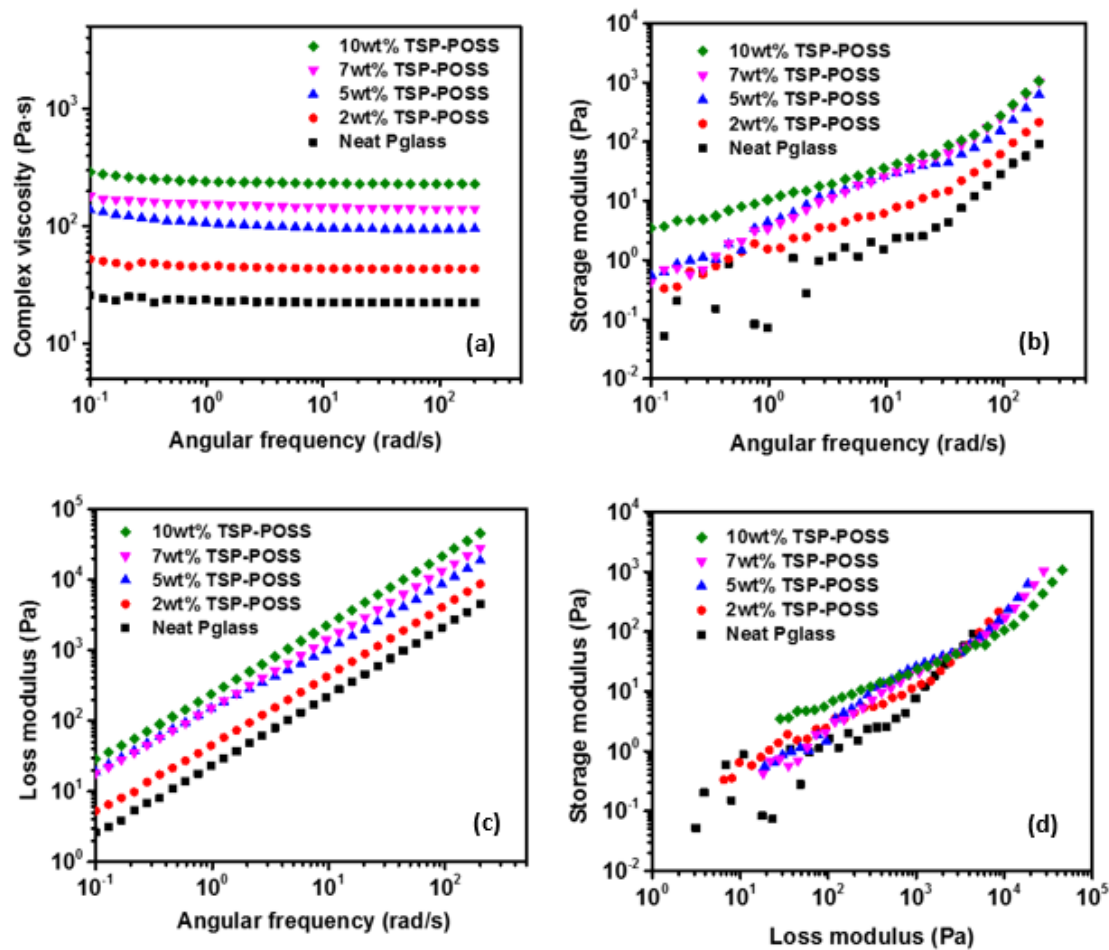
Figure 2.9 Frequency dependencies of (a) complex viscosity, (b) storage modulus and (c) loss modulus for neat Pglass and nanocomposites incorporating TSP-POSS. (d) Han plot for neat Pglass and nanocomposites incorporating TSP-POSS.
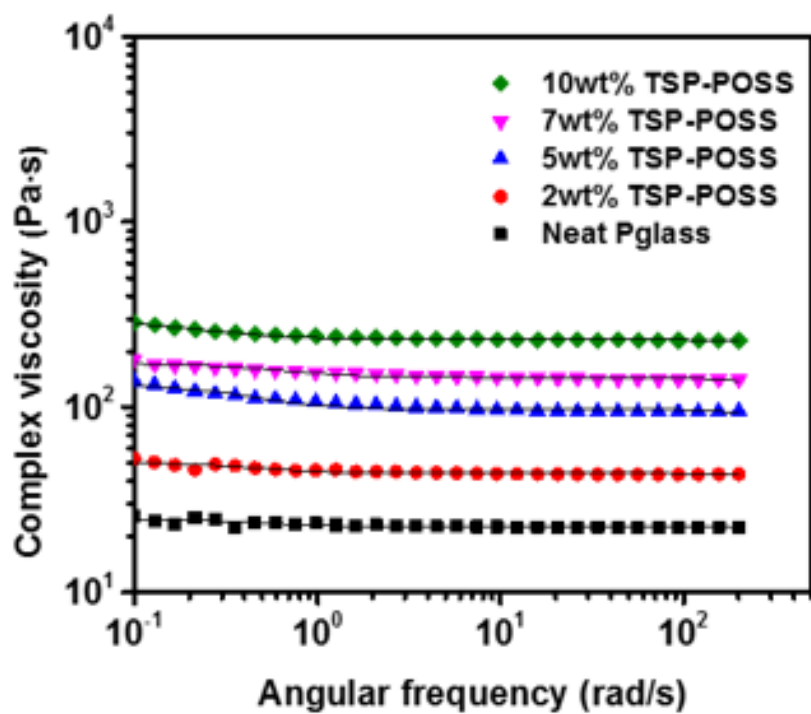
Figure 2.10 Two-parameter Rouse fit (lines) of the complex viscosity data (symbols) as a function of frequency for the neat Pglass and nanocomposites incorporating TSP-POSS.
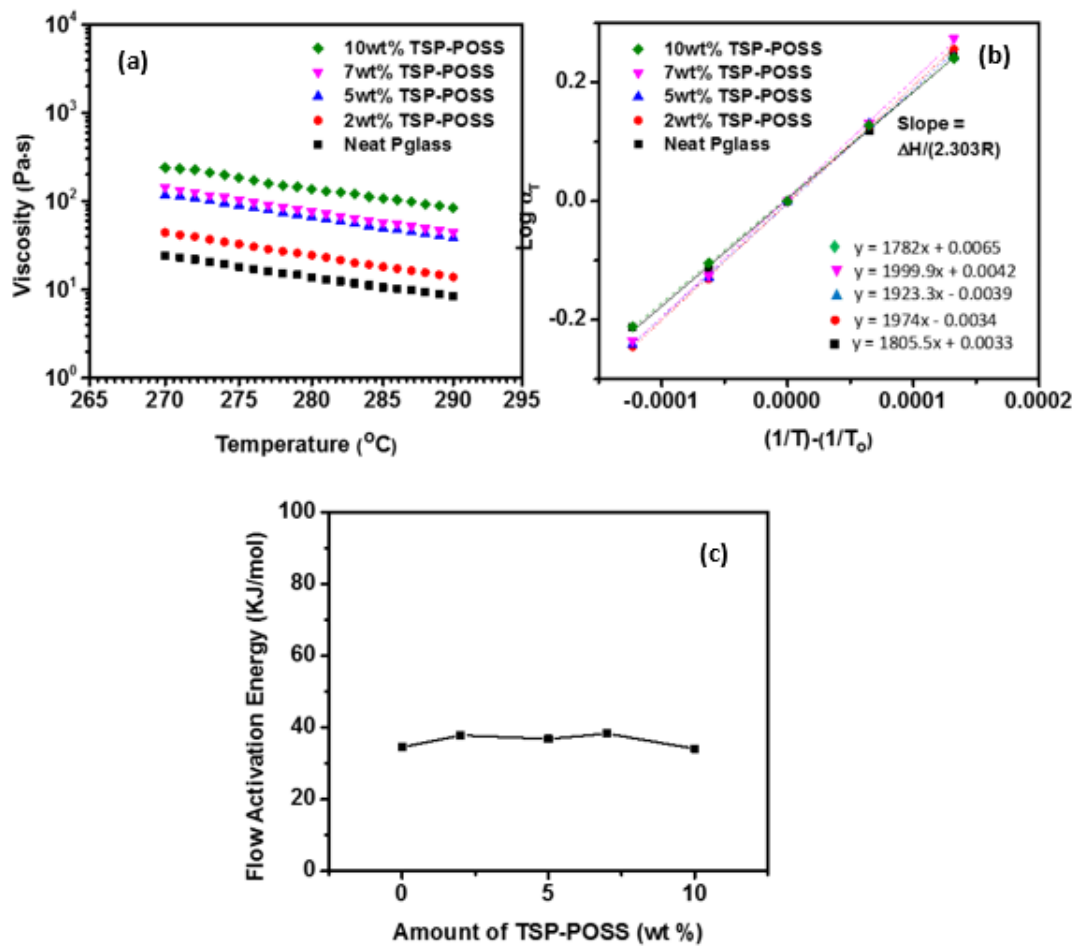
Figure 2.11 (a) Temperature dependency of viscosity at a shear rate of 5 s^{-1}, (b) fitted graphs of equations for flow activation energy calculation described in the text, and (c) calculated flow activation energy of neat Pglass and nanocomposites incorporating TSP-POSS described in the text.
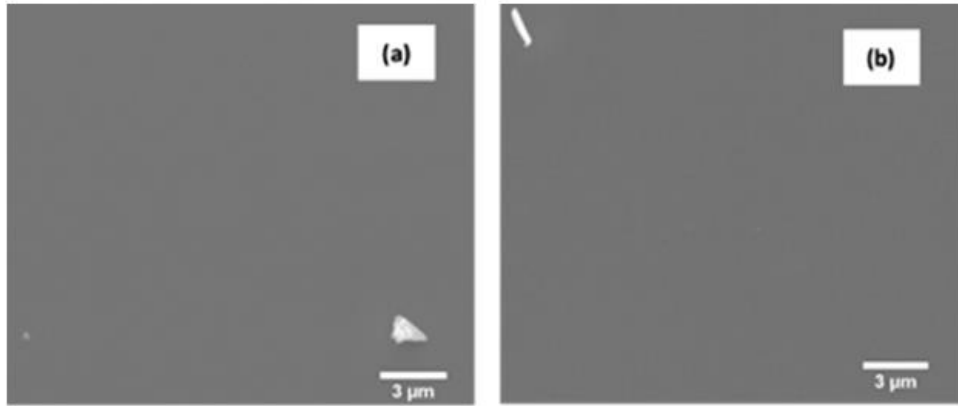
Figure 2.12 SEM images of fracture surface of (a) the neat Pglass and (b) Pglass matrix nanocomposites incorporating 10 wt.% TSP-POSS prepared by synthesis method.
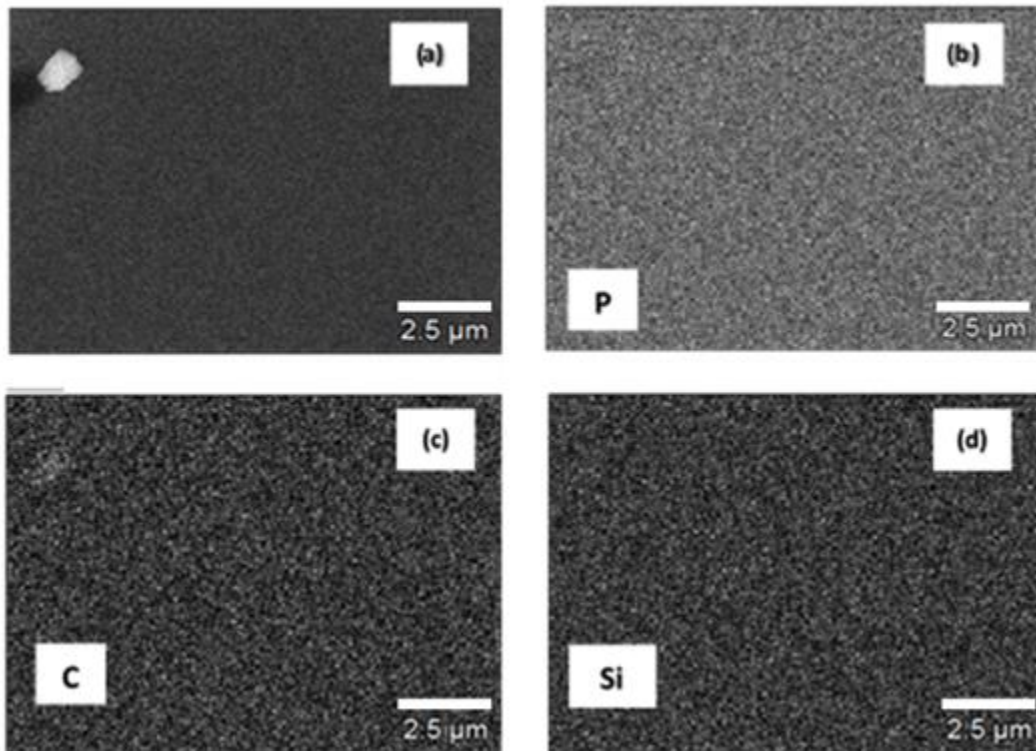
Figure 2.13 (a) SEM image and SEM-EDX mapping images of each element (b) P, phosphorous; (c) C, carbon; (d) Si, silicon on the fracture surface of the Pglass matrix nanocomposites incorporating 10 wt.% TSP-POSS prepared by synthesis method (black background and white spot for each element)
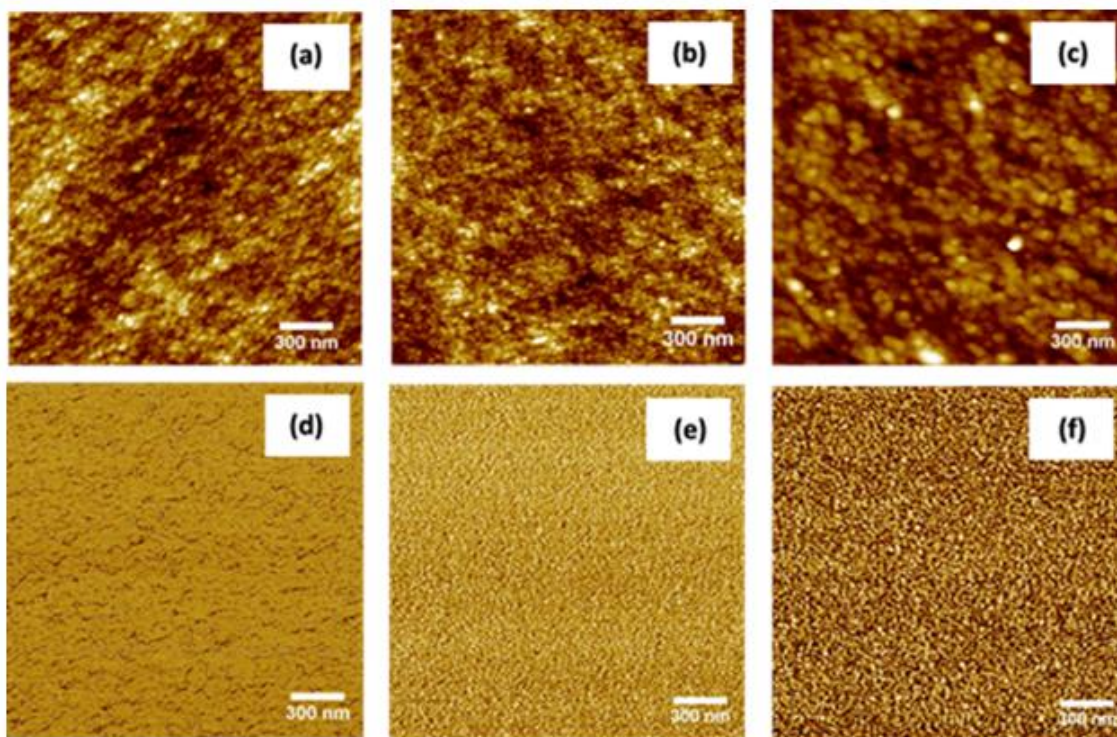
Figure 2.14 AFM height images (2μm × 2μm) on the fracture surface of (a) the neat Pglass, (b) 5 wt.% TSP-POSS and (c) 10 wt.% TSP-POSS incorporated Pglass matrix nanocomposites; AFM phase images of (d) the neat Pglass, (e) 5 wt.% TSP-POSS and (f) 10 wt.% TSP-POSS incorporated in the Pglass matrix nanocomposites.
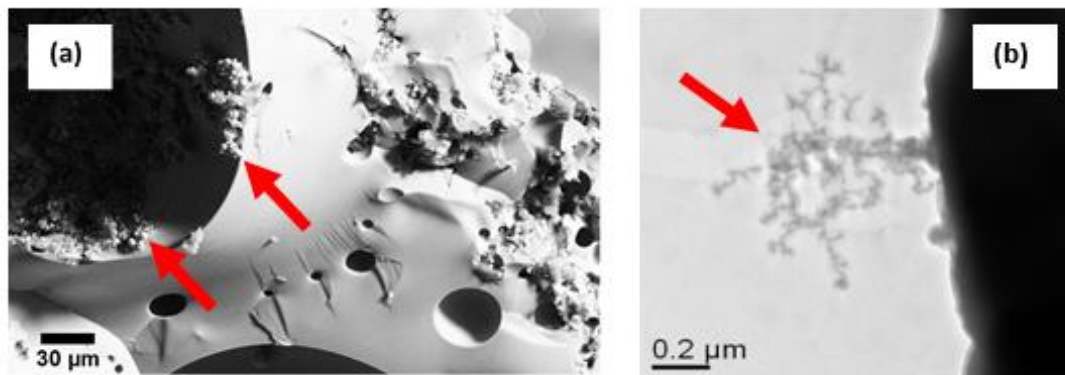
Figure 2.15 (a) SEM image of the physically blended 5 wt.% POSS/Pglass sample showing POSS aggregation (arrows) and (b) TEM image of attached POSS on the surface of heterogeneous POSS/Pglass physically blended 5 wt.% POSS/Pglass sample.
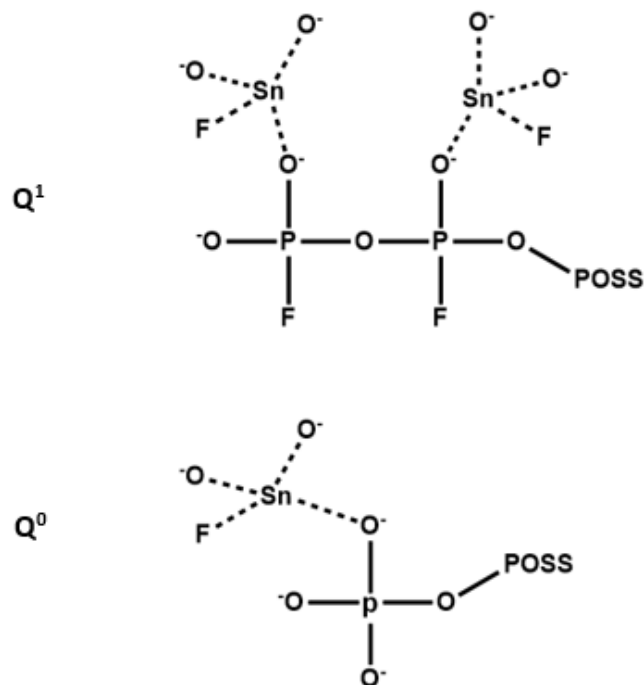
Figure 2.16 The plausible structure of Pglass/TSP-POSS nanocomposites prepared by the synthesis method described in the text (see Fig. 2.1(b) for the chemical structure of POSS).
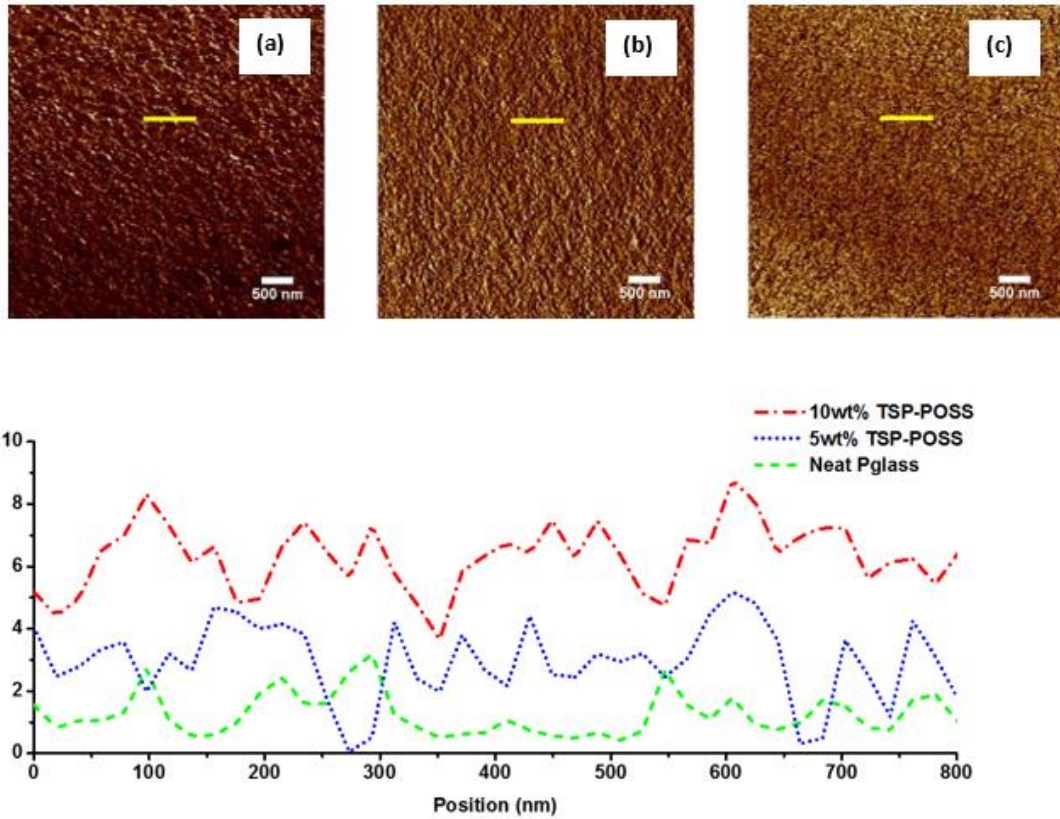
Figure 2.17 Modulus images of (a) neat Pglass (b) 5 wt.% TSP-POSS (c) 10 wt.% TSP-POSS and (d) modulus values along profile on each image described in the text.
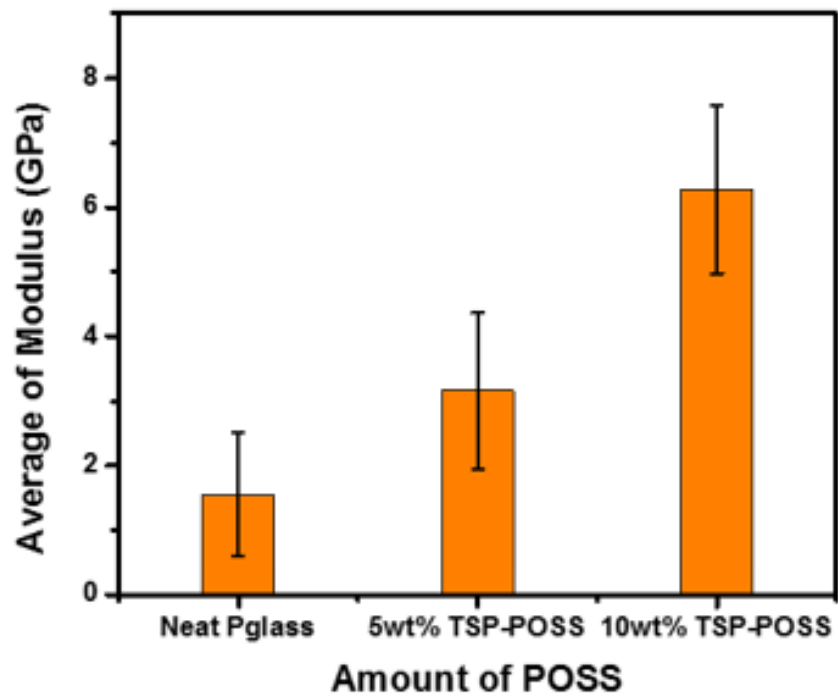
Figure 2.18 Average and standard deviation of modulus with five-profile measurements on each sample.

Table 2.1

The deconvolution of ^{31}P DP MAS NMR data on nanocomposites prepared by synthesis method.

	Neat Pglass (%)	5 wt.% TSP-POSS (%)	10 wt.% TSP-POSS (%)
Q^0	20.5 ± 1	25.7 ± 1	27.1 ± 1
Q^1	79.5 ± 1	74.3 ± 1	72.9 ± 1

Table 2.2

Fit parameters obtained from the 2-parameter Rouse model used for prediction of the complex viscosity as a function of the frequency

	η_1	τ_1	η_2	τ_2
Neat Pglass	2.33	-2.32	22.63	-0.00076
2 wt.% TSP-POSS	6.66	2.44	43.89	-0.00095
5 wt.% TSP-POSS	36.86	2.81	97.62	0.0016
7 wt.% TSP-POSS	27.14	1.72	144.92	-0.0015
10 wt.% TSP-POSS	56.86	4.28	233.23	-0.0012

CHAPTER III – NOVEL POROUS BIOABSORBABLE PHOSPHATE GLASS MATRIX NANOCOMPOSITES INCORPORATING TRISILANOLPHENYL POLYHEDRAL OLIGOMERIC SILSESQUIOXANE PREPARED BY EXTRUSION

Published Manuscript

Abstract

Phosphate glass matrix nanocomposites containing trisilanolphenyl polyhedral oligomeric silsesquioxane (POSS) were investigated for the first time to accelerate efforts to develop novel hybrid phosphate glass/POSS composites with enhanced benefits. Tin fluorophosphate glass (Pglass) having ultra-low glass transition temperature (T_g) was utilized as the matrix material in extrusion at relatively low processing temperature (i.e., $270 \pm 10^{\circ}C$) compared to that of typical borosilicate and sodalime glasses. The resulting nanocomposites materials were highly porous due to evaporation of condensed water produced in situ from polysiloxane condensation reaction between the Pglass and POSS during the extrusion process. As the amount of POSS was increased in the Pglass matrix material, the glass transition temperature was significantly changed by the bulky POSS molecules. The novel porous nanocomposites should find a number of uses in applications at elevated temperatures where conventional organic polymer foam materials are not useable.

3.1 Introduction

　　While novel bioabsorbable phosphate glass-polymer composites [1] and porous scaffolds [2, 3] with enhanced benefits have been reported in the literature, to our knowledge, the work described in this article is the first reported study that demonstrated feasibility of making porous glass matrix nanocomposites using extrusion processing (traditionally used for organic polymer processing) that takes advantage of the relative low-cost and high efficiency in distributing the nanofiller materials in the glass matrix materials [4]. The improved nanofiller dispersion of the trisilanolphenyl polyhedral oligomeric silsesquioxane (TSP-POSS) used here translates to an increase in interfacial surface area of the nanocomposite and improved nano-reinforcement and biomedical function [5]. Other researchers have reported borosilicate glass matrix composites [6] and porous glass foam materials with uses in membrane, catalyst and biotechnology applications with improved properties [7].

　　In the current study, TSP-POSS was incorporated for the first time into a phosphate glass (Pglass) matrix to yield functional micro(nano)structured porosity without using foaming agents such as calcium carbonate to generate the gas phase during the processing [8]. It is worthy to note that phosphate glass was selected for this study because it is the lowest glass transition P-glass (ca. ~100°C) with optimal combination of water resistance and desirable rheological characteristics, as well as, complete and congruent biodegradation and biocompatibility as previously reported [1, 9].

3.2 Experimental

3.2.1 Materials

The Pglass was synthesized with a molar composition of $50SnF_2 + 20SnO + 30P_2O_5$ by heating, in a furnace maintained at $430^\circ C$, a mixture of the stoichiometric amounts of the initial raw materials in an appropriate high-temperature crucible for 30 minutes [9].

Pure Pglass and two different amounts of TSP-POSS (~ 10 wt.%) were used and manually mixed using a mortar and pestle. Trisilanol phenyl POSS (TSP-POSS, $C_{42}H_{38}O_{12}Si_7$, Hybrid Plastics) was used. Analytical grade reagents, Tin(II) oxide (SnO), tin(II) fluoride (SnF_2), ammonium dihydrogen phosphate (($NH_4)H_2PO_4$) were purchased from Sigma-Aldrich and used as received.

3.2.2 Extrusion Processing

The desired amount of Pglass powder and POSS powder was mixed manually and continuously introduced into the feed-throat of a MiniLab® twin-screw extruder and conveyed by the extruder screws through the extruder slit die of 1 mm diameter to yield the glass matrix nanocomposite containing POSS. Specifically, the extrusion process was carried out using a twin-screw extruder (HAAKE Minilab, Thermo Electron Corporation) with the extruder chamber temperature maintained in the range of $260^\circ C$ to $280^\circ C$. The tubular die extension ($70\times20\times30$mm, length×height×width), wrapped with heating tape, was equipped around the extruder exit die and the temperature ($140^\circ C$) was fixed via a digital temperature controller to avoid drastic temperature decrease of the samples at the die exit upon contact with ambient air. The screw speed was maintained between 65 and 80 rpm. The obtained composite materials were homogeneously mixed and a portion of

91

them was ground to powder sieved through a mesh size of 150 μm for thermal and chemical characterizations.

3.2.3 Measurements

Glass transition temperature (T_g) was characterized by differential thermal analysis (PerkinElmer Pyris Diamond® DSC) equipped with an intracooler in a dry nitrogen atmosphere with glass sample particles (< 150 um) in the temperature range from 30ºC to 180ºC and 10 ºC/min rate. The reported T_g data were obtained in the second heating cycle to remove effects of processing history. The result is given as the mean value of at least two measurements. A Zeiss Sigma VP field emission scanning electron microscope (SEM) operating at 20kV with an attached energy-dispersive X-ray spectroscopy (EDX) having a Thermo Scientific UltraDry EDX detector was used to investigate the morphology and elemental compositions of the surface of fractured pure Pglass and Pglass nanocomposites incorporating POSS using NSS3® micro-analysis software. The surface of the glass sample was coated with silver using a Quorum Emitech K550X sputter coater to render it conductive.

^{31}P NMR spectra were obtained on a Bruker Avance® III 600 (9.6 T) NMR instrument using a 4 mm broadband MAS Probe spinning at 12.5 kHz. A single pulse Bloch decay with a 240s recycle delay was used to obtain the 1D spectra. The ^{31}P chemical shift was referenced to $(NH_4)H_2PO_4$ δ = 0.8 ppm with respect to phosphoric acid δ = 0 ppm. ^{13}C Solid-state NMR and Solid-state CP/MAS ^{29}Si NMR spectroscopy was performed on a Varian UNITY INOVA® 400 spectrometer using a standard Chemagnetics 7.5 mm PENCIL^{TM}-style probe. The samples were loaded into zirconia rotor sleeves, sealed with Teflon^{TM} caps, and spun at rate of 4.0 kHz. The standard cross-

polarization/magic angle spinning (CP/MAS) technique was used with high-power

proton decoupling implemented during data acquisition. The data acquisition parameters

were as follows: The ^{1}H 90° pulse width was 5.5μs, the cross-polarization contact time

was 1ms, the dead time delay was 6.4μs, and the acquisition time was 45ms. An overall

recycle delay of 12 seconds between scans was utilized. The number of co-added scans

was 2048. Peaks were referenced externally to the upfield peak of adamantine (29.5

ppm).

Solid-state CP/MAS ^{29}Si NMR spectroscopy was performed on a Varian

UNITYINOVA® 400 spectrometer using a standard Chemagnetics 7.5 mm PENCIL-style

probe. The samples were loaded into zirconia rotor sleeves, sealed with Teflon™ caps,

and spun at rate of 3 kHz. The data acquisition parameters were as follows: A ^{1}H 90°

pulse width was 5.5μs, a cross-polarization time was 5ms, and a dead time delay was

6.4ms, and the acquisition time was 45ms. The overall recycle delay was 12 seconds,

and a ^{1}H decoupling field of 45.5 kHz was implemented during data acquisition. The

number of co-added scans was 512 for the POSS sample and 29,800 for the extruded

nanocomposite material. The NMR peaks were referenced externally to the downfield

peak of tetrakis(trimethylsilyl)silane (-9.8 ppm). The porosity of samples was estimated

by comparing measured density to theoretical density of composites.

3.3 Results and discussion

Fig. 3.1(a) illustrates how the TSP-POSS was dispersed in Pglass matrix via

mechanical mixing and hydrogen bonding in the extrusion process, allowing

condensation reaction between TSP-POSS and Pglass and between two of each material,

that produced water vapor inside of the Pglass matrix, transforming into homogeneous

porosity in the nanocomposites. As the amount of POSS was increased in the Pglass matrix materials, the T_g increased until it finally disappeared as shown in Table 1. This observation suggests that either the glass changed to a glass-ceramic or the T_g value of nanocomposites probably occurred at higher temperature, where thermal degradation prevented its determination. The obtained results suggest that mobility of the Pglass chains is restricted by the addition of the relatively bulky POSS molecules, leading to a decrease of mobility of the Pglass chains that was signaled by the observed increased T_g [10]. The extruded pure Pglass and nanocomposites materials are shown in Fig. 3.1(c).

The molecular structure and miscibility of the nanocomposites and its constituents were analyzed via solid-state NMR studies. ^{29}Si CPMAS NMR was conducted to obtain the local structural information between the Pglass and pure POSS as shown in Fig. 3.2(a). This figure shows that there are two sharp peak areas between -64 ppm and -82 ppm corresponding to T_2 and T_3 sites, indicating silicon connected to hydroxyl group (i.e., opened silicon) and silicon unconnected to hydroxyl group (i.e., closed silicon), respectively [11]. Disappearance of T_2 and the peak around -80 ppm are attributed to disappearance of silanol groups via condensation reactions between the nanocomposites constituents. In addition, the [29]Si spectra considerably broadened due to the reduction of crystallinity of POSS caused by molecular-level dispersion in the nanocomposites. The ^{13}C spectra shown in Fig. 3.2(b) indicate sharp signals corresponding to four phenyl carbons at para (a, 132 ppm), meta (b, 128 ppm), ortho (c, 136 ppm) positions, and phenyl carbon attached to silicon oxide moiety of the POSS cage (d, 130 ppm) in the pure POSS [11]. In contrast, the broad signal shown in the nanocomposites samples indicates a

reduction of crystallinity and homogeneous dispersion of POSS throughout the Pglass matrix.

The stack plot of the isotropic resonance shift obtained from DP/MAS and CP/MAS in ^{31}P NMR for the extruded nanocomposites is shown in Fig. 3.2(c). Upon addition of the TSP-POSS in the Pglass matrix, the ratio of Q^0 to Q^1 (where the numbers 0 and 1 indicate the number of bridging oxygen connected to phosphorous in the Pglass structure) increased as shown in Table 1, indicating that the Pglass chains changed from pyrophosphate to orthophosphate due to the addition of TSP-POSS [9]. Note that for the Pglass nanocomposites containing identical TSP-POSS concentration, changing the extrusion processing conditions did not reveal a significant shift of isotropic resonance in ^{31}P NMR, indicating that the effect on the Pglass structure of the amount of TSP-POSS used is more significant compared to that of the change of extrusion processing conditions used.

The fracture surface of the extruded pure Pglass showed little bubbles (or voids) caused by evaporation of bound water and entrapped air during the extrusion process as shown in Fig. 3.3(a). The nanocomposites contained relatively more porosity (Table 1) that was augmented by increased amount of POSS as shown in Fig. 3.3(b-d) due to *in situ* condensation reaction between the nanocomposites constituents [12]. Fig. 3.3(e-h) shows the distribution of each element in the samples characterized via SEM-EDX analysis on the fracture surface of the extruded nanocomposites incorporating 10 wt.% POSS. Clearly, the phosphorous from Pglass and the carbon and silicon from TSP-POSS are distributed homogeneously in the nanocomposite samples in nanoscale.

95

3.4 Conclusion

This study demonstrates for the first time the feasibility of facile preparation of highly porous Pglass matrix nanocomposites incorporating POSS by extrusion processing. The significant porosity in the samples is ascribed to evaporation of *in situ* condensed water between hydroxyl groups of the Pglass and POSS during the extrusion process. The solid-state NMR data analysis confirmed the chemical functionality of the porous POSS/Pglass nanocomposites, excellent dispersion of the POSS, and associated increase in the interactions between the Pglass and POSS in the new nanocomposites with enhanced benefits in a wide range of potential applications such as biomedical and tissue engineering, heterogeneous catalysis, membrane, and composites, where existing materials cannot be used.

3.5 Reference

1.   Urman, K. and J.U. Otaigbe, New phosphate glass/polymer hybrids—Current status and future prospects. Progress in Polymer Science, 2007. 32(12): p. 1462-1498.

2.   Gentile, P., et al., Bioresorbable glass effect on the physico-chemical properties of bilayered scaffolds for osteochondral regeneration. Materials Letters, 2012. 89: p. 74-76.

3.   Georgiou, G., et al., Polylactic acid–phosphate glass composite foams as scaffolds for bone tissue engineering. Journal of Biomedical Materials Research Part B: Applied Biomaterials, 2007. 80(2): p. 322-331.

4.   Roeder, E., Extrusion of glass. Journal of Non-Crystalline Solids, 1971. 5(5): p. 377-388.

5.   Madbouly, S.A. and J.U. Otaigbe, Recent advances in synthesis, characterization and rheological properties of polyurethanes and POSS/polyurethane nanocomposites dispersions and films. Progress in Polymer Science, 2009. 34(12): p. 1283-1332.

6.   Minay, E., V. Desbois, and A. Boccaccini, Innovative manufacturing technique for glass matrix composites: extrusion of recycled TV set screen glass reinforced with Al 2 O 3 platelets. Journal of materials processing technology, 2003. 142(2): p. 471-478.

7.   Boccardi, E., F.E. Ciraldo, and A.R. Boccaccini, Bioactive glass-ceramic scaffolds: Processing and properties. MRS Bulletin, 2017. 42(3): p. 226-232.

8.   Chen, B., et al., Study of foam glass with high content of fly ash using calcium carbonate as foaming agent. Materials Letters, 2012. 79: p. 263-265.

9.   Kim, K., et al., Synthesis and characterization of novel phosphate glass matrix nanocomposites containing polyhedral oligomeric silsesquioxane with improved properties. Journal of Non-Crystalline Solids, 2017. 463: p. 189-202.

10.   Li, G., et al., Polyhedral Oligomeric Silsesquioxane (POSS) Polymers and Copolymers: A Review. Journal of Inorganic and Organometallic Polymers, 2001. 11(3): p. 123-154.

11.   Misra, R., et al., Molecular miscibility and chain dynamics in POSS/polystyrene blends: control of POSS preferential dispersion states. Polymer, 2009. 50(13): p. 2906-2918.

12.   Kannan, A.G., N.R. Choudhury, and N.K. Dutta, Synthesis and characterization of methacrylate phospho-silicate hybrid for thin film applications. Polymer, 2007. 48(24): p. 7078-7086.
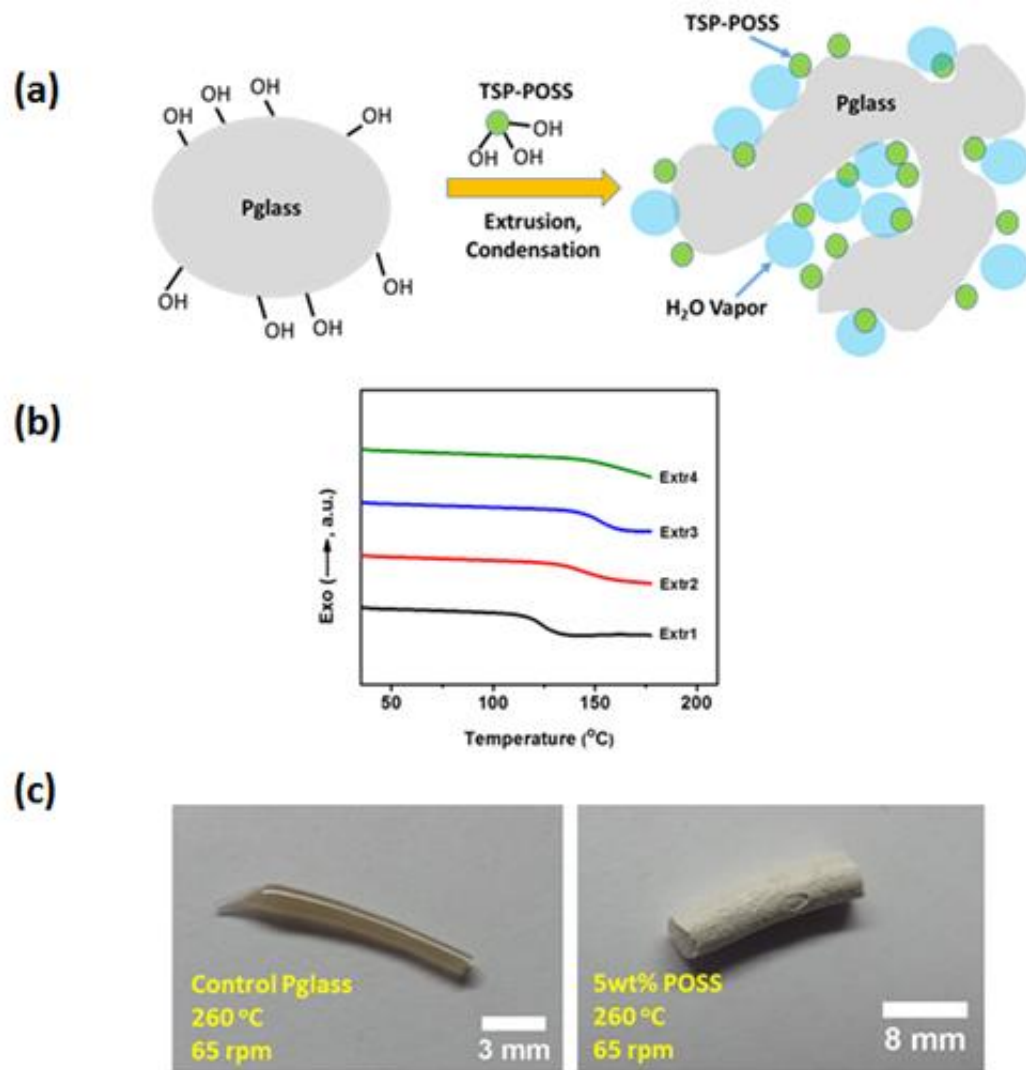
Figure 3.1 (a) The expected macroscopic structure, (b) DSC thermograms, and (c) pictures of Pglass/TSP-POSS nanocomposites prepared by extrusion.
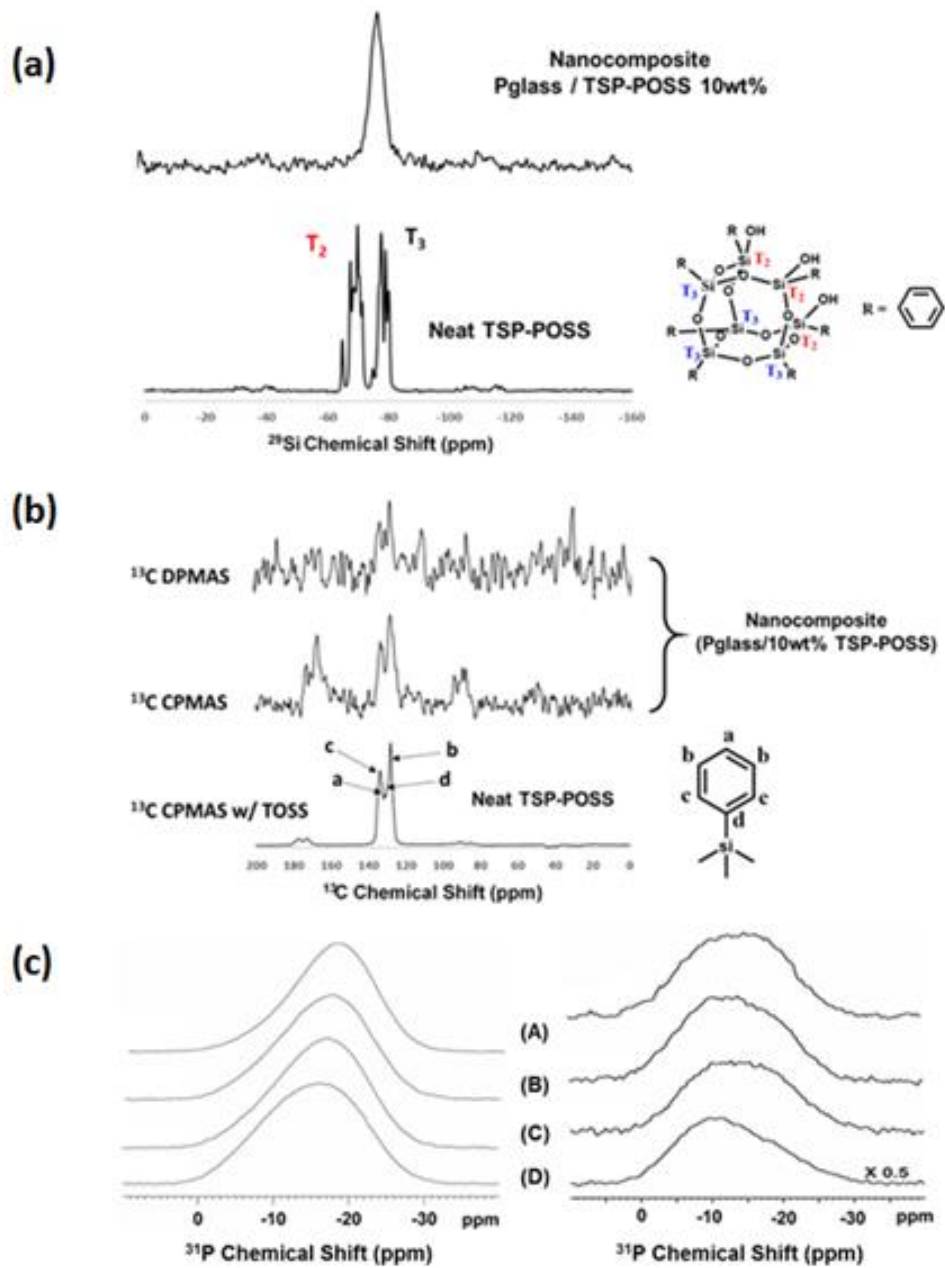
Figure 3.2 (a) ^{29}Si spectra of TSP-POSS, (b) ^{13}C CPMAS spectra of TSP-POSS and ^{13}C CPMAS and DPMAS spectra of Extr4 sample and (c) ^{31}P DP/MAS (left) and ^{31}P CPMAS (right) spectra in (A) Extr1, (B) Extr2, (C) Extr3, and (D) Extr4 samples in solid state NMR analysis; (Extr1: pure Pglass with 260°C/65rpm, Extr2: 5wt.% POSS with 260°C/65rpm, Extr3: 5 wt.% POSS with 280°C/80rpm, Extr4: 10 wt.% POSS with 260°C/65rpm).
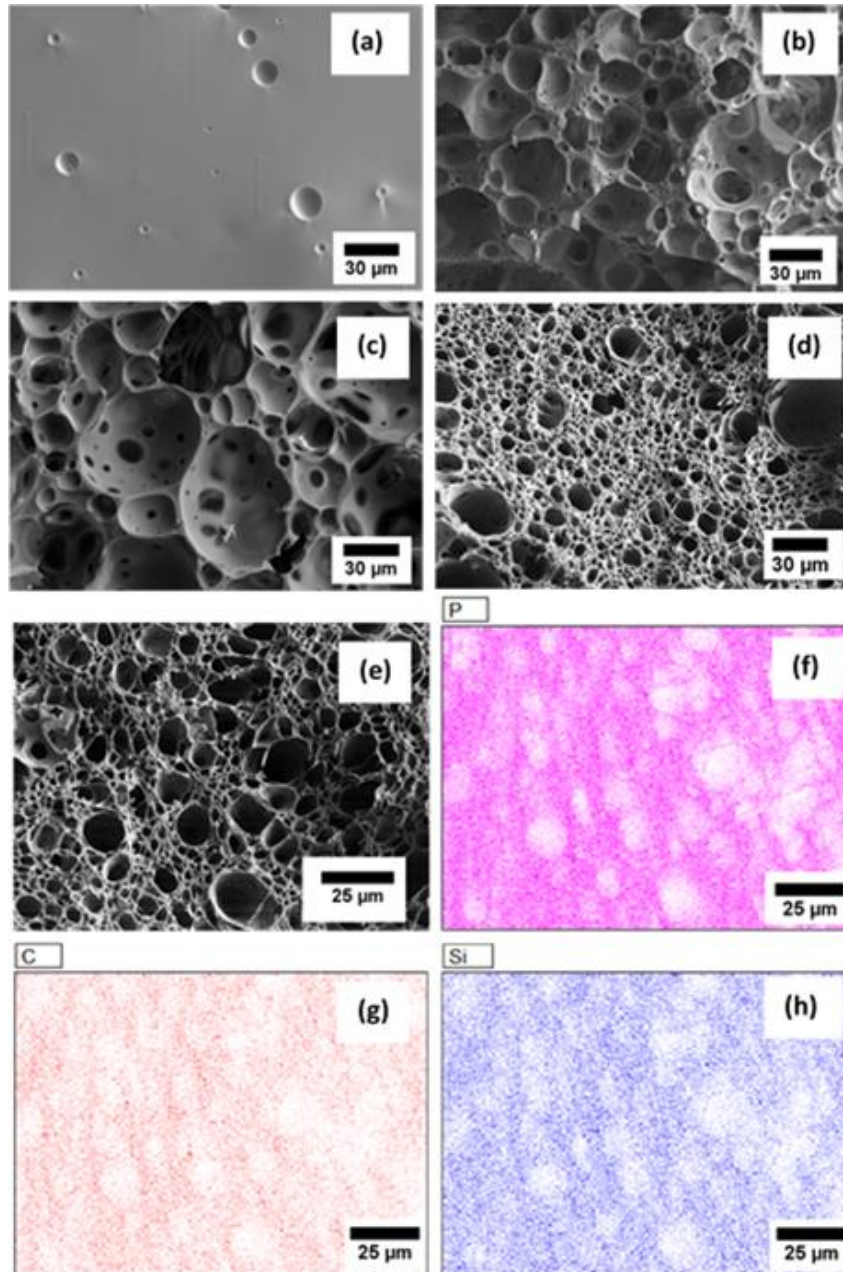
Figure 3.3 SEM images of fracture surface of extruded Pglass and Pglass composite incorporating POSS; (a) Extr1, (b) Extr2, (c) Extr3 and (d) Extr4, and (e) SEM image and EDX mapping images of each element; (f) phosphorous, (g) carbon and (h) silicon in the 10 wt.% POSS incorporated Pglass matrix nanocomposite (white is background the color spots are elements in the EDX images shown in f, g, h).

Table 3.1

Glass transition temperature and the deconvolution of ^{31}P DPMAS solid state NMR data

on neat Pglass and nanocomposites prepared by extrusion method.

Sample	DSC	NMR		Measured	Theoretical	Porosity (%)
	T_g (ºC)	Q^0	Q^1	Density (g/ml)	Density (g/ml)	
Extr1	124.2 ± 0.8	22.0 ± 1	78.0 ± 1	3.39 ± 0.07	3.75	9.7 ± 1.9
Extr2	146.3 ± 1.3	27.3 ± 1	72.7 ± 1	0.65 ± 0.03	3.63	82.2 ± 0.8
Extr3	151.0 ± 0,9	28.5 ± 1	71.5 ± 1	0.71 ± 0.03	3.63	80.6 ± 0.8
Extr4	No T_g	37.1 ± 1	62.9 ± 1	0.85 ± 0.09	3.52	75.8 ± 2.4

Note: Porosity: (1-(measured density / theoretical density)) * 100

CHAPTER IV – PHOSPHATE GLASS MATRIX COMPOSITES INCORPORATING TRISILANOL PHENYL POLYHEDRAL OLIGOMERIC SILSESQUIOXANE PREPARED BY VISCOUS FLOW SINTERING METHOD WITH ENHANCED BENEFITS

Kyoungtae Kim, William L. Jarrett, Todd M. Alam, Joshua U. Otaigbe

Abstract

The effect of mixing and sintering processes to prepare tin fluorophosphate glass (Pglass) matrix composites incorporating trisilanol phenyl polyhedral oligomeric silsesquioxane (TSP-POSS) was investigated by comparing manual and suspension mixing, one-step and stepwise sintering processes to explore the structure dynamics and physical properties in the composites as a function of the different process conditions used. Energy Dispersive X-ray analysis confirmed optimal homogeneous dispersion of the TSP-POSS molecules in the composites prepared by the suspension method. The observed increase of glass transition temperature and the reduction of non-bridging bonds in the composites are believed to be the reason for the effective dispersion of TSP-POSS molecules in the composites. The chemical reaction between the TSP-POSS and Pglass was strongly influenced by the mixing/dispersion and sintering processes investigated. ^{13}C cross polarized magic angle spinning (CP MAS) solid state nuclear magnetic resonance (NMR) spectroscopy confirmed the chemical stability of the TSP-POSS during the sintering process at elevated temperatures. In addition, a chemical reaction between the TSP-POSS and Pglass was evidenced by ^{29}Si CP MAS NMR analysis. This study will provide a better fundamental understanding of the effective dispersion mechanism of the

TSP-POSS molecules in the Pglass matrix that will facilitate tailoring the physicochemical properties of the composites with addition of various small concentrations of TSP-POSS for a number of applications where the pure Pglass is not applicable due to the intrinsic properties of the Pglass.

4.1 Introduction

Nanocomposites containing nano-sized fillers incorporated in organic/inorganic polymer matrix have been great attention in the last 30 years in academic and industrial research because synergistic combinations of matrix materials and small amount of fillers have yielded materials with significant improvements in mechanical, thermal, chemical, barrier, and rheological properties [1, 2]. In addition, the nanocomposites physicochemical properties can be tailored and optimized to address the needs for specific end use applications. In this context, nanocomposites with desirable properties incorporating a number of different types of nanofillers such as carbon nanotubes [3, 4], graphene [5], carbon fibers [6, 7], alumina [8, 9], and layered silicate [10, 11] have been reported in the literature. The special properties of polymer nanocomposites are usually dictated by the combined relatively large interfacial area between the matrix and nanofiller materials that is facilitated by good homogeneous dispersion of the nanofilles in the continuous matrix, resulting in formation of chemical bonds, strong physical interaction, and desirable structure/properties correlation [12, 13]. It is worthy to note that nanoscale materials have a large surface area, which can create new and improved physical and chemical interactions with nanocomposite matrix material at the interface, resulting in the special properties already mentioned [1]. Significant academic and industrial research studies aimed at exploring feasibility of their uses in a wide range of diverse application areas like

automobiles, aerospace components, and packing applications are currently under investigation [14, 15].

Using those fillers, inorganic glass/ceramic matrix (i.e. borosilicate glass, soda-lime glass, phosphate glass, alumina, and glass-ceramic) composites can be prepared as well. Inorganic glass/ceramic matrix composites were developed to improve their mechanical properties such as toughness, strength, and hardness in addition to their intrinsic properties such as thermal stability, corrosion resistance, porosity, and electric insulation [16-19]. Even though the glass-ceramic matrix materials have outstanding mechanical resistance, there is a limitation on some applications due to the brittleness of the glass-ceramic matrix. Significant efforts to overcome these limitations were explored using reinforcement technology with high modulus fillers such as carbon fibers and carbon nanotubes (CNTs). Significant improvements in the mechanical properties have been achieved [20-23] attributed to the debonding and putout mechanism of carbon fibers and CNTs in the glass-ceramic matrix materials [24, 25].

Glass-ceramic matrix composites incorporating fillers are prepared not only to improve the mechanical properties such as toughness and strength, but also thermal, structural, and optoelectronic properties. Balaji et al. [26] reported the fabrication of a photoreactive single wall (SW) CNT/(Pb, Zn)-phosphate glass composite functioning as an efficient photo-carrier generator possibly to be used as a UV-Vis light sensor and a photocurrent converter. Kim et al. [27] reported that polyhedral oligomeric silsesquioxane (POSS) incorporated phosphate glass composites were prepared by extrusion technique, showing impressive porosity (82%) in the composites, which might be utilized as a heterogeneous catalysis, as a membrane, and in biomedical engineering. In addition,

devoted efforts for various applications using glass-ceramic matrix composites, such as tissue engineering and use as heat exchangers, have been provided by other researchers [28, 29].

The functionality of glass-ceramic matrix composites mainly depends on compositions and preparation methods determining their structural and morphological properties, which are closely related with other essential characteristics of composite materials. There are several methods for the preparation of glass-ceramic matrix composites including hot-pressing [30, 31], extrusion [27, 32], sol-gel [33-35], and sintering process [20, 36, 37]. Hot-pressing was widely used to fabricate the ceramic composites because this method has benefits on the reduction of the porosity and enhancement of the mechanical properties of result materials. The extrusion method has an advantage on the series production of composites [32], and the sol-gel method is more appropriate for the fabrication of thin films for surface coating [35]. Sintering processes can also be used for the preparation of composites by the addition of filler materials in the glass-ceramic powders during the regenerating process of the bulk glass-ceramics materials [37].

In the current study, a facile viscous flow sintering process was pursued for the preparation of composites using tin fluorophosphate glass (Pglass) powder as a matrix, and trisilanol phenyl POSS (TSP-POSS) molecules as a filler. As elucidated by Ross et al. [38], glass materials behave as ordinary Newtonian liquids at high temperature, therefore, viscous flow sintering process should be considered for the Pglass powder materials. Processing temperature ranging from 190°C to 250°C was applied to prepare Pglass/polyamide12 (PA12) hybrid composites determining the effective mixing due to the

low viscosity of Pglass at the processing temperature. In addition, as explored by Kim et al. [27, 39] TSP-POSS and Pglass molecules effectively mixed at 260°C and 430°C using extrusion and one pot chemical synthesis methods, respectively. Based on literature, the excellent mixing behavior of Pglass and TSP-POSS molecules is due to the hydrophilic functional groups of each materials.

Inorganic phosphate glasses are considered as inorganic polymer materials due to the their chain structures [40]. Their basic structure of phosphate-based anion tetrahedron (Q^{i}, i is the number of bridging oxygen) has been studied, and phosphate glass can be modified by the addition of various metals (i.e. Li, Na, K) as reported [41] for wide applications such as optical implementations [42, 43], glass fibers [44, 45], glass-to-metal seals [46, 47], nuclear waste storage media [48-50], solid electrolytes [51, 52], and bioceramics [53, 54]. Pglass has a remarkably low glass transition temperature (T_{g}) in the range from 90°C to 140°C, and a relatively low processing temperature compared to other silicate and borate-based glass materials. This unique property of Pglass was utilized in inorganic/organic polymer hybrids prepared by blending the polymer and Pglass in the melt state. The hybrids show remarkable benefits including tunable morphologies and microstructure due to the existence of a liquid state over the wide range of processing temperature. The benefits of Pglass incorporated polymer composites may not be achieved from the conventional polymer/polymer blending and other polymer/inorganic particle composites [55]. Pglass was considered as a matrix material as well as a filler material for the composites because the processing temperature for Pglass was similar to general organic polymers [27]. For the same reason, instruments designed for organic polymer processing can be utilized for Pglass processing.

Recently, Pglass matrix composites were explored using one pot synthesis and extrusion methods with POSS as a filler [27, 39]. It is a challenge to create a new type of composite with inorganic Pglass matrix and POSS, a unique nanostructural material. POSS can be tuned into these two types of materials such as inorganic nanoparticles or organic/inorganic hybrid particles according to the functional groups grafted on the POSS core. In addition, POSS can be utilized in tremendous applications in academic research and industrial applications, both as an additive and a monomer for composites and copolymers, respectively [56, 57]. In general, as shown in Fig. 4.1, TSP-POSS has a spherical cage of $SiO_{1.5}$ (closed-POSS, (a)) at the core on which there are various functional groups providing the possibility of physical and chemical interactions with other materials. Moreover, TSP-POSS with silanol groups (open-POSS, (b)) shows compatibility with Pglass, that facilitates homogeneous dispersion of POSS in the Pglass matrix due to the functional groups of P-OH in Pglass and Si-OH in POSS via the chemical reaction between these two materials [27].

The sintering methodology was applied to prepare the TSP-POSS/Pglass composites because the process is facile and suitable to produce the inorganic matrix composites using inorganic matrix materials in powder form. Dispersion of TSP-POSS in the Pglass matrix was investigated according to the various processing conditions to determine the relations between the properties of the composites and the process conditions. It is hoped that the study will provide fundamental information about physical and chemical relations between an inorganic phosphorous-based glass material and an inorganic silicon-based filler material in the composites, which potentially can be applicable to catalysis support, biomedical, and optoelectronic applications.

108

4.2 Experimental methods

4.2.1 Materials and sample preparation

Tin fluorophosphate glass (Pglass) was prepared with molar composition of $50SnF_2 + 20SnO + 30P_2O_5$ using the analytical grade reagents: tin(II) oxide (SnO), tin(II) fluoride (SnF_2) and ammonium dihydrogen phosphate ((NH_4)H_2PO_4) purchased from Sigma-Aldrich. Trisilanol phenyl POSS (TSP-POSS, solid powder) was supplied by Hybrid Plastics Inc. The mixture of ingredients of Pglass was melted in a carbon crucible at 430°C for 30 min. The obtained melt was quickly poured into a pre-shaped steel mold (19 mm diameter, 2 mm height) at ambient temperature and then annealed for 90 min at 130°C above the T_g estimated from differential scanning calorimetry (DSC) analysis. The prepared Pglass bulk samples were pulverized using mortar and pestle to pass through a 75 µm mesh sieve.

The mixture of pure Pglass and various concentrations of TSP-POSS ranging from 0 wt.% to 10 wt.% were prepared by manual mixing with mortar and pestle. In addition, the suspension mixing method was applied to effectively disperse the TSP-POSS in the Pglass matrix as follows. Various amounts of TSP-POSS were dissolved in 15 ml of acetone followed by adding 5g of Pglass powder (< 75 um) in the TSP-POSS/acetone solution, which was stirred using a magnetic bar for 30 min followed by vortex mixing for 5 min. The acetone was evaporated under vacuum using a water aspirator at room temperature. The obtained samples were subsequently dried in a vacuum oven at 80°C for 1 hr. The aggregated TSP-POSS-coated Pglass was ground into fine powder for other experiments and analyses.

The powdered compacts in cylindrical shape of pure Pglass and TSP-POSS/Pglass mixtures with 15 mm diameter and 3 mm in thickness were prepared by uniaxial cold pressing under 50 MPa to increase the effect of diffusion of TSP-POSS and Pglass molecules during the sintering process. The powder compacts were sintered using two different methods. In the first method, a one-step viscous flow sintering process was applied. Here, the 500 mg of obtained mixtures of TSP-POSS/Pglass using the manual mixing and the suspension mixing, respectively, was placed on the metal mold with 15 mm diameter holes and then sintered using 300°C for 15 min. In the second method, a stepwise sintering process from 30°C to 300°C was applied to improve the diffusion of TSP-POSS in the Pglass matrix. The stepwise sintering process was applied as follows: the temperature was increased from 30°C to 100°C, 100°C to 200°C and 200°C to 300°C, consecutively at the rate of 7 °C/min, and there were 15 min isothermal steps at 100°C, 200°C and 300°C, respectively. A portion of a sample was fractured to investigate the properties of the fracture surface and another portion of a sample was ground into fine powder for the various measurements and analyses including DSC, XRD and NMR described in the following section.

4.2.2 Measurements

4.2.2.1 Thermogravimetric analysis (TGA)

To investigate the thermal stability of the pure Pglass and Pglass matrix composites incorporating TSP-POSS prepared by the different mixing methods and processes already described, TGA was conducted on the samples using a TA instrument Q500 operating from 30°C to 600°C at a heating rate of 10 °C/min with 50 ml/min N_2 sample purge flow.

4.2.2.2 Differential Scanning Calorimetry (DSC)

DSC analysis (TA Q100, TA Instruments) was carried out using the TSP-
POSS/Pglass mixture samples in the temperature ranges of 30° to 180^oC and 30° to 300^oC
with isothermal conditions maintained for 15 min at 180^oC and 300^oC, respectively, to
test the feasibility of the sintering process simulated in the DSC experiments. A 10
^oC/min heating and cooling rate under a dry nitrogen atmosphere with the same sample
size of 5.5 ± 0.5 mg was used to determine the glass transition temperature (T_g). To
investigate the thermal property of the obtained composites samples prepared by the
various conditions (i.e., mixing and sintering process), other DSC experiments were
carried out in the temperature range of 30° to 200^oC at a 10 ^oC/min heating and cooling
rate with isothermal conditions maintained for 1 min at 200^oC.

**4.2.2.3 Scanning electron microscopy (SEM) - Energy Dispersive X-ray
spectroscopy (EDX)**

SEM/EDX analysis was conducted using a Zeiss Sigma VP® field emission
scanning electron microscope (SEM) operating at 20 kV with an attached energy-
dispersive X-ray spectroscopy (EDX) having a Thermo Scientific UltraDry EDX
detector. Elemental compositions of the surface of the fractured samples were analyzed
using the NSS3® micro-analysis software. The surface of the fractured samples was
coated with silver using a Quorum Emitech K550X sputter coater to prevent charging of
the samples.

4.2.2.4 Attenuated total reflectance Fourier transform infrared spectroscopy (ATR-FTIR)

ATR-FTIR spectra were measured on a Fourier transform spectrometer (Thermo Scientific Nicolet 6700) equipped with Smart iTR Attenuated Total Reflectance (ATR) and the sampling accessory having a single bounce diamond crystal. Spectra were recorded over a frequency range of 650 - 4000 cm^{-1}, with a 4 cm^{-1} resolution and 32 scans for each sample at ambient conditions.

4.2.2.5 X-ray diffraction (XRD)

Wide-Angle XRD (WAXD) were performed on the samples via the transmission mode on a laboratory beamline system (Xenocs Inc. Xeuss 2.0) with an X-ray wavelength (λ) of 1.54 Å (Cu-Ka radiation). The powdered samples were kept under vacuum to minimize air scattering. Diffraction images were recorded on a Pilatus 1M detector (Dectris Inc.) with an exposure time of 30 mins and processed using the software Foxtrot. The WAXD patterns were analyzed to determine crystallinity of the samples after the addition of TSP-POSS molecules.

4.2.2.6 Solid-state NMR

Solid state ^{31}P NMR spectra were obtained on a Bruker Avance III 600 (14.09 T) NMR instrument using a 4 mm broadband MAS probe spinning at 12 kHz. Both single pulse Bloch decay spectra with a 240s recycle delay, and CP MAS spectra using a 1 ms contact time were obtained. The ^{31}P chemical shift was referenced to $NH_4H_2PO_4$ $\delta = 0.8$ ppm with respect to phosphoric acid $\delta = 0$ ppm. ^{29}Si CP MAS NMR spectra were obtained on a Bruker Avance III 600 (14.09 T) NMR instrument using a 4 mm broadband MAS probe spinning at 4 kHz, using a 5 ms CP contact time. The ^{29}Si chemical shift was

referenced to Octakis(trimethylsiloxy)-silsesquioxane (Q8M8) with an offset of $\delta = +11.5$

ppm with respect to TMS ($\delta = 0$ ppm). ^{13}C Solid-state CP MAS NMR spectroscopy was

performed on a Varian UNITY INOVA® 400 spectrometer using a standard

Chemagnetics 7.5 mm PENCILTM-style probe. The samples were loaded into zirconia

rotor sleeves, sealed with TeflonTM caps, and spun at a rate of 4.0 kHz.

4.3 Results and discussion

4.3.1 Feasibility of the sintering process

DSC analysis was used to simulate a sintering effect in the mixtures of TSP-POSS

and Pglass on the glass transition temperature (T_g) as functions of the mixing methods

used (i.e. manual mixing and suspension mixing) and the amount of TSP-POSS. As

shown in Fig. 4.2 (a-b), the T_g of the mixed samples prepared by manual mixing and

suspension mixing of TSP-POSS and Pglass was not significantly changed as the amount

of TSP-POSS was increased. This is because the isothermal hold temperature of 180°C in

the DSC process was too low to either allow additional nano-scale mixing of TSP-POSS

and Pglass molecules or to induce the chemical reaction between these two materials. For

the processing temperature of 180°C, the difference of T_g between the manual and

suspension mixing comparing pure Pglass and the 10 wt.% TSP-POSS/Pglass composite

showed 1.7°C and 3.8°C., respectively, which is not a significant effect of the addition of

TSP-POSS molecules in the Pglass matrix.

On the other hand, For the samples processed at 300°C, the effect of TSP-POSS

concentration revealed a significant increase in T_g with increasing TSP-POSS

concentration, as shown in Fig. 4.2 (c-d). This result indicates that there was effective

dispersion of the TSP-POSS in the Pglass, along with the occurence of chemical reactions

between the TSP-POSS and Pglass molecules. This result helps to elucidate the basis for improvement of the thermal property of Pglass composites, which is consistent with previous results reported by Kim et al. [39]. The T_g was measured at the second heating cycle in the DSC process that is a standard method of DSC analysis. It is worth noticing that during the first 300°C heating cycle in the DSC, there was a viscous flow mixing and a chemical reaction between TSP-POSS and Pglass molecules which can change the glass transition temperature of the mixed samples. As depicted in Fig. 4.2 (c-d), there is an apparent difference of T_g between the samples prepared by manual mixing and suspension mixing. In addition, the T_g was increased significantly with increasing amounts of TSP-POSS.

The 10 wt.% TSP-POSS/Pglass sample prepared by suspension mixing showed a T_g of 161.2^{o}C, which is significantly higher than the 147.4^{o}C of the sample prepared by manual mixing. This result provides crucial evidence of the benefit of the suspension mixing method for the following effective sintering process, because the T_g of the samples prepared by the suspension mixing increased up to 35.9^{o}C while the T_g of the samples prepared by manual mixing increased up to 22.1^{o}C compared to that of the pure Pglass, respectively. In addition, the T_g of the samples increased because the number of chemical reaction sites between the TSP-POSS and Pglass molecules increased as the amount of TSP-POSS was increased. The mobility of the Pglass molecules that reacted with the bulky TSP-POSS molecules decreased, resulting in the decrease of T_g. The thermal and structural analysis of composites samples prepared by the different mixing methods is discussed in the next sections.

114

Fig. 4.3 shows SEM/EDX images of TSP-POSS in the mixed samples prepared by the manual mixing and the suspension mixing methods, respectively. Micron-sized TSP-POSS particles were manually mixed with Pglass particles as shown in Fig. 4.3(a). On the other hand, The TSP-POSS molecules were bonded to the Pglass particles via the suspension mixing process as already described in the experimental section. The SEM image in Fig. 4.3(b) did not show microscale TSP-POSS particles. However, the TSP-POSS molecules coated on the Pglass surface were revealed in the elemental EDX mapping image shown in Fig. 4.3(c-d). In the EDX mapping images, most of the mapping area of the phosphorous (P) element of Pglass in Fig. 4.3(c) was covered by the silicon (Si) element of TSP-POSS in Fig. 4.3(d), indicating that the TSP-POSS molecules covered the surface of Pglass particles where the potential reaction sites are located for the condensation reaction between TSP-POSS and Pglass [27, 58].

4.3.2 Thermal analysis

Thermal gravimetric analysis (TGA) was carried out to characterize the thermal stability of the mixed samples and the obtained one-step sintered composite samples of 5 wt.% TSP-POSS/Pglass prepared by the manual mixing method and the suspension mixing method, respectively, as shown in Fig. 4.4. The mixed samples prepared by the manual mixing and suspension mixing showed a similar proportion of decomposition in the range of $30^o \sim 600^oC$. while there is a significant difference in the decomposed portion of the two different composite samples in the TGA analysis. In contrast to the observed 7.5 wt.% decomposition of the sintered composites prepared by manual mixing, only 4 wt.% of sintered composite prepared by suspension method was decomposed. It is worth noting that the suspension mixing method is more effective to make thermally

stable TSP-POSS/Pglass composite using the sintering process compared to the manual mixing method.

The T_g was measured on the samples obtained from in the mixing method and sintering process using Pglass and 10 wt.% TSP-POSS/Pglass composites and the obtained results are shown in Fig. 4.5. This figure shows an effect of the sintering process and the mixing method on T_g change of the obtained TSP-POSS/Pglass composites. These results point to the efficiency of physical mixing and chemical reaction of 10 wt.% TSP-POSS and Pglass in the composites. As already discussed (see Fig. 4.2), the mixing process and the temperature are critical factors in the T_g change because these factors are related to the conditions of the dispersion of TSP-POSS in the Pglass matrix and chemical reactions between TSP-POSS and Pglass molecules. Compared to the T_g (120.2°C) of the control Pglass, the T_g of the composite sample prepared by manual mixing followed by the one-step sintering showed an increase of 12.6°C. When the suspension mixing was applied instead of manual mixing, the T_g of the composite increased up to 30.4°C compared to that of the control Pglass, which is 17.8°C larger than the T_g of the sample prepared by the manual mixing, indicating that the suspension mixing was relatively more efficient in the dispersion of TSP-POSS in the Pglass.

In addition, the stepwise process already described in the experimental section was applied to increase the effectiveness of mixing and chemical reactions between TSP-POSS and Pglass molecules in the preparation of the composites. As expected, the T_g of the composite was significantly increased by 50.2°C compared to that of the control Pglass sample as shown in Fig. 4.5, indicating that physical dispersion of TSP-POSS in the Pglass matrix increased during the stepwise sintering process. Further, the chemical

reaction between TSP-POSS and Pglass molecules was significantly increased due to the increased processing time. As reported in the literature [39], the increase of T_g is attributed to the addition of bulky TSP-POSS molecules on the Pglass molecules, resulting in the restriction of mobility of Pglass molecules. Interestingly, the endothermic heat flow change around the glass transition temperature of the composite samples in the DSC analysis shown in Fig. 4.5 was reduced as the suspension mixing and stepwise sintering were applied to the samples. This indicates that the glassy phase of the composites was reduced due to the suspension mixing and the stepwise sintering process. It is worthy to note that glass-ceramics materials were obtained from the mixture of pure amorphous Pglass and TSP-POSS due to the addition of bulky TSP-POSS molecules using the suspension mixing and stepwise sintering process.

4.3.3 Morphological analysis

Fig. 4.6 shows SEM micrographs of the fracture surfaces of one-step sintered pure Pglass and composites prepared by the suspension mixing of TSP-POSS and Pglass powder and one-step sintering process. The pure Pglass particles were viscous-flow sintered and became the continuous body as shown in Fig. 4.6(a) due to the very low T_g and flow temperature of Pglass. Kim et al. [39] reported the very low viscosity of pure Pglass as 10 Pa•s at 290°C, which is the same viscosity of honey at room temperature. However, it is seen that there are some discontinuous defects in the fractured surface of the sintered pure bulk Pglass because there were air spaces between the glass particles before sintering which produced voids in the sintered Pglass bulk. On the other hand, as the amount of TSP-POSS was increased in the Pglass matrix, it is seen that porosity in the fracture surface of composites was increased and the size of the voids became larger

117

due to the water vapor produced during the sintering process. As discussed by Kim et al. [27], the water vapor was produced via the condensation reactions between -OH of Pglass and -OH of TSP-POSS molecules.

The distribution of TSP-POSS molecules in the Pglass matrix of the composites prepared by suspension mixing method and one-step sintering process was investigated using EDX elemental mapping analysis as shown in Fig. 4.7. The silicon (Si) element of TSP-POSS in the composite (Fig. 4.7(b)) shows homogeneous distribution similar to phosphorous (P) mapping of Pglass as shown in Fig 4.7(a), indicating that TSP-POSS molecules are not aggregated in the Pglass matrix composites. Interestingly, the viscous flow sintering process without an additional mechanical stirring process showed an effective mixing of TSP-POSS and Pglass molecules due to the very low viscous of Pglass at the sintering temperature. This result is consistent with the results of DSC analysis showing significant change of T_g by the sintering process discussed in the previous section.

The crystallinity of the pure TSP-POSS, the pure Pglass, and the TSP-POSS/Pglass composite samples prepared by suspension mixing and stepwise sintering was studied by WAXD. Their WAXD patterns and profiles are compared to investigate the effect of the TSP-POSS molecules on crystallinity of the Pglass matrix in the composites as shown in Fig. 4.8. The WAXD pattern and profile of TSP-POSS showed obvious rings in the pattern and sharp peaks in the profile, respectively. The strong signal of TSP-POSS represents high crystallinity, which is consistent with the results reported for a similar structure of POSS in the literature [59-62]. The weak WAXD patterns of Pglass indicates the amorphous nature of glass material, with a broad peak around 25°

118

(2θ) that is consistent with the results of the broad peak at 20~30 º (2θ) for phosphate glasses reported in literature by a number of researchers [63-67]. The WAXD profile of the composite sample incorporating TSP-POSS is quite similar to that of the amorphous Pglass. There are slightly more scattering intensities in the WAXD pattern of the composite compared to that of Pglass. However, there is not a significant difference in the profile. This result indicates that the addition of TSP-POSS molecules in the Pglass matrix prepared via the sintering process did not significantly change the crystallinity of Pglass matrix composite. It is worth noticing that the opaque property of the composite is not ascribed to the crystallinity of the composites, but it is instead due to the voids in the composites.

It was also observed that the crystalline property of TSP-POSS is not shown in the TSP-POSS/Pglass composites, which is different from the results previously reported in the literature [59, 61]. For example, Zhao et al. [59] reported scattering results of polycarbonate (PC) composites due to the addition of POSS, indicating that POSS keeps its crystalline domains in the POSS/PC composites. Lai et al. [61] reported that POSS-modified POSS/Polyurethane composites showed the same crystallinity of the POSS component, indicating that POSS retains an ability to form a crystalline phase in the organic polymer matrix composites. In contrast, there is not a significant crystalline peak of TSP-POSS in our results, which indicates that TSP-POSS molecules lost their self-assembling ability to produce crystalline phase in the Pglass matrix during the sintering process. This is attributed to good dispersion of TSP-POSS in the Pglass matrix and chemical reactions of TSP-POSS and Pglass.

4.3.4 Structural analysis

The FTIR analysis on the pure Pglass, TSP-POSS and the composites prepared by the various methods used here are shown in Fig. 4.9. The FTIR spectra of pure Pglass sample shows peaks around 920 cm^{-1}, and 740 cm^{-1} associated with the asymmetric and symmetric stretching vibration of P-O-P, respectively [68]. Obviously, the peak of 920 cm^{-1} assigned to asymmetric stretching vibration was not affected by the addition of TSP-POSS because the P-O-P bond is chemically stable in the composites and there is not an overlapped peak from the TSP-POSS molecules. However, the peak at 740 cm^{-1} assigned to symmetric stretching vibration of P-O-P showed an overlapping with the peak around 745 cm^{-1} associated with the out-of-plane deformation of phenyl groups of TSP-POSS molecules [69], resulting in higher and broader peaks after applying the sintering process due to the addition of TSP-POSS molecules in the Pglass matrix. Another peak around 695 cm^{-1} assigned to the out-of-plane deformation of phenyl groups appeared in all the composite samples due to the addition of TSP-POSS molecules to the Pglass matrix, which is evidence of the stability of TSP-POSS molecules in the composites.

The peaks near the 1015 cm^{-1} and 1070 cm^{-1} assigned to the $(-PO_3)^{2-}$ and P—O$^-$ [70-72], respectively, incorporating non-bridging oxygen in the linkages became broader due to the overlapping of peaks of Si-O stretching vibration assigned to 1027 cm^{-1} [73] and Si-O-Si symmetric stretching vibration associated with 1100 cm^{-1} [58, 73]. In addition, a new chemical bond of P-O-Si between TSP-POSS and Pglass assigned to 1160 cm^{-1} and Si-phenyl group bonds deformation in TSP-POSS at 1137 cm^{-1} [69] resulted in the broader peak from 950 cm^{-1} to 1150 cm^{-1} of composites in Fig. 4.9(f)

compared to the peak of the pure Pglass in Fig. 4.9(b). The reduction of the peak of P-F assigned to 840 cm^{-1} [70] is obvious in Fig. 4.9 as the sintering process and suspension mixing were applied to the composites. This indicates that the P-F bond was decomposed and it is believed to be replaced by another bond (P-O-Si or P-O-P) as previously reported [39]. The peak of P-F in the composite in Fig. 4.9(f) is significantly diminished compared to that of pure Pglass in Fig. 4.9(b), which is ascribed to the good dispersion of TSP-POSS in the Pglass matrix and the effective chemical interaction between the TSP-POSS and Pglass molecules during the sintering process similar to that obtained in the synthesis method reported previously [39].

^{31}P CP MAS NMR spectra are shown in Fig. 4.10(a). A broad asymmetric resonance observed at δ = -18 ppm, which can be deconvoluted into Q^0 and Q^1 phosphate species assigned to the peaks between δ = -11 and -9 ppm and δ = -20 and -15 ppm, respectively [39, 74]. The pure Pglass (a1) has the narrowest line width, while the sample (a2) prepared by manual mixing and one-step sintering has the largest line width, showing an apparent shoulder around δ = -11 ppm, which is a different result from other composite materials (a3, a4). This result represents a large ratio of Q^0/Q^1 in the sample (a2) compared to other samples. It is conjectured that the recombination of Pglass particles were hindered by bulky TSP-POSS particles during the sintering process, resulting in increasing the Q^0 portion in the composite. ^{13}C CP NMR MAS spectra are shown in Fig. 4.10(b), representing the peaks assigned to carbon atoms of phenyl groups of TSP-POSS [75] within the composites, which indicates the thermal stability of TSP-POSS molecules in the composites prepared by the viscous flow sintering process with the relatively low temperature used.

121

The ^{29}Si CP MAS NMR result is shown in Fig. 4.11. Disappearance of the peak of Si in the T_2 position (open-Si, R-Si(OH)-O$_2$, R=phenyl) of all sintered samples indicates that the trisilanol were all consumed by condensation reactions of TSP-POSS-Pglass or TSP-POSS–TSP-POSS, which is consistent with the result as already discussed [27]. There are not significant differences in the chemical shifts and line widths of Si of T_3 position (closed-Si,R-Si-O$_3$, R=phenyl) between the three composites as shown in Fig. 4.11(a-c), indicating that all of them have very similar chemistries. However, the ^{29}Si CP MAS NMR of the dehydrated TSP-POSS sample (Fig. 4.11(e)) was prepared from only TSP-POSS molecules. The peak of Si in the T_3 position in the dehydrated TSP-POSS shows an apparent shift compared to the peak of Si in the T_3 position in the composites, indicating that the new Si environments in TSP-POSS-Pglass (Fig. 4.11(a-c)) are different from the Si environments in the dehydrated TSP-POSS (Fig. 4.11(e)), consistent with the formation of Si-O-P bonds in the composite versus Si-O-Si bonds in the dehydrated TSP-POSS. It is worthy to note that TSP-POSS molecules are chemically bonded to Pglass molecules during the sintering process based on the obvious NMR result already discussed, which is closely consistent with the remarkable change of the glass transition temperature of the composites compared to that of the pure Pglass.

4.4 Conclusions

It can be concluded from the results of this study that the increase of glass transition temperature of the TSP-POSS/Pglass composites is attributed to the effective mixing and chemical reaction between these materials. The sintering process worked efficiently in the preparation of composites at the temperature of 300°C and verified in the DSC pre-test data. The T_g of TSP-POSS/Pglass composite increased up to 50.2^{o}C compared to that of

the pure Pglass with the efficient suspension mixing and the stepwise sintering processes. SEM and EDX analyses confirmed that there is not a microscale aggregation in the mixing of these two materials using the suspension mixing and one-step sintering process.

The suspension mixing was effective on the TSP-POSS coating on the Pglass particles before the sintering process as shown in the SEM analysis, resulting in improved dispersion of TSP-POSS molecules in the composites. This effective mixing of TSP-POSS and Pglass by the suspension method increased the interface area between TSP-POSS and Pglass molecules, resulting in more condensation reactions in the composites. The obtained composites showed improved thermal stability and higher glass transition temperature. In addition, the stepwise sintering process as used here provided sufficient time for the efficient mixing and chemical reaction between the TSP-POSS and Pglass molecules in the preparation of TSP-POSS/Pglass composites.

The chemical bonds between the TSP-POSS and Pglass in the composites were evidenced by the reduction of the peaks assigned to non-bridging oxygen and P-F bonds in the obtained FTIR data. In addition, the difference of the ^{29}Si NMR resonances assigned to the T_3 (closed-Si) between dehydrated TSP-POSS and the composites indicates that there is an obvious difference of chemical reactions between TSP-POSS–TSP-POSS in the pure TSP-POSS and TSP-POSS–Pglass in the composites. It is worthy to note that the sintering process is a facile and efficient method to prepare TSP-POSS/Pglass composites due to the benefits of the good compatibility in the mixing between the Pglass with ultra-low T_g and nanoscale TSP-POSS molecules in addition to the chemical reactive sites in both materials. This study is part of a long-range research on novel Pglass matrix composites incorporating POSS prepared via a one pot synthesis

method and the extrusion method previously reported. These research efforts provide fundamental information of POSS/Pglass composite systems that is directly applicable in a wide range of scientific and industrial application areas such as heterogeneous catalysis, optoelectronic components, bioengineering, and biomedical engineering.

Acknowledgements

4.5 Reference

1.   Hussain, F., et al., Polymer-matrix nanocomposites, processing, manufacturing, and application: an overview. Journal of composite materials, 2006. 40(17): p. 1511-1575.

2.   Jancar, J., et al., Current issues in research on structure–property relationships in polymer nanocomposites. Polymer, 2010. 51(15): p. 3321-3343.

3.   Andrews, R. and M. Weisenberger, Carbon nanotube polymer composites. Current Opinion in Solid State and Materials Science, 2004. 8(1): p. 31-37.

4.   Thostenson, E.T., Z. Ren, and T.-W. Chou, Advances in the science and technology of carbon nanotubes and their composites: a review. Composites science and technology, 2001. 61(13): p. 1899-1912.

5.   Potts, J.R., et al., Graphene-based polymer nanocomposites. Polymer, 2011. 52(1): p. 5-25.

6.   Kumar, S., et al., Fibers from polypropylene/nano carbon fiber composites. Polymer, 2002. 43(5): p. 1701-1703.

7.   Chand, S., Review carbon fibers for composites. Journal of materials science, 2000. 35(6): p. 1303-1313.

8.   Hanemann, T., Influence of particle properties on the viscosity of polymer–alumina composites. Ceramics International, 2008. 34(8): p. 2099-2105.

9.   Ash, B., L. Schadler, and R. Siegel, Glass transition behavior of alumina/polymethylmethacrylate nanocomposites. Materials Letters, 2002. 55(1-2): p. 83-87.

10.   Schmidt, D., D. Shah, and E.P. Giannelis, New advances in polymer/layered silicate nanocomposites. Current Opinion in Solid State and Materials Science, 2002. 6(3): p. 205-212.

11.   Ray, S.S. and M. Okamoto, Polymer/layered silicate nanocomposites: a review from preparation to processing. Progress in polymer science, 2003. 28(11): p. 1539-1641.

12.   Chen, Y., et al., Preparation and characterization of nanocomposite polyurethane. Journal of Colloid and Interface Science, 2004. 279(2): p. 370-378.

13.   Ma, D., et al., Influence of nanoparticle surface modification on the electrical behaviour of polyethylene nanocomposites. Nanotechnology, 2005. 16(6): p. 724.

14.   Hussan, F., et al., Review article: Polymer-matrix Nanocomposites, Processing, Manufacturing and Application. J. comp. mat, 2006. 40(17).

15.   Sorrentino, A., G. Gorrasi, and V. Vittoria, Potential perspectives of bio-nanocomposites for food packaging applications. Trends in Food Science & Technology, 2007. 18(2): p. 84-95.

16.   Brennan, J.J. and K.M. Prewo, Silicon carbide fibre reinforced glass-ceramic matrix composites exhibiting high strength and toughness. Journal of Materials Science, 1982. 17(8): p. 2371-2383.

17.   Marshall, D.B. and A.G. Evans, Failure mechanisms in ceramic-fiber/ceramic-matrix composites. Journal of the American Ceramic Society, 1985. 68(5): p. 225-231.

18.   Beyerle, D.S., et al., Damage and failure in unidirectional ceramic–matrix composites. Journal of the American Ceramic Society, 1992. 75(10): p. 2719-2725.

19.   Cho, J., A.R. Boccaccini, and M.S. Shaffer, Ceramic matrix composites containing carbon nanotubes. Journal of Materials Science, 2009. 44(8): p. 1934-1951.

20.   Boccaccini, A., et al., Borosilicate glass matrix composites containing multi-wall carbon nanotubes. Journal of the European Ceramic Society, 2005. 25(9): p. 1515-1523.

21.   Crivelli-Visconti, I. and G. Cooper, Mechanical properties of a new carbon fibre material. Nature, 1969. 221(5182): p. 754.

22.   Ning, J., et al., Fabrication and mechanical properties of SiO_2 matrix composites reinforced by carbon nanotube. Materials Science and Engineering: A, 2003. 357(1-2): p. 392-396.

23.   Boccaccini, A., H. Kern, and I. Dlouhy, Determining the fracture resistance of fibre-reinforced glass matrix composites by means of the chevron-notch flexural technique. Materials Science and Engineering: A, 2001. 308(1-2): p. 111-117.

24.   Bianchi, V., et al., Carbon-fibre-reinforced (YMAS) glass-ceramic matrix composites. I. Preparation, structure and fracture strength. Journal of the European Ceramic Society, 1997. 17(12): p. 1485-1500.

25.   Evans, A.G., The mechanical performance of fiber-reinforced ceramic matrix composites. Materials Science and Engineering: A, 1989. 107: p. 227-239.

26.   Balaji, S., S. Bose, and R. Debnath, Single-walled carbon nanotube/(Pb, Zn)-phosphate glass heterostructure: an optical sensor and efficient photocurrent converter. Journal of Physics D: Applied Physics, 2012. 45(32): p. 325106.

27.   Kim, K., I. Belyamani, and J.U. Otaigbe, Novel porous bioabsorbable phosphate glass matrix nanocomposites incorporating trisilanolphenyl polyhedral oligomeric silsesquioxane prepared by extrusion. Materials Letters, 2018. 210: p. 186-190.

28.   Sommers, A., et al., Ceramics and ceramic matrix composites for heat exchangers in advanced thermal systems—A review. Applied Thermal Engineering, 2010. 30(11): p. 1277-1291.

29.   Habraken, W.J.E.M., J.G.C. Wolke, and J.A. Jansen, Ceramic composites as matrices and scaffolds for drug delivery in tissue engineering. Advanced Drug Delivery Reviews, 2007. 59(4): p. 234-248.

30.   Deng, J., T. Can, and J. Sun, Microstructure and mechanical properties of hot-pressed Al2O3/TiC ceramic composites with the additions of solid lubricants. Ceramics International, 2005. 31(2): p. 249-256.

31.   Sambell, R., D. Bowen, and D. Phillips, Carbon fibre composites with ceramic and glass matrices. Journal of Materials Science, 1972. 7(6): p. 663-675.

32.   Minay, E., V. Desbois, and A. Boccaccini, Innovative manufacturing technique for glass matrix composites: extrusion of recycled TV set screen glass reinforced with Al_2O_3 platelets. Journal of materials processing technology, 2003. 142(2): p. 471-478.

33.   Mackenzie, J.D., Applications of the sol-gel process. Journal of Non-Crystalline Solids, 1988. 100(1): p. 162-168.

34.   Boccaccini, A., C. Kaya, and K. Chawla, Use of electrophoretic deposition in the processing of fibre reinforced ceramic and glass matrix composites: a review. Composites Part A: Applied Science and Manufacturing, 2001. 32(8): p. 997-1006.

35.   Tsionsky, M., et al., Sol-gel-derived ceramic-carbon composite electrodes: introduction and scope of applications. Analytical Chemistry, 1994. 66(10): p. 1747-1753.

36.   Boccaccini, A.R., et al., Sintering, crystallisation and biodegradation behaviour of Bioglass®-derived glass–ceramics. Faraday discussions, 2007. 136: p. 27-44.

37.   Champion, E., Sintering of calcium phosphate bioceramics. Acta biomaterialia, 2013. 9(4): p. 5855-5875.

38.   Ross, J., W. Miller, and G. Weatherly, Dynamic computer simulation of viscous flow sintering kinetics. Journal of Applied Physics, 1981. 52(6): p. 3884-3888.

39.   Kim, K., et al., Synthesis and characterization of novel phosphate glass matrix nanocomposites containing polyhedral oligomeric silsesquioxane with improved properties. Journal of Non-Crystalline Solids, 2017. 463: p. 189-202.

40.   Otaigbe, J.U. and G.H. Beall, Inorganic phosphate glasses as polymers. Trends in Polymer science, 1997. 5(11): p. 369-379.

41.   Beall, G.H., J.E. Dickinson Jr, and C.J. Quinn, Rare earth-containing zinc phosphate glasses. 1991, Google Patents.

42.   Gongyi, G. and C. Yuli, Optical properties of a chemically durable phosphate glass. Journal of materials science letters, 1993. 12(5): p. 265-267.

43.   Aboulfotoh, N., et al., Characterization of copper doped phosphate glasses for optical applications. Ceramics International, 2014. 40(7): p. 10395-10399.

44.   Hosono, H., S. Kawamura, and Y. Abe, Prefered molecular orientation at crystal growth front in Ca $(PO_3)^2$ glass. Journal of materials science letters, 1985. 4(2): p. 244-246.

45.   Brauer, D.S., et al., Degradable phosphate glass fiber reinforced polymer matrices: mechanical properties and cell response. Journal of Materials Science: Materials in Medicine, 2008. 19(1): p. 121.

46.   Wilder Jr, J.A., Glasses and glass ceramics for sealing to aluminum alloys. Journal of Non-Crystalline Solids, 1980. 38: p. 879-884.

47. Wei, T., Y. Hu, and L. Hwa, Structure and elastic properties of low-temperature sealing phosphate glasses. Journal of non-crystalline solids, 2001. 288(1-3): p. 140-147.

48. Sales, B. and L. Boatner, Lead-iron phosphate glass: a stable storage medium for high-level nuclear waste. Science, 1984. 226(4670): p. 45-48.

49. Sales, B. and L. Boatner, Physical and chemical characteristics of lead-iron phosphate nuclear waste glasses. Journal of non-crystalline solids, 1986. 79(1-2): p. 83-116.

50. Sales, B.C. and L.A. Boatner, Lead phosphate glass as a stable medium for the immobilization and disposal of high-level nuclear waste. Materials Letters, 1984. 2(4, Part B): p. 301-304.

51. Minami, T., Y. Takuma, and M. Tanaka, Superionic Conducting Glasses: Glass Formation and Conductivity in the $AgI\text{-}Ag_2 O\text{-}P_2O_5$ System. Journal of The Electrochemical Society, 1977. 124(11): p. 1659-1662.

52. Martin, S.W., Ionic conduction in phosphate glasses. Journal of the American Ceramic Society, 1991. 74(8): p. 1767-1784.

53. Loong, C.-K., et al., Structure and dynamics of phosphate glasses: from ultra-to orthophosphate composition. Physica B: Condensed Matter, 1997. 241: p. 890-896.

54. Mastrogiacomo, M., et al., Role of scaffold internal structure on in vivo bone formation in macroporous calcium phosphate bioceramics. Biomaterials, 2006. 27(17): p. 3230-3237.

55.   Urman, K. and J.U. Otaigbe, New phosphate glass/polymer hybrids—Current status and future prospects. Progress in Polymer Science, 2007. 32(12): p. 1462-1498.

56.   Gnanasekaran, D., K. Madhavan, and B. Reddy, Developments of polyhedral oligomeric silsesquioxanes (POSS), POSS nanocomposites and their applications: A review. 2009.

57.   Li, G., et al., Polyhedral oligomeric silsesquioxane (POSS) polymers and copolymers: a review. Journal of Inorganic and Organometallic Polymers, 2001. 11(3): p. 123-154.

58.   Kannan, A.G., N.R. Choudhury, and N.K. Dutta, Synthesis and characterization of methacrylate phospho-silicate hybrid for thin film applications. Polymer, 2007. 48(24): p. 7078-7086.

59.   Zhao, Y. and D.A. Schiraldi, Thermal and mechanical properties of polyhedral oligomeric silsesquioxane (POSS)/polycarbonate composites. Polymer, 2005. 46(25): p. 11640-11647.

60.   Zheng, L., et al., Polymer nanocomposites through controlled self-assembly of cubic silsesquioxane scaffolds. Macromolecules, 2004. 37(23): p. 8606-8611.

61.   Lai, Y., et al., Structural and electrochemical properties of polyurethanes/polyhedral oligomeric silsesquioxanes (PU/POSS) hybrid coatings on aluminum alloys. Materials Chemistry and Physics, 2009. 117(1): p. 91-98.

62.   Fina, A., et al., Polypropylene–polyhedral oligomeric silsesquioxanes (POSS) nanocomposites. Polymer, 2005. 46(19): p. 7855-7866.

63.   Dias, A., et al., In situ thermal and structural characterization of bioactive calcium phosphate glass ceramics containing TiO_2 and MgO oxides: High temperature–XRD studies. Journal of Non-Crystalline Solids, 2005. 351(10-11): p. 810-817.

64.   Karakassides, M., A. Saranti, and I. Koutselas, Preparation and structural study of binary phosphate glasses with high calcium and/or magnesium content. Journal of Non-Crystalline Solids, 2004. 347(1-3): p. 69-79.

65.   Koo, J., B.-S. Bae, and H.-K. Na, Raman spectroscopy of copper phosphate glasses. Journal of non-crystalline solids, 1997. 212(2-3): p. 173-179.

66.   Chung, J. and B. Ryu, Crystallization behavior of phosphate glasses with hydrophobic coating materials. Journal of Nanomaterials, 2015. 2015: p. 8.

67.   Dabas, P. and K. Hariharan, Lithium rich phosphate glass: Crystallization kinetics, structural and conduction characteristics. Journal of Non-Crystalline Solids, 2012. 358(2): p. 252-260.

68.   Fang, Y., et al., Tin fluorophosphate nonwovens by melt state centrifugal Forcespinning. Journal of materials science, 2014. 49(24): p. 8252-8260.

69.   Fina, A., et al., Polyhedral oligomeric silsesquioxanes (POSS) thermal degradation. Thermochimica Acta, 2006. 440(1): p. 36-42.

70.   Ding, J., et al., The properties and structure of Sn- Ca- P- O- F glasses. Materials chemistry and physics, 2003. 82(1): p. 61-67.

71.   Bartholomew, R.F., Structure and properties of silver phosphate glasses—Infrared and visible spectra. Journal of Non-Crystalline Solids, 1972. 7(3): p. 221-235.

72.   Li, H., et al., The evolution of the network structure in tin-fluoro-phosphate glass with increasing temperature. Journal of Non-Crystalline Solids, 2018. 492: p. 84-93.

73.   Liang, K., et al., Cyanate ester/polyhedral oligomeric silsesquioxane (POSS) nanocomposites: synthesis and characterization. Chemistry of materials, 2006. 18(2): p. 301-312.

74.   Holland, D., et al., Lone-pair effects and structural trends in x SnO·(1− x) P_2O_5 glasses deduced from 31P and 119Sn nuclear magnetic resonance. Journal of Physics: Condensed Matter, 2002. 14(49): p. 13609.

75.   Misra, R., et al., Molecular miscibility and chain dynamics in POSS/polystyrene blends: control of POSS preferential dispersion states. Polymer, 2009. 50(13): p. 2906-2918.

(a) Closed-POSS
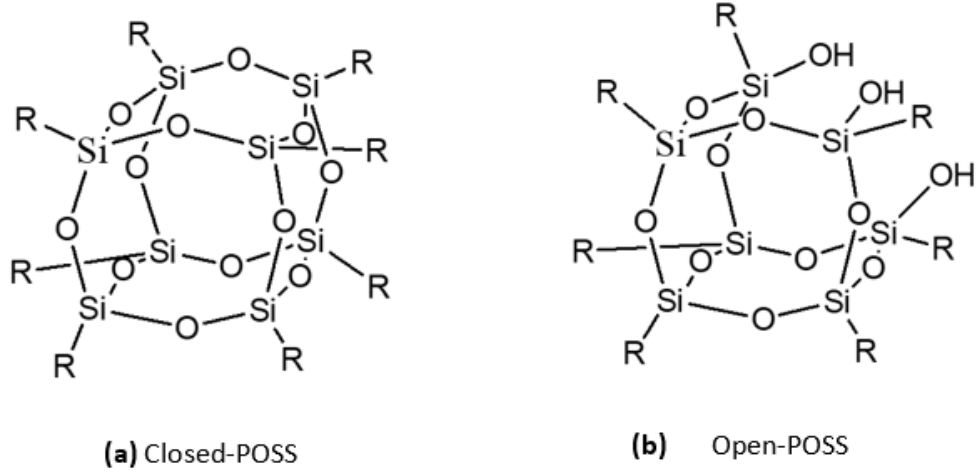
(b) Open-POSS

R = various functional groups

TSP-POSS = open-POSS with (R = phenyl)

Figure 4.1 Structural scheme of (a) closed-POSS and (b) open-POSS
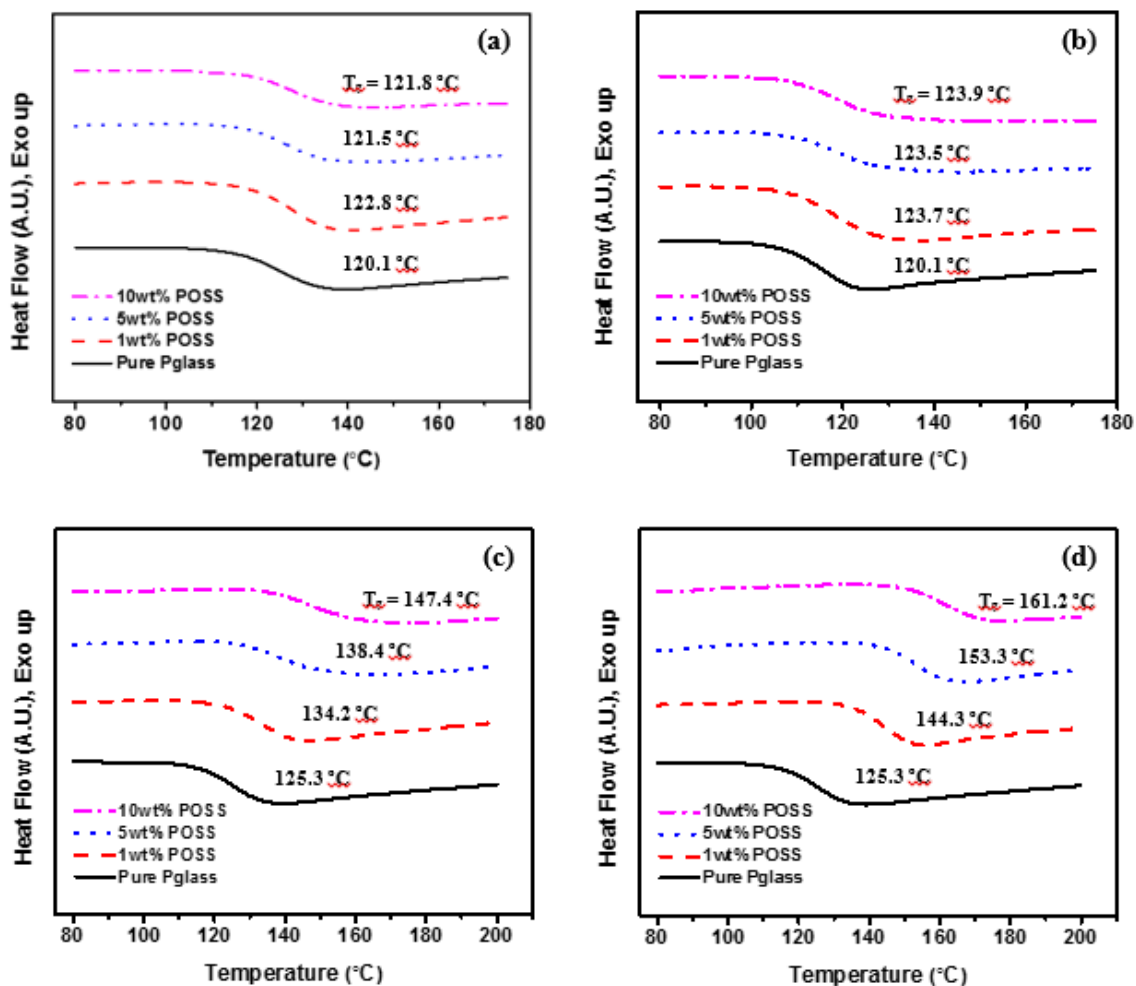
Figure 4.2 DSC thermograms in the range from 30ºC to 180ºC with isothermal conditions of 15 min at 180ºC for the mixture of POSS and Pglass prepared by (a) manual mixing and (b) suspension mixing, and DSC thermogram for the same samples in the range from 30ºC to 300ºC with isothermal conditions of 15 min at 300ºC prepared by (c) manual mixing and (d) suspension mixing.
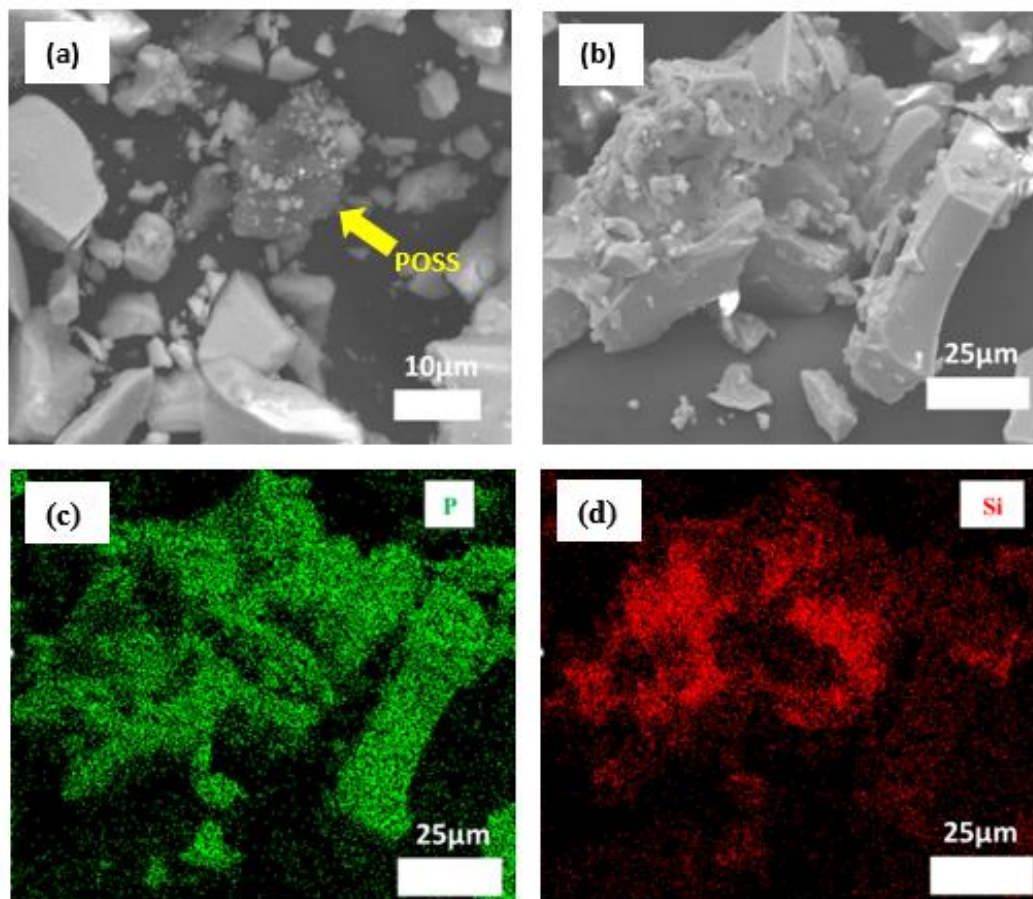
Figure 4.3 SEM images of (a) manually mixed POSS and Pglass particles; (b) SEM image and EDX mapping images of (c) phosphorous, (d) silicon on the POSS coated Pglass using suspension method.
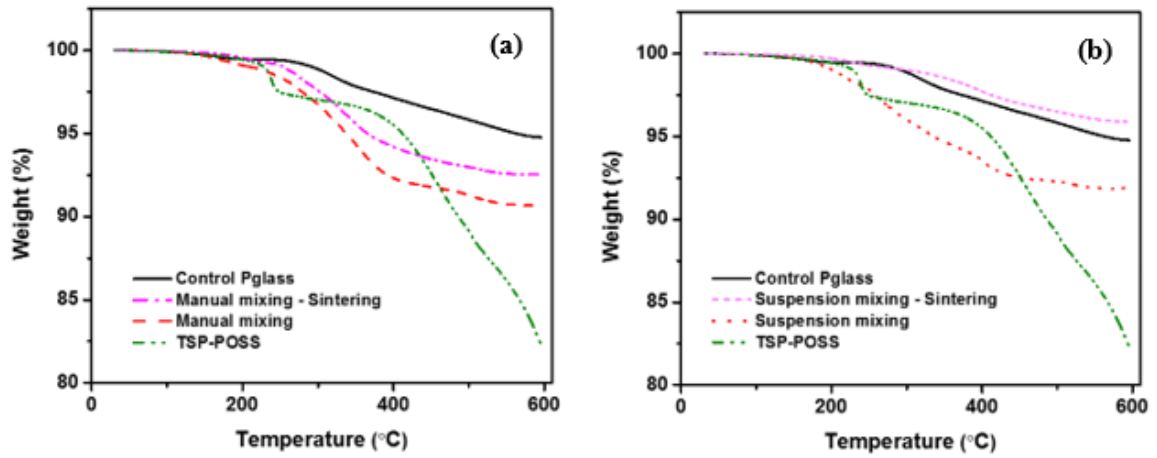
Figure 4.4 TGA graphs for the thermal stability of the mixture of POSS/Pglass and the one-step sintered POSS/Pglass composites incorporating 5 wt.% of POSS prepared by two different mixing methods: (a) manual mixing and (b) suspension mixing methods.
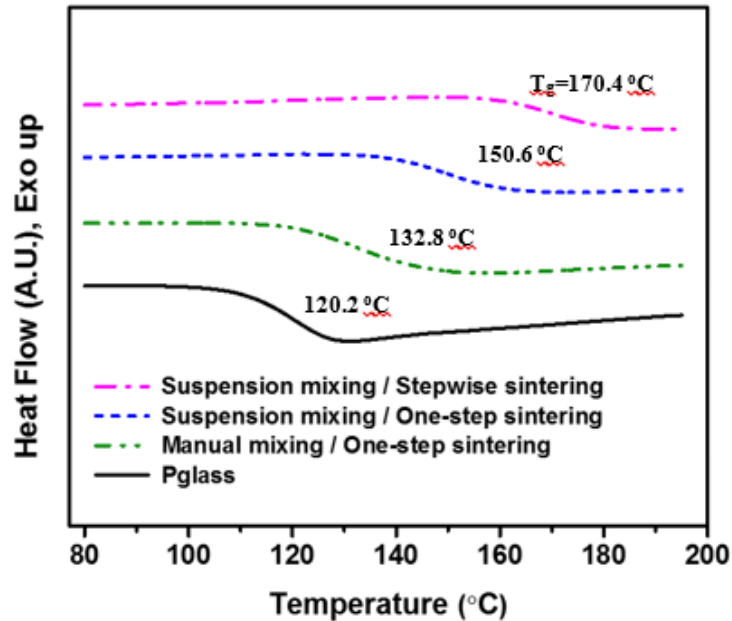
Figure 4.5 DSC thermogram of the pure Pglass and 10 wt.% POSS/Pglass composites prepared by different methods as described in the graph.
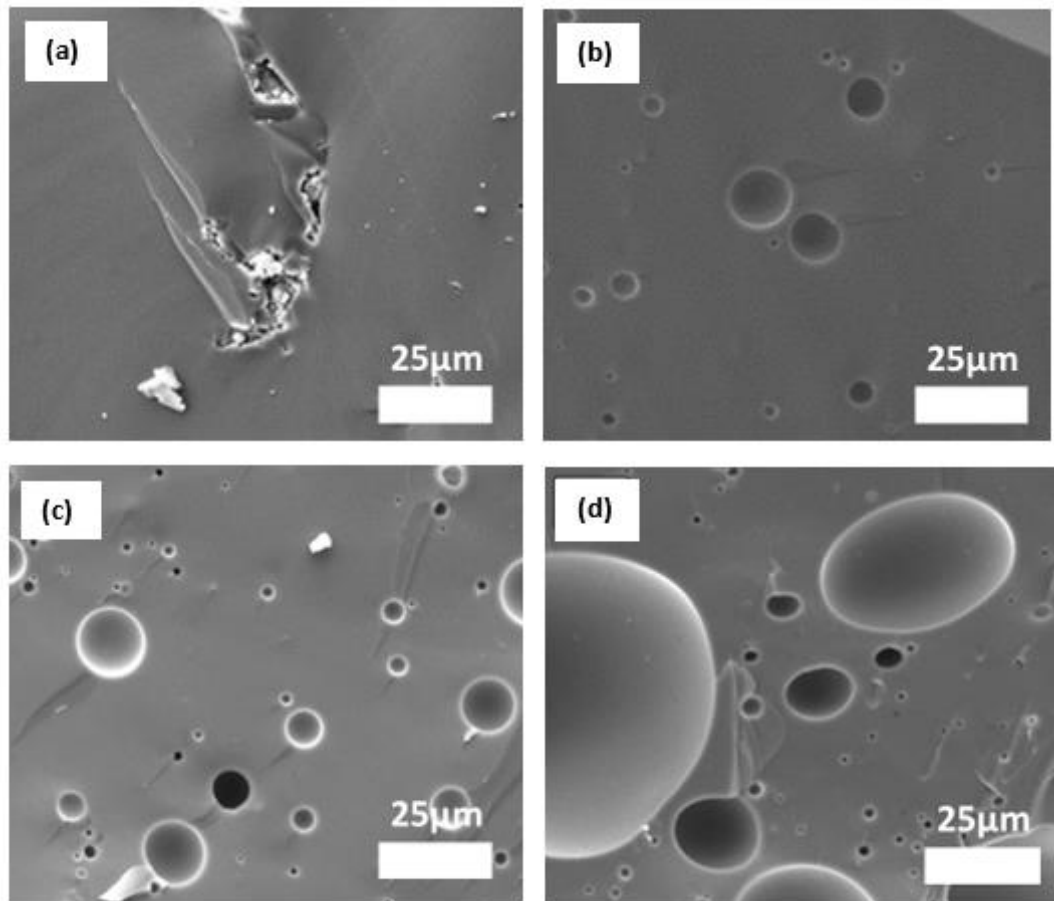
Figure 4.6 SEM Images of fractured surface on one-step sintered (a) control Pglass, (b) 1 wt.% POSS, (c) 5 wt.% POSS, and (d) 10 wt.% POSS composites prepared by suspension mixing method using powder compacts.
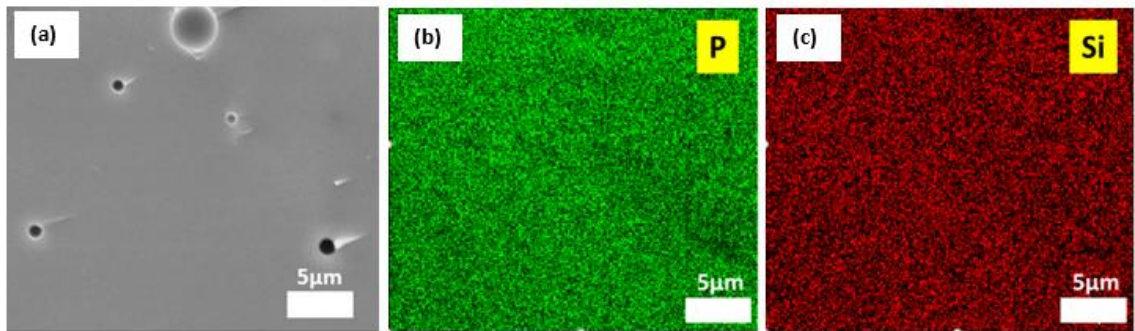
Figure 4.7 (a) SEM Images and EDX mapping images of each element (b) P, phosphorous; (c) Si, silicon on the fractured surface on the 10 wt.% POSS composite prepared using suspension mixing method and the one-step sintering process.
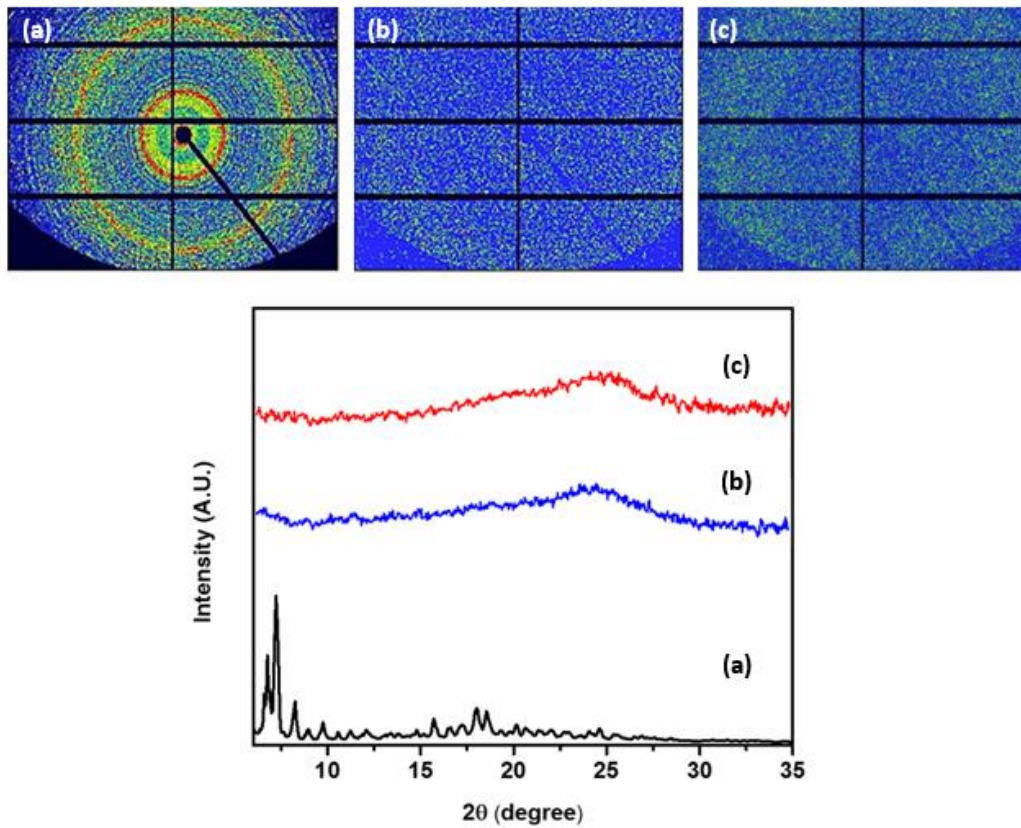
Figure 4.8 XRD patterns and profiles of (a) pure TSP-POSS, (b) pure Pglass, and (c) 10 wt.% TSP-POSS/Pglass composites prepared by suspension mixing method and stepwise sintering process.
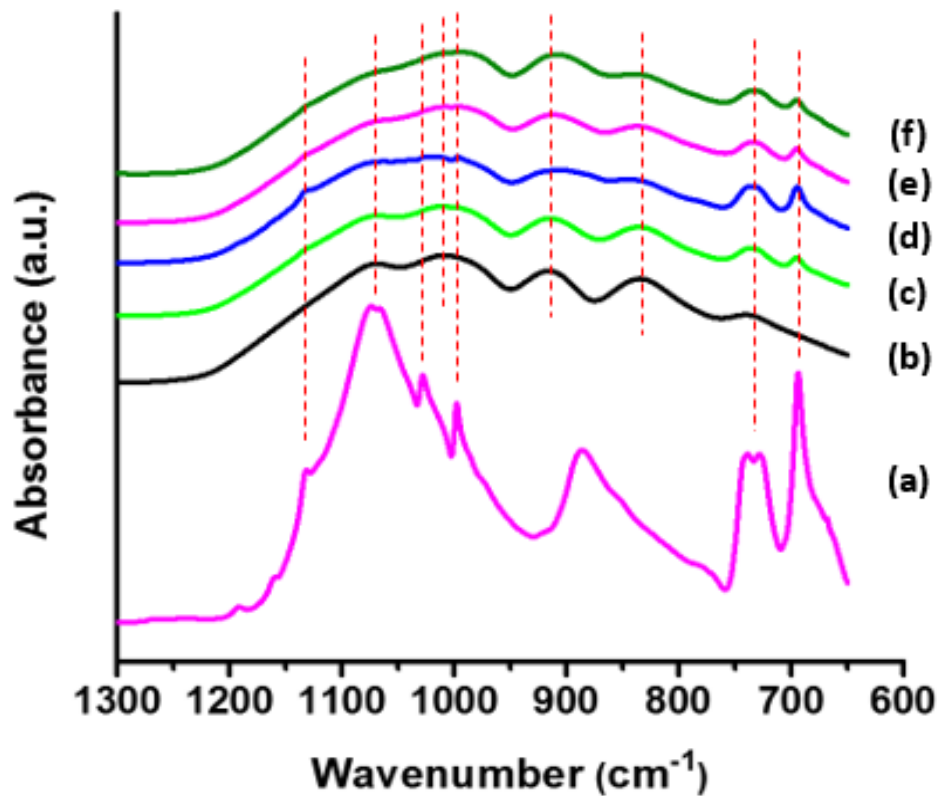
Figure 4.9 ATR-FTIR spectra of the samples: (a) pure TSP-POSS, (b) pure Pglass, (c) 5 wt.% POSS/Pglass composite with manual mixing and one-step sintering, (d) 10wt.%POSS/Pglass composite with manual mixing and one-step sintering, (e) 10 wt.% POSS/Pglass composite with suspension mixing and one-step sintering, and (f) 10 wt.% POSS/Pglass composite suspension mixing and stepwise mixing.
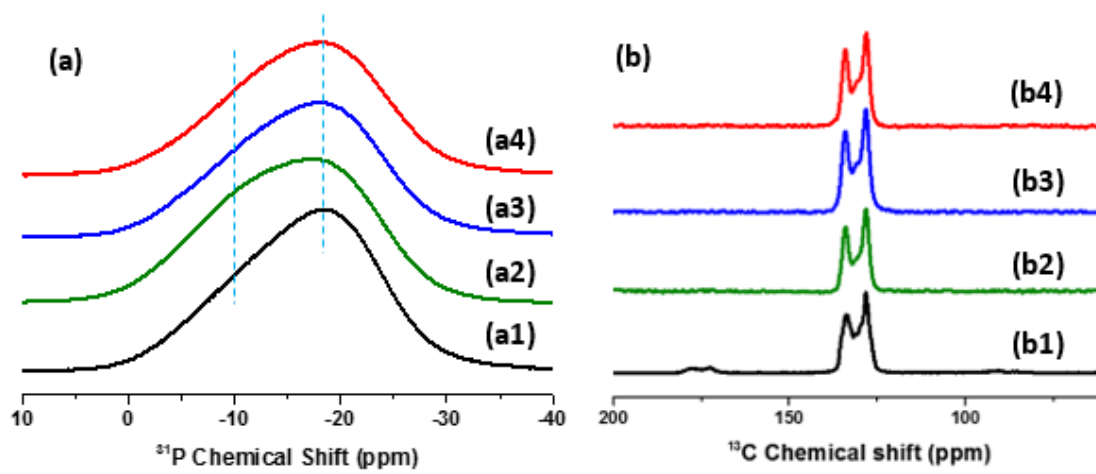
Figure 4.10 (a) ^{31}P CP MAS NMR spectra of pure Pglass and its composites: (a1) pure Pglass, (a2) 10 wt.% POSS with manual mixing and one-step sintering, (a3) 10 wt.% POSS with suspension mixing and one-step sintering, and (a4) 10 wt.% POSS with suspension mixing and stepwise sintering; (b) ^{13}C CP MAS NMR spectra of pure POSS and composites: (b1) pure TSP-POSS, (b2) 10 wt.% POSS with manual mixing and one-step sintering, (b3) 10 wt.% POSS with suspension mixing and one-step sintering, and (b4) 10 wt.% POSS with suspension mixing and stepwise sintering.
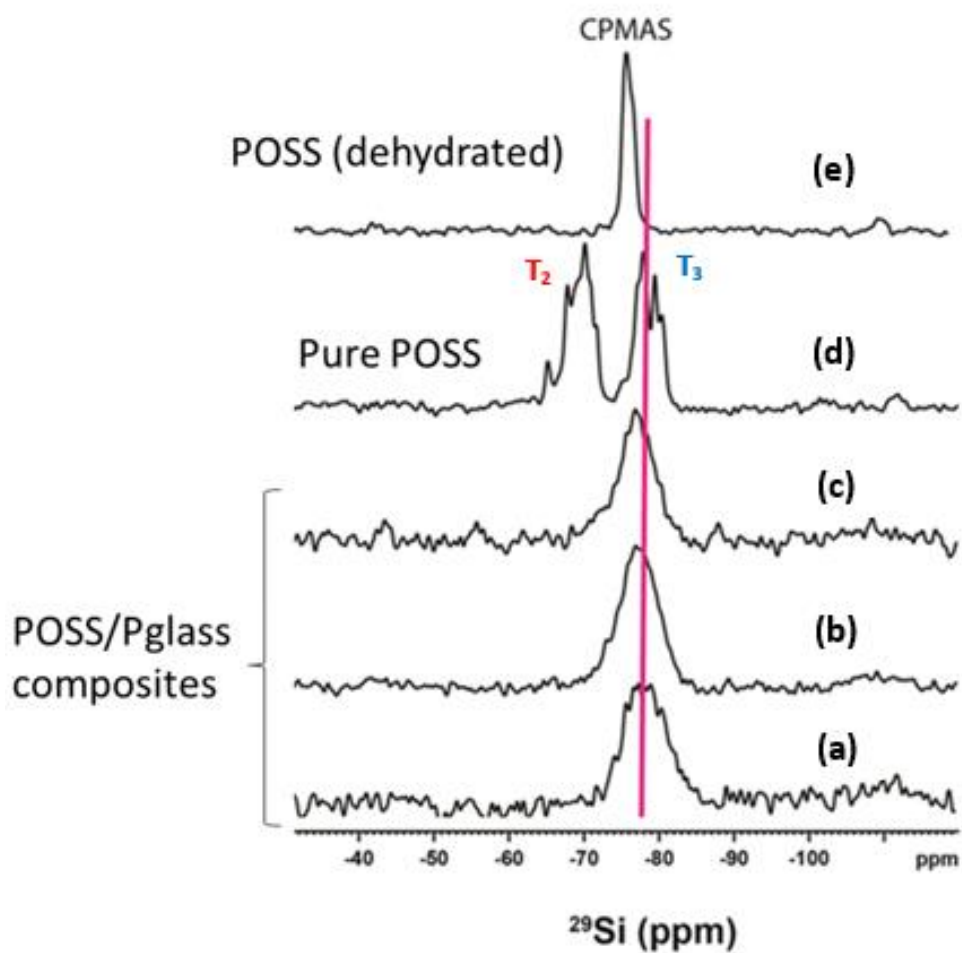
Figure 4.11 ^{29}Si CP MAS NMR spectra of dehydrated POSS, pure TSP-POSS and 10 wt.% POSS/Pglass composites prepared by each method; (a) 10 wt.% POSS with manual mixing and one-step sintering, (b) 10 wt.% POSS with suspension mixing and one-step sintering, (c) 10 wt.% POSS with suspension mixing and stepwise sintering, (d) pure POSS, and (e) dehydrated POSS.

CHAPTER V – FACILE ROUTE TO NATURE INSPIRED

HYDROPHOBIC SURFACE MODIFICATION OF PHOSPHATE GLASS

USING POLYHEDRAL OLIGOMERIC SILSESQUIOXANE WITH IMPROVED

PROPERTIES

Kyoungtae Kim, Joseph D. Lichtenhan, Joshua U. Otaigbe

Abstract

Hydrophobic polyhedral oligomeric silsesquioxane (POSS) molecules were
utilized for the surface coating to improve the hydrophobicity of the surface of phosphate
glass (Pglass). To maximize the Pglass surface hydrophobicity, protrusions on the Pglass
surface were successfully prepared by Pglass glass particles on the surface of the bulk
Pglass to mimick the lotus leaf, which has a superhydrophobic surface. The results
showed that the combination of hydrophobic coating by POSS and improved roughness
prepared by Pglass particles with air trapped on the phosphate glass surface yielded
significantly increased hydrophobicity close to superhydrophobicity of lotus leaf.
Chemical stability tests using ethanol and acetone confirmed stability of POSS on the
Pglass surface. This result was supported by the XPS data showing an increase of
bridging oxygen on the Pglass surface due to the condensation reaction between the
hydroxyl functional groups of the Pglass and POSS. The relatively longer hydrophobic
functional group of isooctyl compared to that of the isobutyl on the POSS cages gave
larger contact angles than that of conventional silane, indicating that the POSS chemicals
used are able to effectively produce the so-called "umbrella effect" mechanism that

covers the intrinsic hydrophilic surface of the phosphate glass using bulky molecules and grafted hydrophobic POSS chemical functional groups.

5.1 Introduction

Water repellency of a solid surface is a very important property in fundamental research and practical applications related to surface structures and properties [1-4]. Water-repellent surfaces are usually prepared by low surface energy materials including alkyl chains [5-7] and fluorinated functional groups [4, 8, 9], showing higher contact angles. In addition, the actual contact area between water and solid surface is a critical factor that is strongly influenced by the surface roughness of solid materials. The contact angle (θ) between a flat solid surface and a liquid droplet is usually calculated using the Young's equation [10] as follows:.

$$\cos \theta = \frac{\gamma_{SV} - \gamma_{SL}}{\gamma_{LV}} \tag{1}$$

where, γ_{SV}, γ_{SL}, and γ_{LV} indicate the interfacial free energies per unit area of the solid-gas, solid-liquid, and liquid-gas interfaces, respectively. However, this equation is applicable only to a flat surface without roughness. For rough surfaces, Wenzel [11] and Cassie [12] proposed models showing the relationship between roughness and water repellency. The Cassie model considered the air captured on the surface, which is a critical factor to achieve a hydrophobic surface. The models just mentioned show that hydrophobicity is governed by a combination of the low surface energy and surface roughness on the solid materials [13]. A number of researchers [14-18] reported application of the fundamental principle of the "lotus effect" to achieve improved contact

144

angle and surface properties such as self-cleaning that is facilitated by water droplets moving easily on the hydrophobic surface to remove the dust from the surface of a lotus leaf. The authors just mentioned focused their research on low surface energy for increased contact angle and on understanding the relation between surface roughness and contact angle for hydrophobicity.

Other researchers have reported research efforts to achieve hydrophobic surface properties by mimicking hydrophobic surface structures in nature and their theoretical relationship between roughness of the surface and contact angle. For example, the effect of fractal structure [19, 20], multiscale roughness [21, 22], molecular level heterogeneity [23], and gravity [24] on hydrophobicity of surface have been studied to understand the structure of hydrophobic surfaces. Based on these theoretical studies, researchers fabricated artificial hydrophobic rough surfaces by various methods [25, 26]. Shibuichi et al. [27] utilized alkylketene dimer (a kind of wax) to form a fractal surface to fabricate effective roughness. Lau et al. [28] used carbon nanotube forest to structure a rough matrix by mimicking the lotus effect using plasma enhanced chemical vapor deposition (PECVD). In addition, other reported methods were used to fabricate rough surfaces using polymer re-conformation [29], lithography [30], and a multilayer method [31]. Note that when a rough surface is not composed of low-surface-energy materials, the surface is modified with low-surface-energy materials having long alkyl chain or fluorinated functional groups to achieve a larger contact angle [32, 33]. According to the Wenzel model [11, 34] as already mentioned, a surface with a contact angle less than 90º will show decreased contact angle as the roughness increased, indicating that an increase

145

of roughness is effective for achieving hydrophobicity when there are low surface energy materials on the solid surface.

It is worthy to note that there are two key factors for developing superhydrophobic surfaces. The first factor is the low-surface-energy materials with long alkyl chains [6, 7] or fluorine functional groups [4, 8] and the second factor is roughness which has a small ratio of contact area of the solid surface-water droplet compared to the air-water droplet as already discussed. A combination of these two key factors yields superhydrophobic surfaces by coating the low surface energy materials on the prepared rough surface. The rough surface can be directly prepared either by using low surface energy materials to achieve a superhydrophobic surface or by using certain materials coated with low surface energy materials. The approach just described was used in the current research.

Specifically, in the current research, hydrophobic polyhedral oligomeric silsesquioxane (POSS) was utilized to coat the rough surface of tin fluorophosphate glass (Pglass) that was previously prepared by grafting microsize (<75 um) Pglass particles. Note that Pglass has ultra-low glass transition temperature (T_g) and processing temperature compared to that of silicate based glasses [35, 36]. The low T_g is a desired property for a wide range of applications of Pglass such as optoelectronics, bioengineering and protective coatings. In addition, the viscosity of Pglass is known to drop remarkably at relatively low temperature, an attribute of the Pglass that is highly desirable during the Pglass processing. For example, the viscosity of Pglass (10 Pa·s) at 290°C is same as that of honey at room temperature. Further, at 270°C the viscosity of Pglass is less than that of Ketchup (50 Pa·s) at room temperature [35], which is a special

intrinsic property of Pglass that is remarkably different from that of other inorganics like borosilicate glass material. To create a hydrophobic surface of the inorganic Pglass of this study, special organic-inorganic hybrid materials (e.g. POSS) were selected to bridge the gap between Pglass surface and hydrophobic organic functional group. Note that POSS has been widely used for bridging materials between organic and inorganic materials [37-39] due to its special chemical structure of $(RSiO_{1.5})_n$ where R is generally organic functional groups grafted on the 3-dimensional inorganic silicate cage which is either open or closed [40]. Pglass coated by hydrophobic POSS is expected to be useful in a number of applications including optoelectronics and protective coating application. After coating hydrophobic POSS on the surface of Pglass, the coated Pglass can effectively protect the substrate from water, air that can cause surface corrosion, and electrical short on the surface of metals and electronic devices. This facile method used in the current study to increase roughness of the Pglass surface using Pglass particles described here will provide a fundamental basis for a better improvement of surface roughness. In addition, the feasibility of creating a hydrophobic coating with a number of POSS chemicals on the inorganic Pglass was evaluated in detail in this study.

5.2 Experimental methods

5.2.1 Materials and sample preparation

Tin fluorophosphate glass (Pglass) was synthesized with molar composition $50SnF_2+20SnO+30P_2O_5$ using analytical grade reagents (i.e. tin(II) oxide (SnO), tin(II) fluoride (SnF_2) and ammonium dihydrogen phosphate $((NH_4)H_2PO_4))$, which were purchased from Sigma-Aldrich and used as received. The mixture of reagents were melted in a carbon crucible under the conditions reported in the literature [35, 41]. The

molten materials in the furnace were poured onto a metal mold to yield disk-shaped pure

bulk Pglass samples. In addition, some of the pure Pglass samples were annealed at

$200^{o}C$ and $250^{o}C$ up to 30min for characterizations of the surface of bulk Pglass after the

prescribed thermal treatments just mentioned.

Subsequently, a portion of the bulk Pglass samples was ground into particles and

then sifted with a sieve of 75 um mesh size. To introduce a rough surface on the bulk

Pglass, a disk shape of the bulk Pglass was placed on the Pglass powder in a glass bottle

as depicted in Fig. 5.1 and rubbed about 5 times followed by tapping gently to remove the

excess Pglass particles locally attached to the bulk Pglass (i.e., those particles that are not

bonded via hydrogen bonds to the bulk Pglass surface). A torch flame was subsequently

utilized to graft the H-bonded Pglass particles onto the bulk Pglass at elevated

temperature to increase the roughness of the bulk Pglass. The Pglass particles and the

surface of bulk Pglass were fused by the torch flame instantaneously.

Three types of POSS chemicals (i.e. trisilanol phenyl POSS (TSP-POSS),

trisilanol isobutyl POSS (TSB-POSS), trisilanol isooctyl POSS (TSO-POSS)) used in this

research were supplied by Hybrid Plastics Inc. These POSS samples with prescribed

alkyl functional groups were used in this research to increase the hydrophobicity of the

surface of Pglass. The bulk Pglass with the increased surface roughness using the grafted

Pglass particles were coated with each POSS by dip coating. Both the bulk Pglass with

fused (or grafted) Pglass particles and the pure bulk Pglass with smooth surface were

dipped in a POSS/acetone solution in the concentration range of 0.1% - 5.0% w/v

(POSS/acetone), followed by the condensation reaction at $170 \sim 250^{o}C$ for 15 min in the

furnace. A vacuum was applied for 2 hours at $110^{o}C$ to dry and increase the condensation

reaction between P-OH of Pglass and Si-OH of POSS. In addition, three different concentrations (0.5%, 1.0% and 5.0% w/v) of TSP-POSS/acetone solution were utilized for TSP-POSS coating on the smooth surface of bulk Pglass to investigate the change of hydrophobicity of the surface of pure bulk Pglass as a function of the amount of POSS on the Pglass samples with smooth surface.

In another experiment, Isobutyl trimethoxy silane (IBTM-silane) (supplied by Gelest Inc.) was utilized as a control for coating the Pglass surface to compare the hydrophobicity among the surfaces coated by IBTM-silane, TSB-POSS, and TSO-POSS. The Pglass bulk samples were dip-coated in the water/ethanol (1:1) solution including hydrolyzed IBTM-silane. Note that for the silane coupling agent, the silanol formation via hydrolysis is necessary because silanes need to be hydrolyzed to have hydroxyl group for physical and chemical interaction with hydroxyl groups of Pglass. In addition, the 140°C condensation temperature was applied because of the low evaporation temperature (154°C) of IBTM-silane. A molar concentration of 6.32×10^{-3} mol/L (equivalent to a concentration of 0.5% w/v) was used for all the three samples (i.e. samples dip-coated with IBTM-silane, TSB-POSS, and TSO-POSS).

5.2.2 Characterizations

5.2.2.1 Scanning electron microscopy (SEM) – energy dispersive X-ray spectroscopy (EDX)

The surface modified bulk Pglass with Pglass particles and POSS were characterized using SEM and EDX to investigate the morphology and the distribution of elemental composition of the surface. The surface of the samples was coated with silver using Quorum Emitech K550X sputter coater to decrease the electric charge on the

surface of the samples. FEI Quanta 200 scanning electron microscope (SEM) operating

with 20 kV and energy dispersive X-ray spectroscopy (EDX) was carried out on the

samples with Thermo Scientific NSS Spectral Imaging System with NSS 2.2 X-Ray

Microanalysis Software.

5.2.2.2 Contact angle

Water contact angle measurement was carried out via the sessile drop technique

using FTA200 optical contact angle measurement system (FTA Inc.) connected to

Prosilica GC750 camera (Allied Vision Technologies). The obtained data from the

contact angle measurements were analyzed with FTA32 software. A sessile drop of 10 μl

of distilled water was deposited with a syringe on the surface of the pure bulk Pglass and

the surface-modified bulk Pglass with Pglass particles for roughness and POSS molecules

for hydrophobicity in air at room temperature. To reduce the influence of the size

difference of the water drop, the contact angle measurement was started within 5 s after

depositing the water drop on the surface of samples. Contact angles were measured 5

times at one point within 5s and repeated for a minimum of at least 3 different points for

each sample. The average and standard deviation of these data were calculated and

reported in this manuscript.

5.2.2.3 Chemical stability of POSS-modified surface.

Chemical stability tests of the POSS-modified surface of the bulk Pglass with

Pglass particles were performed by observing the relationship between the change in the

time evolution and the water contact angles. The contact angles of the surface-modified

samples with the three types of POSS (i.e. TSB-POSS, TSO-POSS, and TSP-POSS) were

measured and the samples were subsequently immersed into acetone and ethanol solvents

for 10 min and 60 min, respectively, to dissolve the POSS molecules. The immersed

samples were shaken about 10 times in the solvents before being taken out and then dried

in the atmosphere for 5 min and followed by vacuum drying for 1 hr at 110°C to

evaporate the solvent completely.

5.2.2.4 Chemical stability of POSS-modified surface.

XPS spectra were obtained on the rectangular samples (1 cm $\times$ 1 cm $\times$ 2 mm)

using a Kratos AXIS 165 spectrometer equipped with monochromatic Al-Kα X-rays at

12 kV and 12 mA as the excitation radiation in UHV, 5×10^{-9} Torr. A charge neutralizer

was utilized to reduce surface charging on the surface modified Pglass samples with

POSS. The obtained spectra were fit and deconvoluted using a Gaussian curve-fitting

method in Origin software (OriginLab Corp.).

5.3 Results and discussion

5.3.1 Characterization of pure Pglass surface

A glass surface such as calcium phosphate glass generally has hydrophilic

properties with contact angles of about 20 ~ 60° due to the hydrophilic [42-44]. The tin

fluorophosphate glass (Pglass) showed about 80° of contact angle due to the fluorine in

the Pglass composition as shown in Fig. 5.2. The Pglass containing fluorine has a unique

fundamental advantage of less hydrophilic surface compared to that of other typical

hydrophilic glasses [44]. The migration to surface of fluorinated compound with

hydrophobic property is well known [4, 45, 46]. For example, Tan et al. [47] reported

results of phase separation of fluorinated urethane phase to the surface of the bulk

samples due to the low surface energy of fluorinated segments, which is consistent with

the result reported by Chapman et al. [48]. The authors just mentioned reported the

151

alignment of fluorocarbon segments of polymer chains on the surface of polymer materials due to the low surface energy of fluorinated side chains. In addition, Clifford [49] reported that phosphate and fluorine cause phase separation in the glass phase. Further, Vogel [50] reported that replacement of oxygen ion by fluorine ion increased the phase separation in silicate glass.

We found an evidence supporting less hydrophilicity of the surface of bulk Pglass according to the distribution of Pglass compositions. Fig. 5.3 (a-b) showed the composition analysis results by EDX on the surface of bulk Pglass and the Pglass particles from the inside of the pure bulk Pglass, respectively. This figure indicates that there is a significant difference of fluorine composition between the surface of bulk Pglass (16.3 wt.%) and the Pglass particle (9.7 wt.%) from the inside of bulk Pglass. This difference of composition of fluorine element is conjectured to be the result of the movement of the hydrophobic fluorinated Pglass molecules to the surface of bulk Pglass. Fluorine in the glass generally disrupts the glass network and replaces bridging oxygen by non-bridging fluorine, which might produce relatively small fluorinated Pglass molecules, and facilitate the phase separation tendency in Pglass materials [49, 51].

As shown in Fig. 5.4 the XPS spectra of Sn describes the ratio of Sn-F_2O and Sn-O_2F on the surface of Pglass and the fracture surface of Pglass. According to this figure, the ratio of the amount of Sn-F_2O to Sn-O_2F is 1.6% to 98.4% on the fracture surface of the bulk Pglass, indicating that the Sn atoms connected with one fluorine is a major portion of the inside of the bulk Pglass, which is consistent with the result reported by York-Winegar [52]. However, the XPS data obtained from the surface of the bulk Pglass showed 45.5% to 54.5% for Sn-F_2O to Sn-O_2F, indicating that there is more Sn

connected with two fluorine atoms on the surface of bulk Pglass. These results suggest that the Pglass molecules with tin connected with two fluorine atoms were phase-separated and moved to the surface of Pglass during the synthesis and cooling process because the molecules with more non-bridging fluorine are small and hydrophobic as already discussed. Overall, the Pglass showed less hydrophilicity due to the fluorine elements on the surface different from other glasses which have very strong hydrophilic surface. It is plausible to propose that the fluorinated Pglass molecules prepared by replacing bridging oxygen with non-bridging fluorine are phase separated in the samples, causing less hydrophilicity on the surface of the bulk Pglass.

5.3.2 Effect of POSS coating on hydrophobicity of the smooth Pglass surface

As already mentioned, Pglass has a hydrophilic surface because the contact angle is about 80° less than 90°, which means that the surface cannot repel water completely. To improve hydrophobicity of the surface of bulk Pglass, various concentrations of TSP-POSS in acetone were applied for hydrophobic coating on the bulk Pglass using a dip coating method because TSP-POSS is known to exhibit hydrophobic properties as reported in the literature [53, 54]. The obtained contact angle data are listed in Table 1 for the surface of the uncoated Pglass and coated Pglass with various TSP-POSS concentrations. The contact angles gradually increased from 81.6^o to 91.3^o with increasing TSP-POSS concentration from 0% w/v to 5.0% w/v (POSS/acetone). A contact angle of more than 90° was achieved using TSP-POSS coating on the bulk Pglass. To protect metal substrates or electric circuits in electronic devices completely from the water vapor, improved hydrophobic surfaces are desirable. Note that superhydrophobicity can be generally achieved by the combination of low surface energy property of surface

153

material and surface roughness. According to the Wenzel model [11, 34] (modified from Young's equation), for a water droplet in contact with a homogeneous rough surface without air pockets, the contact angle is calculated by this equation (2) below.

$$\cos \theta = R_f \, cos\theta_0 \qquad\qquad (2)$$

where, θ_0 is the contact angle for a smooth surface, θ is a rough surface, and R_f (> 1) is a roughness factor defined as the ratio of the solid-liquid area (A_{SL}) to its projection on a flat plane (A_{FP}), $R_f = A_{SL}/A_{FP}$. Based on the Wenzel model, hydrophobicity of a smooth surface with a contact angle greater than 90° will be improved as the R_f is increased. In contrast, the contact angle for the rough surface will be decreased with increasing R_f when θ_0 is less than 90°. The calculated contact angles from equation (2) are listed in Table 2.

To achieve superhydrophobic surface on the Pglass using hydrophobic POSS, the roughness should be applied on the bulk surface and more hydrophobic POSS will be more effective according to the Wenzel model. The TSB-POSS and TSO-POSS used here are good candidates due to their hydrophobic functional groups (i.e., isobutyl and isooctyl, respectively). Three different POSS (TSP-POSS, TSB-POSS, and TSO-POSS) were coated on the smooth surface of bulk Pglass using the dip coating process already described in the experimental section. As expected, the contact angle of the surface of bulk Pglass coated with TSB-POSS and TSO-POSS are found to be larger than that of the TSP-POSS coated sample. The TSB-POSS and TSO-POSS-coated surfaces showed contact angle of 95.2° ± 0.79° and 95.3° ± 1.29°, respectively, which is larger than 91.6° ±

1.21° obtained from the TSP-POSS as shown in Fig. 5.5. These contact angles (greater than 90°) have potential ability to yield superhydrophobic surface with roughness as predicted by the Wenzel model (equation (2)), (see Table 2).

5.3.3 Effect of applying roughness on the surface of bulk Pglass using Pglass particles

Surface roughness is a critical factor to achieve superhydrophobicity on the surface of materials as reported by many researchers [10, 19, 27, 32, 55, 56]. Cassie et al. [12, 57, 58] reported that air pockets in the surface can effectively enhance the hydrophobicity of a rough surface according to the following equation (3):

$$\cos \theta' = f_1 \cos \theta_1 + f_2 \cos \theta_2 \qquad (3)$$

where, the contact angle θ' of a rough hydrophobic surface with trapped air is the combination of a surface area fraction f_1 with a contact angle θ_1 for water-solid surface and the other surface area fraction f_2 with a contact angle θ_2 for water-air surface, indicating that f_2 represents the area fraction of trapped air. Equation (3) can be modified by assuming the water contact angle for air is 180° [10, 57] as follows:

$$\cos \theta' = f_1 \cos \theta_1 + (1 - f_1) \cos 180^o \qquad (4)$$
$$\cos \theta' = f_1 \cos \theta_1 - (1 - f_1) \qquad (5)$$

where, $f_1 + f_2 = 1$ and the equation can be rewritten as following:

$$\cos \theta' = f_1 \cos \theta_1 - f_2 \qquad\qquad (6)$$

where, θ' is the contact angle of a hydrophobic rough surface composed of two different materials (i.e. solid and air), f_1 and f_2 are the fractions of solid surface and air in contact with water droplet, respectively, and θ_1 is the contact angle for the water-solid surface. The dependence of the contact angle on the fraction of solid surface in contact with water droplet is presented in Fig. 5.6 as calculated from equation (6) (Cassie model). This model implies that even if the contact angle of the smooth surface is less than 90°, it can achieve the superhydrophobicity with a small number of f_1 with air trapped in the surface. The actual contact angle data obtained from the samples modified with the three different POSS samples used in the current study are shown together in Fig. 5.6, which indicates that the roughness (f_1) of the samples is 0.3 ~ 0.4. This result suggests that contact angles can be increased if the roughness of the samples has a f_1 value smaller than 0.3. Overall, the contact angle would significantly increase with decreasing f_1, indicating that the decrease of contact area between solid and water droplet on the hydrophobic rough surface with air trapped would increase the contact angle.

Note that hydrophobicity is the combination of hydrophobic materials and rough surface with air pockets in the surface as reported in the literature. TSB-POSS and TSO-POSS were applied in this study to achieve relatively smaller surface energy due to the alkyl chains on the POSS cage with the roughness of the surface of bulk Pglass. As already described in Fig. 5.1 in the experimental section, the micro-sized (<75 um) Pglass powder was applied on the bulk Pglass and fused (or grafted) on the bulk surface using a torch flame. The instantaneously melted Pglass particles and the bulk Pglass surface were

fused together and connected chemically as shown in Fig. 5.7. The micro-sized

protrusions formed by Pglass particles enhanced the roughness of the surface of bulk

Pglass for hydrophobicity. Fig. 5.8 shows effects of POSS type and concentration on the

contact angles of the samples with the rough surfaces. The obtained maximum contact

angles of the POSS-coated samples were obtained at a concentration of 0.5% w/v

(POSS/acetone), showing 125.7$^{\text{o}}$, 130.7$^{\text{o}}$, and 138.2$^{\text{o}}$ of contact angles prepared by using

the TSP-POSS, TSB-POSS, and TSO-POSS, respectively. This result shows a significant

improvement in the contact angle of the samples with rough surfaces compared to that of

the samples with the smooth surface shown in Fig. 5.5. There is a significant change of

the contact angle due to the roughness increase with trapped air in the surface of Pglass as

expected. These results confirm that the hydrophobic property of the surface is the result

of a combination of the surface energy of materials and the roughness with trapped air on

the surface.

Another result illustrating the critical effect of roughness for hydrophobicity is

shown in Fig. 5.9, indicating that higher concentration of POSS on the surface of bulk

Pglass decreased the hydrophobicity significantly reported earlier in Fig. 5.8. For

example, the concentration of 0.5% w/v TSP-POSS achieved 125.7$^{\text{o}}$ while 5.0% w/v

TSP-POSS yielded a contact angle of only 96.4$^{\text{o}}$ contact angle. The roughness of the bulk

Pglass surface with 0.5% w/v TSP-POSS shown in Fig. 5.9 (a) was greater than that of

the bulk Pglass surface with 5.0% w/v TSP-POSS as shown in Fig. 5.9 (c), which

indicates that the relatively thick POSS layer covered a small size of protrusion and

reduced the roughness of the surface, resulting in a decrease of the contact angle. The

EDX data (Fig. 5.9 (b)) with 0.5% w/v TSP-POSS showed that the compositions of

elements at positions #1 and #2 are quite similar to each other, indicating a homogeneous

coating. However, in Fig. 5.9 (d) with 5.0% w/v TSP-POSS the compositions of carbon

and silicon elements from POSS molecules at position #1 (i.e. C=23.2 %, Si=1.3 %) are

larger than that of position #2 (i.e. C=18.4 %, Si=0.7 %), indicating that more POSS was

coated on the surface of the bulk Pglass than on the surface of the protrusion. This result

is another evidence of the thick POSS coating on the bulk Pglass surface, causing the

decrease of the roughness of the surface of samples and the associated reduced contact

angles.

Fig. 5.10 (a) shows the morphology of the POSS-modified surface of bulk Pglass

with increase of the roughness using Pglass particles, which is remarkably similar to the

morphology of the surface of the lotus leaf [6, 15]. This obtained nature-inspired surface

effectively enhanced hydrophobicity of the surface of bulk Pglass. Furthermore, if the f_1

value of solid-water contact ratio can be reduced with regular and sharp protrusion of

Pglass particles on the bulk Pglass surface, superhydrophobicity with more than 150° of

contact angle could be achieved in this system using hydrophobic POSS. The illustrative

schematic description in Fig. 5.11 shows the microstructure of the surface of bulk Pglass

with protrusion prepared using Pglass particles as already described. This rough surface

shown was coated by TSO-POSS and has trapped air. The water droplet could not contact

directly with the surface of bulk Pglass due to the hydrophobic isooctyl chains on POSS

cages on the protrusion of Pglass particles and the trapped air on the surface.

5.3.4 Chemical stabilization of POSS on the bulk Pglass surface

Chemical stability tests were conducted using acetone and ethanol to investigate

the stability of the coated POSS on the surface of bulk Pglass. Acetone was used as a

solvent in TSP-POSS, TSB-POSS, and TSO-POSS solutions due to acetone's outstanding ability to dissolve POSS. In addition, the surface of bulk Pglass was completely wetted by acetone because acetone has both polar and nonpolar properties. The contact angle of the hydrophobic bulk Pglass samples with roughness and hydrophobic POSS was measured after chemical stability tests using the acetone and ethanol for 10 min and 60 min. Before taking samples from each solvent after the test time, the samples were shaken vigorously. The contact angles measured in the chemical stability test using acetone and ethanol solvents from 0 min to 60 min are listed in Table 3. Note that the contact angles of samples in the stability test in the acetone and ethanol did not change significantly, indicating that POSS molecules coated on the Pglass are stable due to the chemical bonds between the hydroxyl group of Pglass and POSS as expected, and as previously reported by other researchers [35, 59, 60]. Chemical reaction between Si-OH of 3-((methacryloyloxy) propyl) trimethoxysilane (MEMO) and P-OH of 2-(methacyloxyloxy)ethyl phosphate (EGMP) resulting in formation of P-O-Si bonds by thermal curing at 120°C was reported by Kannan [59]. In addition, Styskalik et al. reported that P-O-Si bonds are formed by the condensation of Si-OH and P-OH at 150°C, which is a lower temperature than 170°C ~ 250°C applied for the condensation reaction between POSS and Pglass in our experiments.

The XPS O 1s spectra was conducted to estimate the ratio of the non-bridging oxygen (NBO) to bridging oxygen (BO) on the surface of pure Pglass and POSS-coated Pglass. Generally, the BO is related to P-O-P linkage and the NBO is associated with terminal oxygen such as P─O¯ including P-O-Sn in the Pglass as discussed by Brow et al. [61]. The obtained XPS O 1s spectra was deconvoluted to show the peaks that

159

represent BO and NBO as shown in Fig. 5.12. The obtained data show that 64.9% of BO and 35.1% of NBO are observed on the surface of pure Pglass. After TSP-POSS coating on the bulk Pglass, the BO was increased to 70.0% and NBO was decreased to 30%. This finding is attributed to the formation of new chemical bonds of P-O-Si increasing BO and decreasing NBO, which is consistent with the result of chemical stability of POSS on the surface of Pglass. In addition, a portion of BO signal from the POSS-coated Pglass sample might be due to the BO in Si-O-Si of POSS as reported in previous research [35]. Interestingly, the ratio of BO to NBO was 64.9% : 35.1% in the O 1s spectra of the pure bulk Pglass surface in our results which is different from the results of 5%:95% reported by York-Winegar et al. [52] and 5.1%:94.9% reported by Kim et al. [35] on the fractured surface of pure bulk Pglass. As already discussed, we believe that phase separation occurred during the melting and cooling process of Pglass and the relatively hydrophobic molecules with BO were phase-separated to the surface of the pure bulk Pglass.

5.3.5 Umbrella effect of POSS for hydrophobicity

The water repellent property of POSS-coated Pglass was increased due to the hydrophobic functional groups (i.e. phenyl, isobutyl, and isooctyl) on the POSS cage. To further investigate the chemical structure effect of the coating materials for hydrophobicity, a fixed molar concentration of IBTM-silane and TSB-POSS was applied on the bulk Pglass, and then the contact angle was measured. Note that TSB-POSS and IBTM-silane both have isobutyl functional groups. Fig. 5.13 shows an increase of contact angle that is consistent with the structural effect of hydrophobic molecules on the bulk Pglass. In fact, the contact angle of a water droplet on TSB-POSS-coated sample (131.0°) showed higher than that of the IBTM-silane coated sample (126.3°), indicating that there

is a structural effect of functional groups for hydrophobicity. The bulky POSS molecules can cover a relatively wide area of the hydrophilic substrate and have higher contact points with water droplet in the contact angle measurement in agreement with the so-called "umbrella effect" reported in the literature [62-66]. As expected, the longer alkyl functional groups (isooctyl, 138.2°) apparently produced a larger contact angle than that of the shorter alkyl functional group (isobutyl, 131.0°) due to the higher contact point between the relatively longer isooctyl functional groups and water droplets (see Fig. 5.13).

5.4 Conclusions

The results of this study showed that it is possible to significantly improve hydrophobicity of Pglass surface using various POSS chemicals with hydrophobic functional groups such as phenyl, isobutyl, and isooctyl on the POSS cage and Pglass particles for increase of roughness. Interestingly, the surface of pure bulk Pglass showed a less hydrophilic property compared to that of typical glasses (e.g. borosilicate glasses) due to the fluorine in the Pglass molecules. The combination of the increased surface roughness using Pglass particles and low surface energy from the hydrophobic POSS produced significantly improved hydrophobicity close to superhydrophobicity on the surface of bulk Pglass as predicted by the Cassie model, which considers trapped air in the surface of substrate.

The chemical stability test using acetone and ethanol showed that the POSS samples used here were strongly chemically bonded to the surface of Pglass. Acetone used as a solvent in POSS/acetone solution for dip coating of Pglass did not change the hydrophobicity of the Pglass surface, indicating that POSS and Pglass were chemically

bonded via a condensation reaction between Si-OH of POSS and P-OH of Pglass as supported by the observed increased ratio of BO to NBO due to the obtained Si-O-P bond. It was observed that bulky POSS molecules with low surface energy functional groups and longer hydrophobic alkyl chains increased the contact angle because they can cover the hydrophilic surface effectively. This study showed that nature-inspired Pglass surface morphology, resembling lotus leaf, was successfully prepared by using Pglass particles for roughness and hydrophobic POSS for low surface energy. This result is theoretically consistent with that predicted by the Cassie model, which considers air trapped in the surface. Hydrophobically coated Pglass with ultra-low T_g and low processing temperature has the potential to be efficiently used as a sealant and a coating material to protect metal substrates and electronic devices from corrosion and electric short circuits due to water vapor and liquid water, indicating that the materials of this study might be useful for a wide range of industrial applications such as electronic device, biomedical applications, and optoelectronics.

Acknowledgements

5.5 Reference

1.   Yu, M., et al., Positive effect of polymeric silane-based water repellent agents on the durability of superhydrophobic fabrics. Applied Surface Science, 2018. 450: p.492-501.

2.   Tian, P. and Z. Guo, Bioinspired silica-based superhydrophobic materials. Applied Surface Science, 2017. 426: p. 1-18.

3.   Ivanova, N. and A. Zaretskaya, Simple treatment of cotton textile to impart high water repellent properties. Applied Surface Science, 2010. 257(5): p. 1800-1803.

4.   Tuteja, A., et al., Designing superoleophobic surfaces. Science, 2007. 318(5856): p. 1618-1622.

5.   Huo, L., et al., Fabrication and tribological properties of self-assembled monolayer of n-alkyltrimethoxysilane on silicon: Effect of SAM alkyl chain length. Applied Surface Science, 2017. 396: p. 865-869.

6.   Zhang, X., et al., Superhydrophobic surfaces: from structural control to functional application. Journal of Materials Chemistry, 2008. 18(6): p. 621-633.

7.   Gautam, K.S. and A. Dhinojwala, Molecular structure of hydrophobic alkyl side chains at comb polymer-air interface. Macromolecules, 2001. 34(5): p. 1137-1139.

8.   Huang, M. and J. Yang, Long-term performance of 1H, 1H′, 2H, 2H′-perfluorooctyl triethoxysilane (POTS) microcapsule-based self-healing anticorrosive coatings. Journal of Intelligent Material Systems and Structures, 2014. 25(1): p. 98-106.

9.   Mabry, J.M., et al., Fluorinated Polyhedral Oligomeric Silsesquioxanes (F-POSS). Angewandte Chemie, 2008. 120(22): p. 4205-4208.

10.   Yoshimitsu, Z., et al., Effects of surface structure on the hydrophobicity and sliding behavior of water droplets. Langmuir, 2002. 18(15): p. 5818-5822.

11.   Wenzel, R.N., Resistance of solid surfaces to wetting by water. Industrial & Engineering Chemistry, 1936. 28(8): p. 988-994.

12.   Cassie, A. and S. Baxter, Wettability of porous surfaces. Transactions of the Faraday society, 1944. 40: p. 546-551.

13.   Murase, H., et al., Interactions between heterogeneous surfaces of polymers and water. Journal of Applied Polymer Science, 1994. 54(13): p. 2051-2062.

14.   Neinhuis, C. and W. Barthlott, Characterization and distribution of water-repellent, self-cleaning plant surfaces. Annals of botany, 1997. 79(6): p. 667-677.

15.   Barthlott, W. and C. Neinhuis, Purity of the sacred lotus, or escape from contamination in biological surfaces. Planta, 1997. 202(1): p. 1-8.

16.   Liu, H., X. Wang, and H. Ji, Fabrication of lotus-leaf-like superhydrophobic surfaces via Ni-based nano-composite electro-brush plating. Applied Surface Science, 2014. 288: p. 341-348.

17.   Yuan, Z., H. Chen, and J. Zhang, Facile method to prepare lotus-leaf-like super-hydrophobic poly(vinyl chloride) film. Applied Surface Science, 2008. 254(6): p. 1593-1598.

18.   Wei, Z.J., et al., Preparation of lotus-like superhydrophobic fluoropolymer films. Applied Surface Science, 2010. 256(12): p. 3972-3976.

19.   Onda, T., et al., Super-water-repellent fractal surfaces. Langmuir, 1996. 12(9): p. 2125-2127.

20.   Hazlett, R.D., Fractal applications: wettability and contact angle. Journal of Colloid and Interface Science, 1990. 137(2): p. 527-533.

21.   Bittoun, E. and A. Marmur, The role of multiscale roughness in the lotus effect: is it essential for super-hydrophobicity? Langmuir, 2012. 28(39): p. 13933-13942.

22.   Karumuri, A.K., L. He, and S.M. Mukhopadhyay, Tuning the surface wettability of carbon nanotube carpets in multiscale hierarchical solids. Applied Surface Science, 2015. 327: p. 122-130.

23.   Drelich, J., Static contact angles for liquids at heterogeneous rigid solid surfaces. Polish Journal of Chemistry, 1997. 71(5): p. 525-549.

24.   Swain, P.S. and R. Lipowsky, Contact angles on heterogeneous surfaces: A new look at Cassie's and Wenzel's laws. Langmuir, 1998. 14(23): p. 6772-6780.

25.   Abdulhussein, A.T., et al., Current trend in fabrication of complex morphologically tunable superhydrophobic nano scale surfaces. Applied Surface Science, 2016. 384: p. 311-332.

26.   Yan, Y.Y., N. Gao, and W. Barthlott, Mimicking natural superhydrophobic surfaces and grasping the wetting process: A review on recent progress in preparing superhydrophobic surfaces. Advances in colloid and interface science, 2011. 169(2): p. 80-105.

27.   Shibuichi, S., et al., Super water-repellent surfaces resulting from fractal structure. The Journal of Physical Chemistry, 1996. 100(50): p. 19512-19517.

28.	Lau, K.K., et al., Superhydrophobic carbon nanotube forests. Nano letters, 2003. 3(12): p. 1701-1705.

29.	Erbil, H.Y., et al., Transformation of a simple plastic into a superhydrophobic surface. Science, 2003. 299(5611): p. 1377-1380.

30.	Shiu, J.-Y., et al., Fabrication of tunable superhydrophobic surfaces by nanosphere lithography. Chemistry of materials, 2004. 16(4): p. 561-564.

31.	Zhang, X., et al., Polyelectrolyte multilayer as matrix for electrochemical deposition of gold clusters: toward super-hydrophobic surface. Journal of the American Chemical Society, 2004. 126(10): p. 3064-3065.

32.	Guo, Z., et al., Stable biomimetic super-hydrophobic engineering materials. Journal of the American Chemical Society, 2005. 127(45): p. 15670-15671.

33.	Shi, F., et al., To adjust wetting properties of organic surface by in situ photoreaction of aromatic azide. Langmuir, 2007. 23(3): p. 1253-1257.

34.	Jung, Y.C. and B. Bhushan, Contact angle, adhesion and friction properties of micro-and nanopatterned polymers for superhydrophobicity. Nanotechnology, 2006. 17(19): p. 4970.

35.	Kim, K., et al., Synthesis and characterization of novel phosphate glass matrix nanocomposites containing polyhedral oligomeric silsesquioxane with improved properties. Journal of Non-Crystalline Solids, 2017. 463: p. 189-202.

36.	Kim, K., I. Belyamani, and J.U. Otaigbe, Novel porous bioabsorbable phosphate glass matrix nanocomposites incorporating trisilanolphenyl polyhedral oligomeric silsesquioxane prepared by extrusion. Materials Letters, 2018. 210: p. 186-190.

37.   Dhanapal, D., A.K. Srinivasan, and N. Ramalingam, Role of POSS as Coupling Agent for DGEBA/GF Reinforced Nanocomposites. Silicon, 2018. 10(2): p. 537-546.

38.   Zhao, F. and Y. Huang, Grafting of polyhedral oligomeric silsesquioxanes on a carbon fiber surface: novel coupling agents for fiber/polymer matrix composites. Journal of Materials Chemistry, 2011. 21(11): p. 3695-3703.

39.   Wamke, A., et al., Hydrophobic ultrathin films formed by fluorofunctional cage silsesquioxanes. Applied Surface Science, 2018. 443: p. 280-290.

40.   Misra, R., et al., POSS-nylon 6 nanocomposites: Influence of POSS structure on surface and bulk properties. Journal of Polymer Science Part B: Polymer Physics, 2009. 47(11): p. 1088-1102.

41.   Adalja, S.B., J.U. Otaigbe, and J. Thalacker, Glass-polymer melt hybrids. I: Viscoelastic properties of novel affordable organic-inorganic polymer hybrids. Polymer Engineering & Science, 2001. 41(6): p. 1055-1067.

42.   Vo, D.-T. and C.-K. Lee, Cells capture and antimicrobial effect of hydrophobically modified chitosan coating on Escherichia coli. Carbohydrate polymers, 2017. 164: p. 109-117.

43.   Navarro, M., et al., Surface characterization and cell response of a PLA/CaP glass biodegradable composite material. Journal of Biomedical Materials Research Part A, 2008. 85(2): p. 477-486.

44.   Duta, L., et al., Thickness influence on in vitro biocompatibility of titanium nitride thin films synthesized by pulsed laser deposition. Materials, 2016. 9(1): p. 38.

45.   Biffinger, J.C., H.W. Kim, and S.G. DiMagno, The polar hydrophobicity of fluorinated compounds. ChemBioChem, 2004. 5(5): p. 622-627.

46.   Ganesh, V.A., et al., Superhydrophobic fluorinated POSS–PVDF-HFP nanocomposite coating on glass by electrospinning. Journal of Materials Chemistry, 2012. 22(35): p. 18479-18485.

47.   Tan, H., et al., The effect of fluorinated side chain attached on hard segment on the phase separation and surface topography of polyurethanes. Polymer, 2004. 45(5): p. 1647-1657.

48.   Chapman, T.M., et al., Determination of low critical surface energies of novel fluorinated poly (amide urethane) block copolymers. 1. Fluorinated side chains. Macromolecules, 1995. 28(1): p. 331-335.

49.   Clifford, A. and R. Hill, Apatite-mullite glass-ceramics. Journal of Non-Crystalline Solids, 1996. 196: p. 346-351.

50.   Vogel, W., Phase separation in glass. Journal of Non-Crystalline Solids, 1977. 25(1-3): p. 170-214.

51.   Rafferty, A., et al., Influence of Fluorine Content in Apatite–Mullite Glass-Ceramics. Journal of the American Ceramic Society, 2000. 83(11): p. 2833-2838.

52.   York-Winegar, J., et al., Structure of SnF2-SnO-P2O5 Glasses. Physics Procedia, 2013. 44: p. 159-165.

53.   Nowacka, M., D. Ambrożewicz, and T. Jesionowski, TiO 2-SiO 2/Ph-POSS functional hybrids: preparation and characterisation. Journal of Nanomaterials, 2013. 2013: p. 19.

54.   Fina, A., O. Monticelli, and G. Camino, POSS-based hybrids by melt/reactive blending. Journal of Materials Chemistry, 2010. 20(42): p. 9297-9305.

55.   Feng, L., et al., Super-hydrophobic surface of aligned polyacrylonitrile nanofibers. Angewandte Chemie, 2002. 114(7): p. 1269-1271.

56.   Shibuichi, S., et al., Super water-and oil-repellent surfaces resulting from fractal structure. Journal of Colloid and Interface Science, 1998. 208(1): p. 287-294.

57.   Cassie, A., Contact angles. Discussions of the Faraday society, 1948. 3: p. 11-16.

58.   Li, S., et al., Super-hydrophobicity of large-area honeycomb-like aligned carbon nanotubes. The journal of physical chemistry B, 2002. 106(36): p. 9274-9276.

59.   Kannan, A.G., N.R. Choudhury, and N.K. Dutta, Synthesis and characterization of methacrylate phospho-silicate hybrid for thin film applications. Polymer, 2007. 48(24): p. 7078-7086.

60.   Styskalik, A., et al., Synthesis of homogeneous silicophosphate xerogels by non-hydrolytic condensation reactions. Microporous and Mesoporous Materials, 2014. 197: p. 204-212.

61.   Brow, R.K., R.J. Kirkpatrick, and G.L. Turner, Nature of alumina in phosphate glass: II, structure of sodium alurninophosphate glass. Journal of the American Ceramic Society, 1993. 76(4): p. 919-928.

62.   Hozumi, A., C. Urata, and J.B. Masheder, Organic/inorganic transparent hybrid films and a process for producing the same. 2016, Google Patents.

63.   Thakur, N., et al., Thermoresponsive Cellulose Acetate–Poly (N-isopropylacrylamide) Core–Shell Fibers for Controlled Capture and Release of Moisture. ACS applied materials & interfaces, 2017. 9(34): p. 29224-29233.

64.   Çamurlu, H.E., et al., Modification of hexagonal boron nitride nanoparticles with fluorosilane. Ceramics International, 2016. 42(5): p. 6312-6318.

65.   Reinerth, B. Poss for Surface Modification and Corrosion Prevention. in Nanostructured Chemicals Workshop, Huntington Beach, California. 2000.

66.   Maji, K. and D. Haldar, POSS-Appended Diphenylalanine: Self-Cleaning, Pollution-Protective, and Fire-Retardant Hybrid Molecular Material. ACS Omega, 2017. 2(5): p. 1938-1946.
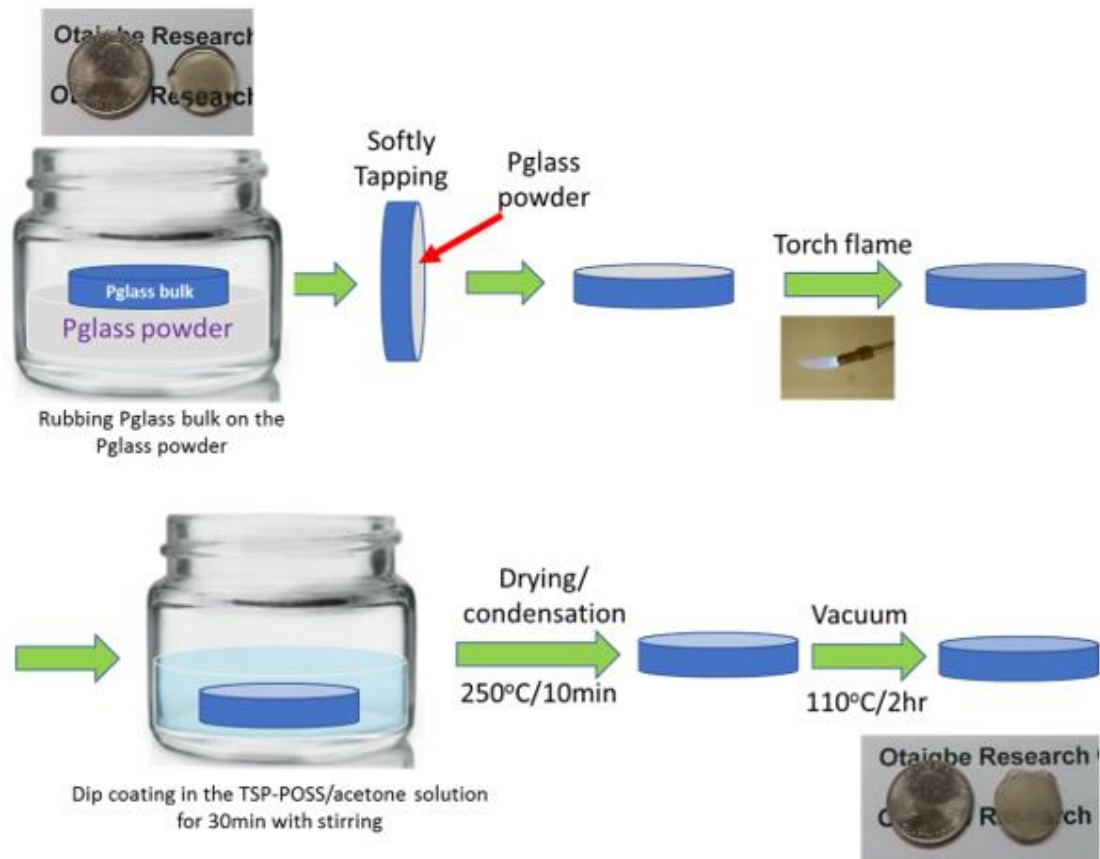
Figure 5.1 Schematic description of the surface modification of bulk Pglass with Pglass particles and POSS.
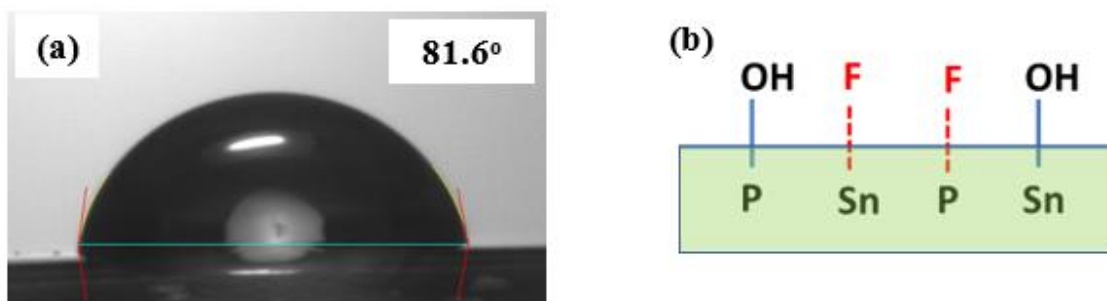
Figure 5.2 (a) Contact angle on the surface of pure bulk Pglass and (b) elemental compositions of surface of Pglass.

Element	Surface of bulk Pglass Wt.%
O	26.2
F	16.3
P	11.0
Sn	46.5

Element	Pglass Particle Wt.%
O	21.0
F	9.7
P	11.8
Sn	57.6
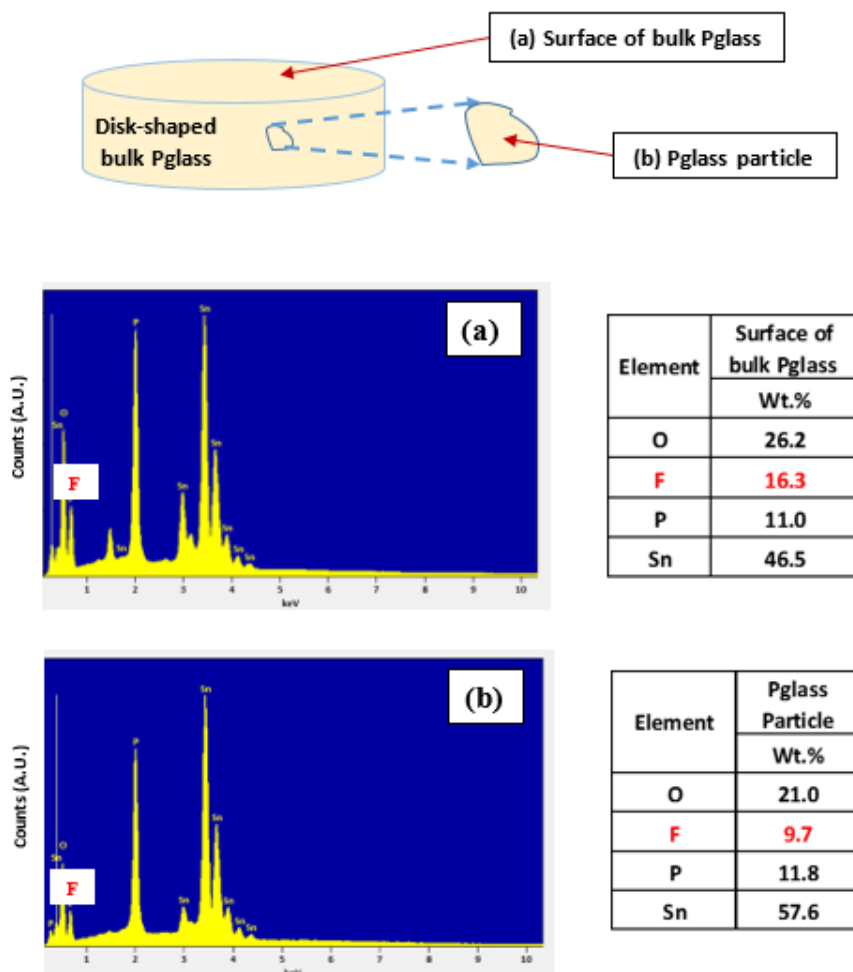
Figure 5.3 EDX results of the surface of (a) the pure bulk Pglass and (b) the Pglass particle as described in the text.

172
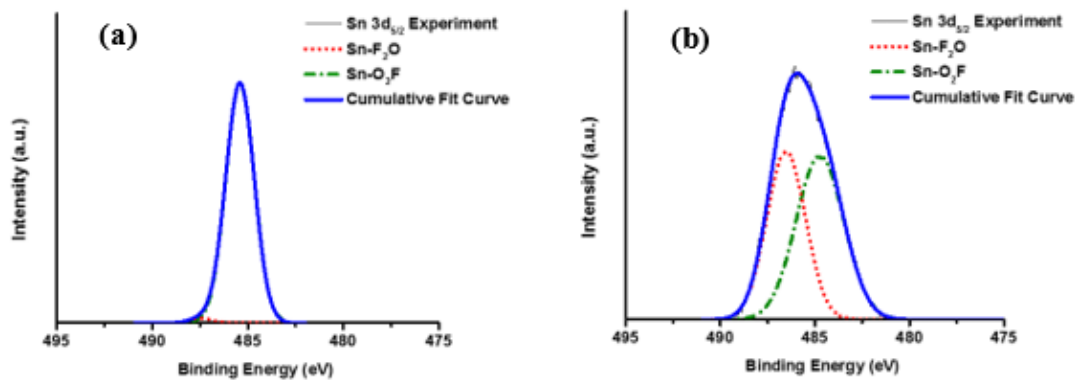
Figure 5.4 XPS spectra of (a) the fractured surface of bulk Pglass and (b) the surface of bulk Pglass.
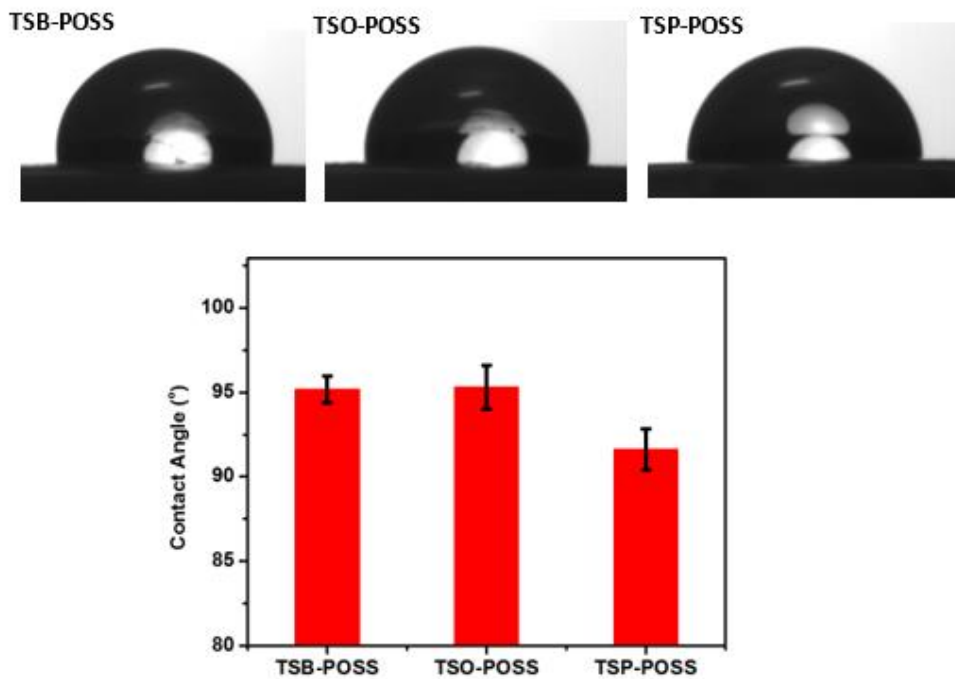
Figure 5.5 Contact angle of the smooth surface of bulk Pglass with TSB-POSS, TSO-POSS, and TSP-POSS coating.
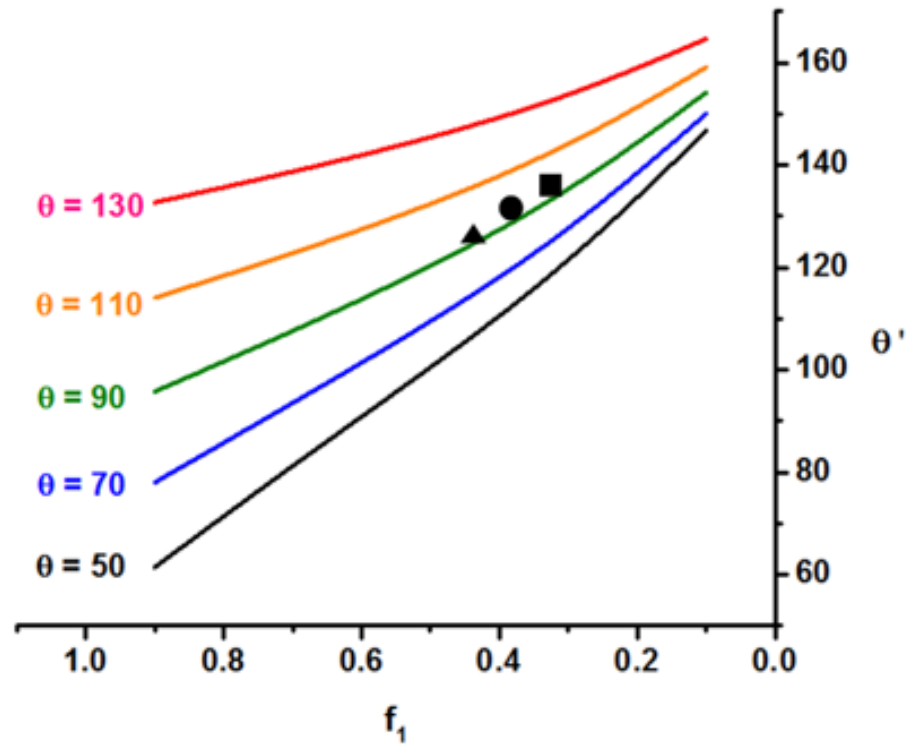
Figure 5.6 Contact angle (θ') for hydrophobic rough surface with trapped air as a function of the wetted solid surface area fraction (f_1) for various contact angles with respect to the Cassie model. (Superposition of actual contact angle data obtained from samples prepared by the surface coating with ▲: TSP-POSS, ●: TSB-POSS, ■: TSO-POSS).
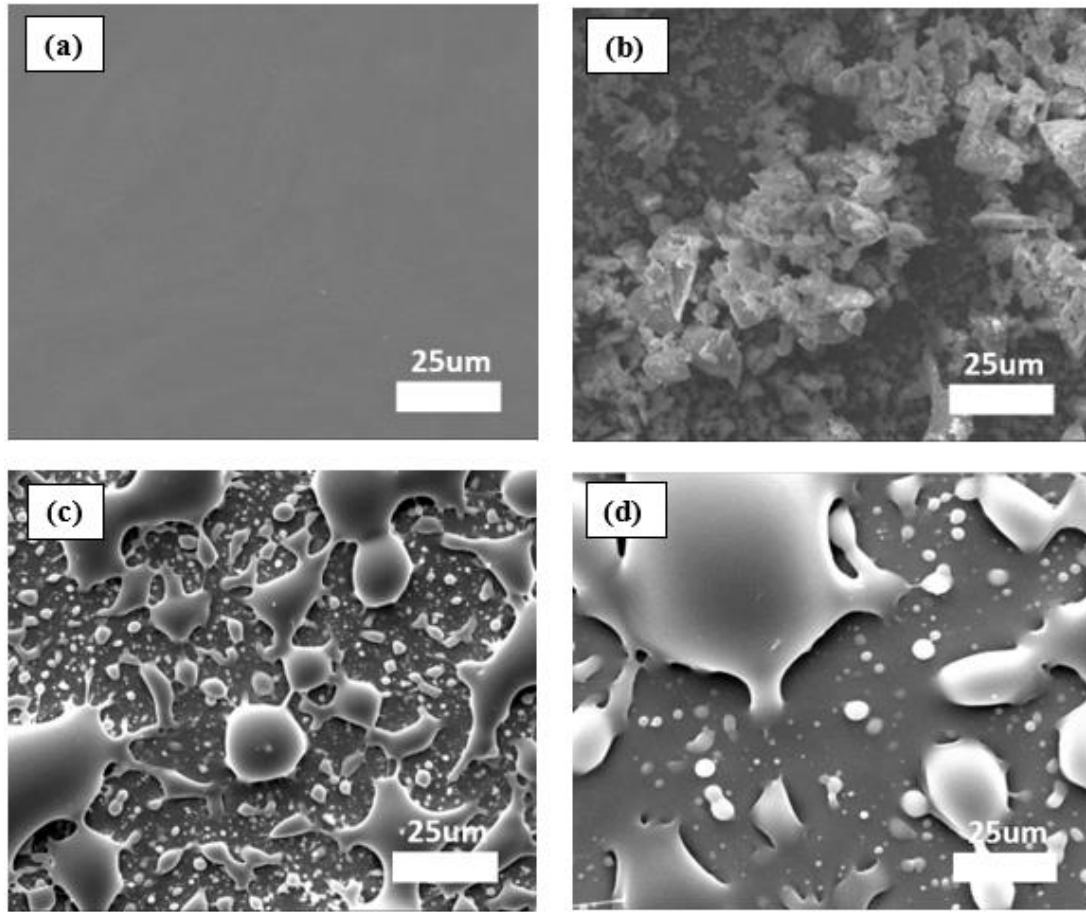
Figure 5.7 SEM images of the surface of (a) the pure bulk Pglass, (b) the bulk Pglass with particles, (c) the bulk Pglass with distribution of protrusions prepared by Pglass particles, and (d) bulk Pglass fused with Pglass particles as described in the text.
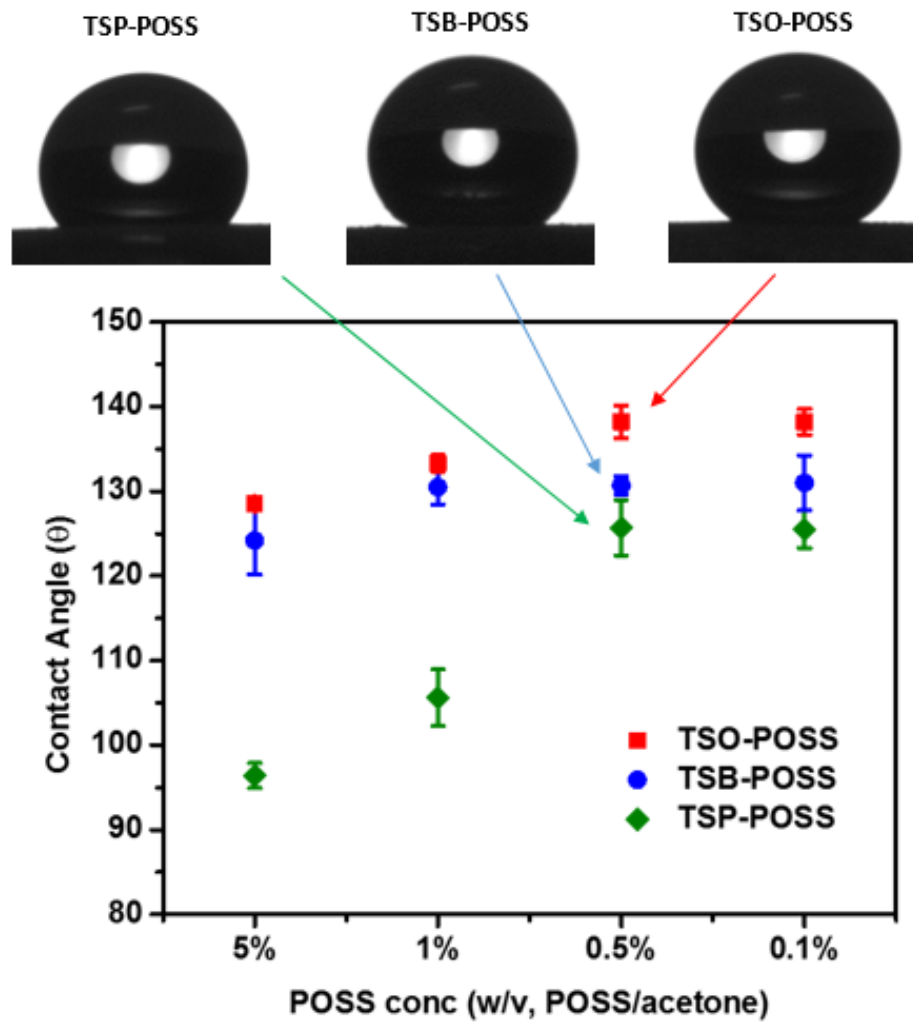
Figure 5.8 Effect of POSS type and concentration on contact angle.

Element	#p1 (Wt.%)	#p2 (Wt.%)
C	12.6	14.6
O	25.8	26.9
F	4.7	5.4
Si	0.4	0.3
P	11.0	10.2
Sn	45.6	42.7

Element	#p1 (Wt.%)	#p2 (Wt.%)
C	23.2	18.4
O	18.6	19.6
F	2.5	4.2
Si	1.3	0.7
P	9.2	10.2
Sn	45.2	46.9
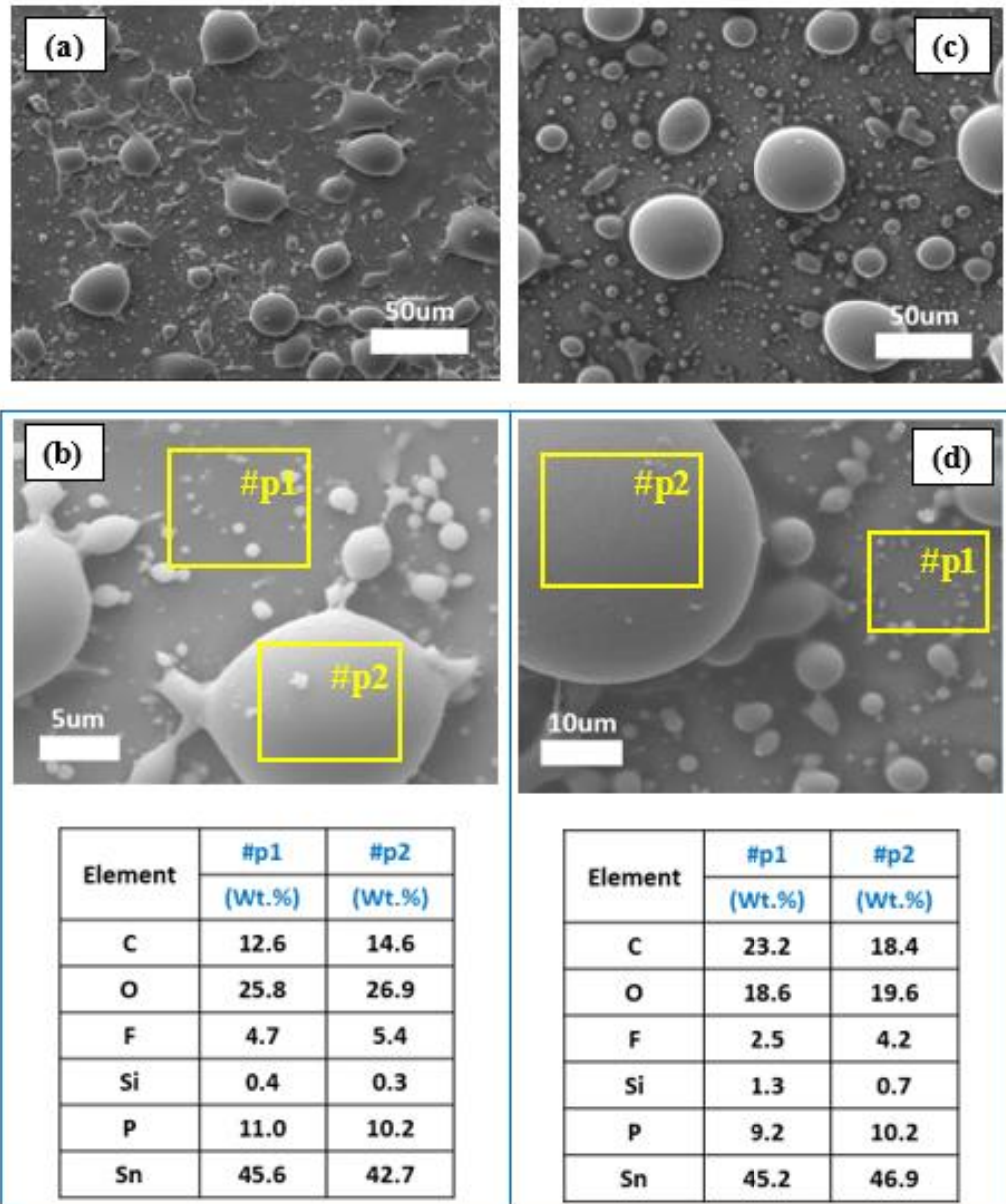
Figure 5.9 (a) SEM image and (b) EDX result on the surface of bulk Pglass coated with 0.5% w/v TSP-POSS/acetone and (c) SEM image and (d) EDX result on the surface of bulk Pglass coated with 5.0% w/v TSP-POSS/acetone.

177
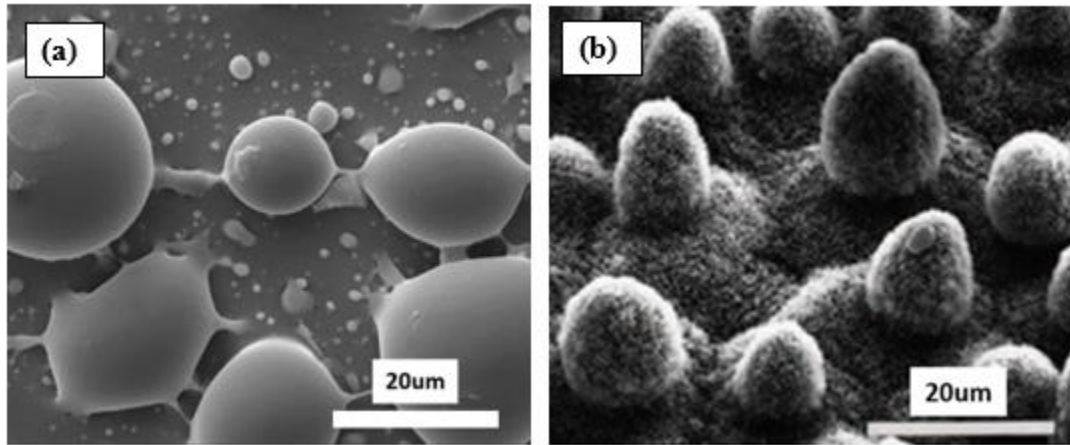
Figure 5.10 SEM image of (a) nature inspired hydrophobic Pglass surface modified by Pglass particles for roughness and POSS coating for low surface energy, and (b) the surface structure of lotus leaf having super-hydrophobicity. (Fig. 5.10(b) is reproduced with permission from ref. 15. Copyright (1997), Springer Nature).
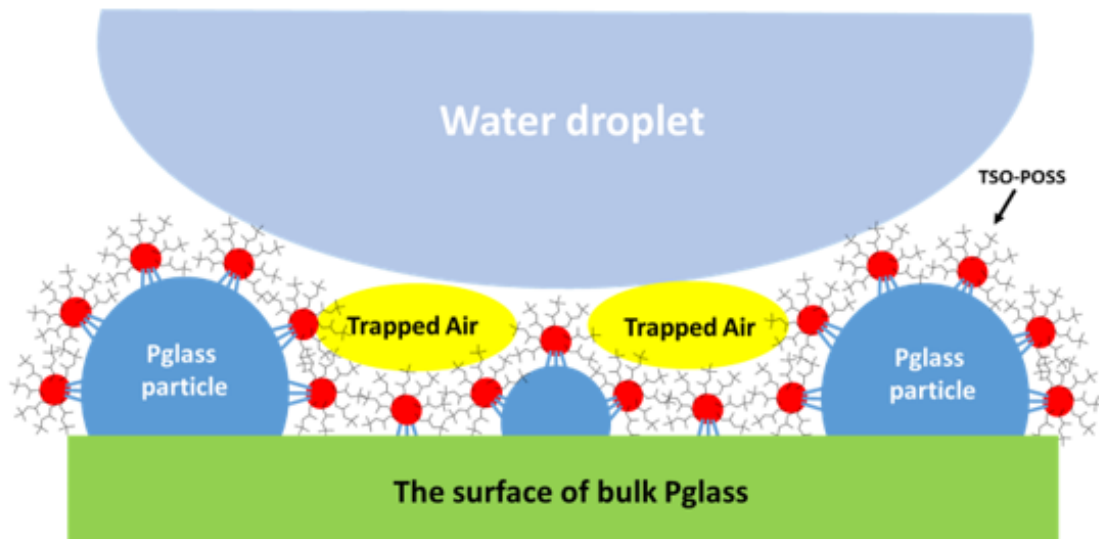
Figure 5.11 Schematic description of microstructure of the surface of bulk Pglass with protrusion, TSO-POSS coating, and trapped air for enhanced hydrophobicity.
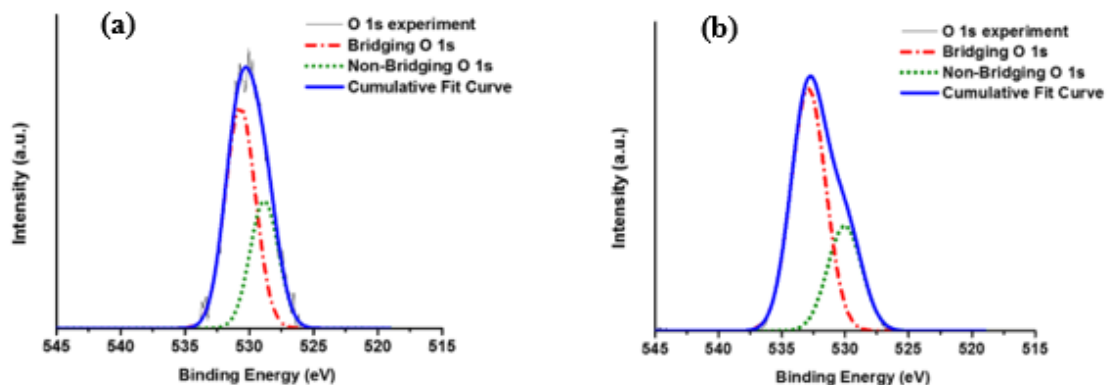
Figure 5.12 The XPS O 1s spectra of (a) the surface of pure bulk Pglass and (b) the TSP-POSS coated surface of bulk Pglass.
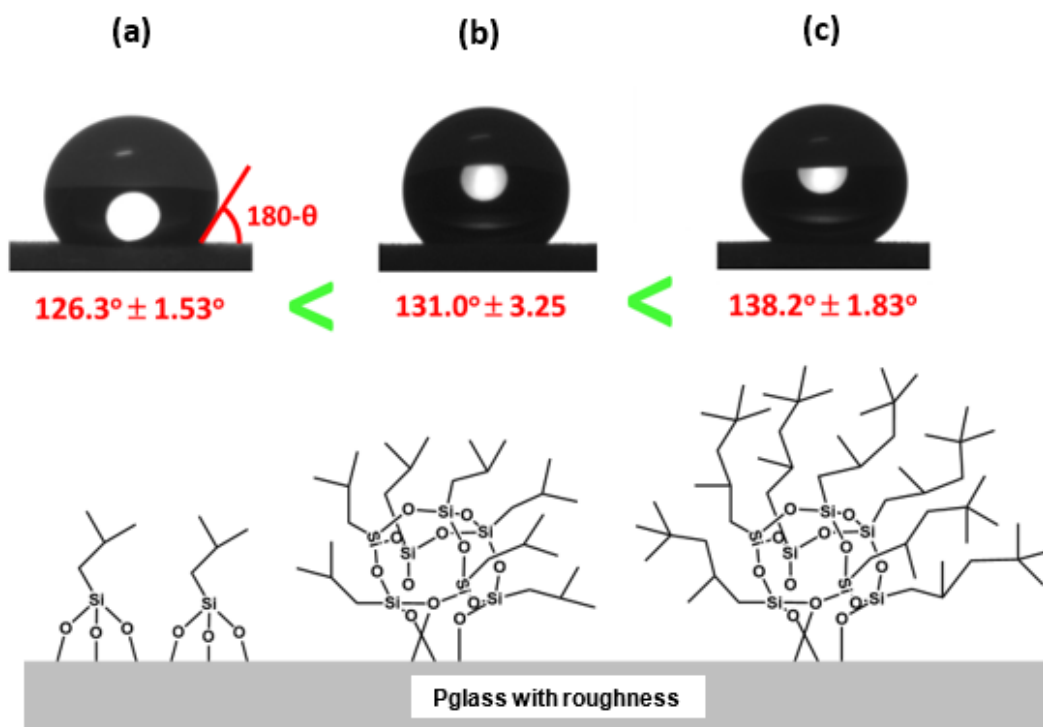
Figure 5.13 The structural effect on the contact angle of bulk Pglass as a function of the coating materials of (a) IBTM-silane, (b) TSB-POSS, and (c) TSO-POSS.

Table 5.1

Contact angle data on samples after POSS coating on the smooth surface of bulk Pglass.

Sample (TSP-POSS/acetone)	Contact angle (°)	Std
Pure TFP	81.6	2.64
0.1% w/v	84.8	2.31
0.5% w/v	91.6	1.21
1.0% w/v	89.4	1.93
5.0% w/v	91.3	0.34

Table 5.2

Calculated contact angle for rough surface (θ) as a function of the roughness factor (R_f) for various arbitrary contact angles for smooth surface (θ_0) from the Wenzel model.

	R_f (1)	R_f (1.2)	R_f (1.5)	R_f (1.7)	R_f (2.0)
Initial Angle (θ_0)	Angle of rough surface (θ)				
50	50	39.5	15.4	< 0	< 0
70	70	65.8	59.1	54.4	46.8
90	90	90.0	90.0	90	90
110	110	114.2	120.9	125.6	133.2
130	130	140.5	164.6	> 180	> 180

Table 5.3

Chemical stability of coated-POSS on the surface of bulk Pglass.

Time	TSP-POSS, 0.5% w/v		TSB-POSS, 0.5% w/v		TSO-POSS, 0.5% w/v	
	Acetone	Ethanol	Acetone	Ethanol	Acetone	Ethanol
0 min	125.3º ± 2.76º	124.8º ± 3.84º	129.1º ± 1.03º	128.0º ± 2.70º	135.4º ± 1.51º	134.4º ± 2.00º
10 min	122.4º ± 4.86º	124.1º ± 1.77º	128.7º ± 1.20º	127.4º ± 1.89º	135.1º ± 1.69º	134.8º ± 2.39º
60 min	125.1º ± 5.07º	124.3º ± 3.56º	128.4º ± 1.03º	128.5º ± 1.95º	133.4º ± 1.99º	134.5º ± 5.05º

CHAPTER VI – UNEXPECTED EFFECTS OF INORGANIC PHOSPHATE GLASS

ON CRYSTALLIZATION AND THERMO-RHEOLOGICAL BEHAVIOR OF

POLYETHYLENE TEREPHTHALATE

Abstract

The effects of ultra-low glass transition temperature (T_g) phosphate glass (Pglass)

on the thermal, morphological, rheological, mechanical, and crystallization properties of

hybrid Pglass/poly(eththylene terephthalate)(PET) were investigated. Nano- and micro-

scale distribution of the Pglass in the PET polymer matrix was observed. The

polydispersed Pglass in the PET matrix functioned as a nucleation agent, resulting in

increasing crystallization temperature. The Pglass in the PET matrix decreased the T_g,

indicating a plasticizing effect of the Pglass in the hybrids that was confirmed by the

significantly decreased complex viscosity of the PET matrix. In addition, with increasing

temperature, a non-terminal behavior of the viscoelastic properties occurred due to the

hybrid structural changes and improved miscibility of the hybrid components. Further,

the obtained solid-state variable temperature ^{31}P and ^{1}H NMR results showed strong

Pglass concentration dependency of the interactions at the PET-Pglass interface.

6.1 Introduction

Conventional polymer matrix composites are composed of organic polymer

matrix and various fillers to improve their mechanical, thermal and rheological properties

[1-3] and to cost-effectively meet the specific requirements of various industrial applications [4, 5]. However, new technologies are growing fast and often require optimized materials for specific applications where current traditional polymer composites are not useable. Consequently, development of functional organic/inorganic hybrids materials with prescribed properties and functions are needed for a number of industrial uses. Note that hybrid materials are defined as materials with organic and inorganic components, displaying better properties than that of the original components [6-8]. In general, hybrid materials consist of organic polymer materials as the continuous matrix and inorganic materials as the filler that are combined with physical mixing or chemical reaction, resulting in new materials with a microstructure and physicochemical interactions with enhanced benefits in the targeted applications [8].

Poly(ethylene terephthalate) (PET) is a semi-crystalline thermoplastic polyester widely used in various applications such as fiber, films and various injection molded parts due to its excellent physical properties including chemical resistance, optical clarity, dimensional stability and high strength [9-11]. However, PET exhibits a relatively slow crystallization rate and a low thermal distortion temperature, limiting its extensive applications in injection molding and engineering plastic applications [12-14]. In order to improve the thermal, morphological and mechanical properties of PET polymer matrix, nanoscale materials such as CNTs [15], clay [16, 17], and SiO_2 [18] are incorporated into the PET polymer matrix as reported in the literature.

Inorganic phosphate glass is typically used in optical and biomedical applications due to their excellent mechanical property, optical clarity and biocompatibility [19, 20]. As an example, a new class of tin fluorophosphates glass (hereinafter referred to as

Pglass) can be efficiently combined with organic polymer materials using melt processing methods like extrusion and injection molding to prepare composite materials with improved properties because Pglass has ultra-low T_g values between 90°C to 140°C, which enables facile mixing and processing of the Pglass with polymer composite components to achieve desired properties already mentioned [6, 19-21]. In this context, Urman et al. [20] reported that Pglass in polyamide 6 affected the crystallization process and properties such as the crystallization growth rate and the percent of crystallinity of the polymer material. Guschl et al. [19] reported that Pglass in polypropylene (PP) and polyethylene (PE) matrix changed the percentage crystallinity and onset temperature of crystallization of the matrix polymers by acting as the polymer crystal nucleation agent in the Pglass/polymer hybrid materials.

In the current study, Pglass was processed with PET using conventional polymer processing methods in the liquid melt state due to the ultra-low T_g of Pglass [22]. The morphology of cryo-fractured surfaces of the hybrids and polymer crystals were investigated using microscopic analysis techniques; and isothermal crystallization kinetics were characterized by differential scanning calorimetry (DSC) analysis to understand the thermal behavior of the Pglass/PET hybrid system. The current study reported here is focused on detailed investigation and analysis of effects of Pglass molecules in the PET matrix on the thermal, morphological and thermo-rheological properties of the hybrid materials. In particular, the distribution of nano- or micro-sized Pglass particles was investigated to understand the origin of the unique mechanical, crystallization, and rheological properties, making it possible to discover and control mechanisms that develop on nanometer length scales, influence the microscale, and

impact the macroscale. Typically, a molecular level mixture of matrix polymers and fillers prepares a large fraction of filler molecules interacting with polymer molecules, which leads to strong interfacial interaction between filler molecules and matrix polymer molecules. In this study, molecular dispersed Pglass molecules are effectively able to increase the polymer-Pglass particle interfacial area, improving a function of Pglass molecules as a nucleation agent and solid state mechanical properties as well as modifying the rheological properties. In addition, the effect of Pglass content and its correlation with temperature on the rheological and dynamic mechanical properties of the hybrids under test conditions that the materials are likely to encounter during use are discussed. It is hoped that this study will provide a better understanding of the Pglass/PET hybrid materials and other similar organic/inorganic hybrid materials in general.

6.2 Experimental methods

6.2.1 Materials and preparation of hybrids

The PET (obtained from DAK America) used in this study has a melting point of 240°C and intrinsic viscosity of 0.79 ± 0.02 dl/g. Analytical reagent grade tin(II) oxide (SnO), tin(II) fluoride (SnF$_2$) and ammonium dihydrogen phosphate ((NH$_4$)H$_2$PO$_4$) were purchased from Sigma-Aldrich and used as received to prepare the tin fluorophosphates glass used in this study. The tin fluorophosphates (Pglass) was synthesized with a molar composition of 50SnF$_2$ + 20SnO + 30P$_2$O$_5$ at 430°C for 30min, to yield the Pglass with ultra-low glass transition temperature (T$_g$) about 123°C [6]. The Pglass melt was taken out of furnace (after Pglass synthesis) and subsequently poured into a pre-shaped steel mold (19 mm diameter, 2 mm height) at ambient temperature to form solid chunks of

Pglass. Then they were annealed around their glass transition temperature at 130°C for 90

min. The obtained sample was ground into powder using mortar and pestle and then

sifted through a sieve with 75 μm mesh [23]. The Pglass/PET hybrids with various

desired concentrations of Pglass ranging from 0 wt.% to 50 wt.% were prepared using a

Thermo-Haake Polydrive$^{®}$ melt mixer equipped with roller rotors. In addition, samples

with higher concentration of 30 wt.% and 50 wt.% Pglass were prepared and used

exclusively for rheological characterization in order to magnify the effects of relatively

higher Pglass content in the polymer matrix. The obtained hybrid materials from the

Polydrive$^{®}$ melt mixer were cryo-fractured prior to morphological analysis. A portion of

the obtained hybrid materials was compression-molded using 40 MPa into thin films at

260°C and cooled down with 20 ^{o}C/min cooling rate for polarized optical micrograph

(POM). Some of thin films were ground into powder for ATR-FTIR and solid-state NMR

analysis. All the hybrid samples were dried over-night to constant weight in a vacuum

oven maintained at 80°C prior to testing.

6.2.2 Measurements

6.2.2.1 Thermal gravimetric analysis (TGA)

Thermogravimetric analysis (TGA) tests were performed on the samples using a

TA instruments Q500 equipment operating from 30°C to 600°C at a heating rate of 10

^{o}C/min under a nitrogen atmosphere. Thermal decomposition temperature was defined as

the onset temperature of the thermal degradation of samples, which was obtained using

the universal analysis software from TA instruments.

6.2.2.2 Scanning electron microscopy (SEM) and Energy Dispersive X-ray spectroscopy (EDX)

The processed PET (control) and Pglass/PET hybrid samples were cryo-fractured after immersion in liquid nitrogen and subsequently coated with silver using a Quorum® Emitech K550X sputter coater to make the samples conductive for optimal observation of the morphology of the fractured surface of the Pglass/ PET hybrids. A Zeiss Sigma VP® field emission scanning electron microscope (SEM) operating at 20kV with an attached energy-dispersive X-ray spectroscopy (EDX) having a Thermo Scientific UltraDry EDX detector was utilized to investigate the morphology and elemental compositions on the surfaces of the fractured samples. The obtained elemental data were analyzed using NSS3® micro-analysis software.

6.2.2.3 Scanning electron microscopy (SEM) and Energy Dispersive X-ray spectroscopy (EDX)

TEM experiments were performed on a Zeiss 900® with an acceleration voltage of 50 kV to identify the homogeneous dispersion of nano- or micro-size Pglass particles in the nanocomposites. The specimens for TEM were prepared by microtome sectioning and the specimen sections were placed in 200 mesh copper grids for observation.

6.2.2.4 Polarized optical microscopy (POM)

The crystallization behavior of the hybrids was investigated using a Nikon Optihot2® optical microscope equipped with a Metler Toledo® hot stage. A film sample with about 60~70 um thickness was prepared by compression molding and sandwiched between two glass plates. Subsequently, the sample was rapidly heated to 280°C and kept at this temperature for 10mins to melt the residual crystals in the sample, and then the

sample was rapidly cooled to the desired crystallization temperature to observe isothermal crystallization behavior. The evolution of the morphology of crystalline growth was observed using POM equipped with crossed polarizers after the isothermal crystallization process for 30min at 226°C.

6.2.2.5 DSC measurements

Thermal and crystallization behavior of hybrids with various amounts of Pglass concentrations (up to 15wt.%) were measured by DSC using a TA instrument Q100 in a dry nitrogen atmosphere. The samples were subjected to a heat-cool-heat cycle; heating rate of 10 $^{\circ}$C/min from 30°C to 280°C with a 5 min isothermal condition at each selected temperature; and then subsequently cooled to 30°C at a rate of 10 $^{\circ}$C/min followed by reheating at a rate 10 $^{\circ}$C/min to 280°C. The peak of the crystallization temperature (T_p) of the sample was obtained. In the case of the isothermal crystallization kinetics experiments, the samples were heated to 280°C at a rate of 10 $^{\circ}$C/min and held at this temperature for 10min to remove all previous thermal history, and then followed by rapid cooling to the desired three different crystallization temperatures (T_c) ranging of 204° – 208°C for 20 min to achieve complete crystallization. Specimens weighing 4.5 ± 0.4 mg were used to eliminate temperature gradients in the samples.

6.2.2.6 Dynamic mechanical analysis (DMA)

Dynamic mechanical analysis (DMA) was carried out using the TA instrument Q800 following standard procedures operating in the tension mode at a frequency of 1.0Hz with a pre-load of 0.01N. The temperature was scanned from 0°C to 180°C with 2 $^{\circ}$C/min heating rate. The storage (E') and loss (E'') moduli were measured as a function

of temperature. The glass transition temperature (T_g) of the samples was defined as the temperature at the peak of the loss modulus.

6.2.2.7 Rheological measurements

Rheological experiments were performed on a MCR501 rheometer (Anton Paar) using a parallel plate geometry with plates of 25mm in diameter and a gap of 1 mm. The frequency sweep experiments were performed using a 5% strain that was previously found to be in the linear viscoelastic region and angular frequency in the range of 0.1 to 100 rad/s. All experiments were done under a dry nitrogen atmosphere to prevent or minimize thermal degradation of the samples.

6.2.2.8 Solid state NMR

^{13}C MAS NMR spectra were obtained on a Bruker Avance III 400 (9.6 T) NMR instrument using a 4 mm broadband magic-angle spinning (MAS) probe. The samples were packed in 4 mm rotors. All spectra were obtained at room temperature and spinning at 10-12 kHz. The cross polarization (CP) MAS (or CPMAS) NMR spectra were obtained using a single pulse Block decay using a 1 sec recycle delay, a $\pi/2$ pulse, and a CP contact time of 3 ms. The direct polarization (DP) MAS NMR spectra were obtained with a recycle delay of 60 sec. The ^{13}C chemical shift was referenced to tetramethylsilane. All spectra deconvolutions were done with DMFIT software. Static ^{1}H and ^{31}P NMR spectra were obtained on a Bruker Avance III 400 (9.6 T) NMR instrument using a 7 mm broadband DOTY High Temperature Probe in the static mode. 1D NMR spectra were obtained using a Hahn Echo with a 10 s recycle delay for ^{1}H and a 60 s recycle delay for ^{31}P.

6.3 Results and discussion

6.3.1 Thermal characteristics

Fig. 6.1 shows the nonisothermal crystallization behavior of the control PET and hybrids samples containing three different amounts of Pglass at the cooling rate of 10 ºC/min from the melting state. The figure indicates a gradual shift of the peak crystallization temperature (T_p) to higher temperatures in the 204.6ºC to 210.4ºC temperature range. This observation is attributed to the increasing amount of the Pglass in the hybrids. It is worthy to note that the PET polymer crystallized at an early stage (i.e., higher temperature) of the cooling process because the dispersed molecular sized Pglass particles functioned as nucleation agents in the PET matrix hybrids and found to be consistent with previously reported results [23, 24]. In contrast, Liu et al. [25] reported that the value of T_p was not significantly influenced by the amount of Pglass in the PET polymer matrix hybrids using a 10 ºC/min of cooling rate. In addition, with a 30 ºC/min of cooling rate, T_p was decreased. Compared to previously reported work by Liu et al. [27], using melt-blending process in a twin-screw extruder different from a batch mixer in our study with regard to the residence time of the components in the mixing process, this different result in the current study can be attributed to the effective dispersion of Pglass utilizing the melt mixing process already described in the experimental section. In addition, it is believed that the obtained hybrid materials showed heterogeneous nucleation and crystallization behavior due to the polydispersed sizes of Pglass particles in the PET matrix resulting in different rates of crystallization. The observed shoulder at lower crystallization temperature represents this irregularity in the crystallization process.

190

The crystallinity of the Pglass/PET hybrids were further investigated using solid state ^{13}C NMR technique. The obtained NMR plots are shown in Fig. 6.2. In order to assess the crystallinity of the samples, a combination of the peak and the shoulder of the peaks in the range of 60-70 ppm were considered. This peak is associated with the methyl groups of the aliphatic segment of the PET polymer. The main and shoulder were deconvoluted into the individual construction peaks at 63 and 66 ppm which respectively, correspond to *trans* and *gauche* configurations of the aliphatic segment. Using the relative ratio of these peaks, the crystallinity index of the 10wt.% Pglass sample was estimated as a *trans*/*gauche* ratio of 63/37, corresponding to 63% crystallinity or "ordered" phase in the matrix [26]. This ratio is further reduced to 50/50 in the sample with 50% Pglass. These results clearly show that with increasing Pglass concentrations, the ratio of ordered (or crystalline) phase to less ordered structure is reduced, which is associated with the reduction of overall crystallinity of the hybrid samples. This observation will be further investigated and confirmed in the kinetic study and polarized optical micrographs showing more defective crystals in the hybrid samples.

The thermal stability of the samples is depicted in Fig. 6.3 showing the TGA curves of the control PET and the PET matrix hybrids incorporating Pglass. There is no significant difference in the onset temperature of thermal degradation between that of the control PET and hybrids at the experimental temperature range tested (i.e., 30 °C to 600 °C). Clearly, the residual amounts of samples after heating to 600ºC increased as the amount of Pglass was increased in the hybrids due to the addition of inorganic Pglass as a filler, which is a non-decomposable inorganic material.

191

6.3.2 Morphological analysis

Fig. 6.4 shows SEM photomicrographs of the cryo-fractured surface of the control PET and Pglass/PET hybrids containing 5wt.% to 15wt.% of Pglass. As the amount of Pglass was increased, the size and the number of droplets of Pglass in the PET matrix increased, indicating a phase separation between Pglass and PET in the hybrids. However, EDX analysis showed another interesting result that Pglass was dispersed in nanoscale in the PET matrix. The EDX image in Fig. 6.5 shows the distribution of phosphorus in the Pglass/PET hybrids, indicating presence of phosphorous not only as discrete micro-size droplets of Pglass but also as droplets dispersed in the PET matrix phase. Note that Pglass is distributed at both the microscale and nanoscale in the PET matrix materials. In addition, it is noteworthy that the Pglass droplets prepared by droplet coalescence were encased by PET polymer matrix due to the effective hydrogen bonding interaction between the hydrogen donor in hydroxyl groups from the Pglass and oxygen acceptor atoms in the ester from the PET polymer [20, 25, 27].

As shown in the EDX data of Fig. 6.5 (c), the PET matrix dominated region (point #2) showed significant weight percent portion of fluorine (F), phosphorous (P), and tin (Sn) elements of the Pglass due to the homogeneous nanoscale dispersion of Pglass in the PET matrix that is ascribed to the low T_g of Pglass and the physical and chemical compatibility between Pglass and PET matrix materials. These obtained SEM-EDX results are supported by the TEM analysis shown in Fig. 6.6. This provides a direct evidence of the nano- and micro-scale dispersion of Pglass in the PET polymer matrix via the mixing process in the melt state of the two organic and inorganic components of the hybrid materials studied. The good dispersion of Pglass in the PET matrix is attributed to

the formation of hydrogen bonds between the hydrogen and carbonyl group of PET and hydroxyl and fluoride of the Pglass.

The crystalline morphology for the control PET and its hybrids was investigated using polarized optical microscopy (POM) analysis as shown in Fig. 6.7, which were observed after completion of the isothermal crystallization of samples at the designated crystallization temperature and cooling to the room temperature. As shown in Fig. 6.7 (a), crystals with a spherulite morphology (Maltese cross pattern) are observed in the control PET samples after isothermal crystallization. In contrast, for the 10wt.% Pglass/PET hybrid (see Fig. 6.7 (b)), a relatively large number of discrete crystals were observed due to the heterogeneous nucleation sites (Pglass particle surface) and subsequent impingement of crystals during the growth process attributed to the close distance between the crystals. It is worthy to note that the addition of Pglass increased the heterogeneity of the polymer crystal growth in the hybrids is ascribed to crystal nucleating effect of Pglass molecules in the hybrids as already described. This last observation is consistent with the result of the shift of the peak of crystallization temperature in the cooling process already mentioned. In addition, it was observed that the increased heterogeneous nucleation obstructed the crystal growth, resulting in the observed decrease of overall crystallinity of PET polymer in the hybrids as already discussed.

6.3.3 Nucleation effect of Pglass in isothermal melt crystallization

Fig. 6.8 (a) shows the plot of relative crystallinity X(t) versus crystallization time (min) for the isothermal crystallization of the control PET and its hybrids. The relative crystallinity at time t, X(t) is defined as shown in Eq. (1) [28, 29].

$$X(t) = \frac{X_c(t)}{X_c(t_\infty)} = \frac{\int_0^t \frac{dH_c(t)}{dt} dt}{\int_0^{t_\infty} \frac{dH_c(t)}{dt} dt} \qquad (1)$$

where $H_c(t)$ is the crystallization enthalpy at time t and $dH_c(t)/dt$ is the rate of heat

evolution. Fig. 6.8 (a) shows that the characteristic sigmoidal isotherms are shifted to the

left with increasing amount of Pglass in the hybrids, indicating a faster crystallization rate

caused by the addition of Pglass. Another critical parameter is the half-time of

crystallization ($t_{1/2}$) indicating the time at which X(t) is 50% and G is defined as the

reciprocal of $t_{1/2}$ which represents the crystallization rate [30]. The $t_{1/2}$ can be directly

derived from experimental X(t) data or calculated using the following equation [31]:

$$t_{1/2} = \left(\frac{\ln 2}{K}\right)^{1/n} \qquad (2)$$

where n is Avrami constant and K is crystallization rate constant. To obtain the maximum

crystallization, the following equation can be applied as reported by Lin [32].

$$t_{max} = \left(\frac{n-1}{nK}\right)^{1/n} \qquad (3)$$

The half-time of crystallization ($t_{1/2}$), the reciprocal of $t_{1/2}$ (i.e., G parameter) indicating

crystallization rate, and the time for maximum crystallization, t_{max}, are summarized in

Table 1. The Table shows that $t_{1/2}$ of Pglass/PET hybrids decreased from 1.170 to 0.677 as the amount of Pglass increased from 0wt.% to 15wt.%, indicating that the crystallization rate (G) increased and the time for maximum crystallization (t_{max}) decreased. This observed increase of crystallization rate in isothermal crystallization is consistent with the results of Pglass/PP hybrid system reported by Guschl et al. [19] and of clay/PET hybrid system reported by Wan et al. [16].

The characteristic sigmoidal isotherms were shifted to the right with increasing crystallization temperatures (T_c) as depicted in Fig. 6.9 (a) and (b), indicating that the crystallization rate becomes slower for both the control PET and the Pglass/PET hybrids. Using these relative crystallization data, an Avrami analysis was carried out to investigate the isothermal crystallization kinetics for the samples. The general form of Avrami equation [33-35] is

$$X(t) = 1 - \exp(-Kt^n) \qquad (4)$$

where n is an Avrami constant which is related to dimensional features of crystal nucleation and growth and K is the crystallization rate constant related to nucleation and growth rate of crystal in crystallization process. Eq. (4) can be written in another form after taking logarithm two times as follows:

$$\log \{ - \ln(1 - X(t))\} = n \log t + \log K \qquad (5)$$

Using the logarithm form of Avrami equation, Eq. (5), the plots of $\log \{ - \ln(1 - X(t))\}$ versus $\log t$ was obtained (see Fig. 6.10). The Avrami constant (n) and crystallization rate

constant (K) were obtained from the slope and intercept of the straight line, respectively, by fitting the data using the Avrami model. Rahimi et al. [28] separated the overall crystallizations into three sections consisting of initial stage (nucleation), linear stage (growth of crystallization), and final stage (impingement of crystallization) to focus on the growth stage on the linear portion of Avrami plot. In the current study, the linear stage was determined between 5% and 70% of relative degree of crystallization and the Avrami graph was plotted using the linear range shown earlier in Fig. 6.8(b).

The obtained kinetic parameter data from the Avrami model analysis is summarized in Table 1 for the isothermal crystallization of the Pglass/PET hybrids incorporating various Pglass concentration. As proposed by Bian et al. [36], the Avrami constant, n, is related to the number of growth points in crystal nuclei. Typically, n values of the 2D lamellar crystals are 2 or 3, and the 3D spherulite crystals are 3 or 4. A schematic diagram of the evolution of the spherulite crystal of PET was reported by Lee et al. [37], showing that 3D spherulites are formed by the growth of branches of 2D lamellae. In the current study, the n values were found to be about 3 or 4, indicating formation of 3D spherulite crystals during the PET crystallization process. The kinetic parameters obtained from the Avrami analysis of the data shown in Fig. 6.10 for the isothermal crystallization of the control PET and 15wt.% Pglass/PET hybrids at three different isothermal crystallization temperatures are listed in Table 2. Interestingly, the n value of control PET is larger than that of its hybrids, indicating that incorporation of Pglass reduces the dimensions of the PET crystals. In other words, the presence of Pglass particles in the PET matrix results in development of less perfect spherulitic crystals. As shown earlier in Fig. 6.7, It is worthy to note that there are more nucleation sites

produced by Pglass molecules in the hybrids compared to that of the control PET which

is responsible for the observed increase of the crystallization sites and the associated

decrease of the crystal dimensions in the hybrids, as other researchers have previously

reported for similar systems [14, 18, 38]. As shown in Tables 1 and 2 the values of K and

G corresponding to the crystallization growth rates significantly increased due to the

decrease of the values of maximum crystallization time (t_{max}) and the half-time of

crystallization ($t_{1/2}$)) as the amount of Pglass was increased. This indicates that nano- and

micro-scale dispersed Pglass particles in the hybrids effectively functioned as the

polymer crystal nucleation agents. In addition, the crystallization rate (i.e. K) decreased

as the crystallization temperature (T_c) increased from 204°C to 208°C both for the control

PET and 15 wt.% Pglass/PET hybrid. Clearly, this is due to the relatively slower

exothermal heat transfer during the crystallization at the higher temperature, resulting in

the observed increase of maximum crystallization time (t_{max}) and the half-time of

crystallization ($t_{1/2}$) shown in Table 2.

6.3.4 Mechanical properties

Dynamic mechanical analysis was carried out on the materials to investigate their

mechanical properties such as storage (E') and loss (E") which respectively indicates the

energy stored as elastic energy and the energy dissipated due to the friction of polymer

chain movement. Fig. 6.11(a) shows the variation of E' versus temperature for the control

PET and its hybrids. The E' increased with increasing Pglass content up to 15 wt.%,

indicating the stiffening effect of the inorganic Pglass molecules in the PET polymer

matrix. In addition, the increase of E' was relatively higher at temperatures below the T_g

compared to that observed at higher temperatures in agreement with the previously

reported results in the literature [20]. The E" plotted as a function of temperature is

shown in Fig. 6.11(b). This graph shows that the glass transition temperature (T_g) defined

as the maximum value of loss modulus slightly shifted to the left (i.e. decrease of T_g) due

to the addition of Pglass. This shows that the Pglass functioned as a plasticizer in the

Pglass/PET hybrids. This observed decrease of T_g is consistent with the previously

reported work by Urman et al [6] on polyamide matrix containing a Pglass filler. The

authors just mentioned that the plasticizing effect is caused by higher mobility of polymer

chains at the interfacial areas between the filler and matrix material in the hybrids [39,

40] due to the smooth surface of Pglass particles.

6.3.5 Rheological properties

The rheological properties of the Pglass/PET hybrids were studied using dynamic

small amplitude oscillatory shear rheology to assess the effect of microstructure

development and the potential effects of the interactions at the PET-Pglass interfacial

area on melt rheological properties. The variation of the complex viscosity versus angular

frequency is shown in Fig. 6.12 (a-c) for the pure PET, Pglass and the hybrids at different

temperatures of 255°C, 265°C and 280°C, respectively. This figure shows that the pure

Pglass exhibits a Newtonian behavior at all three temperatures studied [21]. This last

observation is ascribed to the relatively small size of inorganic Pglass chain segments.

The pure PET matrix shows a Newtonian behavior in the studied conditions.

Interestingly, with the addition of the Pglass, the complex viscosity of the hybrids

dropped to lower values compared to that of the neat PET and Pglass. As can be seen in

Fig. 6.12, with the addition of the 5 wt.% Pglass to PET, the sample showed relatively

lower complex viscosity values throughout the whole range of frequencies studied

compared to that of neat components (i.e., PET and Pglass). With further increase in the

Pglass content, a further decrease in the viscosity values for 10 wt.% and 30 wt.% of

Pglass hybrids was observed. Note that the observed viscosity reduction of polymers with

addition of Pglass is similar to our previously reported systems of polyamide and Pglass

[21]. There are a number of possible reasons for such observation: firstly, it is believed

that the Pglass could potentially impose an interfacial lubrication effect due to the low

molecular weight and oligomeric nature of Pglass chains causing the PET chains to slide

pass each other. Secondly, the presence of Pglass could disrupt the chain entanglement in

the PET matrix which consequently promotes the viscous flow of the hybrid melt. This

non-Einstein-like decrease of viscosity in polymer melts due to the presence of

nanoparticulate inclusions have been previously reported in the literature by a number of

researchers [41, 42]. In addition, the strong interaction of Pglass with PET through

hydrogen bonding can disrupt the inter- and intra-molecular hydrogen bonding of the

PET chains, resulting in observed viscosity changes.

Here, we also speculate that Pglass may disrupt (depolymerize) the PET chains

through transesterification of the ester bond via the nucleophilic attacks of the anionic

form of the phosphate groups (PO_4^{3-}) which reduces the molecular weight the PET and

subsequently reduces the melt viscosity. This hypothesis is currently under further

investigation that will be reported elsewhere. Note that the current Pglass/PET hybrids

show a different behavior at the terminal zone of the dynamic shear flow compared to

that of the pure components. The results show that, while the hybrid sample with 5 wt.%

Pglass exhibits a similar behavior to that of pure PET matrix, as the Pglass content is

increased, there appears to be a sharp increase in the complex viscosity in the low

frequency region ($\omega < 1$ rad/s). This sharp increase in viscosity in the low frequency range is clearly observed in the 10 wt.% Pglass/PET hybrid sample. However, this observed viscosity increase is most significant in the 30 wt.% Pglass/PET hybrid. The evolution of such nonterminality of complex viscosity is associated with the development of an elastic structure and yield stress behavior [43-45].

In order to further elaborate on this observation, the variation of storage modulus (G') of the samples at all three different temperatures is shown in Fig. 6.13 (a-c). First, it is seen that the G' of the hybrids is lower than that of the pure component at 255°C which is consistent with the lubrication effect as already described. Second, as the Pglass content is increased in the hybrids from 5 to 30 wt.%, the G' increased (relative to that of the hybrids) which is due to the presence of the Pglass component, especially in the low frequency region. In addition, the slope of the terminal zone of the hybrid samples shows that with increasing the Pglass content, the slope of the G' curve is reduced where the frequency region of 0.1-0.5 rad/s was used. For example, the slope of the terminal zone of the G' for samples with 5, 10 and 30% Pglass are respectively 1.26, 1.11 and 0.89 at 255 °C. Same behavior is observed for the samples at higher testing temperatures. These observations suggest that increasing the Pglass content is associated with enhancement of elasticity within the PET matrix. In addition, is it seen that the increasing the temperature results in further enhancement of elastic properties (especially by considering the low frequency regions of the G' curve) where the G' of the 10 wt.% and 30 wt.% Pglass samples at 280°C become higher than of the pure matrix. Typically, in particulate filled systems the contributions of the elasticity of the particles (and potential 3D network formation) combined with strong polymer-particle interactions can develop such solid-

like behavior at low frequency regions of the G' curve, however in the current system since the Pglass is in liquid state, it is speculated that with increasing the temperature, Pglass phase undergoes structural reorganization such as formation of intermediate-ranged structures with significantly prolonged relaxation times. In addition, the improvement of the compatibility of the Pglass phase with the PET matrix at higher temperatures that results in enhancement of the interfacial interactions, is thought to be another contributing factor in the observed melt elasticity and changes in the relaxation behavior of the PET-Pglass hybrids.

The effects of composition and temperature on the compatibility of the hybrids components can be further studied using the log G' vs log G", modified Cole-Cole plots (or Han plots) which have been used in a number of previous studies on various polymer blend systems [46]. The Han plots of neat PET and the Pglass/PET hybrids are shown in Fig. 6.14 (a-d) at three different temperatures of 255°C, 265°C and 280°C. As can be seen in this figure, for the neat PET, there is a temperature independence for log G' vs log G". Interestingly, as the Pglass content is increased in the system from 5 to 30 wt.%, the temperature independence of the Han plot is broken down. For the 5 wt.% Pglass, this deviation is relatively less compared to that observed at higher concentrations, showing good compatibility between the hybrid components and microstructure, indicating less influence by the temperature. As the Pglass content is increased, especially for 30 wt.% hybrid, there is a larger deviation of the Cole-Cole diagram from temperature independence. This deviation is associated with a microstructure that is dependent on the temperature. It is evident that with increasing Pglass content in the hybrids, the samples become rheologically complex fluids with clear dependency on the temperature. In fact, it

is believed that with increasing temperature, the interfacial interactions between the PET and Pglass are strengthened, which can improve the miscibility of the components. Such improvement of the interactions and interfacial miscibility could be a contributing factor in the earlier observation that with increasing the temperature, the nonterminality of the plots of η^* and G' versus frequency was promoted especially as the Pglass content was increased in the blend.

6.3.6 Variable-temperature (VT) ^{31}P and ^{1}H solid state NMR.

The static variable-temperature (VT) ^{31}P NMR for pure Pglass and two hybrids is shown in Fig. 6.15. The local chain fluctuations of materials will produce signal narrowing with increasing amounts of motion attributed to increased temperature [47, 48] until the molecules are freely motioning like a liquid. It is obvious that pure Pglass melted out to form sharp lines at high temperature as shown in Fig. 6.15(a) different from that of the other two hybrids, showing broad peaks at high temperature. This result indicates that Pglass in the hybrids did not melt in this temperature range and showed a very minor reduction in linewidth with increasing temperature due to the addition of Pglass causing interfacial interaction between PET and Pglass molecules.

In addition, Fig. 6.16 elucidates that average ^{31}P linewidths of 50 wt.% Pglass sample are smaller than that of 10 wt.% Pglass sample as the temperature increased, indicating that Pglass molecules in 50 wt.% Pglass sample has more mobility than that of 10 wt.% Pglass. This result shows that with increasing Pglass content from 10 wt.% to 50 wt.%, the compatibility of the PET and Pglass phases reduces (i.e., the sample with lower Pglass showed relatively stronger interfacial interactions at the interface of Pglass droplets and PET matrix phase that restricts the molecular the molecular mobility of the

hybrid components. At high Pglass concentrations, the PET and Pglass phases become increasingly less compatible, generating more unfavorable interactions and associated increased molecular mobility. This observation is consistent with the SEM images showing relatively bigger Pglass droplets as the Pglass content was increased in the hybrids. These larger droplets provide less interfacial area for PET-Pglass interactions and consequently, the chain dynamics of the hybrids with higher Pglass concentration and larger droplets shows the increased molecular mobility of the Pglass as evidenced in the VT 31P NMR results. It is very interesting to note that pure Pglass showed significantly increased mobility at higher temperatures while the nano- and micro-sized Pglass particles dispersed in the PET matrix showed only a slight increase of motion with increasing temperatures. This last result is attributed to the nano- and micro-scale interfacial interactions between Pglass and PET molecules.

Further, the obtained VT ^{1}H NMR [47, 49] results are depicted in Fig. 6.17. In this figure, the pure PET showed a relatively larger linewidth at lower temperature, reflecting higher rigidity (due to higher crystallinity) in the pure PET compared to that of the PET phase in the hybrids. At higher temperatures around melting point of PET, the pure PET showed decreased linewidth compared to that of the hybrids, implying that the mobility of the PET polymer chains near the Pglass molecules in the hybrids is restricted by the Pglass molecules. It is worthy to note that the average ^{1}H rigid linewidth of the PET decreased slightly (i.e., increased chain mobility) with increasing Pglass content from 10 wt.% to 50 wt.% due to the reduced compatibility and less favorable interfacial interactions at higher Pglass concentrations together with the change in the morphology

of the hybrids and formation of the larger Pglass droplets (i.e., less interfacial area) in the PET matrix.

6.4 Conclusion

In this study, PET matrix hybrid incorporated with polydispersed ultra low T_g Pglass was characterized by a number of characterizations and analysis methods to study the physical properties of hybrids. The morphology of the fracture surface of samples was investigated by the SEM. In addition, the dispersion of Pglass molecules in the PET matrix was observed by EDX, which showed that Pglass was polydispersed in the PET matrix hybrids. These results were confirmed by TEM analysis showing various sizes of Pglass particles from nano- to micro-meter in the polymer matrix. In addition, the results showed that the nanoscale and microscale dispersed Pglass in the hybrid materials functioned as a nucleation agent based on the results that the peak of crystallization temperature shifted to a higher temperature with increasing concentrations of Pglass in the PET matrix during the non-isothermal crystallization at $10\,^oC$/min cooling rate. In the isothermal crystallization process, Avrami analysis showed that K (crystallization rate constant) and G (reciprocal of $t_{1/2}$) values increased as the amount of Pglass was increased in the hybrids materials at the given specific isothermal crystallization temperature, indicating that the addition of Pglass molecules in the hybrids enhanced nucleation process and crystal growth rate. In contrast, crystallinity of the hybrids was reduced as the amount of Pglass increased due to the defective crystals prepared by heterogeneous nucleation of the Pglass particles.

The addition of Inorganic Pglass in the PET matrix caused the observed increase of the storage modulus due to the stiffening effect of inorganic filler in the polymer

204

matrix. It was also observed that Pglass functioned as a plasticizer in the hybrids. The glass transition temperature was shifted to the left (i.e. decrease of T_g) in the reported loss modulus data, indicating that Pglass functioned as a plasticizer, which would be caused by higher mobility of polymer chains at the interfacial areas between the filler and matrix material in the hybrids. Overall, it can be concluded from the results of this study that Pglass molecules showed crystal nucleation activity, as well as, plasticizing effect in the PET polymer matrix. This latter remarkable lubrication effect is consistent with the obtained results of rheological properties of hybrids, indicating that the viscosity was decreased as Pglass content in the hybrids increased. In addition, the observed development of nonterminal behavior and the temperature dependence on the rheological properties with increasing the Pglass content and temperature indicate that the Pglass induces rheological complexity to the hybrid systems. Further, the variable temperature NMR results showed a strong concentration-dependent interfacial interaction between the Pglass and PET. These remarkable special properties of Pglass in the polymer matrix hybrids will provide useful information for a better understanding of the fundamental physical properties of Pglass/polymer hybrids for a number of application areas where traditional polymer composites are not useable.

6.5 Reference

1. Gao, F., Clay/polymer composites: the story. Materials today, 2004. 7(11): p. 50-55.

2. Ray, S.S. and M. Okamoto, Polymer/layered silicate nanocomposites: a review from preparation to processing. Progress in polymer science, 2003. 28(11): p. 1539-1641.

3. Han, Z. and A. Fina, Thermal conductivity of carbon nanotubes and their polymer nanocomposites: a review. Progress in polymer science, 2011. 36(7): p. 914-944.

4. Nandan, B., L. Kandpal, and G. Mathur, Poly (ether ether ketone)/poly (aryl ether sulfone) blends: melt rheological behavior. Journal of Polymer Science Part B: Polymer Physics, 2004. 42(8): p. 1548-1563.

5. Tucker III, C.L. and P. Moldenaers, Microstructural evolution in polymer blends. Annual Review of Fluid Mechanics, 2002. 34(1): p. 177-210.

6. Urman, K. and J.U. Otaigbe, New phosphate glass/polymer hybrids—Current status and future prospects. Progress in Polymer Science, 2007. 32(12): p. 1462-1498.

7. Arkles, B., Commercial applications of sol-gel-derived hybrid materials. MRS bulletin, 2001. 26(5): p. 402-408.

8.   Loy, D.A., Hybrid organic–inorganic materials. MRS Bulletin, 2001. 26(5): p. 364-367.

9.   Reinsch, V.E. and L. Rebenfeld, Crystallization processes in poly (ethylene terephthalate) as modified by polymer additives and fiber reinforcement. Journal of applied polymer science, 1994. 52(5): p. 649-662.

10.   Anand, K.A., U. Agarwal, and R. Joseph, Carbon nanotubes induced crystallization of poly (ethylene terephthalate). Polymer, 2006. 47(11): p. 3976-3980.

11.   Gao, Y., et al., Functionalized multi-walled carbon nanotubes improve nonisothermal crystallization of poly (ethylene terephthalate). Polymer Testing, 2008. 27(2): p. 179-188.

12.   Wang, Y., et al., Study on mechanical properties, thermal stability and crystallization behavior of PET/MMT nanocomposites. Composites part B: engineering, 2006. 37(6): p. 399-407.

13.   Jiang, X., et al., Effect of nucleating agents on crystallization kinetics of PET. Express Polym Lett, 2007. 1(4): p. 245-251.

14.   Run, M., et al., Melting behaviors and isothermal crystallization kinetics of poly (ethylene terephthalate)/mesoporous molecular sieve composite. Polymer, 2005. 46(14): p. 5308-5316.

15.   Yoo, H.J., et al., Effects of carbon nanotube functionalization and annealing on crystallization and mechanical properties of melt-spun carbon nanotubes/poly (ethylene terephthalate) fibers. Composites Science and Technology, 2012. 72(15): p. 1834-1840.

16.   Wan, T., et al., Crystalline morphology and isothermal crystallization kinetics of poly (ethylene terephthalate)/clay nanocomposites. Journal of Applied Polymer Science, 2004. 94(4): p. 1381-1388.

17.   Wang, Y., et al., Nonisothermal melt crystallization kinetics of poly (ethylene terephthalate)/clay nanocomposites. Journal of applied polymer science, 2004. 91(1): p. 308-314.

18.   Ke, Y.-C., T.-B. Wu, and Y.-F. Xia, The nucleation, crystallization and dispersion behavior of PET–monodisperse SiO2 composites. Polymer, 2007. 48(11): p. 3324-3336.

19.   Guschl, P.C. and J.U. Otaigbe, Crystallization kinetics of low-density polyethylene and polypropylene melt-blended with a low-Tg tin-based phosphate glass. Journal of applied polymer science, 2003. 90(12): p. 3445-3456.

20.   Urman, K. and J. Otaigbe, Novel phosphate glass/polyamide 6 hybrids: miscibility, crystallization kinetics, and mechanical properties. Journal of Polymer Science Part B: Polymer Physics, 2006. 44(2): p. 441-450.

21.   Urman, K., T. Schweizer, and J.U. Otaigbe, Rheology of tin fluorophosphate glass/polyamide 12 hybrids in the low concentration regime. Journal of rheology, 2007. 51(6): p. 1171-1187.

22.   Adalja, S.B. and J.U. Otaigbe, Melt rheology of tin phosphate glasses. Appl Rheol, 2001. 11(1): p. 10-18.

23.   Chae, D.W. and B.C. Kim, Thermal and rheological properties of highly concentrated PET composites with ferrite nanoparticles. Composites science and technology, 2007. 67(7): p. 1348-1352.

24.   Ke, Y.-C., T.-B. Wu, and Y.-F. Xia, The nucleation, crystallization and dispersion behavior of PET–monodisperse SiO 2 composites. Polymer, 2007. 48(11): p. 3324-3336.

25.   Liu, H., et al., The effect of Pglass state on the non-isothermal cold and melt crystallization processes of PET matrix. Thermochimica Acta, 2015. 613: p. 1-8.

26.   Huang, J.-M., P. Chu, and F.-C. Chang, Conformational changes and molecular motion of poly (ethylene terephthalate) annealed above glass transition temperature. Polymer, 2000. 41(5): p. 1741-1748.

27.   Lommerse, J.P., S.L. Price, and R. Taylor, Hydrogen bonding of carbonyl, ether, and ester oxygen atoms with alkanol hydroxyl groups. Journal of computational chemistry, 1997. 18(6): p. 757-774.

28.   Rahimi, S.K. and J.U. Otaigbe, The role of particle surface functionality and microstructure development in isothermal and non-isothermal crystallization behavior of polyamide 6/cellulose nanocrystals nanocomposites. Polymer, 2016. 107: p. 316-331.

29.   Chiu, F.-C., Y. Peng, and Q. Fu, Bulk crystallization kinetics of metallocene polyethylenes with well-controlled molecular weight and short chain branch content. Journal of Polymer Research, 2002. 9(3): p. 175-181.

30.   Knauer, K.M., et al., Rheological and crystallization enhancement in polyphenylenesulfide and polyetheretherketone POSS nanocomposites. Journal of Applied Polymer Science, 2017. 134(7).

31.   Chen, X., C. Li, and W. Shao, Isothermal crystallization kinetics and melting behaviour of PET/ATO nanocomposites prepared by in situ polymerization. European polymer journal, 2007. 43(8): p. 3177-3186.

32.   Lin, C., The rate of crystallization of poly (ethylene terephthalate) by differential scanning calorimetry. Polymer Engineering & Science, 1983. 23(3): p. 113-116.

33.   Avrami, M., Kinetics of phase change. I General theory. The Journal of Chemical Physics, 1939. 7(12): p. 1103-1112.

34.   Avrami, M., Granulation, phase change, and microstructure kinetics of phase change. III. The Journal of chemical physics, 1941. 9(2): p. 177-184.

35.   Avrami, M., Kinetics of phase change. II transformation-time relations for random distribution of nuclei. The Journal of Chemical Physics, 1940. 8(2): p. 212-224.

36.   Bian, J., S.R. Ye, and L.X. Feng, Heterogeneous nucleation on the crystallization poly (ethylene terephthalate). Journal of Polymer Science Part B: Polymer Physics, 2003. 41(18): p. 2135-2144.

37.   Lee, C.H., H. Saito, and T. Inoue, Time-resolved light scattering studies on the early stage of crystallization in poly (ethylene terephthalate). Macromolecules, 1993. 26(24): p. 6566-6569.

38.   Canetti, M. and F. Bertini, Supermolecular structure and thermal properties of poly(ethylene terephthalate)/lignin composites. Composites Science and Technology, 2007. 67(15–16): p. 3151-3157.

39. Ash, B.J., R.W. Siegel, and L.S. Schadler, Glass-transition temperature behavior of alumina/PMMA nanocomposites. Journal of Polymer Science Part B: Polymer Physics, 2004. 42(23): p. 4371-4383.

40. Sun, Y., et al., Glass transition and relaxation behavior of epoxy nanocomposites. Journal of Polymer Science Part B: Polymer Physics, 2004. 42(21): p. 3849-3858.

41. Mackay, M.E., et al., Nanoscale effects leading to non-Einstein-like decrease in viscosity. Nature materials, 2003. 2(11): p. 762-766.

42. Tuteja, A., et al., Effect of ideal, organic nanoparticles on the flow properties of linear polymers: non-Einstein-like behavior. Macromolecules, 2005. 38(19): p. 8000-8011.

43. Hoffmann, B., et al., Rheology of nanocomposites based on layered silicates and polyamide-12. Colloid & Polymer Science, 2000. 278(7): p. 629-636.

44. Jafari, S., et al., Multicomponent blends based on polyamide 6 and styrenic polymers: morphology and melt rheology. Polymer, 2002. 43(25): p. 6985-6992.

45. Rahimi, S.K. and J.U. Otaigbe, The effects of the interface on microstructure and rheo-mechanical properties of polyamide 6/cellulose nanocrystal nanocomposites prepared by in-situ ring-opening polymerization and subsequent melt extrusion. Polymer, 2017. 127: p. 269-285.

46. Han, C.D. and H.K. Chuang, Criteria for rheological compatibility of polymer blends. Journal of applied polymer science, 1985. 30(11): p. 4431-4454.

47.   Goward, G.R., et al., High-resolution solid-state NMR studies of imidazole-based proton conductors: Structure motifs and chemical exchange from 1H NMR. The Journal of Physical Chemistry B, 2002. 106(36): p. 9322-9334.

48.   Kapur, G., et al., Studies on competitive interactions and blending order of engine oil additives by variable temperature 31P-NMR and IR spectroscopy. Tribology transactions, 1999. 42(4): p. 807-812.

49.   Apperley, D.C., et al., Characterisation of indomethacin and nifedipine using variable-temperature solid-state NMR. Magnetic Resonance in Chemistry, 2005. 43(11): p. 881-892.
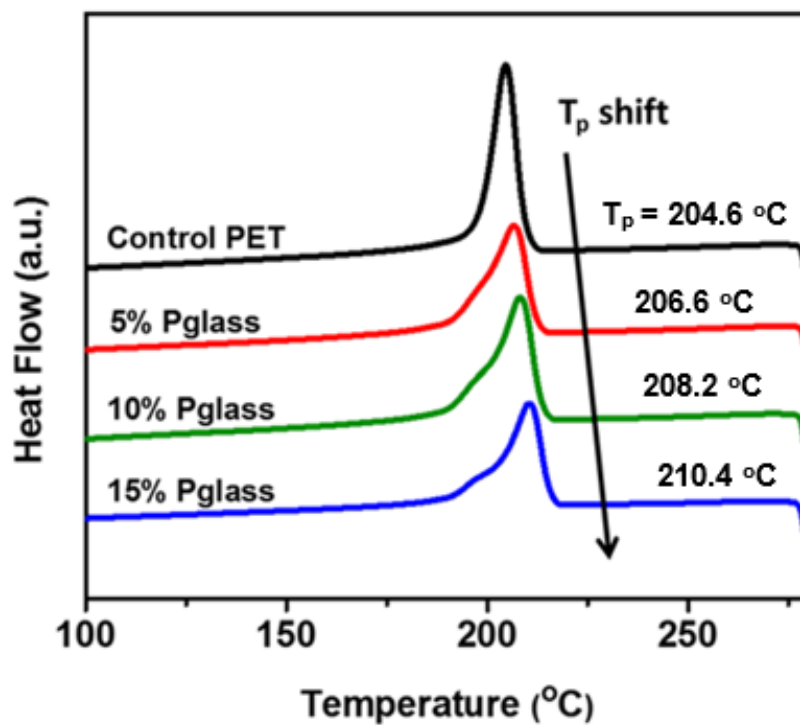
Figure 6.1 The DSC thermograms of the peaks of the crystallization temperature (T_p) in the PET matrix hybrids incorporating 0 – 15 wt.% Pglass.
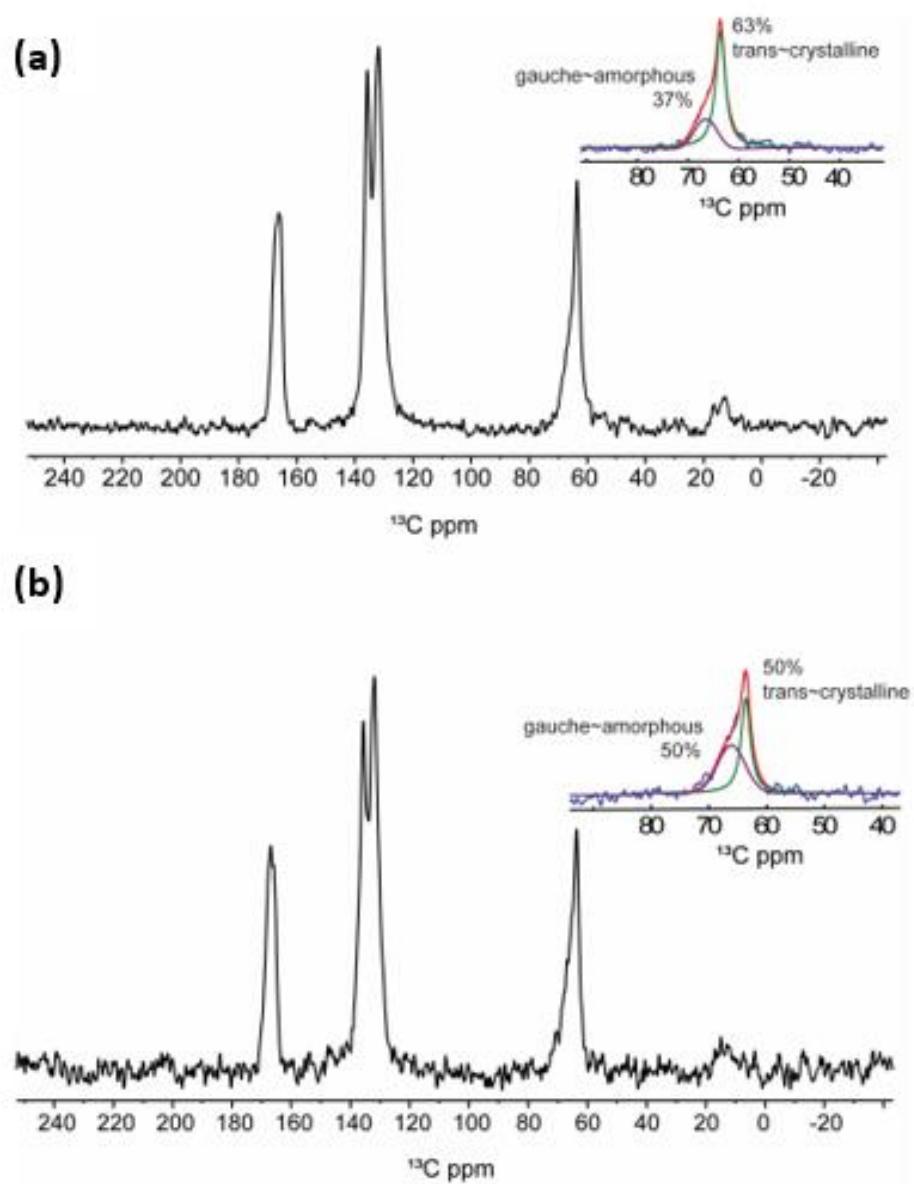
Figure 6.2 ¹³C DPMAS solid-state NMR spectra. (a) 10 wt.% Pglass composite and (b) 50 wt.% Pglass hybrids. Spectra were fitted for methylene resonance using Gaussian/Lorentzian functions.
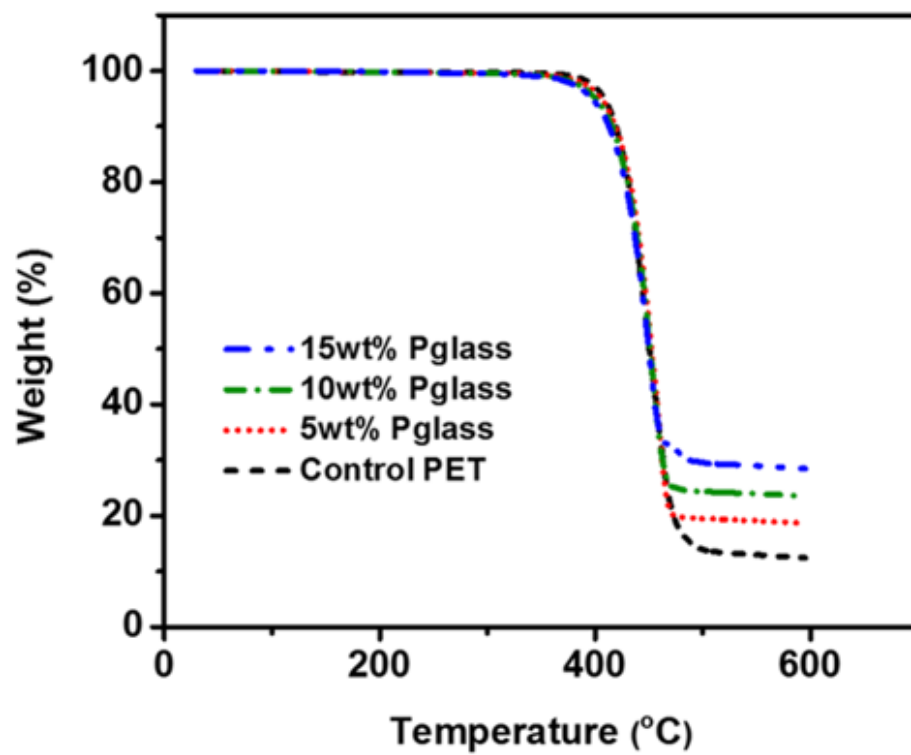
Figure 6.3 ^{13}C DPMAS solid-state NMR spectra. (a) 10 wt.% Pglass composite and (b) 50 wt.% Pglass hybrids. Spectra were fitted for methylene resonance using Gaussian/Lorentzian functions.
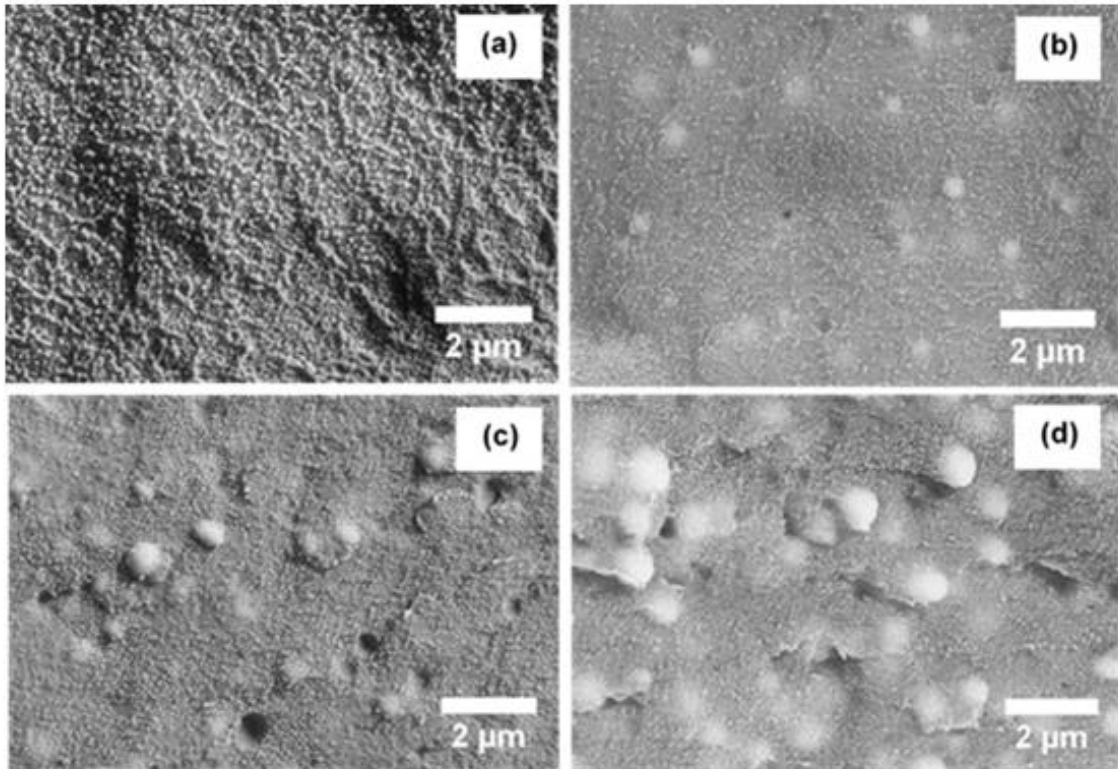
Figure 6.4 SEM images of fracture surface of (a) the control PET and PET matrix hybrids incorporating (b) 5 wt.%, (c) 10 wt.%, and (d) 15 wt.% Pglass.

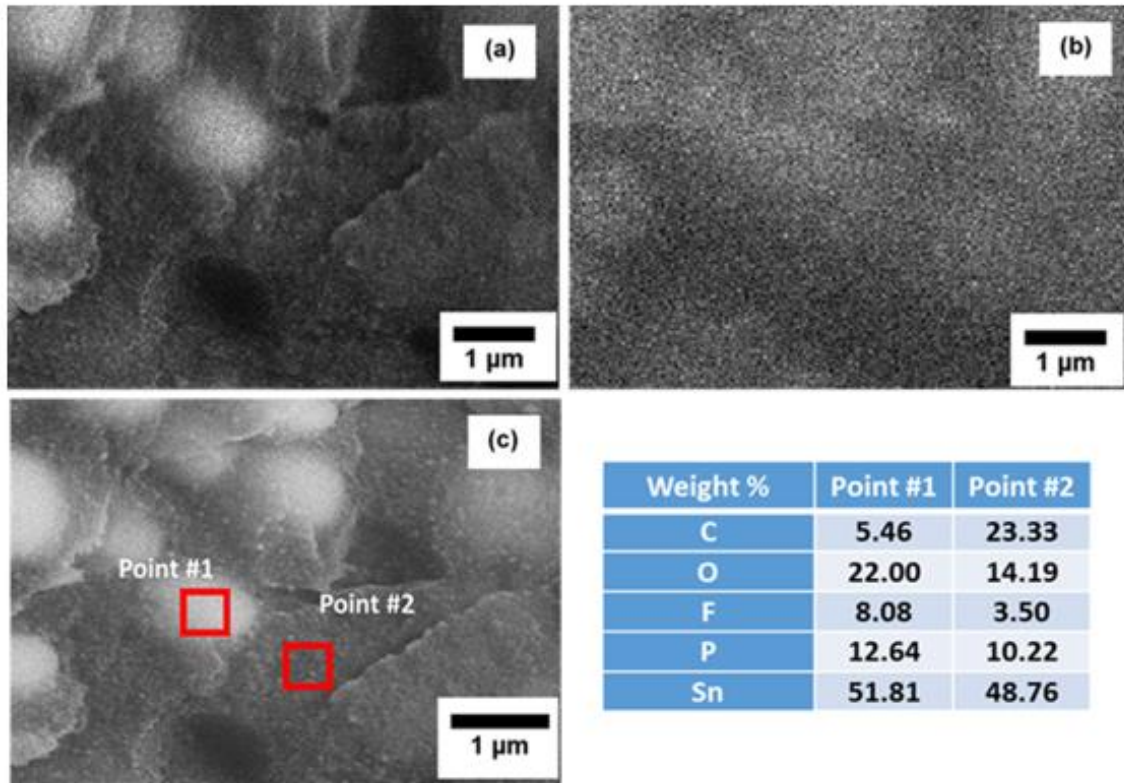| Weight %	Point #1	Point #2
C	5.46	23.33
O	22.00	14.19
F	8.08	3.50
P	12.64	10.22
Sn	51.81	48.76

Figure 6.5 (a) SEM image and EDX mapping images of (b) phosphorous (black background and white spot for each element) on the fracture surface of 15 wt.% Pglass/PET hybrids, and (c) elemental distribution analysis in two different regions in the hybrids.
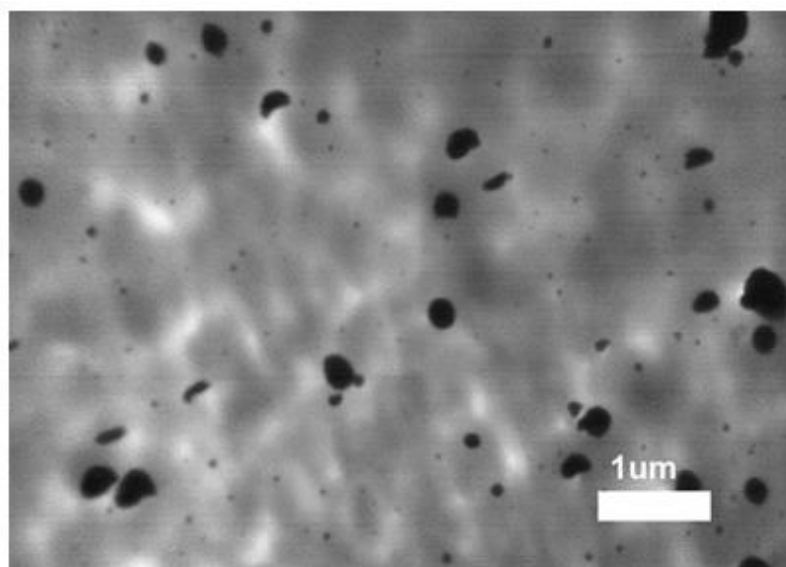
Figure 6.6 TEM image of nano- and micro-scale dispersed Pglass particles in the 5 wt.% Pglass/PET hybrids (black spots: Pglass particles, white/gray area: PET polymer).
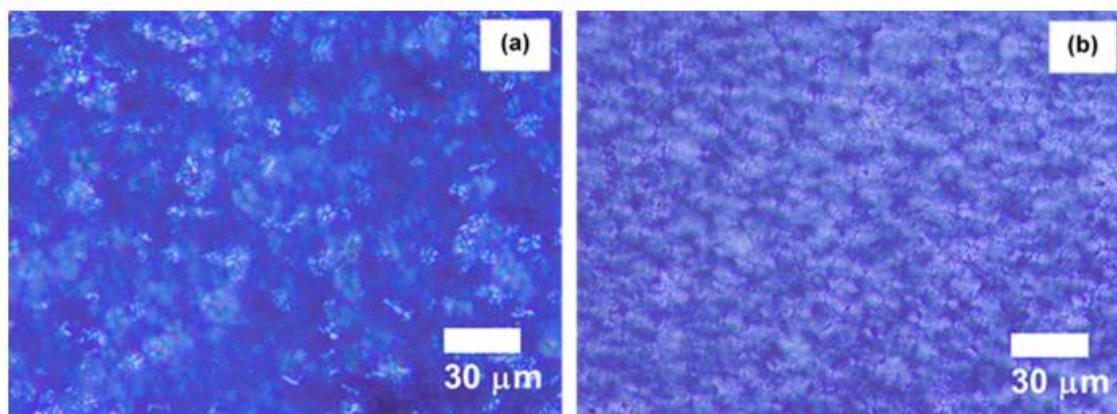

Figure 6.7 POM pictures of (a) pure PET and (b) 10 wt.%Pglass/PET hybrids isothermally crystallized at 226ºC after rapid cooling to crystallization temperature from the melting state at 280ºC.
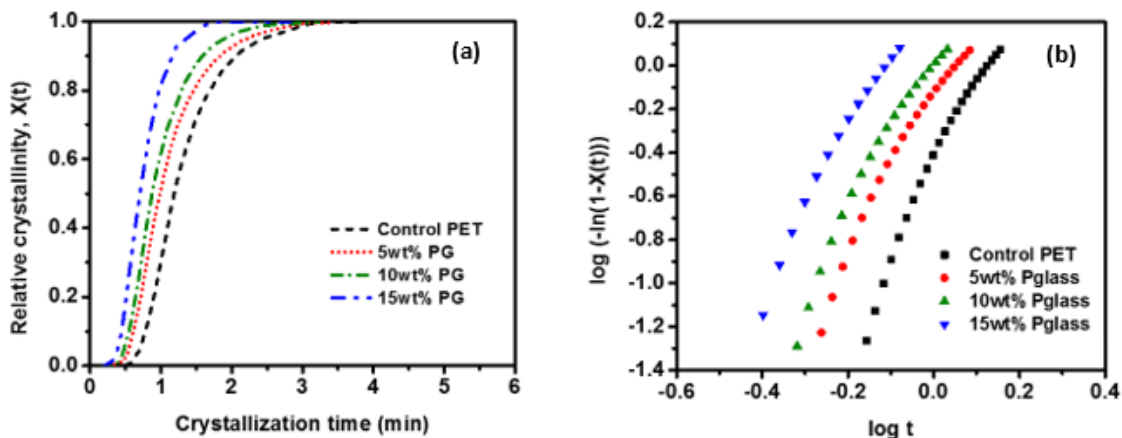
Figure 6.8 (a) Plots of relative crystallinity X(t) versus crystallization time (min) and (b) Avrami plot (linear portion, 5% < X(t) < 70% crystallinity) of log{-ln(1-X(t))} versus log t for isothermal crystallization for four different concentrations of Pglass in the PET matrix hybrid samples.
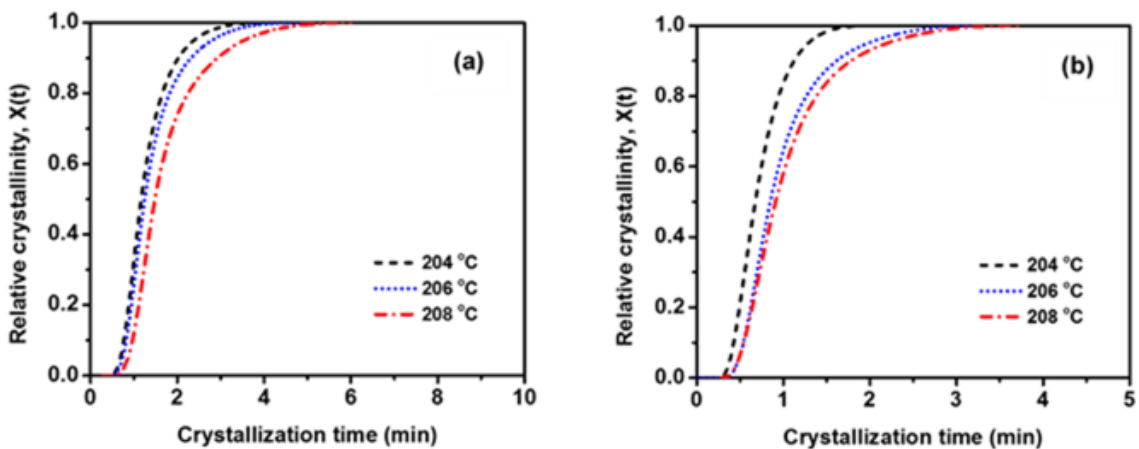

Figure 6.9 Relative crystallinity X(t) versus crystallization time (min) for crystallization of (a) control PET and (b) Pglass/PET hybrid samples (15 wt.% Pglass) at the indicated temperatures.
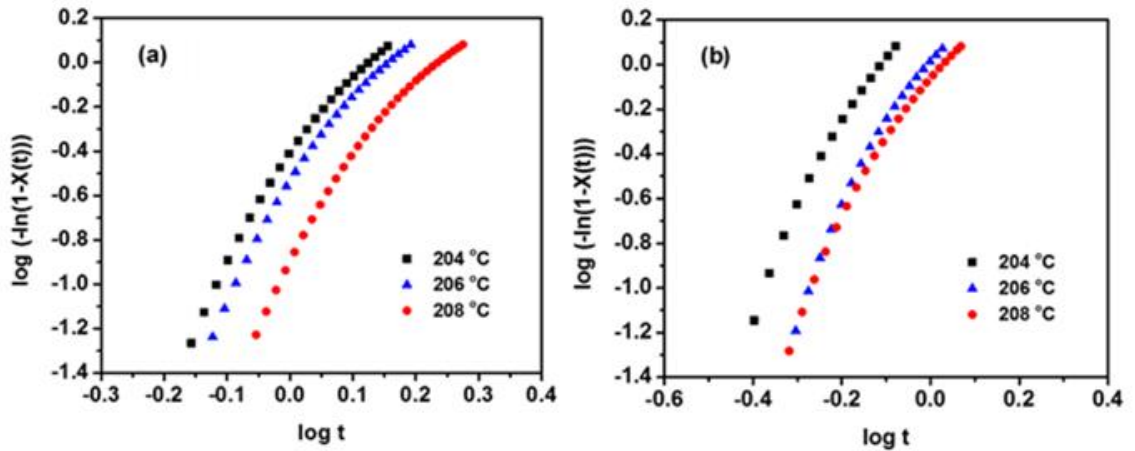
Figure 6.10 Avrami plot (linear portion, 5% < X(t) < 70% crystallinity) of log{-ln(1-X(t))} versus log t for isothermal crystallization of (a) control PET and (c) 15 wt.%Pglass/PET hybrids at the indicated temperature.
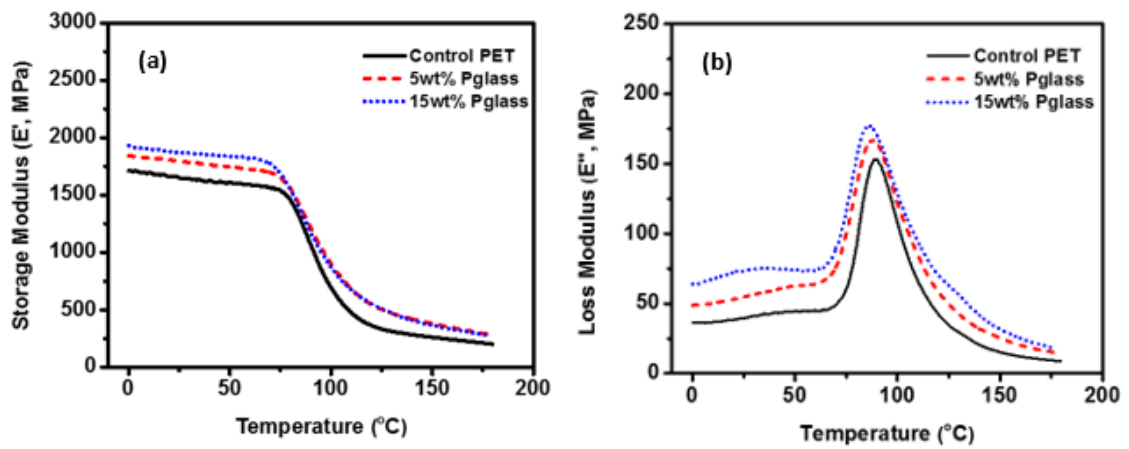
Figure 6.11 The effect of the Pglass concentration on (a) storage and (b) loss moduli of the PET and its hybrids incorporating Pglass.
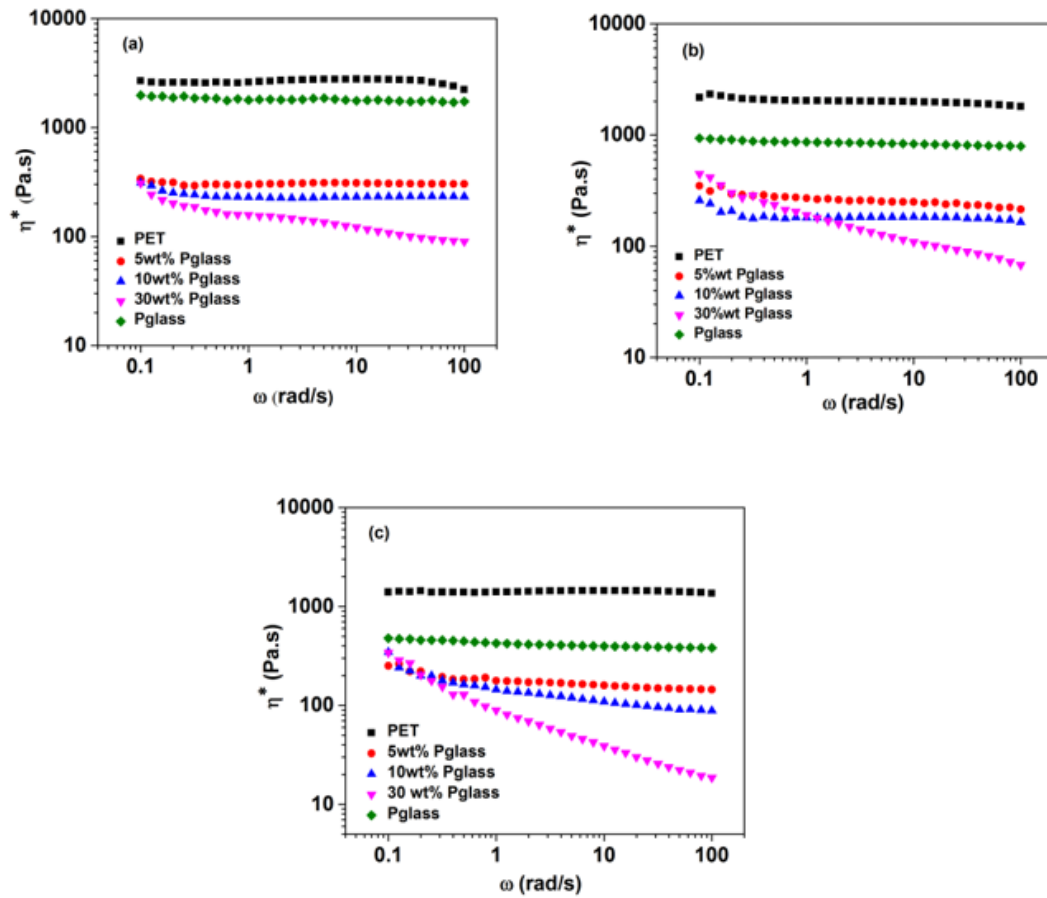
Figure 6.12 Variation of complex viscosity versus frequency for PET, Pglass and Pglass/PET hybrids at (a) 255°C, (b) 265°C and (c) 280°C.
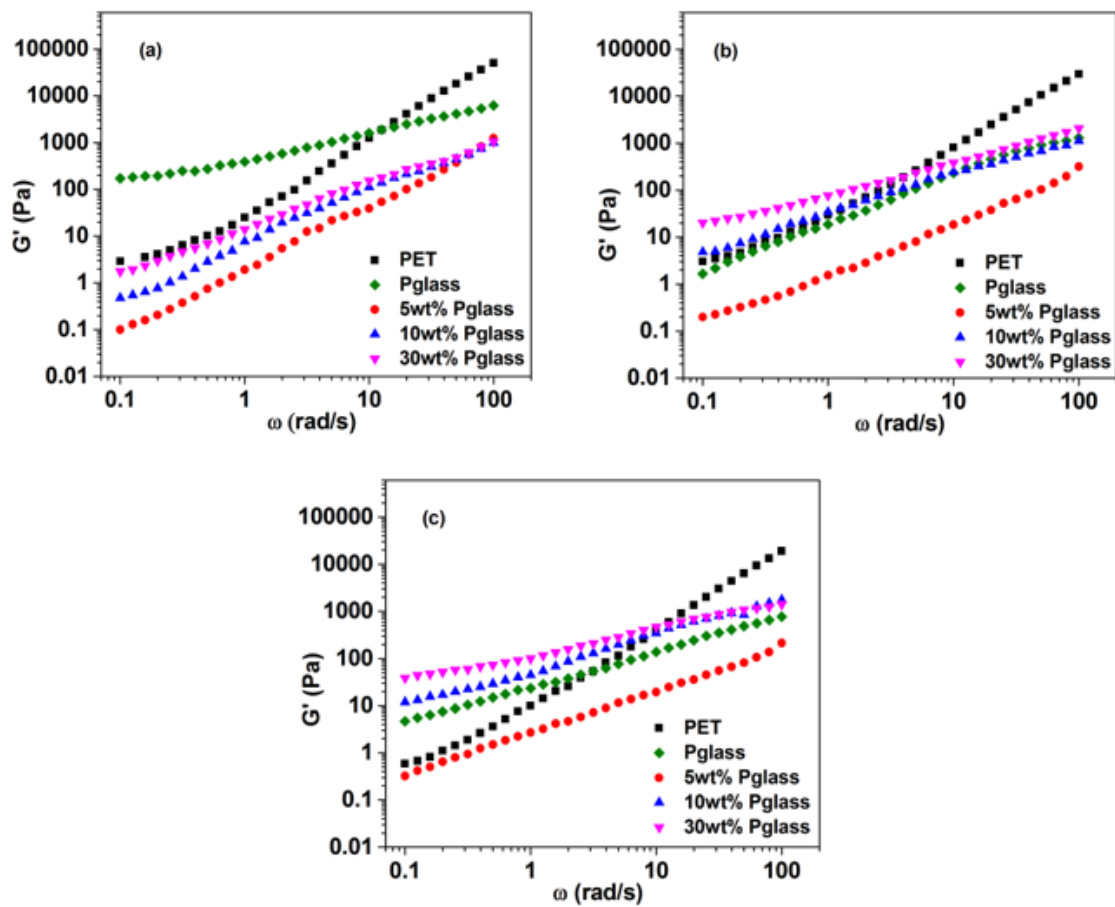
Figure 6.13 Variation of storage modulus versus frequency for PET, Pglass and Pglass/PET hybrids at (a) 255°C, (b) 265°C and (c) 280°C.
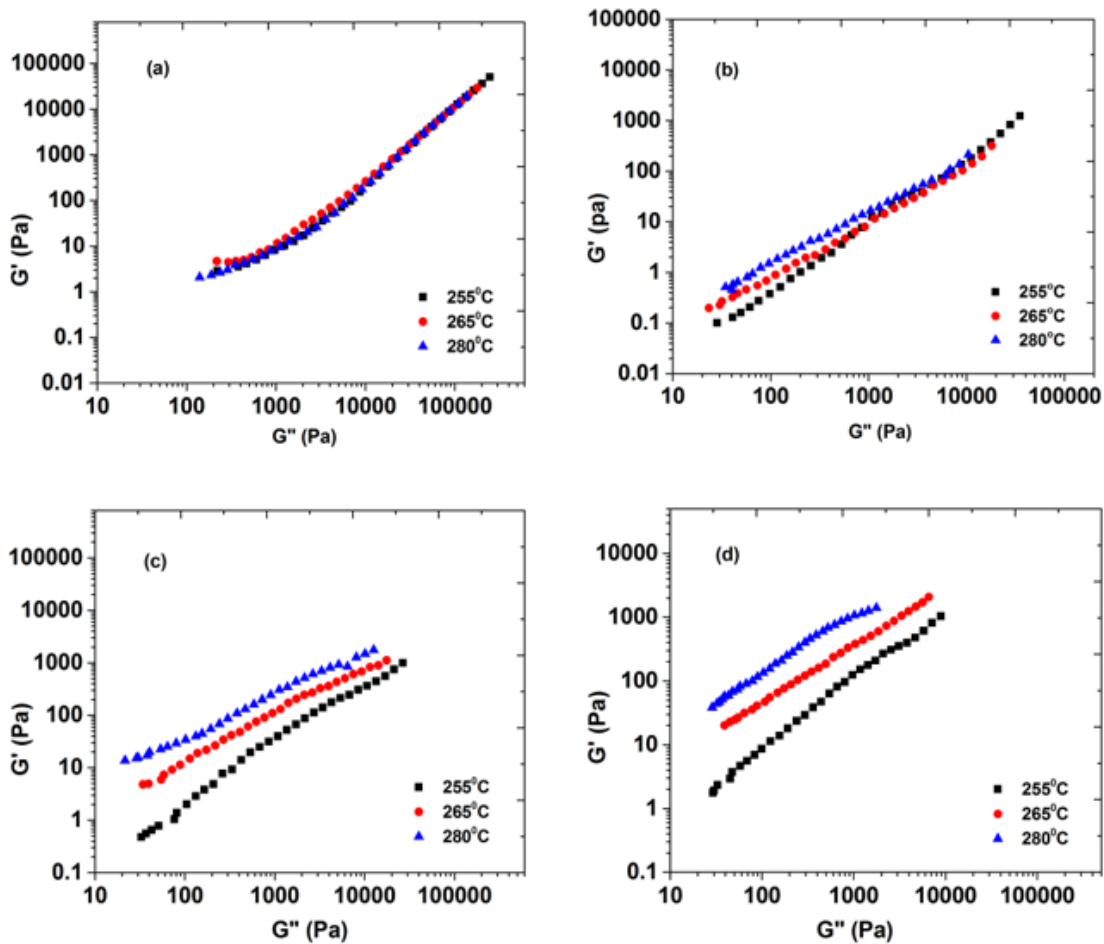
Figure 6.14 Han plots for (a) PET, (b) 5% Pglass, (c) 10% Pglass and (d) 30% Pglass hybrids at three experimental temperatures of 255°C, 265°C and 280°C.
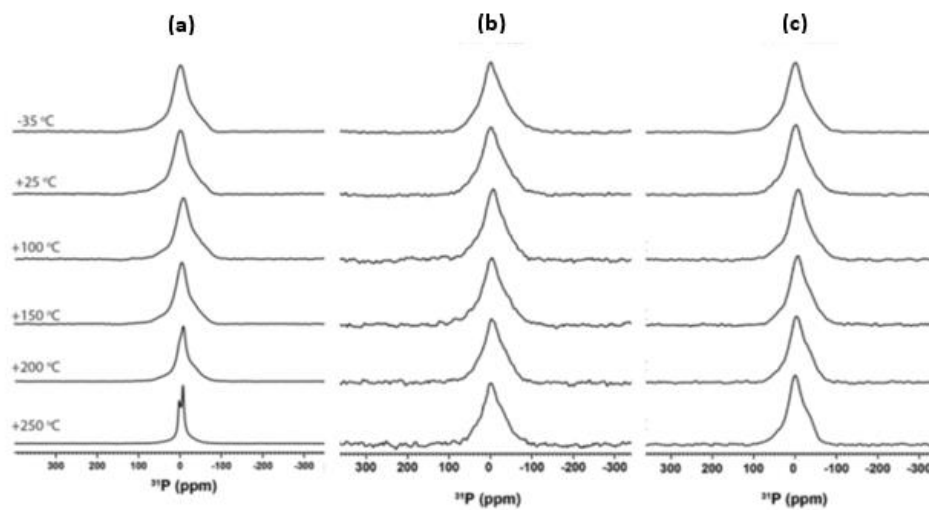
Figure 6.15 ^{31}P variable-temperature static NMR spectra for (a) pure Pglass, (b) 10 wt.%
Pglass, and (c) 50 wt.% Pglass hybrids.
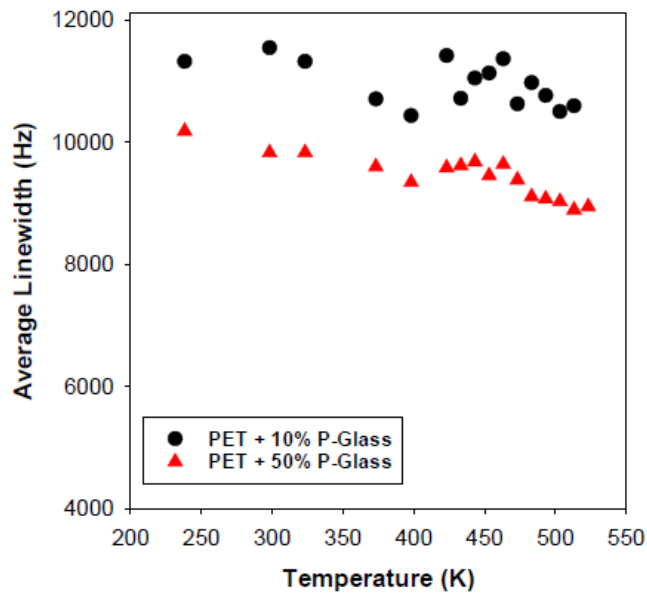
Figure 6.16 Average ^{31}P linewidth of 10 wt.% and 50 wt.% Pglass hybrids as a function
of temperature.
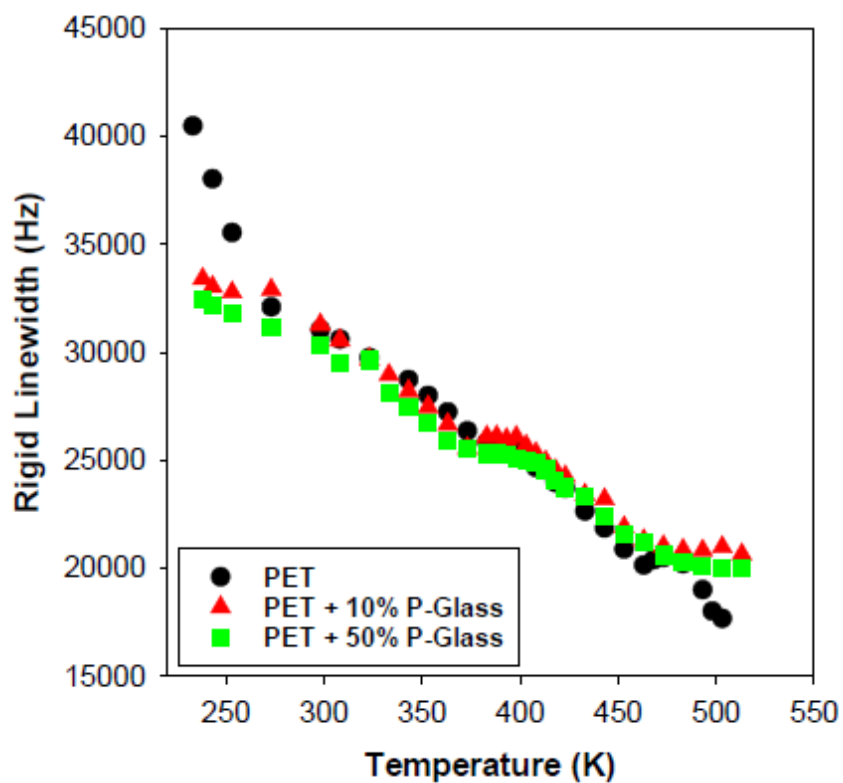
Figure 6.17 Average ^{1}H rigid linewidth of control PET, 10 wt.% and 50 wt.% Pglass samples as a function of temperature.

Table 6.1

Kinetic parameters from Avrami analysis for the isothermal crystallization of the Pglass/PET hybrids incorporating various concentration of Pglass.

| Sample	T_c (^{o}C)	n	K (min^{-1})	t_{max} (min)	$t_{1/2}$ (min)	G (min^{-1})
Control PET	204	4.113	0.339	1.216	1.170	0.855
5wt.%Pglass/PET	204	3.546	0.730	0.995	0.967	1.034
10wt.%Pglass/PET	204	3.621	1.128	0.885	0.857	1.167
15wt.%Pglass/PET	204	3.769	2.901	0.695	0.677	1.477

Table 6.2

Kinetic parameters from Avrami analysis for the isothermal crystallization of the control PET and 15 wt.%Pglass/PET hybrids at indicated crystallization temperatures.

	T_c (^{o}C)	n	K (min^{-1})	t_{max} (min)	$t_{1/2}$ (min)	G (min^{-1})
	204	4.113	0.339	1.216	1.170	0.855
Control PET	206	4.056	0.256	1.305	1.253	0.798
	208	3.877	0.135	1.552	1.487	0.672
	204	3.769	2.901	0.695	0.677	1.477
15 wt.% Pglass/PET	206	3.700	1.172	0.880	0.850	1.176
	208	3.302	0.887	0.930	0.910	1.099

CHAPTER VII – CONCLUSIONS AND POTENTIAL FUTURE RESEARCH

CONSIDERATIONS

The dissertation investigates the novel inorganic phosphate glass matrix nanocomposites incorporating POSS, in addition to the Pglass/PET hybrid material which is an inorganic/organic hybrid showing unique properties different from conventional polymer blends. The main focusof this study was to explore the preparation processes and characterizations of new POSS/Pglass composite materials prepared by the Pglass with the ultra-low glass transition temperature and POSS with nanoscale molecular structure. POSS was successfully applied to the Pglass matrix as a filler and as a coating material to achieve new and improved properties, using one pot synthesis, extrusion, sintering, and coating methods. This result is mainly attributed to the liquid state of Pglass over the process temperature. The homogeneously dispersed nanoscale POSS molecules increase the interface area between POSS and Pglass phases, determining the tunable composite material properties.

The inorganic Pglass matrix composites incorporating trisilanolphenyl polyhedral oligomeric silsesquioxane (TSP-POSS) were successfully prepared by one pot synthesis method. The obtained composites are still transparent with improved thermal, mechanical, and rheological properties compared to the pure Pglass. It was found that T_g of the nanocomposites gradually increased with increasing POSS contents up to 10 wt.% compared to that of pure Pglass (from 121.6°C to 147.6°C), which indicates a significant influence of bulky POSS molecules on the glass transition relaxation process in the Pglass matrix nanocomposites, attributed to the chemical and physical interactions between Pglass and POSS molecules. ^{31}P CP MAS analysis revealed that, as the amount

POSS in the nanocomposites increased up to 10 wt.%, the ratio of Q^0 to Q^1 increased from 20.5% to 27.1%. This result elucidates that the addition of POSS molecules in the Pglass matrix cause the decrease of the molecular size of the Pglass because the bulky POSS molecules are chemically and physically interacted with the Pglass molecules and restricted the increase of the molecular size of Pglass during the synthesis process.

It is found that as the amount of POSS increased up to 10 wt.% in the Pglass matrix nanocomposites prepared by synthesis method, the viscosity steadily increased, attributed to the addition of bulky POSS molecules in the liquid state of Pglass matrix. Han plot with storage modulus and loss modulus of pure Pglass and nanocomposites shows temperature dependency on the structure of samples at the specific temperature. The storage modulus of nanocomposites at the low frequency shows relatively higher than that of pure Pglass, indicating that the addition of POSS increased the elastic property of nanocomposites compared to that of pure Pglass. In addition, the complex viscosities of nanocomposites were fitted properly with 2-parameter Rouse model on the obtained nanocomposite samples, which is consistent with the NMR analysis showing two different small sizes of structures such as Q^0 and Q^1 in the Pglass.

Analysis of morphology of the fractured surface of the pure Pglass and nanocomposites showed smooth surfaces. On the other hand, AFM analysis with nanoscale resolution on the fractured surface revealed the increased nanoscale granule size on the fractured surface of nanocomposites due to the addition of POSS molecules compared to that of the pure Pglass. In addition, it is seen that there are obviously two phases on the fractured surface of the nanocomposites compared to a homogeneous one phase on the fractured surface of the pure Pglass. Nanomechanical properties of the

228

fractured surface of nanocomposites can be analyzed using AFM PeakForce Quantitative Nanomechanical Mapping (QNM) with tapping mode. It is observed that as the amount of POSS increased in the nanocomposites, the elastic modulus of the fractured surface of the nanocomposites increased due to the homogeneously dispersed rigid POSS molecules in the nanocomposites.

Extrusion process was used to prepare the glass matrix nanocomposites incorporating POSS which plays an important role as a foaming agent in addition to a filler material in the obtained nanocomposites. The obtained nanocomposites showed highly porous morphology on the fractured surface compared to the extruded pure Pglass. The morphology of the samples was tunable by an amount of POSS and conditions of extrusion process including process temperature and screw speed. A small number of voids are shown in the extruded pure Pglass due to a small amount of bounded water while a large number of voids were formed in the nanocomposites due to in situ condensation reaction between POSS and Pglass. Interestingly, the size of the voids in the nanocomposites was larger due to a merger between bubbles during the extrusion process with increasing screw speed and process temperature causing a higher mechanical energy and lower viscous of the nanocomposites. On the other hand, with increasing the amount of POSS in the nanocomposites, the number of voids became larger and the size of voids was decreased due to homogeneous dispersion of POSS molecules in the nanocomposites. In the solid-state NMR analysis, the complete consumption of silanol functional groups of the POSS was observed indicating that most of silanol groups were consumed via condensation reactions of POSS-Pglass and POSS-POSS, producing water vapor in the nanocomposites. Analysis of ^{31}P CP MAS showed

229

the increase of the ratio Q^0/Q^1 indicating that the addition of POSS molecules on the Pglass matrix reduced Q^1 structure of Pglass consistent with the result in the one pot synthesis system.

Incorporation of POSS in the Pglass matrix was carried out using the facile sintering process. The prepared composites showed the improved thermal stability and glass transition temperature with respect to a mixing method and a condition of sintering process. The DSC analysis revealed that the glass transition temperature significantly increased (50.2°C) due to the suspension mixing and stepwise sintering process, which is ascribed to the effective dispersion of POSS molecules. The suspension mixing method and the stepwise process efficiently facilitate the distribution of POSS molecules in the Pglass particles, resulting in the increased glass transition temperature due to enhanced interaction and chemical reaction between POSS and Pglass molecules. The result of the WAXD analysis showed that opaque property of the composites is not attributed to crystallinity of the composites. In addition, disappearance of crystallinity of POSS molecules in the composites is an evidence of molecular structural change of POSS due to the nanoscale distribution and chemical reactions in the composites. Investigation of ^{29}Si CP MAS solid-state NMR on the obtained composites showed that the silanol groups of POSS molecules completely consumed for the condensation reactions. Moreover, the position of the peak of closed-Si in the dehydrated POSS sample is obviously different from the position of the peak of closed-Si in the composites, indicating that the formation of Si bonds with Pglass in the composite is different from Si bonds in the dehydrated POSS.

The hydrophobic surface modification of bulk Pglass using hydrophobic POSS was studied to mimic a lotus leaf showing superhydrophobicity. The hydrophobicity is mainly achieved by the combination of low surface energy of the surface material and surface roughness. A combination of POSS with hydrophobic functional groups utilized as a coating material for the low surface energy and microsized Pglass particles used for rough surface on the bulk Pglass successfully achieved significantly improved hydrophobic property of the surface of the bulk Pglass. This study revealed an increase in contact angle from 81.6° on the pure bulk Pglass to 138.2° on the surface modified bulk Pglass using Pglass particles for roughness and trisilanol isooctyl POSS (TSO-POSS) for low surface energy. The investigation of chemical stability of POSS bonded to the surface of Pglass by strong solvents (acetone and ethanol) shows that POSS and Pglass were chemically bonded via condensation reaction. This result is supported by the XPS analysis showing the increase of bridging oxygen on the POSS modified Pglass bulk surface. POSS molecules with bulky and longer alkyl chains contributed to the higher contact angles by covering hydrophilic glass surface and shifting the contact point between water droplet and the hydrophobic surface higher from the surface of the bulk Pglass, which is the so-called "umbrella effect".

In addition, the properties of inorganic phosphate glass (Pglass)/organic polymer hybrids prepared by a mixing process are investigated. Poly(ethylene terephthalate) (PET) was mixed with Pglass in melt state, attributed to the ultra-low processing temperature of Pglass compared to normal glasses (i.e., borosilicate glass). The nano- and micro-scale dispersed Pglass particles in the composites were effectively investigated by SEM/EDX and TEM analysis. The thermal observation of the hybrids using DSC

231

revealed that polydispersed Pglass particles functioned as a nucleation agent, resulting in a shift of the peak crystallization temperature (T_p). The interesting result was the observation of the reduction of overall crystallinity of the hybrids with increasing Pglass concentrations, which is associated with the heterogeneous nucleation and impingement of crystals during the crystallization process, producing incomplete crystals in the hybrids.

Rheological analysis of the Pglass/PET hybrids showed the viscosity drop due to the interfacial lubrication effect in the hybrids. Pglass molecules might disrupt the chain entanglement of PET polymer molecules, inducing an interfacial lubricant effect on the hybrids resulting in the reduction of viscosity. Relationship between microstructure and temperature of hybrids was investigated by using the Cole-Cole diagram as functions of temperature and Pglass concentration. This result indicates that the interactions between Pglass and PET molecules in the hybrids were significantly improved with increasing temperature due to the enhanced miscibility of two components. Another analysis of temperature effect on the structural properties of hybrids was studied using variable-temperature (VT) solid-state NMR study. The mobility of pure Pglass observed in VT 31P NMR increased with increasing temperature up to 250°C while hybrids did not show significant change in the mobility due to the interfacial interaction between Pglass and PET molecules. The result acquired from VT 1H NMR showed that the mobility of the PET polymer chains at the interface of the two components is restricted by the Pglass molecules and is a function of Pglass concentration.

This dissertation will provide fundamental information for future studies related to the inorganic glass matrix composites incorporating inorganic or hybrid type of filler.

An understanding of the chemical structure and molecular scale distribution of filler in the composites is essential to improve the properties of composites because physical properties, such as thermal, mechanical, morphological, rheological, and crystalline properties of composites, will be defined by their chemical structure and formation of molecules. One of possible methods to investigate the effects of molecular structure of the final materials properties is computer simulation, which can achieve synergetic results with the empirical studies.

The work of hydrophobic surface modification using POSS on the Pglass could be extended in order to study how to make better transparent and hydrophobic Pglass. Materials and shapes of protrusion applicable on the Pglass surface could be selected and developed to improve optical properties. Hydrophobic transparent glass will be widely used for optical applications due to their self-cleaning function. The one pot synthesis and sintering methods could be extended with POSS as a nanoscale filler to other glasses including alkali zinc phosphate (AZP) glass, which have higher process temperature. This unique material of POSS has a nanoscale inorganic core composed of silicon oxide, which is thermally stable at the high temperature. Even though the grafted organic functional groups on the core of the molecules would be decomposed, the spherical core of POSS will be stable and implement the "nano effect" in the composites. Vacuum process during the sintering process at high temperature would be applicable to prepare transparent sintered composites without voids in the final materials. In addition, POSS molecules would be tunable with inorganic functional groups for the improved thermal stability at a high process temperature. Finally, the extrusion process used to prepare highly porous POSS/Pglass composites would be extended to producing functionalized

surface of porous glass-ceramic composites using modified POSS molecules for targeted

functions of heterogeneous catalysis and filter.